

Fluid dynamic modeling and simulation of supersonic flows and associated aerosol impaction processes in the mesosphere

by

Birte Salome Klug
from Frankenthal (Pfalz)

Accepted Dissertation thesis for the partial fulfillment of the
requirements for a Doctor of Natural Sciences

Fachbereich Natur- und Umweltwissenschaften
Rheinland-Pfälzische Technische Universität
Kaiserslautern-Landau

Thesis examiners:

Prof. Dr. Anna Hundertmark, RPTU Kaiserslautern-Landau
Dr. Ralf Weigel, JGU Mainz

Date of the oral examination: 26.04.2024

Ich versichere, dass ich die eingereichte Dissertation selbstständig verfasst habe und alle von mir für die Arbeit benutzten Hilfsmittel und Quellen in der Arbeit angegeben sind. Es sind keine weiteren Autoren und Autorinnen zu nennen, da keine anderen Personen Teile dieser Dissertation verfasst haben.

Ich habe keine entgeltliche Hilfe von Vermittlungs- oder Beratungsdiensten (Promotionsberater oder andere Personen) in Anspruch genommen.

Ich habe die Dissertation nicht in gleicher oder ähnlicher Form als Prüfungsarbeit für eine staatliche oder andere wissenschaftliche Prüfung im In- oder Ausland eingereicht.

Ich habe keine gleiche oder eine andere Abhandlung in einem anderen Fachbereich oder einer anderen wissenschaftlichen Hochschule als Dissertation eingereicht.

Mir ist bewusst, dass ein Verstoß gegen einen der vorgenannten Punkte den Entzug des Dokortitels bedeuten und gegebenenfalls auch weitere rechtliche Konsequenzen haben kann.

Landau in der Pfalz, den 24.07.2024

Birte Klug
Institut für Mathematik
FB Natur- und Umweltwissenschaften
RPTU Kaiserslautern-Landau
Fortstraße 7
D-76829 Landau

Schriftliche Darstellung zu dem eigenen Anteil bei Beiträgen

Die eingereichte Dissertation verweist an entsprechenden Stellen auf einen veröffentlichten Konferenzbeitrag Klug, B. S. et al. [2023] der *Comsol Conference 2023 Munich*. Autoren sind Birte Salome Klug, Prof. Dr. Anna Hundertmark sowie Dr. Ralf Weigel.

Ich versichere, dass ich aktiv an der Aufstellung des Strömungsmodells beteiligt war und seine Verallgemeinerung für kompressible Fluide im supersonischen Strömungsregime, die in Zusammenarbeit mit allen Coautor*innen entstanden ist. Die zugrundeliegende numerische Modellierung und die Simulationen habe ich eigenständig durchgeführt, analysiert, dargestellt und dokumentiert. Den Konferenzbeitrag habe ich selbstständig verfasst und erstellt. Die Coautor*innen haben anschließend ihre Verbesserungen hinsichtlich Formulierungen eingebracht.

Zusammenfassung

Taglich gelangen bis zu Hunderte von Tonnen kosmischen Materials in die Erdatmosphare, wobei eintreffende interplanetare Festkorper geeigneter Groe und Geschwindigkeit oberhalb von 80 km Hohe vergluhen. Die anschließende Rekombination und Polymerisation des verdampften Materials und die weitere Agglomeration bilden nanometergroe Aerosole, die als meteorische Rauchpartikel (MSP) bezeichnet werden. In entsprechenden Hohen zwischen 80 und 85 km treten mesospharische Eiswolken auf, sogenannte nachleuchtende Wolken (NLC). Bislang ist die Art der Kondensationskerne fur die Bildung von NLC-Elementen noch nicht abschließend geklart. Bisherige Studien deuten daraufhin, dass MSP als mogliche Eiskondensationskerne dienen konnen, experimentelle Nachweise fehlen allerdings. Um diese Annahme zu uberprufen, sind In-situ-Messungen zur Sammlung von Wolkenelementen (als Sammlung auf Substraten mit anschließender Laboranalyse) erforderlich. In-situ-Messungen in solchen Hohen sind jedoch aufwandig und kostenintensiv und nur mit Hilfe von Hohenforschungsraketen moglich, weshalb die Messdatenbasis sparlich ist. Ziel dieser Studie ist es, die Entwicklung des Konzepts eines tragheitsbasierten Partikel-sammlers fur den Messeinsatz auf einer Hohenforschungsrakete zu unterstutzen: Dies erfolgt durch die Aufstellung und Anwendung mathematischer und numerischer Modelle der Partikeltrajektorien und -kollisionen in einem an die Fluid-dynamik gekoppelten Verfahren. Mit Hilfe der numerischen Stromungsmechanik (unter Verwendung der kompressiblen Navier-Stokes-Gleichungen) wird das uberschallstromungsfeld mit Machzahlen von 1,31 und 1,75 in 85 km Hohe um das Instrumentenmodul der Hohenforschungsrakete unter verschiedenen Fluglagen analysiert und die Stromungsmuster untersucht, um die Anordnung und aerodynamische Auslegung der Sammler vorzuschlagen. Die Simulationen der Partikeltrajektorien basierend auf dem zweiten Newtonschen Axiom unter Beruck-sichtigung von Stokesscher Widerstands- und Brownscher Kraft in einer uberschallstromung. Die Analyse der Partikeltrajektorien, insbesondere im Nahfeld der Sammler unter verschiedenen Fluglagen und Partikelanzahlkonzentrationen bestatigen die Effektivitat der Sammlung von Partikeln durch das entwickelte Design. Anschließende physikalisch-chemische Analysen des gesammelten Partikelmaterials konnen das vermutete Vorhandensein von MSP bestatigen und Informationen uber die Zusammensetzung und Morphologie liefern. Zudem kann die Hypothese, ob MSP als Kondensationskerne fur die Bildung von NLC-Elementen dienen, anhand des Vorhandenseins in der Probe verifiziert werden.

Abstract

Up to hundreds of tons of cosmic material enter the Earth's atmosphere every day, where incoming interplanetary solids of suitable size and speed ablate at altitudes above 80 km. Subsequent recombination and polymerization of the vaporized material and further agglomeration is thought to form nanometer-sized aerosols, which are denoted as meteoric smoke particles (MSP). At the appropriate altitude between 82 and 85 km, mesospheric ice clouds, so-called noctilucent clouds (NLC), occur. Till now, the nature of condensation nuclei for the formation of NLC elements has not been conclusively explained. However, existing studies suppose that MSP can serve as possible ice condensation nuclei, but experimental evidence is lacking heretofore. To gain further insights into high atmosphere processes, in-situ measurements to collect cloud elements (as impactions on substrates, with subsequent physico-chemical analyses) are required. However, measurements at such altitudes are complex and cost-intensive and are only possible by means of sounding rockets, which is why only a sparse measurement database is available. The aim of this study is the mathematical and numerical modeling of the impaction processes coupled to the fluid dynamics to support the development of an inertia-based probe collector mounted on a sounding rocket. Compressible Navier-Stokes equations are numerically solved to analyze the supersonic flow field with Mach numbers of 1.31 and 1.75 at 85 km altitude around the instrument module of the sounding rocket under various flight attitudes. Flow patterns are investigated for the arrangement, orientation, and aerodynamic design of the collectors. Simulations of particle trajectories based on Newton's second law under the consideration of the Stoke's drag and Brownian force in the near-field of the collectors under consideration of different flight attitudes and particle number concentrations in a supersonic flow confirm the effectivity of the particle collection by the developed design of the collectors. Simulation results show that impactions on the designated collector surfaces are highly probable. Subsequent physico-chemical analyses of the collected particulate material may provide observational evidence for the presumed presence of MSP as well as information on the morphology and chemical composition. Consequently, their presence in the sample can confirm the hypothesis of the role of MSP as condensation nuclei for mesospheric ice particles.

Contents

1	Introduction	1
2	Mathematical modeling of fluid and particle motion	5
2.1	Modeling of fluid dynamics	5
2.1.1	Continuum or free molecular flow	5
2.1.2	Compressible and incompressible fluid motions	6
2.1.3	Navier-Stokes equations	8
2.1.4	Equations of the compressible fluid motion	19
2.2	Modeling of particle trajectories	19
2.2.1	Particle volume fraction	20
2.2.2	Stokes number	22
2.2.3	Equation of motion of a particle	22
2.2.4	Forces acting on particles	23
2.2.5	Comparison of the forces	30
2.2.6	Analytical solution of the particle equation of motion	30
2.3	Discretization methods	33
2.3.1	Finite element method	33
2.3.2	Stabilization techniques	35
2.3.3	Time discretization for fluid equations	41
2.3.4	Discretization for particle equations	43
3	Supersonic flow simulations around a sounding rocket payload and simulations of impaction-based collection of submicron aerosols	46
3.1	Meteoric smoke: potential condensation nuclei for NLC formation	48
3.2	Noctilucent clouds	51
3.3	The envisaged rocket flight	55
3.4	Supersonic flow simulations	58
3.4.1	Parameters for supersonic flow simulations	59
3.4.2	Model setup for supersonic flow simulations	61

Contents

3.4.3	Flow simulations to design the SPICE instrument	69
3.5	Collection of mesospheric particles on substrate mounts	104
3.5.1	Properties of MSP and NLC elements	104
3.5.2	Parameters for particle modeling	105
3.5.3	Equation of motion of particles	107
3.5.4	Solver settings for particle simulations	109
3.5.5	Model setup for particle simulations	110
3.5.6	Investigation of the particle size	115
3.5.7	Efficiency of inertia-based particle collection	120
3.5.8	Summary of particle collection investigations	126
4	Outlook for future development of the SPICE instrument	128
5	Summary and conclusion	132
	Appendices	135
A	List of abbreviations	136
B	Nomenclature	137
C	Mathematical notation	141
D	Mathematical formulas	143
E	Formulas of material properties	146
F	Determination of particle numbers	148
G	Tables of simulation data	149
	List of Figures	173
	List of Tables	179
	Bibliography	182

1 Introduction

As planet Earth moves along its orbit through our dusty solar system, cosmic dust accumulates in its atmosphere, where Plane, J. M. C. [2012] estimates a mass input of up to 300 tonnes within 24 hours. Incoming interplanetary solids (asteroids or meteoroids of diameters larger than 10 μm) with high speeds (of more than 40 km s^{-1}) ablate due to frictional heating from collisions with air molecules mainly at altitudes of 80 to 90 km [Plane, J. M. C., 2003]. Subsequently, the vaporous components recombine forming nanometer-sized aerosols, denoted as meteoric smoke particles (MSP) (hereafter often referred to as particles). Accordingly, since the end of the 19th century the phenomenon of noctilucent clouds (NLC) formation in the summer mesosphere (night shining clouds, with an appearance altitude of 82 to 85 km, presumably consisting of ice particles [Von Cossart, G. et al., 1999; Hervig, M. et al., 2001]) [Blackhouse, T. W., 1885; Jesse, O., 1890] is known and was frequently reported.

Although observations indicate small amounts of meteoric smoke in mesospheric ice particles [Hervig, M. E. et al., 2012; Hedin, J. et al., 2014], it is not yet known whether MSP are either involved in heterogeneous nucleation (which e.g. Rapp, M. and Thomas [2006] considers most likely) or are captured by coagulation on the surfaces of the ice particles after nucleation of the mesospheric ice particles [Wilms, H. et al., 2016]. Moreover, the chemical composition of MSP has not yet been conclusively clarified [Hervig, M. E. et al., 2012; Asmus, H. et al., 2014]. However, since MSP are thought to form from the material of ablated meteoroids, a corresponding composition is expected [Hunten, D. M. et al., 1980]. Nevertheless, MSP are assumed to play a crucial role in the formation of mesospheric phenomena: they are expected to act as condensation nuclei for ice particles of NLC [Rosinski, J. and Snow, 1961; Hunten, D. M. et al., 1980; Rapp, M. and Thomas, 2006; Hedin, J. et al., 2007a; Plane, J. M. C. et al., 2015; Wilms, H. et al., 2016]. To verify this

1 Introduction

assumption, in-situ measurements are required. So far, only a sparse database is available, leading to large uncertainties about the interaction process and possible interdependencies between the formation and existence of MSP and NLC elements, which in turn mainly leads to the formulation and discussion of theories and assumptions. One reason for the research deficit is the difficulty of sampling or physico-chemically analyzing the mesospheric particles: Soundings and analytical investigations at such altitudes are only possible at large effort and considerable costs by using sounding rockets. Currently, the working group Mobile Rocket Base (MORABA) of the German Aerospace Center (Deutsches Zentrum für Luft- und Raumfahrt, DLR) together with Bayern-Chemie is developing a sounding rocket, the so-called High Atmosphere Soarer (HAS) [Naumann, K. et al., 2020], with the purpose to conduct scientific measurements in the high atmosphere.

In this thesis, the computational fluid dynamics model is derived and coupled with a model to compute particle trajectories for the simulation of particle impactions of MSP. The derived model can be used to support the development of an inertia-based probe collector, called **Supersonic PartIcle CollEctor** (SPICE), through numerical simulations using COMSOL Multiphysics® [2023] PDE software. The overarching goal of the SPICE development is to collect mesospheric particles during a sounding flight. The SPICE instrument will consist of booms radially adjacent to the instrument module of the HAS. At the tips of the booms are substrate mounts installed with substrates on which the impacting particles will be sampled. Off-line analyses (using scanning electron microscopy techniques) of the collected particulate material may provide observational evidence for the presumed presence of MSP in the mesosphere, and their presentation on the sample (as an externally mixed deposit or embedded in a matrix of cloud particulate material) may shed light on the role of MSP, for example, as condensation nuclei for NLC elements. In addition, information on the number, size, morphology, and chemical composition of those particles sampled may be extracted.

In this regard, the development process of the SPICE instrument raises the following questions: Of particular interest is the evaluation of the evolving flow field around the instrument module of a sounding rocket at free stream Mach

1 Introduction

numbers of $Ma_1 = 1.31$ and $Ma_2 = 1.75$ at (85 km altitude), where the formation of a shock wave is expected.

- 1) Does the shock wave affect the particle collection?

To ensure that the boundary layer does not artificially influence the impact processes, the thickness of the boundary layer is investigated with regard to the following question:

- 2) What are the requirements on the geometry of the probe collector (i.e., the length of the booms) to allow the particle collection well outside the boundary layer of the rocket fuselage?

Given the arrangement of the substrate mounts and the demand that particle impactions on the substrates are to be achieved, a careful aerodynamic design of the substrate mounts is of crucial importance. To make predictions about whether particle collection on the final design of the substrate mounts will be successful, particle trajectories are calculated taking ambient conditions into account, and the questions arise:

- 3) Is the design developed effective for particle impactions? Is the collection area sufficient? How efficient is the collection mechanism? Is the efficiency sensitive to the angles of attack?

The answers to these questions are approached by means of numerical simulations presented here. Thus, the simulations will allow both prediction of the impaction processes and conclusions about particle sampling efficiencies under mesospheric conditions.

The outline of the present thesis is organized as follows: After the introduction in Chapter 1, the mathematical model of the fluid dynamics as well as the particle motions are described in Chapter 2, which is concluded with numerical analyses of the chosen numerical discretization methods. Subsequently, the current state of knowledge of meteoric smoke and noctilucent clouds is compiled in Sections 3.1 and 3.2. This is followed by the description of the supersonic flow simulations, beginning with the model setup in Paragraph 3.4.2 and ending with the analysis of the simulation results in Paragraph 3.4.3. Then, particle simulations are conducted in Section 3.5, starting with the model setup in Section 3.5.2, followed

1 Introduction

by effectiveness and efficiency analysis of the SPICE instrument in Sections 3.5.7 ff. Finally, the outlook in Chapter 4 is followed by the summary and conclusion in Chapter 5.

2 Mathematical modeling of fluid and particle motion

2.1 Modeling of fluid dynamics

Our Earth system is covered and surrounded by fluids, i.e., both the oceans as a liquid component and the gaseous atmosphere surrounding Earth's surface. The motions, dynamics of and the interactions between the fluid's constituents in both regimes are described by conservative laws of fluid mechanics. One of the mathematical models is the system of Navier-Stokes equations describing viscous fluid motions in both compressible and incompressible cases. When the maximum flow velocities are much smaller than the speed of sound, the natural dynamics of the atmosphere can be considered as a nearby incompressible continuum flow and can be described by the Navier-Stokes equations for incompressible fluids. These equations also apply to the motions and dynamics in water. However, when special flow conditions prevail (i.e., when the Mach number is greater than 0.3), air is usually considered compressible [Anderson, J. D., 2010]. In this case, strong temperature, pressure, fluid density, and velocity gradients occur in compression zones and require consideration. In the following, assumptions for the application of incompressibility are formulated and both the compressible and incompressible Navier-Stokes equations are derived.

2.1.1 Continuum or free molecular flow

In this thesis, the continuum fluid model is considered. Prior to the mathematical discussion of fluid dynamics, it is required to point out the limitations of the considered models for continuum flow dynamics, where the motions of viscous fluids can be described by the Navier-Stokes or Euler equations.

In general, the flow regime is characterized by the dimensionless Knudsen

number $Kn = \frac{\lambda}{L}$. If this fraction of the mean free path length λ of molecules (i.e., the mean distance for collisions between molecules), and the characteristic length L of an obstacle, payload, or gauge, is much smaller than one ($Kn \ll 1$) [Kulkarni, P. et al., 2011], the flow regime is described as a continuum flow. Here, an object embedded in the fluid perceives continuous collisions of molecules. These take place in such a multitude and frequency that a distinction of the individual molecular collisions is not possible and the fluid is perceived as a continuum [Anderson, J. D., 2010]. A Knudsen number of $Kn \gg 1$ requires a molecular dynamic flow description, since molecular collisions do not occur frequently and an embedded body can perceive individual collisions. Between these indicated regions, a transition flow regime is present from $Kn = 0.2$ to 20, and the continuum assumption is not valid here [Bird, G. A., 1994; Kulkarni, P. et al., 2011]. For the vertical profile of the Knudsen number in the Earth's atmosphere, this characteristic dimensionless quantity decreases rapidly with altitude.

To determine the appropriate Knudsen number, the mean free path λ is calculated by [Willeke, K., 1976]:

$$\lambda = \lambda_0 \left(\frac{p_0}{p} \right) \left(\frac{T}{T_0} \right) \left(\frac{1 + S_\mu/T_0}{1 + S_\mu/T} \right), \quad (2.1)$$

where $\lambda_0 = 0.0664 \mu\text{m}$ is the reference mean free path in air (at the pressure $p_0 = 101 \text{ kPa}$ and at the temperature $T_0 = 293 \text{ K}$, where the index 0 used refers to this conditions of air). The expression p states the pressure with $[p] = \text{kPa}$, T is the temperature with $[T] = \text{K}$, and $S_\mu = 110 \text{ K}$ (for air) corresponds to the Sutherland constant, which varies for different gases.

2.1.2 Compressible and incompressible fluid motions

Considering fluids at the molecular level, they are more or less compressible (i.e., the fluid density is variable). In many atmospheric applications of fluid dynamics and its simulations, the Navier-Stokes equations for incompressible fluids (where the density is constant) are applied. The assumptions under which the fluid can be considered as incompressible are [Pruppacher, H. R. and Klett, 2010]:

- 1.) $u \ll c$

2 Mathematical modeling of fluid and particle motion

This means, that the characteristic flow velocity u must be much smaller than the speed of sound c in air, which leads to the Mach number Ma connecting the two quantities:

$$Ma = \frac{|u|}{c}, \quad (2.2)$$

where the speed of sound is calculated by:

$$c = \sqrt{\gamma R_s T}, \quad (2.3)$$

where $\gamma = 1.4$ is the ratio of specific heats, $R_s = 287.05 \text{ J (kg K)}^{-1}$ is the specific gas constant, and T the temperature with $[T] = \text{K}$.

In general, air flows with a small Mach number of $Ma < 0.3$ can be considered as incompressible [Anderson, J. D., 2010]. If, on the other hand, the Mach number exceeds the value of one ($Ma > 1$), as may be the case in aerodynamic applications, the flow is said to be supersonic, and the compressibility of the air flow, which already starts at $Ma > 0.3$, must be taken into account. This leads to so-called shock regions with strong velocity, temperature, fluid density, and pressure gradients.

Further assumptions that need to be satisfied for the incompressibility assumption of air are: The frequency f of the oscillations in the air flow [Vladimirov, V. A. et al., 2015] (e.g., detectable by velocity fluctuations due to turbulence in vortex street wakes [Katopodes, N. D., 2018]) must satisfy to be less than the fraction of the speed of sound c and the characteristic length L of the obstacle,

$$2.) \quad f \ll \frac{c}{L}.$$

Third, it should hold that the static pressure difference of two points distant on the characteristic length scale L , $|p_{L_1} - p_{L_2}|$ is much smaller than the absolute (static) pressure magnitude p_a :

$$3.) \quad |p_{L_1} - p_{L_2}| \ll p_a.$$

Static pressure is the pressure that exists in the fluid at rest (e.g., the atmospheric pressure recorded by a ground sensing station) or at a great distance

from an embedded obstruction. Dynamic pressure is the pressure exerted by an obstacle embedded in a flow field, or when the obstacle is moving in the fluid because the fluid is backing upstream. This dynamic pressure, which affects the obstacle, is then higher than the static pressure.

Finally also the magnitude of the difference of the obstacle temperature T_d to the surrounding air temperature T_a needs to be much smaller than the air temperature for the incompressible model to apply:

$$4.) |T_d - T_a| \ll T_a.$$

Under the assumptions 1.) to 4.) the fluid can be modeled as incompressible without significant decrease of accuracy.

2.1.3 Navier-Stokes equations

The simulation of atmospheric fluid dynamics with its applications requires the numerical solution of the unknown three-dimensional flow field (i.e., the unknown flow velocity \vec{u}) and pressure p for an incompressible fluid. The equations used to determine the unknowns are the Navier-Stokes equations, derived in the following for incompressible as well as compressible fluids. An explanation can be found in the book by Anderson, J. D. [2010] and in Schmidt, H. and Suter [2009] or Prof. Dr. J. Lorenz [1994], which the content of this chapter refers to.

Let us assume a fluid particle ξ of a continuum starting at a certain position in space at a time $t_0 = 0$ s. Different approaches can be used to describe the fluid motion. In the Lagrangian approach, the change of the fluid particle position is used to describe the fluid motion, i.e., the particle position at the beginning is described by $\vec{x}(\xi, t_0) = \xi$ and at time $t > 0$ by $\vec{x}(\xi, t)$. This means that the fluid motion is described from the perspective of the particle and by its trajectory T with $T = \{(\vec{x}(\xi, t), t) | t \in I\}$ and $I \in [0; \infty)$. To determine the velocity of the particle and thus the velocity of the fluid

$$\vec{u}(\xi, t) = \frac{\partial \vec{x}}{\partial t}(\xi, t) \tag{2.4}$$

2 Mathematical modeling of fluid and particle motion

applies. In the Eulerian approach the fluid motion is described by the spatial point $\vec{x} = (x, y, z)^T = \vec{x}(\xi, t_0) = \xi$ with fixed spatial coordinates. The velocity $\vec{u}(\vec{x}, t)$ in the spatial point and hence of the fluid is obtained by the time derivation of the position vector:

$$\vec{u}(\vec{x}, t) = \vec{u}(\xi, t) = \frac{\partial \vec{x}}{\partial t}(\xi, t), \quad (2.5)$$

whereby $\vec{x} = \mathcal{L}_t(\xi) = \vec{x}(\xi, t)$, where \mathcal{L}_t is the Lagrangian mapping between the reference and actual material volume.

The Navier-Stokes equations are introduced by the Eulerian description as the preferred approach of fluid mechanics [Altenbach, H., 2012]. The first physical principle that introduces the Navier-Stokes continuum equation is the principle of the mass m conservation, which states that mass can neither be created nor destroyed. For the derivation of the continuity equation, a spatially fixed (i.e., constant in time) small control volume V is assumed within the flowing fluid. Thus, the fluid enters and leaves the volume through a surface S , and the total mass contained in the volume may change with time.

Let us first introduce the mass flow in one dimension: For this purpose, a surface S orthogonal to the flow direction is considered. The area of S is assumed to be so small that the flow velocity u_n flows through S without fluctuations, where u_n is the velocity component normal to S . The mass of the fluid m (with $m = \rho V$) flowing through the area S with velocity u_n after a finite time dt is calculated by:

$$m = \rho (u_n dt) S. \quad (2.6)$$

The resulting mass flow $\frac{dm}{dt}$, i.e., the fluid mass flowing through area S in a time interval dt , is calculated as

$$\frac{dm}{dt} = \rho u_n S, \quad (2.7)$$

which leads to the so called mass flux $\frac{dm}{dtS}$ (mass flow per area S), with

$$\frac{dm}{dtS} = \rho u_n. \quad (2.8)$$

2 Mathematical modeling of fluid and particle motion

As will be seen, the mass flux term is retrieved in the following equations. Coming back to the fixed finite, fluid-filled control volume V , where the net mass flow (i.e., the difference between incoming and outgoing mass flow) from the control volume (by convection) over a surface S needs to equal the change of the mass over time within the control volume V . Starting with the representation of a vector term of the net mass flow, considering a vector elementary surface $d\vec{S}$, it reads:

$$\rho \vec{u} \cdot d\vec{S}, \quad (2.9)$$

where $d\vec{S}$ points out of the control volume by convention (i.e., $d\vec{S} = \vec{n} dS$, where \vec{n} is the outer normal vector to the surface S) and \vec{u} is the velocity vector of the fluid. To obtain the total mass flow through the entire control surface S , the individual mass flows of the elemental surfaces are summed up resulting in the integral equation

$$\int_S \rho \vec{u} \cdot d\vec{S}. \quad (2.10)$$

The mass contained in the control volume V is given by $m = \int_V \rho dV$. If the mass in the control volume V changes with time, it is described by

$$\int_V \frac{\partial \rho}{\partial t} dV. \quad (2.11)$$

Combining both equations, the behavior of the fluid flowing through the fixed control volume is expressed by

$$\int_S \rho \vec{u} \cdot d\vec{S} = - \int_V \frac{\partial \rho}{\partial t} dV, \quad (2.12)$$

where the change of mass in a fixed volume V is balanced by the mass flow over its surfaces. Note: the decreasing density in the volume V requires mass outflow (i.e., $\vec{u} \cdot d\vec{S}$ is positive). Finally, equation 2.12 becomes

$$\frac{d}{dt} m = \int_V \frac{\partial \rho}{\partial t} dV + \int_S \rho \vec{u} \cdot d\vec{S} = 0. \quad (2.13)$$

Considering the mass contained in the control volume in a fixed time t , this mass can be advected to a different spatial position and volume, but does not change. $V = V(t)$ can be considered as a mapping of the initial material volume V_0 , and the conservation of mass along advection (i.e., $\int_{V(t)} \frac{\partial \rho}{\partial t} dV(t)$) holds. Tracking the

2 Mathematical modeling of fluid and particle motion

mass in the fixed control volume in time and applying the Reynold's transport theorem (cf. Appendix D), one comes to equation 2.13 as well. Utilizing Gauss theorem to the surface integral (see Appendix D), equation 2.13 becomes

$$\int_V \frac{\partial \rho}{\partial t} dV + \int_V \nabla \cdot (\rho \vec{u}) dV = 0. \quad (2.14)$$

In terms of the integral average (cf. Appendix D) the equation holds for any arbitrary small volume V , where the resulting partial differential equation is

$$\underbrace{\frac{\partial \rho}{\partial t}}_{\substack{\text{temporal change} \\ \text{of mass}}} + \underbrace{\nabla \cdot (\rho \vec{u})}_{\substack{\text{change} \\ \text{of mass flux}}} = 0. \quad (2.15)$$

Assuming now an incompressible fluid, where $\rho \neq 0$ is constant, equation 2.15 becomes

$$\rho \nabla \cdot \vec{u} = 0, \quad (2.16)$$

and further simplifies to the incompressible continuity equation of:

$$\nabla \cdot \vec{u} = 0. \quad (2.17)$$

The next equation is the momentum equation, whose physical principle is based on Newton's second law:

$$\vec{F} = \frac{d}{dt}(m\vec{u}), \quad (2.18)$$

where the change in momentum over time (i.e., the product of the mass m and velocity \vec{u}) of a body is equal to the general force \vec{F} acting on it. Let us consider the forces that occur when a fluid flows through a control volume fixed in space. Here, body forces as well as surface forces occur. For example, the most common body force is the gravitational force acting on the entire control volume, and surface forces are caused by compressive or shear stresses.

For the transfer of the left side and to determine the total force \vec{F} , let us first consider the net body force per unit mass \vec{f} acting on the fluid inside the control volume V . The body force exerted on an elemental volume dV is thus $\rho \vec{f} dV$

and the total body force \vec{F}_b is given by

$$\vec{F}_b = \int_V \rho \vec{f} dV. \quad (2.19)$$

Considering next the external pressure p acting on the elemental control volume as a surface force described by $-p d\vec{S}$ (acting in the opposite direction of $d\vec{S}$), the total pressure force on the surface is obtained:

$$\vec{F}_p = - \int_S p d\vec{S}. \quad (2.20)$$

The next surface force to be considered is the viscous force, with the viscous stress tensor τ acting on the surface $d\vec{S}$ of the elemental control volume, where the total viscous force becomes

$$\vec{F}_v = \int_S \tau \cdot d\vec{S}. \quad (2.21)$$

As the surface forces are summarized, they combine to the Cauchy stress tensor σ (including the surface pressure and the viscous stress), which is $\sigma = -p\mathbf{I} + \tau$, where $\mathbf{I} := (\delta_{ij})_{i,j \in \{1,2,3\}}$ is the identity matrix.

The following approach is used for τ :

$$\tau = 2\mu D - \frac{2}{3}\mu(\nabla \cdot \vec{u})\mathbf{I}, \quad (2.22)$$

with the dynamic viscosity μ , and the deformation tensor D , with

$$D = \frac{1}{2}(\nabla \vec{u} + (\nabla \vec{u})^T) = \frac{1}{2} \left(\frac{\partial u_i}{\partial x_j} + \frac{\partial u_j}{\partial x_i} \right)_{i,j \in \{1,2,3\}}. \quad (2.23)$$

Summing the individual forces, the total force \vec{F} acting on a fixed control volume while the flow passes through it is given by

$$\vec{F} = \int_V \rho \vec{f} dV + \int_S \sigma \cdot d\vec{S}. \quad (2.24)$$

Applying the Gauss theorem to transform the surface into volume integrals, the

equation becomes:

$$\vec{F} = \int_V \rho \vec{f} dV + \int_V \nabla \cdot \sigma dV, \quad (2.25)$$

with

$$\nabla \cdot \sigma = -\nabla \cdot p\mathbf{I} + \nabla \cdot \left[\mu \left(\nabla \vec{u} + (\nabla \vec{u})^T \right) - \frac{2}{3} (\nabla \cdot \vec{u}) \mathbf{I} \right], \quad (2.26)$$

which results, under consideration of the row-wise application (cf. Appendix C) with $\nabla \cdot (\nabla \vec{u} + (\nabla \vec{u})^T) = \Delta \vec{u} + \nabla (\nabla \cdot \vec{u})$ and with $\nabla \cdot \vec{u} = 0$ for the incompressible case, in

$$\nabla \cdot \sigma = -\nabla \cdot p\mathbf{I} + \mu (\Delta \vec{u}). \quad (2.27)$$

The right-hand side of equation 2.18 describes the change in momentum of the fluid within the fixed control volume as it flows through (e.g., due to the forces described). The change in momentum with time t is

$$\frac{d(m\vec{u})}{dt} = \frac{d}{dt} \left[\int_V \rho \vec{u} dV \right]. \quad (2.28)$$

As this equation is a vector equation, the three scalar equations are $\frac{d(mu_i)}{dt} = \frac{d}{dt} \int_V \rho u_i dV$, where the index $i = 1, 2, 3$ stands for the three spatial directions. Analogous to the mass conservation, the overall momentum change in a fixed control volume is described by the temporal change of the momentum within volume V and the net flow leaving the volume through the surface S :

$$\frac{d(mu_i)}{dt} = \int_V \frac{\partial(\rho u_i)}{\partial t} dV + \int_S \rho u_i \vec{u} \cdot d\vec{S}. \quad (2.29)$$

Applying the Gauss theorem to convert the surface into a volume integral, equation

$$\frac{d(mu_i)}{dt} = \int_V \frac{\partial(\rho u_i)}{\partial t} dV + \int_V \nabla \cdot (\rho u_i \vec{u}) dV \quad (2.30)$$

results. Focussing on the term $\nabla \cdot (\rho u_i \vec{u})$ the derivative yields:

$$\nabla \cdot (\rho u_i \vec{u}) = \sum_{j=1}^3 \frac{\partial}{\partial x_j} (\rho u_i u_j) = \sum_{j=1}^3 \frac{\partial}{\partial x_j} (\rho u_j) u_i + \sum_{j=1}^3 \rho u_j \frac{\partial}{\partial x_j} u_i, \quad (2.31)$$

where $\sum_{j=1}^3 u_j \frac{\partial}{\partial x_j} = \vec{u} \cdot \nabla$. Thus, the derivative for the i -th component is:

2 Mathematical modeling of fluid and particle motion

$\nabla \cdot (\rho u_i \vec{u}) = \nabla \cdot (\rho \vec{u}) u_i + \rho (\vec{u} \cdot \nabla) u_i$, and coming back to a vectorial description under consideration of the dyadic product (cf. Appendix C), following yields:

$$\nabla \cdot (\rho \vec{u} \cdot \vec{u}^T) = \nabla \cdot (\rho \vec{u}) \vec{u} + \rho (\vec{u} \cdot \nabla) \vec{u}. \quad (2.32)$$

Focussing on the incompressible fluid case with $\rho = \text{const.}$, the derivative yields: $\nabla \cdot (\rho \vec{u} \cdot \vec{u}^T) = \rho (\vec{u} \cdot \nabla) \vec{u}$. Combining the equations introduced so far with respect to the previous calculations, the so-called Navier-Stokes momentum equation for $\rho = \text{const.}$ and thus $\nabla \cdot \vec{u} = 0$ in integral form is obtained:

$$\int_V \frac{\partial}{\partial t} (\rho \vec{u}) + \rho (\vec{u} \cdot \nabla) \vec{u} dV = \int_V \nabla \cdot \sigma + \rho \vec{f} dV. \quad (2.33)$$

Since 2.33 holds for arbitrary small V , under consideration of a constant fluid density and the integral average, the differential equation for incompressible fluids is derived:

$$\underbrace{\rho \frac{\partial \vec{u}}{\partial t}}_{\text{temporal change of momentum}} + \underbrace{\rho (\vec{u} \cdot \nabla) \vec{u}}_{\text{change of momentum by advection}} = \underbrace{-\nabla p \mathbf{I}}_{\text{pressure force}} + \underbrace{\mu \Delta \vec{u}}_{\text{viscous shear force}} + \underbrace{\rho \vec{f}}_{\text{body force}} \quad (2.34)$$

Without the simplification of assuming $\rho = \text{const.}$, the equation for compressible fluids is (note that equation 2.32 can be applied):

$$\frac{\partial(\rho \vec{u})}{\partial t} + \nabla \cdot (\rho \vec{u} \cdot \vec{u}^T) = -\nabla p \mathbf{I} + \nabla \cdot \left[\mu \left(\nabla \vec{u} + (\nabla \vec{u})^T - \frac{2}{3} (\nabla \cdot \vec{u}) \mathbf{I} \right) \right] + \rho \vec{f}. \quad (2.35)$$

In summary, the dynamics of incompressible viscous fluids are described by the two equations 2.15 and 2.34 for the unknown quantities velocity and pressure. Furthermore, fluid density and temperature are assumed to be constant for incompressible flows. As mentioned in Section 3.4.2, air is considered compressible when the Mach number exceeds the limit of about 0.3, and assumes supersonic velocity when the Mach number is greater than 1. For compressible flows, where the fluid density is not constant and thus unknown, a further equation is required to describe the system, which is the energy equation. However, the energy equation contains the internal energy e , where the consideration of the internal energy equation becomes necessary. Thereby, the equation of the internal energy contains the temperature as an unknown quantity and the ideal

2 Mathematical modeling of fluid and particle motion

gas law is introduced. Thus, the five unknowns that now underlie the system require five equations to solve. In this way, high velocity, pressure, and fluid density gradients leading to sharp temperature gradients can be solved, with energy being a necessary and important additional issue to be considered.

For the compressible case, the energy equation is introduced, whose physical principle is the conservation of energy. It states that energy can neither be destroyed nor created, but only transformed. The energy equation is based on the first law of thermodynamics, assuming a fixed volume with an amount of internal energy δe . This amount of energy changes when either heat is added to the system, which is expressed as δq , or when work is done on the system δw . Both heat and work are forms of energy and thus are responsible for energy changes. The underlying equation is:

$$\delta e = \delta q + \delta w. \quad (2.36)$$

Consider again a small control volume V of fluid fixed in space embedded in a fluid flow. Let us focus on the energy change within an elemental volume caused by heating. Let $\vec{q} = -k\nabla T$ be the heat flow vector, with k the thermal conductivity and T the temperature. The energy in form of heat, flowing through the surface into the control volume is expressed by $-\int_S \vec{q} \cdot d\vec{S}$, which results (under application of the Gauss theorem) in $-\int_V \nabla \cdot \vec{q} dV$, and indicates the rate of heat addition to the control volume V . Together with the term $Q = Q(\vec{x}, t)$, which contains the heat sources, the total rate of heat addition to the control volume results in

$$-\int_V \nabla \cdot \vec{q} dV + Q. \quad (2.37)$$

The energy of the control volume also changes due to work done on the fluid within the control volume, both by surface and body forces. Consider a moving volume to which a general force \vec{F} is applied. The work done on the body within a small time interval dt as it is displaced by a distance $d\vec{x}$ is described by $\vec{F} \cdot \frac{d\vec{x}}{dt} = \vec{F} \cdot \vec{u}$, where \vec{u} is again the velocity vector of the fluid.

In terms of the surface force exerted on an elemental surface element of the control volume (with the total stress tensor $\sigma = -p\mathbf{I} + \tau$), the expression is given by $(\sigma\vec{u}) \cdot d\vec{S}$, and the summation over the entire surface gives the equation

in the limiting case:

$$\int_S (\sigma \vec{u}) \cdot d\vec{S}. \quad (2.38)$$

Applying Gauss's theorem, the equation becomes:

$$\int_V \nabla \cdot (\sigma \vec{u}) dV. \quad (2.39)$$

On the other hand, considering the body force \vec{f} , which exerts work on the fluid throughout the volume, the equation is:

$$\int_V \rho \vec{f} \cdot \vec{u} dV. \quad (2.40)$$

Thus, the work done on the fluid in form of surface and body forces can be summed up as:

$$\int_V \nabla \cdot (\sigma \vec{u}) + \rho \vec{f} \cdot \vec{u} dV. \quad (2.41)$$

Considering the total energy contained in the control volume, a part of it corresponds to the internal energy e resulting from random molecular motions within the volume. The other part is the kinetic energy per unit mass $\frac{1}{2}u^2$ of the fluid moving at a certain velocity \vec{u} within the fixed fluid volume, i.e., the total energy per unit mass is given by $e + \frac{1}{2}u^2$, where $u = \|\vec{u}\|$ is the velocity magnitude. The change in total energy within the volume as the fluid flow passes through the control volume is described by $(e + \frac{1}{2}u^2)(\rho \vec{u} \cdot d\vec{S})$ (i.e., energy times mass flow through the surface). Summing over the entire surface in the limiting case, the equation becomes:

$$\int_S (e + \frac{1}{2} u^2) (\rho \vec{u} \cdot d\vec{S}). \quad (2.42)$$

The temporal change of the total energy within the volume is:

$$\int_V \frac{\partial}{\partial t} \rho (e + \frac{1}{2} u^2) dV, \quad (2.43)$$

and taken together, this gives the familiar form of:

$$\int_V \frac{\partial}{\partial t} \rho (e + \frac{1}{2} u^2) dV + \int_S \rho (e + \frac{1}{2} u^2) \vec{u} \cdot d\vec{S}. \quad (2.44)$$

2 Mathematical modeling of fluid and particle motion

Applying the Gauss theorem, the expression becomes

$$\int_V \frac{\partial}{\partial t} \rho \left(e + \frac{1}{2} u^2 \right) dV + \int_S \nabla \cdot \left[\rho \vec{u} \left(e + \frac{1}{2} u^2 \right) \right] dV. \quad (2.45)$$

Summing the obtained terms for a fluid flowing through a fixed volume, where heat is added to the fluid within the control volume, work is done, so that the energy of the fluid within the fixed control volume changes as the fluid flows through, and since the obtained equations hold for arbitrary small V , under consideration of the integral average, the following differential equation is obtained:

$$\underbrace{\frac{\partial}{\partial t} \left[\rho \left(e + \frac{u^2}{2} \right) \right]}_{\text{temporal change of total energy}} + \underbrace{\nabla \cdot \left[\rho \vec{u} \left(e + \frac{u^2}{2} \right) \right]}_{\text{change of total energy by advection}} = \underbrace{-\nabla \cdot \vec{q} + Q}_{\text{heat addition}} + \underbrace{\nabla \cdot (\sigma \vec{u})}_{\text{work due to surface forces}} + \underbrace{\rho(\vec{f} \cdot \vec{u})}_{\text{work due to body force}}. \quad (2.46)$$

As can be seen, equation 2.46 contains two more unknowns (i.e., the temperature T and the internal energy e). At the moment, there are three equations for five unknowns, namely p , \vec{u} , ρ , e , and T . To complete this system, a fourth equation for the internal energy is considered, with

$$e = c_v T, \quad (2.47)$$

where $c_v = \frac{\gamma R_s}{\gamma - 1}$ is the specific heat capacity, γ is the specific heat ratio and R_s is the specific gas constant. The last equation needed to solve for the temperature is the ideal gas law

$$\rho = \frac{p}{R_s T}, \quad (2.48)$$

which relates the fluid density to pressure and temperature, which is the usual approach of the atmosphere [Lohmann, U. et al., 2016].

In summary, these five equations for five unknowns form a system that is applied to simulate supersonic and compressible flow conditions in a high Mach number model. This system of equations determines the velocity field \vec{u} , pressure p , density ρ , energy e and temperature distribution T .

2 Mathematical modeling of fluid and particle motion

The ideal gas law assumption further allows the application of Sutherland's Law [Sutherland, W., 1893] to approximate the thermal conductivity k as well as the dynamic viscosity μ of the ideal gas depending on the temperature, which reads [White, F. M. and Majdalani, 2006]

$$k = k_{ref} \left(\frac{T}{T_{ref}} \right)^{\frac{3}{2}} \frac{T_{ref} + S_k}{T + S_k}, \quad (2.49)$$

and

$$\mu = \mu_{ref} \left(\frac{T}{T_{ref}} \right)^{\frac{3}{2}} \frac{T_{ref} + S_\mu}{T + S_\mu}. \quad (2.50)$$

Here, k_{ref} is the reference thermal conductivity, T_{ref} the reference temperature, and S_k the Sutherland constant for the thermal conductivity. The second equation includes the parameters μ_{ref} , which denotes the reference dynamic viscosity, and S_μ denoting the Sutherland constant for the dynamic viscosity. The corresponding values are listed in Section 3.4.1.

2.1.4 Equations of the compressible fluid motion

$$\frac{\partial \rho}{\partial t} + \nabla \cdot (\rho \vec{u}) = 0 \quad (2.15)$$

continuity equation

$$\frac{\partial(\rho\vec{u})}{\partial t} + \nabla \cdot (\rho\vec{u}\cdot\vec{u}^T) = -\nabla p\mathbf{I} + \nabla \cdot \left[\mu \left(\nabla\vec{u} + (\nabla\vec{u})^T - \frac{2}{3}(\nabla \cdot \vec{u})\mathbf{I} \right) \right] + \rho\vec{f} \quad (2.35)$$

momentum equation

$$\frac{\partial}{\partial t} \left[\rho \left(e + \frac{u^2}{2} \right) \right] + \nabla \cdot \left[\rho\vec{u} \left(e + \frac{u^2}{2} \right) \right] = -\nabla \cdot \vec{q} + Q + \nabla \cdot (\sigma\vec{u}) + \rho(\vec{f} \cdot \vec{u}) \quad (2.46)$$

energy equation

$$e = c_v T \quad (2.47)$$

internal energy equation

$$\rho = \frac{p}{R_s T} \quad (2.48)$$

ideal gas law

2.2 Modeling of particle trajectories

Numerical simulations allow for understanding and predicting particle motion (solid particles) contained in a fluid, accurately tracking the trajectory of each particle, and analyzing particle trajectories at a resolution of microseconds or even higher. Particle trajectories serve to provide dynamic information; they enable visualization and analysis of vector fields within flow regimes. Moreover, particle properties such as their kinetic energy or temperature can be studied as a function of particle material properties.

This work addresses the study of particles' motion behavior in a special environment: a mesospheric region enriched with particles is considered to be penetrated by a particle-impaction sampler moving at supersonic speeds. The motion behavior of the particles is of interest in that their agility to evade impaction or their inertia leading to successful sample collection on substrates is to be investigated. The following Sections 2.2.1 to 2.2.4 give an overview of the theory of the airborne particles for which particle trajectories are to be calculated. A compilation of all forces acting on the particles under given conditions and thus influencing the particles' motion is included in the following (cf. Paragraph 2.2.5 Table 2.1). The parameters related to

- 1) the mesospheric region to be examined and
- 2) the particular properties of the particles expected in the target region (mesosphere)

are highly individualized and are discussed in the later Chapter 3 (see Sections 3.4 and 3.5, respectively). The numerical simulations presented provide insights into the impactions of particles on the substrates and allow an estimation of the efficiency of particle sampling.

2.2.1 Particle volume fraction

The numerical simulation of particle transport in flow regimes includes the modeling of the continuous phase (the driven phase, the fluid) and the discrete phase, the particle motion (the advected phase). The equation of motion for the continuous phase is presented in Section 2.1. The simulation of particle trajectories with one-way coupling, where only the influence of the fluid on the particle motion is considered, but not vice versa, always requires the simulation of the continuous phase first, on the basis of which the particle trajectories are subsequently calculated.

In addition, other coupling mechanisms are possible in which the particles exert an influence on the fluid or the particles influence each other. Depending on the underlying physical problem, the possible interactions between the two phases must be estimated and taken into account [Gimenez, J. M. et al., 2012]. Which

2 Mathematical modeling of fluid and particle motion

type of interaction applies depends on the concentration of the particles and is quantified by the dimensionless parameter of the volume fraction of the particles Φ_p according to Elghobashi, S. [1994], with

$$\Phi_p = \frac{nV_p}{V}, \quad (2.51)$$

where n stands for the number of particles, V_p for the volume of a single particle and V denotes the total volume (i.e., $V = nV_p + V_f$), which is composed of the volume of the particles and the liquid volume V_f . Due to low number concentration or nanometer-sizes of the particles, the particle volume can be much smaller than the volume of the fluid containing the particles. This results in particle volume fractions with values of $\Phi_p \leq 10^{-6}$, which means that the particle laden fluid flow is a sparse flow. Here, the particle advection depends on the background flow at the particle position but the particle number concentration is negligibly small that the momentum transfer (of the particle movement) to the fluid flow does not considerably influence the fluid flow. The subsequent simulation of particle motions in Section 3.5 uses the one-way (or unidirectional) coupling [COMSOL[®], 2012]. In contrast, a two-way coupling physics is assumed for values $10^{-6} < \Phi_p \leq 10^{-3}$, where the particle number concentration is higher or the particle diameters are larger, resulting in a larger particle volume fraction. In this case, the fluid flow affects the particle motions, however the momentum transfer of the particles affects the fluid flow as well. For cases of so called dense suspensions, the volume fraction of particles becomes $\Phi_p > 10^{-3}$, where mean distances between single particles decrease resulting in a higher probability of particle interactions and additionally internal forces due to particle interactions have to be taken into account, which is known as a four-way coupling.

In the present thesis, the simulated particles are assumed to be spherical solid particles with a defined diameter d_p , where V_p is calculated by

$$V_p = \frac{\pi}{6} d_p^3. \quad (2.52)$$

2.2.2 Stokes number

Another classification of particle properties is made by the Stokes number St which determines how responsive a particle is referred to changes in the continuous phase. Calculated is the dimensionless parameter by [Breuer, M. et al., 2006; Kulkarni, P. et al., 2011]:

$$St = \frac{C_c \rho_p d_p^2 u_f}{18 \mu_f L}, \quad (2.53)$$

where u_f states the mean fluid velocity, ρ_p is the particle density, d_p is the particle diameter, L is the characteristic dimension of an obstacle, μ_f is the fluid viscosity, and C_c the Cunningham slip corrector (Section 2.2.4). One can show that $St = \frac{\tau_p}{\tau_f}$, where τ_p is the particle, and τ_f is the fluid response time. Since the Stokes number is proportional to the squared diameter of the particle, it is sensitive to small diameter changes and increases fast by increasing particle diameter. Thereby, $St \ll 1$ states that the particles are small such that response times τ_p are smaller than the fluid time scale τ_f , and thus, react immediately to changes. Particles exactly follow streamlines for $St \rightarrow 0$. $St \approx 1$ states that particles are not following eddies exactly anymore, but rather centrifuge out. For $St \gg 1$, $\tau_p \gg \tau_f$ holds, and thus, particles can not respond to changes adequately resulting in diverging motions compared to the fluid motion [Roy, G., 2006; Pruppacher, H. R. and Klett, 2010].

2.2.3 Equation of motion of a particle

The particle motion is described by the second Newton's law

$$\frac{d}{dt}(m_p \vec{v}_p) = \frac{d}{dt}(m_p \frac{d\vec{x}_p}{dt}) = \vec{F}_t, \quad (2.54)$$

where m_p determines the particle mass and $\vec{v}_p = \frac{d\vec{x}_p}{dt}$ denotes the particle velocity vector with \vec{x}_p as the particle position vector. Equation 2.54 represents the relation between the inertial force on the left-hand side, which is proportional to the particle mass m_p and its acceleration $\frac{d^2\vec{x}_p}{dt^2}$. The total force \vec{F}_t on the right-hand side (the sum of all forces acting on a particle) depends on the particle size and shape [Sommerfeld, M., 2008]. The forces, which make up the total force, are induced by external fields and are, for example, the drag force or the gravitational force. Modeling the time-dependent velocity and particle position

requires the specification of all forces acting on the particle, which are described below.

2.2.4 Forces acting on particles

In the present thesis, the behavior of nanometer-sized particles in air is studied. Solid spherical particles advected by an air stream are considered for which the condition $\frac{\rho_f}{\rho_p} < 1$ holds (where ρ_p is the particle density and ρ_f the fluid density). In such cases, the dominant forces acting on the moving particles are the drag force and the Brownian force, while additional but much smaller forces are given inter alia by the lift force and the net gravity force (i.e., total gravity minus buoyancy) [Sommerfeld, M., 2008; Kuerten, J. G. M., 2016]. In the following, the aforementioned forces are described and a brief overview of further forces that possibly act on moving particles are given.

Drag force

The resistance of a particle is reflected by its (in)ability to follow streamlines. Small and light particles can easily follow streamlines and adapt almost instantaneously to changes in velocity and direction, while heavier and larger particles with higher inertia (i.e., particles larger than 0.5 μm in diameter) cannot adequately follow streamlines [Lohmann, U. et al., 2016]. In particular, when considering particle collisions and impactions with flow obstacles, particles with higher inertia are more likely to collide or impact with an obstacle.

For small, spherical, solid particles embedded in a flow and whose velocity relative to the fluid is small, the drag force \vec{F}_D is determined according to Stokes' law with [Breuer, M. et al., 2006; Pruppacher, H. R. and Klett, 2010; Burgmann, S. et al., 2011]:

$$\vec{F}_D = m_p \frac{\vec{u}_r}{\tau_p}, \quad (2.55)$$

where m_p is the particle mass, τ_p is the particle response time, and \vec{u}_r is the relative particle velocity, with

$$\vec{u}_r = \vec{u}_f - \vec{v}_p, \quad (2.56)$$

2 Mathematical modeling of fluid and particle motion

where \vec{v}_p represents the particle velocity and \vec{u}_f the flow velocity at the particle position. The response time of a particle is calculated as follows:

$$\tau_p = \frac{4 \rho_p d_p^2}{3 \mu_f C_D Re_r}, \quad (2.57)$$

with the particle density ρ_p , the dynamic viscosity of the fluid μ_f , the particle diameter d_p , the drag coefficient C_D , and the particle relative Reynolds number Re_r . The particle response time describes the inertia of particles by abrupt acceleration or decelerations, i.e. the ability of the particles to follow sudden changes in the fluid flow. Larger or denser particles have much larger values of τ_p than smaller and lighter particles; moreover, τ_p is inversely proportional to the viscosity of the fluid. If the particles follow a strongly decelerated air flow, small particles will match the fluid velocity much earlier than larger particles due to the shorter response time. Furthermore, Re_r is derived from [Pruppacher, H. R. and Klett, 2010; Burgmann, S. et al., 2011]

$$Re_r = \frac{\rho_f d_p |\vec{u}_r|}{\mu_f}. \quad (2.58)$$

For small particle relative Reynolds numbers (i.e., when $Re_r \ll 1$, which is denoted as the Stokes regime), the drag coefficient C_D , which depends on the particle Reynolds number, is given by

$$C_D = \frac{24}{Re_r}, \quad (2.59)$$

and finally, the response time of the particles in the Stokes regime is defined by

$$\tau_p = \frac{\rho_p d_p^2}{18 \mu_f}, \quad (2.60)$$

according to equation 2.57. The well-known Stokes' drag law is thus given by

$$\vec{F}_D = 3 \pi \mu_f d_p \vec{u}_r, \quad (2.61)$$

resulting from equation 2.55.

Drag coefficient for larger particles

The drag force for small spherical particles is calculated according to equation 2.61. For larger relative Reynolds numbers associated with the presence of larger particles (i.e., $Re_r < 800$, where inertial forces dominate over viscous forces [Kulkarni, P. et al., 2011; Hinds, W. C. and Zhu, 2022]), however, the equation 2.61 is no longer valid and a correction factor α_{C_D} must be applied to the drag coefficient, given as [Naumann, Z. and Schiller, 1935]:

$$\alpha_{C_D} = 1 + 0.15 Re_r^{0.687}. \quad (2.62)$$

This results in a modified drag coefficient \tilde{C}_D [Naumann, Z. and Schiller, 1935]:

$$\tilde{C}_D = \frac{24}{Re_r} \alpha_{C_D} = \frac{24}{Re_r} (1 + 0.15 Re_r^{0.687}). \quad (2.63)$$

Since the drag coefficient is included in the calculation of τ_p (equation 2.57), and the particle response time in turn is part of the drag force, \vec{F}_D is obtained by [Kulkarni, P. et al., 2011; Hinds, W. C. and Zhu, 2022]:

$$\vec{F}_D = \frac{\pi}{8} d_p^2 \vec{u}_r^2 \tilde{C}_D \rho_f. \quad (2.64)$$

Cunningham slip corrector

The Cunningham slip corrector C_c is a correction function applied onto the Stokes' drag force when the size of the embedded particles falls within the range of the mean free path λ of the fluid or is much smaller, i.e., when the Knudsen number of particles Kn_p , with

$$Kn_p = \frac{2\lambda}{d_p}, \quad (2.65)$$

where λ is the mean free path (cf. Paragraph 2.1.1), becomes larger than 1 ($Kn_p > 1$) [Kulkarni, P. et al., 2011]. Below this limit (i.e., $Kn_p \leq 1$), the particle is assumed to be in a continuum flow where the particle is much larger than the mean free path and individual collisions are negligible. However, when λ increases or d_p decreases so that the particle diameter is smaller than λ , the distance between air molecules increases such that a particle literally slips through this empty inter-molecular space, which is called a slip flow regime.

As a result, the velocity of the particle increases (due to fewer collisions with molecules). To take this into account, a so called Cunningham slip correction factor C_c , which is dimensionless, with

$$C_c = 1 + Kn_p \left[\alpha + \beta \exp \left(-\frac{\gamma}{Kn_p} \right) \right] \quad (2.66)$$

is applied to the Stokes' drag [Knudsen, M. and Weber, 1911; Millikan, R. A., 1923]. Hereby, the unitless constants α , β , and γ are assigned different values in the literature but do not differ significantly. The default values used by COMSOL® [2020] are $\alpha = 2.514$, $\beta = 0.8$, and $\gamma = 0.55$ [Davies, C. N., 1945]. A comprehensive list of coefficients reported by various authors can be found in Allen, M. D. and Raabe [1982]; Allen, M. D. and Raabe [1985]. The equation of the drag force 2.61, which takes into account the slip correction, reads as

$$\vec{F}_D = \frac{3 \pi \mu_f d_p \vec{u}_r}{C_c}. \quad (2.67)$$

Brownian force

For particle sizes smaller than 0.1 μm , the particle flow is affected by the Brownian motion of air molecules (particle diffusion) caused by random motion. Therefore, in the implementation of the Brownian force, the randomness of the motion is achieved by a white (stochastic) noise term $\vec{Z}(t)$ [Volpe, G. and Volpe, 2013] multiplied by the diffusion term D_d [Volpe, G. and Volpe, G., 2013]:

$$\vec{F}_{Brown} = \vec{Z}(t) \sqrt{D_d}, \quad (2.68)$$

with $D_d = k_B T 6 \pi \mu_f d_p$, where k_B is the Boltzmann constant, and T the absolute temperature. $\vec{Z}(t)$ is a discontinuous function with infinite variation, for which an approximation at times t_i is not possible. To discretize the white noise term, a discrete sequence of random numbers \vec{Z}_i with zero mean and variance of Δt^{-1} is considered. In this way, a dimensionless vector of independent, normally distributed Gaussian random numbers $\vec{\zeta}_i$ is generated for which the following equation holds:

$$\vec{Z}_i = \frac{\vec{\zeta}_i}{\sqrt{\Delta t}}, \quad (2.69)$$

where Δt is the computational time step to solve for the particle trajectories.

Thus, when implementing the Brownian force, the consideration of the movement's randomness within COMSOL[®] [2017a] is achieved by implementing the force

$$\vec{F}_{Brown} = \vec{\zeta}_i \sqrt{\frac{6 \pi \mu_f k_B T d_p}{\Delta t C_c}} \quad (2.70)$$

[Zhao, Y. et al., 2014; Dong, S. et al., 2014], where the Cunningham slip corrector C_c is considered according to Stoke's drag regime [García Pérez, M. et al., 2016] regarding the slip effect (cf. Paragraph 2.2.4). Furthermore, entries of $\vec{\zeta}_i$ are randomly generated for the Brownian force for each time step t_i and for each particle.

Gravitational force

For a particle with mass m_p the gravitational force \vec{F}_G acting on the particle is given by

$$\vec{F}_G = m_p \vec{g} = \frac{\pi}{6} d_p^3 \rho_p \vec{g}, \quad (2.71)$$

where \vec{g} is the gravitational acceleration vector. Since this force is proportional to the mass of the particle and thus to the particle's volume and density, particles are increasingly less affected by this force as their diameter decreases.

The particles experience an acceleration due to the gravitational field, which also causes an additional buoyancy force, resulting - according to Archimedes' principle - from the volume of the fluid displaced by the particle volume. The buoyancy force \vec{F}_B is equal to the displaced fluid mass m_f multiplied by the acceleration due to gravity:

$$\vec{F}_B = -m_f \vec{g}, \quad (2.72)$$

where the minus sign indicates that the direction of the buoyancy force is opposite to gravity. Thus, the total force $\vec{F}_{G,tot}$ caused by the external field acceleration of gravity is given by:

$$\vec{F}_{G,tot} = \vec{F}_G + \vec{F}_B = m_p \frac{\rho_p - \rho_f}{\rho_p} \vec{g}. \quad (2.73)$$

The quotient $\frac{\rho_p - \rho_f}{\rho_p}$ approaches almost unity for a particle density much greater than the fluid density and the buoyancy effect can be neglected.

Pressure gradient force

If a particle is located within a fluid pressure gradient, the particle experiences a fluid force, the so called pressure gradient force \vec{F}_p (cf. equation 2.20). The expression below for \vec{F}_p is obtained by integrating the pressure over the particle surface, applying Gauss's theorem and assuming a constant pressure gradient in the particle environment [Yin, C. et al., 2003; Shimazaki, Y. et al., 2009]:

$$\vec{F}_p = -\frac{m_f}{\rho_f} \nabla p \quad (2.74)$$

Note that the viscous forces (cf. equation 2.21) are neglected since fluid shear forces on the surfaces of small particles are negligible.

Added mass force

An accelerated particle within a fluid imparts the acceleration to the surrounding fluid that also constitutes an inert mass. This inert (fluid) mass in turn exerts a force on the particle, which is denoted as the added mass force¹ \vec{F}_{am} and which represents a surcharge on the drag. It is described by the added (fluid) mass multiplied by its acceleration, which is the change in particle velocity relative to the fluid velocity:

$$\vec{F}_{am} = m_f c_{am} \frac{d(\vec{u}_f - \vec{v}_p)}{dt} = m_p \frac{\rho_f}{\rho_p} c_{am} \frac{d(\vec{u}_f - \vec{v}_p)}{dt}, \quad (2.75)$$

where

$$\frac{d(\vec{u}_f - \vec{v}_p)}{dt} = \frac{\partial(\vec{u}_f - \vec{v}_p)}{\partial t} + \vec{v}_p \cdot \nabla(\vec{u}_f - \vec{v}_p), \quad (2.76)$$

and c_{am} is the added mass coefficient for spherical particles, which is set to $c_{am} = 0.5$ [Brennen, C. E., 1982; Crowe, C. T. et al., 2012; Kuerten, J. G. M., 2016]. It is to bear in mind that the force is proportional to the ratio of $\frac{\rho_f}{\rho_p}$ and thus is greater in magnitude at a fluid density higher than the particle density. Furthermore, if the relative acceleration (i.e. the acceleration of the particle relative to the fluid) is small, the added mass force is neglectable. Since \vec{F}_{am} has the form of an accelerating force (i.e., $m \frac{d\vec{u}}{dt}$), it can be written to the left-hand side of equation 2.54. This term is often referred as the 'added mass' [Brennen, C. E., 1982] of air that is accelerated when a particle is accelerated.

¹Also denoted as virtual mass force.

Saffman (lift) force

A particle embedded and moving in a fluid experiences a force when it enters an area of shear flow perpendicular to the relative motion of particle and fluid (e.g., when it enters an area with a flow field influenced by walls). The velocity gradient around the particle causes the flow velocity on one side of the particle to be higher than on the other. This causes a non-uniform pressure field on the particle surface. The resulting force is the so-called Saffman-force \vec{F}_S (derived from Saffman, P. G. T. [1965], written for a simplified two-dimensional case). It is perpendicular to the direction of the flow field, it is proportional to the velocity shear $|\frac{\partial \vec{u}_f}{\partial y}|$, and it faces towards the positive velocity gradient:

$$\vec{F}_S = 1.615 \vec{u}_r d_p^2 \sqrt{\rho_f \mu_f \left| \frac{\partial \vec{u}_f}{\partial y} \right|}. \quad (2.77)$$

The derivation of the Saffman-force is based on the presumption of a particle Reynolds number of $Re_r < 1$. It can be shown that an extending of equation 2.77 yields to:

$$\vec{F}_S = 1.615 d_p^2 \vec{L}_f \sqrt{\rho_f \mu_f \frac{|\vec{u}_r|}{|\vec{L}_f|}}, \quad (2.78)$$

where

$$\vec{L}_f = \vec{u}_r \times [\nabla \times \vec{u}_r], \quad (2.79)$$

with the cross product \times (cf. Appendix C). After some calculation, one obtains

$$\vec{F}_S = 1.615 d_p^2 \vec{L}_f \sqrt{\rho_f \mu_f \frac{1}{|\nabla \times \vec{u}_r|}}. \quad (2.80)$$

Apparently, the force is proportional to the square root of the shear rate and is therefore only relevant for particles moving in a flow field constituting a velocity gradient. However, for particles with higher Reynolds numbers, the Saffman force must be adapted, where the respective formula is derived by Mei, R. and Klausner [1994].

2.2.5 Comparison of the forces

Since forces listed in Section 2.2.4 depend on different variables and cases, the individual forces are put in relation to Stokes' drag force \vec{F}_D presented in Table 2.1.

forces and their relation to the Stokes' drag force	importance in reference to Stokes' drag force
Brownian force: $\left \frac{\vec{F}_{Brown}}{\vec{F}_D} \right \sim \sqrt{\frac{1}{d_p \bar{u}_r^2}}$	\vec{F}_{Brown} is indispensable for nanometer-sized particles.
pressure gradient force: $\left \frac{\vec{F}_p}{\vec{F}_D} \right \sim \frac{d_p^2 \nabla p}{\bar{u}_r}$	\vec{F}_p neglectable for nanometer-sizes of d_p and small pressure gradients around the particle.
gravitational force: $\left \frac{\vec{F}_g}{\vec{F}_D} \right \sim \frac{d_p^2}{\bar{u}_r}$	\vec{F}_g neglectable for nanometer-sized particles.
Saffman force: $\left \frac{\vec{F}_L}{\vec{F}_D} \right \sim d_p \sqrt{\frac{\bar{u}_r \times [\nabla \times \bar{u}_r]}{\bar{u}_r}}$	\vec{F}_L neglectable for nanometer-sized particles or small relative velocities.
added mass force: $\left \frac{\vec{F}_{am}}{\vec{F}_D} \right \sim d_p^2 \frac{d(\bar{u}_f - \bar{v}_p)}{dt}$	\vec{F}_{am} neglectable for nanometer-sized particles and for a small relative acceleration of the particle.

Table 2.1: Relation of different forces to Stokes' drag force.

Thus, the influence of individual variables can be estimated and the impact of respective forces can be analyzed in relation to Stokes' drag force \vec{F}_D . From the comparisons in Table 2.1, it can be deduced that the pressure gradient force \vec{F}_p , the gravitational force \vec{F}_g , the Saffman lift force \vec{F}_L , and the added mass force \vec{F}_{am} are negligible compared to the drag force \vec{F}_D when the particles considered are on the nanometer scale. However, the importance of the Brownian force \vec{F}_{Brown} increases with decreasing particle diameter.

2.2.6 Analytical solution of the particle equation of motion

The goal of this section is to derive the analytical solution of the ordinary differential equation 2.54, which is now simplified so that an analytical solution can be easily found. Only the drag force is considered. Furthermore, a uniform one-dimensional flow with $u = \text{const.}$ is assumed. The initial particle velocity v

2 Mathematical modeling of fluid and particle motion

at $t_0 = 0$ is defined as $v_0 = v(t_0)$ and the particle position for the initial state as $x_0 = x(t_0)$. The underlying equation

$$\frac{d^2x}{dt^2} = \frac{dv}{dt} = \frac{1}{\tau_p}(u - v) \quad (2.81)$$

can be analytically integrated with the assumed simplifications leading to the following result for the particle velocity v :

$$\begin{aligned} \int_{v_0}^v \frac{1}{u - v'} dv' &= \int_{t_0}^t \frac{1}{\tau_p} dt' \\ \Leftrightarrow -\ln\left(\frac{u - v}{u - v_0}\right) &= \frac{t}{\tau_p} - \frac{t_0}{\tau_p} \quad t_0 \equiv 0 \quad \frac{t}{\tau_p} \\ \Leftrightarrow u - v &= (u - v_0) \exp\left(-\frac{t}{\tau_p}\right) \\ \Leftrightarrow v(t) &= u \left[1 - \exp\left(-\frac{t}{\tau_p}\right)\right] + v_0 \exp\left(-\frac{t}{\tau_p}\right). \end{aligned} \quad (2.82)$$

Integrating a second time to determine the particles position x , the result is

$$x(t) = x_0 + u \left[t - \tau_p \left(1 - \exp\left(-\frac{t}{\tau_p}\right)\right) \right] + \tau_p v_0 \left[1 - \exp\left(-\frac{t}{\tau_p}\right)\right]. \quad (2.83)$$

The analytical solution is possible due to the simplifications made mainly due to the one-dimensional assumption of a constant flow velocity in time. However, in real applications the equation of motion of particles is more complex (cf. equation 3.13 in Section 3.5.3). Furthermore, the flow field is spatially variable (i.e., $\vec{u}(\vec{x}(t), t)$) which makes it impossible to find an exact analytical solution for the whole domain. This is where the numerical solution of the equation of motion of particles comes into play to approximate the real particle motion. With respect to the particle response time τ_p , which indicates how fast the particles react to sudden changes in the ambient flow (see Section 2.64), it is recommended that the time-dependent solver chooses time steps comparable to the particle response time or smaller. In this way abrupt decelerations of particles down to low velocities are resolved. Taken together, τ_p determines the step size for appropriate accuracy [Boucher, C., 2020] (more on this in Section 3.5.5).

2 Mathematical modeling of fluid and particle motion

To investigate the particles' velocity evolution with time (according to equation 2.82) together with the distance covered by the particle (cf. equation 2.83), the particle response time $\tau_p = 2.67 \cdot 10^{-11}$ s (for particles with diameters of $1.2 \cdot 10^{-9}$ m, according to the following investigations in Section 3.5) is applied. Furthermore, the time t , particle velocity v , and particle position x are transferred into dimensionless variables t_d , v_d , and x_d according to Boucher, C. [2020] with:

$$t_d = \frac{t}{\tau_p}, \quad v_d = \frac{v}{u}, \quad x_d = \frac{x}{u\tau_p}. \quad (2.84)$$

The resulting dimensionless analytic solutions (by replacing the variables in equations 2.82 and 2.83 by the dimensionless variables from 2.84) are:

$$v_d = 1 - \exp(-t_d), \quad (2.85)$$

$$x_d = t_d + \exp(-t_d) - 1. \quad (2.86)$$

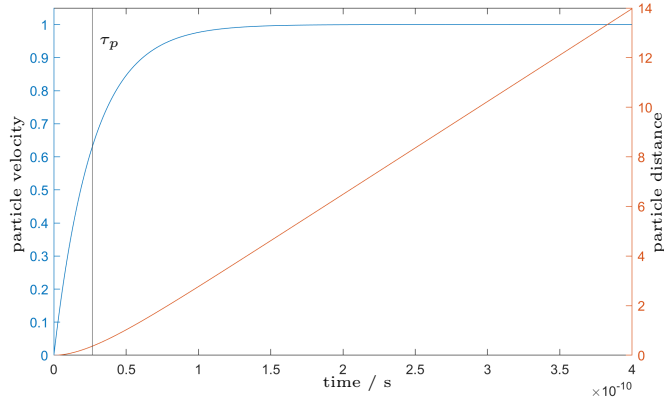


Figure 2.1: Particle velocity evolution and particle distance with time of a particle with a diameter of $1.2 \cdot 10^{-9}$ m initially at rest. The vertical marker depicts the particle's response time of $\tau_p = 2.67 \cdot 10^{-11}$ s.

Figure 2.1 depicts the dimensionless velocity, and the position evolution of a particle with respect to time t , for a particle initially at rest (i.e., with $v = 0$ m s $^{-1}$ at $t_0 = 0$ s). The asymptotic course of the particle velocity can be seen, with the highest particle acceleration at the beginning of the particle motion. The distance traveled by the particle after the initial acceleration phase shows a linear progression. The vertical line marks the particle reaction time τ_p , where

2 Mathematical modeling of fluid and particle motion

(starting from a particle at rest at time $t_0 = 0$ s) the particle reaches 63.2% of the fluid velocity [Novotný, J. and Manoch, 2012]. The effect of an additionally considered Brownian force (see equation 2.70) in equation 2.81, i.e.:

$$m_p \frac{d^2 \vec{x}}{dt^2} = \zeta \sqrt{\frac{6 \pi \mu_f k_B T d_p}{\Delta t C_c}} + \frac{3 \pi \mu_f d_p \vec{u}_r}{C_c}, \quad (2.87)$$

on the particle velocity evolution is depicted in Figure 2.2, where the solution is achieved numerically by the explicit Euler method. The effect of the force inherent with the Brownian molecular motion is clearly visible in the random characteristics.

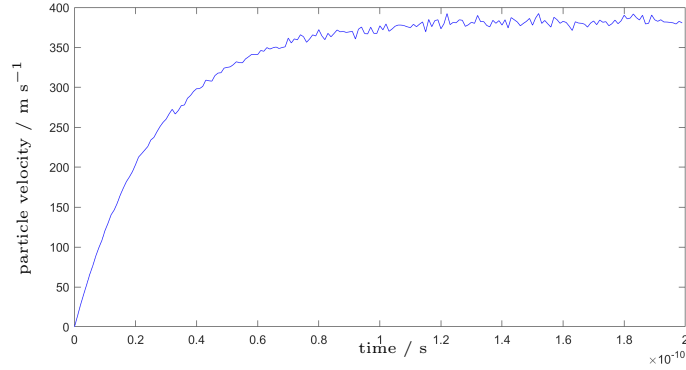


Figure 2.2: Particle velocity evolution with time under consideration of the Stokes' drag and the Brownian force of a particle with a diameter of $1.2 \cdot 10^{-9}$ m initially at rest.

2.3 Discretization methods

2.3.1 Finite element method

Since the analytical solution of the system of incompressible Navier-Stokes equations (cf. Paragraph 2.1.4) is hardly possible (due to complexity and nonlinearity), and if, only in certain points, an approximate solution in nodal points can be found by the finite element method (FEM) spatial discretization. The nodal points result from the structuring of the geometry by small elements, which in sum cause the formation of a mesh. This method leads to a discrete solution of the problem in space. Advantageous of the finite element method is its flexibility to discretize complex three-dimensional geometries with a variety of different

element shapes [Lewis, R. W. et al., 2004; Date, A. W., 2005]. To numerically solve the system of equations (Section 2.1.4), the FEM based simulation software COMSOL Multiphysics® [2023] is utilized.

Mesh generation

In the FEM, the simulation volume is discretized into non-overlapping finite elements [Knothe, K. and Wessels, 2017]. Thereby, for the three-dimensional space, element shapes of tetrahedral, pyramidal, prismatic or hexahedral can be used [COMSOL®, 2018b]. All elements together form a generated mesh, with mesh elements specified by a discrete number of nodes. How many nodes are generated per element type depend on the shape (interpolation) function used (see Section 2.3.1), and is related to the accuracy of the FEM. In this thesis, the fluid domain is discretized by a combination of tetrahedral, pyramidal as well as prismatic mesh elements. In the simulations presented in the following Chapter 3, the details of the meshes (e.g., element sizes and number of generated elements) are given due to the different shapes and complexity of the geometry in different simulation studies.

Spatial discretization

After mesh generation, the discrete approximation of the partial differential equations is performed, resulting in numerical model equations. A detailed example of the application of the FEM to the one-dimensional heat equation can be found in Klug, B. S. [2018]. The application of one dimensional up to three dimensional elements is explained in Lewis, R. W. et al. [2004] and Reddy, J. N. and Gartling [2010]. For further details, please see the corresponding pages. A general overview of the FEM is given here, with emphasis on stabilization strategies used in fast advection regimes, as is the case in supersonic flows.

First, so-called shape functions (or basis functions or interpolation functions, since they interpolate values between nodes) are defined on the mesh elements. Which shape functions are used depend on the order of convergence of the method (i.e., the accuracy of the discrete approximation), with the goal to represent field quantities restricted to certain areas [Lewis, R. W. et al., 2004]. In this context, shape functions are polynomial functions (linear, quadratic or cu-

bic polynomial functions are applied). The shape functions have the property of taking the value one at one of the nodes of an element and being zero at the other nodes [Frei, W., 2016]. The accuracy of the interpolation increases with increasing polynomial order. Consequently, however, with higher polynomial order the number of nodes increases, which directly affects the computation time. To formulate the numerical model, equations of the mathematical model are transferred into a weak formulation, where the equation needs to be fulfilled only in an integral sense [Reddy, J. N. and Gartling, 2010; Knothe, K. and Wessels, 2017]. To obtain the element equations, a linear combination of the unknown field variables multiplied by the corresponding shape function is inserted instead of the continuous solution, resulting in a system of equations (one equation for each node). Once the system is solved (i.e., for velocity, pressure, energy, temperature, and density), the field variables for individual points (e.g., the velocity or pressure) are determined in each node [Schwarz, H.-R. and Köckler, 2013].

2.3.2 Stabilization techniques

Numerical approximation methods such as the finite element method develop instabilities when modeling convection-diffusion equations in convection-dominated regimes [Bayramov, N. R. and Kraus, 2015]. If convective terms are discretized by central differences in the finite difference method (FDM), explicit time discretization leads to unconditionally instability, which can be shown (cf. Rezzolla, L. [2013]). Using linear shape functions in FEM leads to similar difficulties. As a result, the stabilization of the numerical scheme is required (which can be achieved on the one hand by choosing mesh element sizes appropriately (refinement of mesh elements), leading to an increase in computational costs [Schlegel, F., 2014]), where a stable discretization can be achieved by adding artificial diffusion terms. In the following, two methods of artificial diffusion stabilization are described, which are applied in the context of FEM and FDM:

- 1) the convection term is approximated by the *upwind* finite difference scheme, which results in adding an artificial diffusion term (appended to the physical diffusion) to the central differences of the convective term. The disadvantage of the upwind scheme is its first-order accuracy in space, but the advantage of good stability properties in convection-dominated regimes

[Brooks, A. N. and Hughes, 1982],

- 2) the so-called *streamline diffusion* finite element method is applied, where artificial diffusion is added only in the flow (streamline) direction [Semper, B., 1994; John, V. and Schmeier, 2009].

In the following, both methods are explained for a simplified linearized case of a constant convective velocity. Consider a bounded domain Ω in \mathbb{R}^2 . The two-dimensional mass-conserving convection-diffusion equation is given by:

$$\frac{\partial c}{\partial t} + \nabla \cdot (\vec{v}c) - \epsilon \Delta c = 0, \quad (2.88)$$

with the concentration $c(x, y, t) : \mathbb{R}^2 \times \mathbb{R}^+ \rightarrow \mathbb{R}$ of a substance at location (x, y) and time t , the flow velocity $\vec{v} = (v_1, v_2)^T \in \mathbb{R}_2^+$, and \vec{v} being constant and positive in both spatial directions, and the diffusion coefficient $\epsilon \in \mathbb{R}$. The initial value and boundary condition are given by:

$$c(x, y, t = 0) = c_0(x, y), \quad (2.89)$$

$$(\epsilon \nabla c - \vec{v}c) \cdot \vec{n} = 0, \quad (2.90)$$

with \vec{n} the outer normal vector to the boundary $\partial\Omega$ of Ω . The spatial finite difference approximation of equation 2.88 by the *upwind* scheme (1) with the temporal discretization by implicit Euler results in:

$$\frac{c_{ij}^{n+1} - c_{ij}^n}{\Delta t} + v_1 \frac{c_{ij}^{n+1} - c_{i-1,j}^{n+1}}{\Delta x} + v_2 \frac{c_{ij}^{n+1} - c_{i,j-1}^{n+1}}{\Delta y} - \epsilon D^2(c_{ij}^{n+1}) = 0, \quad (2.91)$$

with $D^2(c_{ij}^{n+1}) = \frac{c_{i-1,j}^{n+1} - 2c_{i,j}^{n+1} + c_{i+1,j}^{n+1}}{\Delta x^2} + \frac{c_{i,j-1}^{n+1} - 2c_{i,j}^{n+1} + c_{i,j+1}^{n+1}}{\Delta y^2}$, the central approximation of Δc . Equation 2.91 can be rearranged to

$$c_{ij}^{n+1} - c_{ij}^n + \frac{v_1 \Delta t}{\Delta x} (c_{ij}^{n+1} - c_{i-1,j}^{n+1}) + \frac{v_2 \Delta t}{\Delta y} (c_{ij}^{n+1} - c_{i,j-1}^{n+1}) - \Delta t \epsilon D^2(c_{ij}^{n+1}) = 0, \quad (2.92)$$

and rewritten under consideration of the central differences $D_x(c_{ij}^{n+1}) =$

2 Mathematical modeling of fluid and particle motion

$\frac{1}{2\Delta x}(c_{i+1,j}^{n+1} - c_{i-1,j}^{n+1})$ and $D_y(c_{ij}^{n+1}) = \frac{1}{2\Delta y}(c_{i,j+1}^{n+1} - c_{i,j-1}^{n+1})$ to:

$$\begin{aligned} & c_{ij}^{n+1} - c_{ij}^n + v_1 \Delta t D_x(c_{ij}^{n+1}) - \frac{v_1 \Delta t \Delta x}{2} D_x^2(c_{ij}^{n+1}) + \\ & v_2 \Delta t D_y(c_{ij}^{n+1}) - \frac{v_2 \Delta t \Delta y}{2} D_y^2(c_{ij}^{n+1}) - \epsilon D^2(c_{ij}^{n+1} t) = 0 \end{aligned} \quad (2.93)$$

and with the step size $h = \Delta x = \Delta y$, together with $\nabla^h := (D_x, D_y)^T$ to:

$$c_{ij}^{n+1} - c_{ij}^n + \Delta t \vec{v} \cdot \nabla^h c_{ij}^{n+1} - \underbrace{\frac{\Delta t h}{2} (v_1 D_x^2 c_{ij}^{n+1} + v_2 D_y^2 c_{ij}^{n+1})}_{\text{artificial diffusion}} - \Delta t \epsilon D^2(c_{ij}^{n+1}) = 0. \quad (2.94)$$

It is shown that the upwind scheme leads to central differences in the convective term and an artificial (isotropic) diffusion term. However, the upwind method has been criticized since its additive diffusion term can falsify the underlying physical transport process [de Vahl Davis, G. and Mallinson, 1976]. The artificial diffusion term is supposed to be considerably less than the physical diffusion [Gresho, P. M. and Lee, 1981]. Furthermore, a fine mesh resolution is required (the amount of the added diffusion depends on the mesh size). Note that the added artificial mass diffusion is of order $\mathcal{O}(h^2)$, if the Courant-Friedrichs-Lewy condition holds (i.e., $\alpha = \frac{\Delta t \|\vec{u}\|}{h} \leq 1$) [Courant, R. et al., 1928]. This is the necessary condition to obtain stable numerical solutions by explicit time discretizations.

COMSOL Multiphysics[®] applies by default the so-called *streamline diffusion*, which is an upwind-like method, but is not part of the critique with regard to the added artificial diffusion [Brooks, A. N. and Hughes, 1982], since the diffusion is added only in the advection direction. It is based on the addition of a so-called streamline diffusion term to equation 2.88. In the following, the convective diffusion equation 2.88 is considered in the weak formulation for an arbitrary test function $\phi \in V = H^1(\Omega)$, where V is the Sobolev space, with $\phi|_{\partial\Omega} = 0$:

$$\int_{\Omega} \frac{c^{n+1} - c^n}{\Delta t} \phi \, dx + \int_{\Omega} \nabla \cdot (\vec{v} c^{n+1}) \phi \, dx - \epsilon \int_{\Omega} \Delta(c^{n+1}) \phi \, dx = 0, \quad (2.95)$$

2 Mathematical modeling of fluid and particle motion

where backward Euler (time discretization) is applied. By the application of the spatial discretization of the domain, the integration by parts, and the Gauss theorem, the equation results in:

$$\int_{\Omega_h} c_h^{n+1} \phi \, dx - \Delta t \int_{\Omega_h} \vec{v} c_h^{n+1} \cdot \nabla \phi \, dx + \Delta t \epsilon \int_{\Omega_h} \nabla c_h^{n+1} \cdot \nabla \phi \, dx = \int_{\Omega_h} c_h^n \phi \, dx, \quad (2.96)$$

with $\Omega_h = \sum_K \Omega_K$, where K states the specific mesh cell. Rewriting equation 2.96 with the use of the scalar product in $L^2(\Omega_h)$ ($\langle \cdot, \cdot \rangle_{L^2(\Omega_h)}$) leads to (omitting the spatial discretization index):

$$\langle c^{n+1}, \phi \rangle_{L^2(\Omega_h)} + \Delta t \langle \nabla \phi, (-\vec{v} c^{n+1} + \epsilon \nabla c^{n+1}) \rangle_{L^2(\Omega_h)} = \langle c^n, \phi \rangle_{L^2(\Omega_h)}. \quad (2.97)$$

For the streamline diffusion method, a directional derivative of the residual term

$$\sum_K \tau_K \Delta t \langle \text{Res}, \vec{v} \cdot \nabla \phi \rangle_{L^2(\Omega_h)} \quad (2.98)$$

is added to equation 2.97 for stabilization [Johnson, C. et al., 1987] (i.e., streamline change of the Residuum [Bayramov, N. R. and Kraus, 2015] in the direction of convection [John, V. and Schmeier, 2009]), where τ_K is a parameter depending on the mesh cell and is called the streamline-diffusion parameter [Roos, H.-G. and Zarin, H., 2003], where the literature gives various proposals (e.g., $\tau_K = \frac{h_K}{2\Delta t \|\vec{v}\|_2}$, cf. equation 2.107, where $\|\cdot\|_2$ is the Euclidean norm of a vector, with the size h_K of the domain element Ω_K), and the residual Res, with [Bayramov, N. R. and Kraus, 2015]:

$$\text{Res} := c^{n+1} - c^n + \Delta t \nabla \cdot (\vec{v} c^{n+1} - \epsilon \nabla c^{n+1}), \quad (2.99)$$

which describes the numerical error of the discrete approximation scheme. Equation 2.96 states now:

$$\begin{aligned} \int_{\Omega_h} c^{n+1} \phi \, dx - \Delta t \int_{\Omega_h} \vec{v} c^{n+1} \cdot \nabla \phi \, dx + \Delta t \int_{\Omega_h} \epsilon \nabla c^{n+1} \cdot \nabla \phi \, dx + \\ \sum_K \tau_K \Delta t \langle \text{Res}, \vec{v} \cdot \nabla \phi \rangle_{L^2(\Omega_h)} = \int_{\Omega_h} c^n \phi \, dx, \end{aligned} \quad (2.100)$$

2 Mathematical modeling of fluid and particle motion

where the integral form of the added term yields:

$$\begin{aligned} \sum_K \tau_K \Delta t \left[\int_{\Omega_h} (c^{n+1} - c^n) \vec{v} \cdot \nabla \phi \, dx + \Delta t \int_{\Omega_h} [\vec{v} \nabla \cdot (\vec{v} c^{n+1})] \cdot \nabla \phi \, dx \right] \\ - \sum_K \tau_K (\Delta t)^2 \int_{\Omega_h} \vec{v} (\nabla \cdot (\epsilon \nabla c^{n+1})) \cdot \nabla \phi \, dx. \end{aligned} \quad (2.101)$$

Thus, with the application of the scalar product in L^2 , the final equation (after adding the residual terms) states:

$$\begin{aligned} \sum_K \langle c^{n+1}, \phi \rangle_{L^2(\Omega_h)} + \sum_K \Delta t \langle \epsilon \nabla c^{n+1} - \vec{v} c^{n+1}, \nabla \phi \rangle_{L^2(\Omega_h)} + \\ \sum_K \tau_K \Delta t \langle (c^{n+1} - c^n), \vec{v} \cdot \nabla \phi \rangle_{L^2(\Omega_h)} + \\ \sum_K \tau_K (\Delta t)^2 \langle \nabla \cdot (\vec{v} c^{n+1} - \epsilon \nabla c^{n+1}), \vec{v} \cdot \nabla \phi \rangle_{L^2(\Omega_h)} = \sum_K \langle c^n, \phi \rangle_{L^2(\Omega_h)}. \end{aligned} \quad (2.102)$$

To show the effect of the added terms, let us consider the convective terms of equation 2.102 in the integral form:

$$-\Delta t \sum_K \int_{\Omega_h} \vec{v} c^{n+1}(x) \cdot \nabla \phi \, dx + \sum_K \tau_K (\Delta t)^2 \int_{\Omega_h} \vec{v} \nabla \cdot (\vec{v} c^{n+1}(x)) \cdot \nabla \phi \, dx \quad (2.103)$$

with $x \in \Omega_h$. Rearranging 2.103 results in:

$$-\Delta t \sum_K \int_{\Omega_h} \vec{v} \left[c^{n+1}(x) - \tau_K \Delta t \nabla \cdot (\vec{v} c^{n+1}(x)) \right] \cdot \nabla \phi \, dx, \quad (2.104)$$

where, considering the directional derivative $(\nabla \cdot (\vec{v} c(x))) = \vec{v} \cdot \nabla c(x) = \frac{\partial c}{\partial \vec{v}}$, where vector \vec{v} is of arbitrary length in this case), 2.104 is transformed into:

$$-\Delta t \sum_K \int_{\Omega_h} \vec{v} \left(c^{n+1}(x) - \tau_K \Delta t \frac{\partial c^{n+1}}{\partial \vec{v}} \right) \cdot \nabla \phi \, dx. \quad (2.105)$$

Finally, using Taylor's expansion for c and omitting error terms, we get:

$$-\Delta t \sum_K \int_{\Omega_h} \vec{v} c^{n+1}(x - \tau_K \Delta t \vec{v}) \cdot \nabla \phi \, dx, \quad (2.106)$$

2 Mathematical modeling of fluid and particle motion

where equation 2.106 is the weak form of the total convective term with the displacement of c in the *upwind* direction (i.e., into the opposite \vec{v} direction). For the approximation point x within Ω_h , the argument can be shifted by $\tau_K \Delta t \|\vec{v}\|_2 \leq \frac{h_K}{2}$, i.e.,

$$\tau_K \leq \frac{h_K}{2\Delta t \|\vec{v}\|_2} \quad (2.107)$$

holds. This means that the shift of the x -argument (x is located centrally in Ω_h) does not exceed the considered mesh cell.

To explain how the added convective terms are associated with the artificial diffusion in *streamline* direction, let us consider the convective part of the residual again:

$$\sum_K \tau_K (\Delta t)^2 \int_{\Omega_K} \vec{v} (\nabla \cdot (\vec{v} c^{n+1})) \cdot \nabla \phi \, dx, \quad (2.108)$$

which can be rewritten under consideration of the integration by parts to

$$\begin{aligned} & \sum_K \tau_K (\Delta t)^2 \int_{\Omega_K} [\vec{v} (\vec{v} \cdot \nabla c^{n+1})] \cdot \nabla \phi \, dx = \\ & - \sum_K \tau_K (\Delta t)^2 \int_{\Omega_K} \nabla \cdot (\vec{v} (\vec{v} \cdot \nabla c^{n+1})) \phi \, dx, \end{aligned} \quad (2.109)$$

which results under application of the directional derivative of c in direction of \vec{v} in

$$- \sum_K \tau_K (\Delta t)^2 \int_{\Omega_K} \nabla \cdot \left(\vec{v} \frac{\partial c^{n+1}}{\partial \vec{v}} \right) \phi \, dx, \quad (2.110)$$

and further in

$$- \sum_K \tau_K (\Delta t)^2 \int_{\Omega_K} \vec{v} \cdot \nabla \frac{\partial c^{n+1}}{\partial \vec{v}} \phi \, dx. \quad (2.111)$$

Finally, under consideration of the directional derivative, the added convection term 2.108 forms into

$$\begin{aligned} & - \sum_K \tau_K (\Delta t)^2 \int_{\Omega_K} \frac{\partial}{\partial \vec{v}} \frac{\partial c^{n+1}}{\partial \vec{v}} \phi \, dx = \\ & - \sum_K \tau_K (\Delta t)^2 \int_{\Omega_K} \frac{\partial^2}{\partial \vec{v}^2} c^{n+1}(x) \phi \, dx, \end{aligned} \quad (2.112)$$

which is the second directional derivative with regard to the streamline (convective) direction, called the *streamline diffusion*.

Analogously to 2.106 it can be shown that the mass term of equation 2.102 is evaluated in a point lying backward along the streamline (thus, in upwind direction):

$$\sum_K \int_{\Omega_h} (c^{n+1} - c^n) \phi \, dx + \sum_K \tau_K \Delta t \int_{\Omega_h} \vec{v} (c^{n+1} - c^n) \cdot \nabla \phi \, dx, \quad (2.113)$$

which is rewritten into (under consideration of the integration by parts):

$$\sum_K \int_{\Omega_h} (c^{n+1} - c^n) \phi \, dx - \sum_K \tau_K \Delta t \int_{\Omega_h} \nabla \cdot (\vec{v} (c^{n+1} - c^n)) \phi \, dx, \quad (2.114)$$

and under consideration of the directional derivative to

$$\sum_K \int_{\Omega_h} \left[(c^{n+1} - c^n)(x) - \tau_K \Delta t \frac{\partial (c^{n+1} - c^n)(x)}{\partial \vec{v}} \right] \phi \, dx. \quad (2.115)$$

Subsequently, with the consideration of the Taylor expansion (omitting the higher order terms), the final equation is reached:

$$\sum_K \int_{\Omega_h} (c^{n+1} - c^n)(x - \tau_K \Delta t \vec{v}) \phi \, dx, \quad (2.116)$$

where again the argument of function c is shifted in the opposite direction of \vec{v} (i.e., upstream). One can show, using the same technique, that by adding a viscous residual term, the corresponding viscous terms in equation 2.102 are evaluated at a point $x - \tau_K \Delta t \|\vec{v}\|_2$, i.e., shifted by length $\tau_K \Delta t \|\vec{v}\|_2$ in the opposite (upstream) \vec{v} direction, which is analogous to the upstream strategy.

2.3.3 Time discretization for fluid equations

For the discretization in time of the fluid problem, COMSOL Multiphysics[®] applies the method of backward differentiation formulas (BDF). In contrast to a classical approach of solving the equations by numerical integration in time, the BDF is based on numerical differentiation. In the BDF method, the initial value problem with the unknown function

$$y'(t) = f(t, y(t)), \quad (2.117)$$

with the initial condition of $y(t_0) = y_0$, approximations $y^{n+1} \approx y(t^{n+1})$ of previous values y^{n-k+1}, \dots, y^n at times t^{n-k+1}, \dots, t^n are considered. Here, the integer k represents the applied number of previous approximations (steps). The general backward differentiation formula to determine y^{n+1} is [Voß, H., 2010]:

$$\sum_{i=0}^k \alpha_i \nabla^i y^{n+1} = \Delta t f(t^{n+1}, y^{n+1}). \quad (2.118)$$

Here, α_i is a coefficient and Δt denotes the time step. For the coefficient α_i following holds: $\alpha_0 = 0$ and $\alpha_i = \frac{1}{i}$ for $i \geq 1$ [Voß, H., 2010]. The backward differer $\nabla^i y^n$ are defined by $\nabla^0 y^n := y^n$ and $\nabla^{i+1} y^n := \nabla^i y^n - \nabla^i y^{n-1}$. Considering the one and two steps ($k = 1$ and $k = 2$) of the BDF method [Hairer, E. et al., 2000; Prof. J. M. Melenk, 2010] following discretization methods are obtained, having the orders of convergence one and two:

$$\begin{aligned} k = 1 : y^{n+1} - y^n &= \Delta t f(t^{n+1}, y^{n+1}); \\ k = 2 : 3y^{n+1} - 4y^n + y^{n-1} &= 2\Delta t f(t^{n+1}, y^{n+1}). \end{aligned}$$

Note that the BDF with $k = 1$ is the backward Euler method (used in the previous Section 2.3.2 on the stability of the spatial discretization method). Higher orders of the BDF are not explicitly listed here since they are not applied in this study. The BDF methods are advantageous due to their good stability behavior, characterized by unbounded stability regions. The stability regions are the set of permitted Δt to reproduce the decreasing behavior of the solution to the test equation $y' = \lambda y$, $y \in \mathbb{C}^-$. For lower orders $k = 1$ and $k = 2$, the BDF methods are absolutely stable, where the stability region contains the entire negative complex plane. Higher order BDF have the property that the negative real axis describing values of $\lambda \Delta t$ lies entirely in the stability region, but only a sector of the negative complex plane is contained in the stability region, which is determined by an angle α . This angle is given as the angle between a tangent line to the inner edge of the stability region, starting at the origin, and the negative real axis. If α is less than 90° (i.e., $\alpha \lesssim 90^\circ$), there is no absolute stability, but still a method with good stability properties,

which makes the BDF method advantageous for stiff problems [Quarteroni, A. et al., 2010; Bärwolff, G., 2015]. Note that for BDF with $k = 2$, $\alpha = 90^\circ$, and the method is A-stable. Higher order BDF methods ($k \geq 3$ to $k \leq 6$) are so-called $A(\alpha)$ -stable, where α is the aperture angle of the stability sector at which $\alpha \in (0, \frac{\pi}{2})$, as shown in Figure 2.3 for the BDF order $k = 4$ with $\alpha = 73^\circ$. The BDF with $k = 1$ and $k = 2$ are implemented in COMSOL[®] for this investigation for the time discretization.

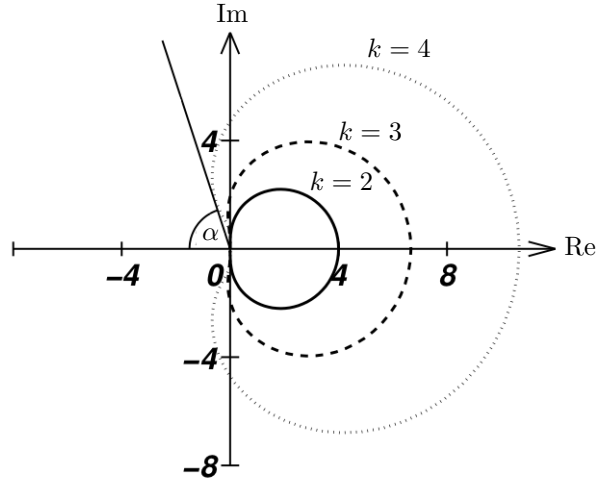


Figure 2.3: Boundaries of stability regions of different orders k of the BDF method, absolute stability (A-stability) is guaranteed for the order up to $k = 2$, where Re states the real axis and Im the imaginary axis. Higher orders up to $k \leq 6$ are $A(\alpha)$ -stable (based on [Bärwolff, G., 2015]).

2.3.4 Discretization for particle equations

The equation for particle dynamics is represented by a second order linear differential equation

$$\mathbf{M} \ddot{\vec{x}}(t) = \vec{f}(t, \vec{x}, \dot{\vec{x}}) \quad (2.119)$$

with initial conditions $\vec{x}(0) = \vec{x}_0 = \vec{d}$ and $\dot{\vec{x}}(0) = \dot{\vec{x}}_0 = \vec{v}_0$ (cf. Section 2.2.6). The expression $\mathbf{M} \in \mathbb{R}^{n \times n}$ is the constant mass matrix, $\vec{a}(t) = \ddot{\vec{x}}(t) \in \mathbb{R}^n$ is a vector of acceleration and $\vec{f}(t, \vec{x}, \dot{\vec{x}}) \in \mathbb{R}^n$ is the vector representing the acting forces. For simplicity in this section, dots mark time derivatives with respect to time t . Recall that $\vec{v}(t) = \dot{\vec{x}}(t) \in \mathbb{R}^n$ is the vector of velocity and $\vec{x} \in \mathbb{R}^n$ the vector of the particle positions. Reforming equation 2.119 into a system of first

2 Mathematical modeling of fluid and particle motion

order differential equations it yields to

$$\begin{aligned}\dot{\vec{x}} &= \vec{v} \\ \ddot{\vec{x}} &= \dot{\vec{v}} = \vec{a} \\ \mathbf{M} \vec{a} &= \vec{f}(t, \vec{x}, \dot{\vec{x}}).\end{aligned}\tag{2.120}$$

For the system 2.120, the generalized alpha method was developed by Chung, J. and Hulbert [1993], which is a non-standard implicit second order method [Jay, O. L. and Negrut, 2009]. By this method, one step from $(t^n, \vec{x}^n, \vec{v}^n, \vec{a}^{n+\alpha})$ to $(t^{n+1}, \vec{x}^{n+1}, \vec{v}^{n+1}, \vec{a}^{n+1+\alpha})$ where $t^{n+1} = t^n + \Delta t$, and with $\vec{x}^n, \vec{v}^n, \vec{a}^{n+\alpha}$ the approximations of $\vec{x}(t^n), \vec{v}(t^n), \vec{a}(t^n + \alpha\Delta t)$ (where α represents the shift in the acceleration evaluation position) is performed as follows: first, the equation $\ddot{\vec{x}} = \vec{a}$ is approximated by the second difference

$$\ddot{\vec{x}} \approx \frac{\vec{x}^{n+1} - 2\vec{x}^n + \vec{x}^{n-1}}{(\Delta t)^2}.\tag{2.121}$$

By using $\vec{x}^{n-1} = \vec{x}^n - \vec{v}^n \Delta t$ it results in the following approximation for \vec{x}^{n+1} :

$$\vec{x}^{n+1} = \vec{x}^n + \Delta t \vec{v}^n + (\Delta t)^2 \left(\left(\frac{1}{2} - \beta \right) \vec{a}^{n+\alpha} + \beta \vec{a}^{n+1+\alpha} \right),\tag{2.122}$$

with the application of the algorithmic parameter β (cf. equation 2.125). The next approximation of $\dot{\vec{v}} = \vec{a}$ with a linear combination of $\vec{a}^{n+\alpha}$ and $\vec{a}^{n+1+\alpha}$ results in:

$$\vec{v}^{n+1} = \vec{v}^n + \Delta t \left((1 - \gamma) \vec{a}^{n+\alpha} + \gamma \vec{a}^{n+1+\alpha} \right)\tag{2.123}$$

and the last equation $\mathbf{M} \vec{a} = \vec{f}(t, \vec{x}, \dot{\vec{x}})$ is discretized by

$$\mathbf{M} \left[(1 - \alpha_m) \vec{a}^{n+1+\alpha} + \alpha_m \vec{a}^{n+\alpha} \right] = \vec{f}(t^{n+1}, \vec{x}^{n+1}, \vec{v}^{n+1}) (1 - \alpha_f) + \vec{f}(t^n, \vec{x}^n, \vec{v}^n) \alpha_f,\tag{2.124}$$

with $\vec{x}_0 = \vec{d}, \vec{v}_0 = \vec{v}$ and $\vec{a}_0 = \mathbf{M}^{-1} \vec{f}(0)$. The following algorithmic parameters $\beta, \gamma, \alpha_m, \alpha_f$ usually applied are [Chung, J. and Lee, 1994; Bonelli, A. et al., 2002; Fung, T. C., 2003; Jay, O. L. and Negrut, 2009]:

$$\alpha_m = \frac{2\rho_\sigma - 1}{1 + \rho_\sigma}, \quad \alpha_f = \frac{\rho_\sigma}{1 + \rho_\sigma}, \quad \beta = \frac{(1 - \alpha)^2}{4}, \quad \gamma = \frac{1}{2} - \alpha,\tag{2.125}$$

with $\alpha := \alpha_m - \alpha_f$ and $\rho_\sigma \in [0, 1]$ which controls numerical dissipation and

damping of high frequency numerical modes of no interest (with $\rho_\sigma = 1$ there is no numerical dissipation) [Erlicher, S. et al., 2002; Arnold, M. and Brüls, 2007].

For special cases of the above algorithmic parameters, well known discretization methods are achieved. Assume the algorithmic parameter $\rho_\sigma = 1$, with $\alpha_m = \frac{1}{2}$ and $\alpha_f = \frac{1}{2}$ resulting in $\alpha = 0$, and $\beta = \frac{1}{4}$ and $\gamma = \frac{1}{2}$, which gives the well known trapezoidal rule:

$$\bar{x}^{n+1} = \bar{x}^n + \Delta t \bar{v}^n + \frac{(\Delta t)^2}{2} \left(\frac{1}{2} \bar{a}^n + \frac{1}{2} \bar{a}^{n+1} \right) \quad (2.126)$$

$$\bar{v}^{n+1} = \bar{v}^n + \frac{\Delta t}{2} (\bar{a}^n + \bar{a}^{n+1}) \quad (2.127)$$

$$\mathbf{M} \left(\frac{1}{2} \bar{a}^{n+1} + \frac{1}{2} \bar{a}^n \right) = \frac{1}{2} \vec{f}(t^{n+1}, \bar{x}^{n+1}, \bar{v}^{n+1}) + \frac{1}{2} \vec{f}(t^n, \bar{x}^n, \bar{v}^n). \quad (2.128)$$

By choosing $\alpha_m = 0$ and $\alpha_f = 0$ resulting in $\alpha = 0$ and choosing $\beta = 0$ independently on equations 2.125 and $\gamma = \frac{1}{2}$, the algorithm of Störmer and Verlet, L. [1967] is achieved, with

$$\bar{x}^{n+1} = \bar{x}^n + \Delta t \bar{v}^n + \frac{h^2}{2} \bar{a}^n \quad (2.129)$$

$$\bar{v}^{n+1} = \bar{v}^n + \frac{\Delta t}{2} (\bar{a}^n + \bar{a}^{n+1}) \quad (2.130)$$

$$\mathbf{M} \bar{a}^{n+1} = \vec{f}(t^{n+1}, \bar{x}^{n+1}, \bar{v}^{n+1}). \quad (2.131)$$

The advantage of the generalized alpha method lies in its structure by allowing a much lower damping effect compared to low orders of BDF, so it is more accurate. This method is implemented in the COMSOL[®] particle tracking module and is applied in these studies.

3 Supersonic flow simulations around a sounding rocket tip and simulations of the impaction-based collection of submicron aerosols

The existence of mesospheric noctilucent clouds (NLC) (or night shining clouds) is known since the end of 19th century and they were first observed and reported by Blackhouse, T. W. [1885] and Jesse, O. [1890]. The main occurrence of NLC is in the summer months (June/July) and at altitudes of 82 to 85 km [Turco, R. P. et al., 1982; Baumgarten, G. and Fiedler, 2008; Hervig, M. E. et al., 2011]. So far, the composition of NLC elements, especially the nature of condensation nuclei onto which the NLC elements can form at this altitude has not yet been conclusively explained [Lübken, F.- J., 2005].

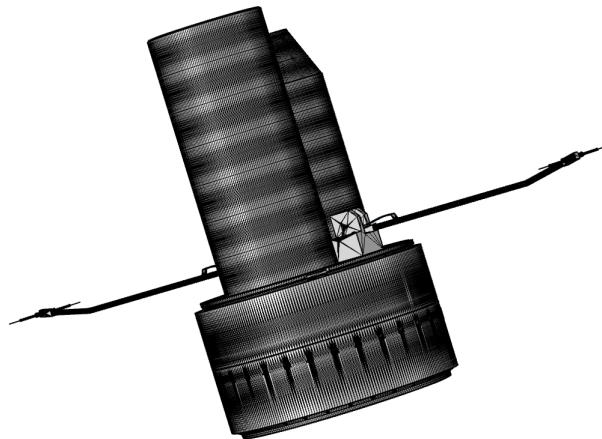


Figure 3.1: Detailed geometry of the instrument module.

In contrast to the lower atmosphere, where troposphere and tropopause have been extensively studied, the mesosphere and lower thermosphere have been

3 *Supersonic flow simulations and impaction processes*

insufficiently explored, as here in-situ measurements are associated with a high level of technical complexity and effort. High altitude aircrafts and research balloons do reach altitudes above 20 to 45 km [Plane, J. M. C., 2012]. Although remote sensing methods such as Lidar or Radar ensure a continuous data acquisition, the measurement information is limited. To investigate the mesosphere and lower thermosphere (MLT region), and in particular to collect mesospheric particles, atmospheric soundings by rockets seem to be alternativeless.

In this Chapter the numerical modeling of supersonic fluid dynamics around the instrument module of a sounding rocket and of the sampling efficiencies concerning impaction-based collection of mesospheric particles are provided. Mesospheric particles, presumably meteoric smoke particles (see Section 3.1), may have a significant importance in the formation of mesospheric ice particles (as ice condensation nuclei), such as in the formation of noctilucent clouds (see Section 3.2). The geometry of the instrument module of a sounding rocket typically used for investigations in the summer mesopause region under ambient conditions (see Section 3.3 ff.), is shown in Figure 3.1. For the development of the so-called SPICE instrument, the fluid dynamics simulations around this geometry are performed. Particular attention will be paid to the aerodynamic effects. Of special interest is the evaluation of the supersonic flow (with $Ma_1 = 1.31$ and $Ma_2 = 1.75$ at the altitude of 85 km) in view of its variables (e.g., velocity, pressure, temperature). Moreover, the thickness of the boundary layer, which builds up around the flow obstacle, is investigated in order to be considered in the collector's design (i.e., substrate mounts) and to ensure a particle sampling well outside this boundary layer. Other tasks for simulations are aimed at the design or arrangement of the SPICE booms with the substrate mounts, onto which the atmospheric particles are to hit on substrates for collection. Calculations of particle trajectories under various conditions of flight attitude and as a function of particle number concentrations finally confirm possible impaction processes based on the developed design and geometry of the SPICE instrument.

The following Sections 3.1 and 3.2 begin with a summary of the current state of research on meteoric smoke as well as of noctilucent clouds. Section 3.3 presents

the envisaged rocket flight pattern to collect mesospheric particles, which differs in its flight path from conventional sounding flights. The description of the numerical modeling setup (Sections 3.4.1 and 3.4.2), used to calculate the air flow around the instrument module under supersonic conditions, follows. The analysis of the supersonic flow field around the instrument module and the substrate mounts is then provided in Paragraph 3.4.3. Moreover, the simulation details and the model equation of the particle tracking are provided in Sections 3.5.1 to 3.5.5. Thereby, the previously obtained results of the flow simulation are incorporated into the calculation of the particle trajectories. Subsequently, after the solver settings are provided in Section 3.5.4, the results obtained are discussed regarding to what extent the efficiency of the particle impaction can be estimated in Section 3.5.7.

3.1 Meteoric smoke: potential condensation nuclei for NLC formation

It is known that large quantities of cosmic material enter the Earth's atmosphere every day. Plane, J. M. C. [2012] estimates the daily input of cosmic dust at 3 to 300 tons. Some of the very small extraterrestrial dust particles (smaller than 1 μm , approximately 7 tons per day) penetrate the atmosphere without altering [Plane, J. M. C., 2012]. Larger cosmic bodies, however, ablate due to frictional heating from collisions with air molecules as they enter the upper atmosphere, releasing a trail of volatilized meteoric material [Plane, J. M. C., 2003, 2012; Plane, J. M. C. et al., 2015]. The recombination and polymerization of the vapor molecules into clusters and the subsequent agglomeration of these form nanometer-sized meteoric smoke particles (called MSP) [Rosinski, J. and Snow, 1961; Hunten, D. M. et al., 1980; Megner, L. et al., 2006; Saunders, R. W. et al., 2012; Plane, J. M. C. et al., 2015; Wilms, H. et al., 2016; Frankland, V. L. et al., 2017; James, A. D. et al., 2018]. The vapor of ablated cosmic bodies consists of the main metallic components: Fe, Mg, Si, Al, Ni, Ca, and Na, which are also found in chondritic meteorites [Plane, J. M. C., 2003, 2012; Hedin, J. et al., 2014]. Accordingly, MSP have mainly amorphous silicate structures with iron and magnesium as major constituents, which form after ablation and recondensation of the abundant metals [Plane, J. M. C., 2012; Kleko-ciuk, A. R. et al., 2005; Hervig, M. E. et al., 2009; Hervig, M. E. et al., 2012;

3 *Supersonic flow simulations and impaction processes*

Saunders, R. W. et al., 2012; James, A. D. et al., 2017]. The iron-magnesium silicate composition of the MSP (i.e., FeMgSiO_2), corresponding to olivine from a mineralogical point of view, was furthermore confirmed in laboratory studies [Asmus, H. et al., 2014; Plane, J. M. C. et al., 2015]. Mass spectrometric studies of particles from lower altitudes indicate their meteoric origin due to their chemical composition [Schneider, J. et al., 2021; Appel, O. et al., 2022].

Sources of the cosmic input are dust trails from sublimated comets in their orbit around the sun or from the asteroid belt [Ceplecha, Z. et al., 1998; Murad, E. and Williams, 2002]. Upon entering the Earth's atmosphere with high velocities and with increasing air density at decreasing altitude, the collisions of the cosmic body with air molecules rise, which enhances the frictional heating (up to temperatures of >1800 K) and consequently, the temperature of the entering cosmic body [Plane, J. M. C., 2012]. It is assumed that the gradual temperature rise of the cosmic body on its passage through the atmosphere causes a so-called differential ablation, whereby at the outer atmosphere (low temperature rise) initially the most volatile components evaporate (e.g., alkali metals Na or K) while later, along the track and with increasing body temperature, the less volatile components (e.g., Fe, Mg, Si, Ca, etc.) evaporate [Janches, D. et al., 2009; Plane, J. M. C., 2012]. Ablation is believed to proceed mainly above 80 to 90 km altitude. The reason for this is the sufficiently high temperatures reached by cosmic bodies (masses $> 10^{-7}$ g and sizes larger $10 \mu\text{m}$ [Plane, J. M. C., 2003]) at which entire vaporization of its components is likely, and which represent by far the most common events of cosmic material passages through the atmosphere. Events with much larger cosmic bodies (masses > 1 g and diameters of more than a few millimeters), which evaporate at even lower latitudes, are much rarer (cf. Plane, J. M. C. [2012]). Very large cosmic bodies may break up during passage by burst-like fragmentation (cf. Chelyabinsk meteor, Ural region, Russia, 15 Feb 2012). A detailed description about MSP properties is found in Section 3.5.1.

Although MSP are suspected to play a crucial role in mesospheric phenomena, still very little is known about these particles. A database of in-situ observation data or particle samples for off-line physico-chemical analyses of these particles, which would allow for characterizing the NLC elements as well as their

3 Supersonic flow simulations and impaction processes

constituents, is lacking so far. Despite the wide estimated range of incoming cosmic material (cf. Plane, J. M. C. [2012]), the presence of MSP is ubiquitous in higher atmospheric layers. MSP can be detected, for example, by radar backscatter [Strelnikova, I. et al., 2007; Fentzke, J. T. et al., 2009] or measured directly above 70 km altitude by particle detectors on rockets [Rapp, M. et al., 2007; Gelinias, L. J. et al., 2005; Lynch, K. A. et al., 2005; Rapp, M. et al., 2010]. Furthermore, a layer of enriched metallic constituents is found (between 80 and 100 km altitude), with a maximum density at about 95 km, probably due to the ablation of cosmic material [Kopp, E., 1997]. This assumption is supported by the increased abundance of metallic atoms and ions in the lower thermosphere after meteor showers, which correlate with elemental abundances in chondritic meteorites.



Figure 3.2: Noctilucent clouds [Süßen, M., 2019].

MSP are thought to serve as possible ice condensation nuclei (i.e., for heterogeneous processes) in noctilucent clouds [Rosinski, J. and Snow, 1961; Hunten, D. M. et al., 1980; Rapp, M. and Thomas, 2006; Plane, J. M. C. et al., 2015; Wilms, H. et al., 2016]. The composition of the NLC elements and thus the proof that MSP act as condensation nuclei of NLC at appropriate altitudes, as well as the size distribution and concentration of MSP have not yet been experimentally determined. The main reason for this relates to the difficulty of taking particle samples and analytical investigation at such altitudes, where only measurements and probe sampling with the help of sounding rockets are

possible. The goal of the high-altitude research is to develop and characterize the performance of the impaction-based particle collector SPICE and to examine and provide a proof of concept for conducting samples based on free-flowing particle impactions in the supersonic stream radially aside the payload. The knowledge gained could be successively applied to the development of the acquisition system. This collection system aims at sampling the cloud elements (ice particles) of NLC along with the presumably contained ice nuclei (IN) to confirm or disconfirm the role of IN (e.g., MSP) as prerequisite for ice formation in the mesosphere. The question of the IN's physical properties and chemical composition could also be addressed by physico-chemical analyses.

The main challenges of in-situ sampling at MLT altitudes are inherent with aerodynamic effects caused by the supersonic motion of the sounding rocket and the properties of the particles. Due to their small sizes (NLC elements $< 0.12 \mu\text{m}$ in diameter [Tozer, W. F. and Beeson, 1974; Turco, R. P. et al., 1982; Thomas, G. E., 1991; Lübken, F.- J., 2005; Rapp, M. and Thomas, 2006; Baumgarten, G. and Fiedler, 2008; Hervig, M. E. et al., 2009], and MSP $< 9 \text{ nm}$ in diameter [Horányi, M. et al., 1999; Rapp, M. and Thomas, 2006; Strelnikova, I. et al., 2007; Rapp, M. et al., 2010, 2012; Hedin, J. et al., 2014; Asmus, H. et al., 2014]), the fundamental challenge in sampling mesospheric particles during a sounding flight is the design of a probe taking aerodynamics into account. Even up to elevated flow velocities (near sonic speeds), the MSP very well follow streamlines around the sounding rocket and the instrumental payload due to their nanometer size. The nanometer-sized particles therefore rarely hit the substrate mounts with impaction substrates intended for this purpose. However, when the MSP are embedded in much larger NLC elements, this allows for an inertia-based collection of NLC elements and thus sampling of the incorporated substances.

3.2 Noctilucent clouds

Since the end of the 19th century, the appearance and composition of the summer mesospheric phenomenon of noctilucent clouds has been scientifically studied. Due to their occurrence location poleward of about 50° N [Rapp, M. and Thomas, 2006] at typical altitudes of 82 to 85 km [Turco, R. P. et al., 1982; Baum-

3 Supersonic flow simulations and impaction processes

garten, G. and Fiedler, 2008; Hervig, M. E. et al., 2011], noctilucent clouds with a vertical thickness of 1 to 5 km and broad horizontal extend ($10^4 - 4 \cdot 10^6 \text{ km}^2$) are visible to the human eye (shown in Figure 3.2) when sunlight reflects off cloud particles while the observer is unilluminated (i.e., during night time), giving them their name. Apart from the visible light event, another phenomenon associated with the occurrence of NLC are so-called polar mesosphere summer echoes (PMSE), which are detected by means of backscattered radar signals through small layers of ice particles [Rapp, M. and Lübken, 2004]. With a size of $< 20 \text{ nm}$ in diameter, ice particles do not contribute to refraction with the wavelength range of visible light. The origin of these PMSE is located above the occurrence of NLC, mainly at 85 to 90 km altitude [Hervig, M. E. et al., 2011]. Descending ice particles become larger and therefore optically visible as NLC elements, provided they are present in sufficient numbers.

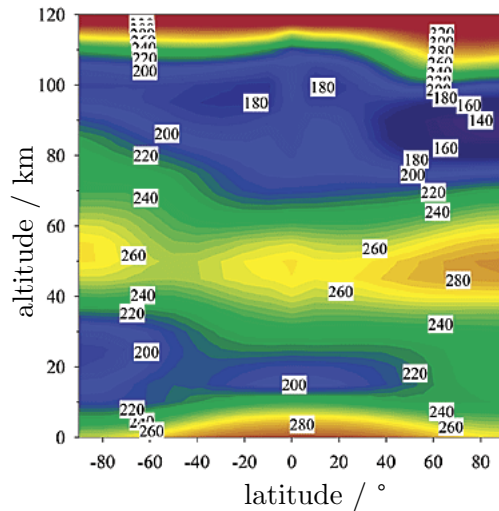


Figure 3.3: Temperature distribution (in K) as a function of latitude for July [Plane, J. M. C., 2003] from MSIS-E-90 model.

The occurrence of the phenomena is of seasonal nature and depends on the prevailing atmospheric conditions. During summer months, temperatures in the summer mesopause region drop to an absolute minimum and reach temperatures of $T \approx 140 \text{ K}$ [Theon, J. S. et al., 1967] or to even colder values [Turco, R. P. et al., 1982; Lübken, F.-J., 1999; Vincent, R. A., 2015], which provide the coldest place in Earth's system. In addition, the temperature minimum at this altitude forms the upper boundary of the mesosphere, i.e., the location of the

mesopause. Figure 3.3 shows the temperature profile with altitude in July for different latitudes, from the summer to the winter pole. Clearly visible is the temperature minimum at altitudes of 80 to 100 km for the summer pole. If only radiation processes are considered, i.e., the incident solar radiation on the summer hemisphere and the outgoing infrared radiation on the winter polar region, the temperature pattern should be opposite (i.e., have a temperature maximum at the mesopause in the summer hemisphere and a temperature minimum at the mesopause in the winter hemisphere). The prevailing low temperatures can only be explained by adiabatic cooling at the summer pole by rising and thus expanding air. However, the temperature distribution is not yet understood in detail and is the subject of current research. Clear is, however, that the mesosphere is subject to meridional circulation [Plane, J. M. C., 2003] driven by gravity waves from deeper atmospheric layers. As a result, air begins to rise at the summer pole and sinks at the winter pole, resulting in the lowest atmospheric temperatures at the summer pole in the mesosphere.

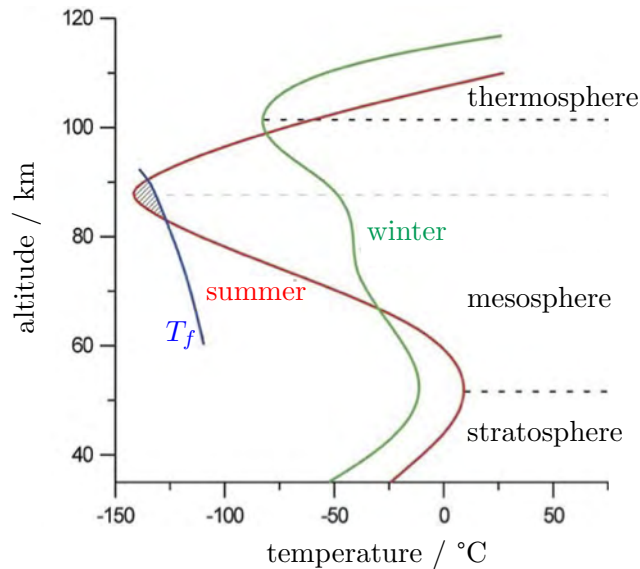


Figure 3.4: Vertical temperature profile for the upper atmosphere in polar regions. The red line shows the vertical profile as found in summer months, the green line is the vertical profile for winter months. The frost point temperature T_f is represented by the blue line [Lübken, F.- J., 2005].

According to the low temperatures, NLC elements are assumed to consist of water ice [Von Cossart, G. et al., 1999; Hervig, M. et al., 2001]. Figure 3.4

shows vertical profiles of mean air temperatures in the upper atmosphere at polar latitudes for summer seasons (red line) and winter seasons (green line). Unfortunately, Lübken, F.- J. [2005] does not mention over which time span the measured values were averaged or from which measurement they originate. The mesosphere is separated from the stratosphere by the stratopause, which is characterized in both seasons by a local temperature maximum. The local temperature maximum results from effective absorption of incoming solar radiation by ozone molecules, whose photodissociation occurs due to the high-energy UV radiation and thermal energy is released. Clearly visible is the temperature minimum (about 140 K) for summer temperatures in the mesopause region at 85 km, where NLC formation occurs and PMSE emerge. The blue line shows the frost point temperature T_f and indicates supersaturated conditions from 81 to 90 km altitude, where water molecules start to condense onto existing surfaces, as for instance provided by aerosols, if in place.

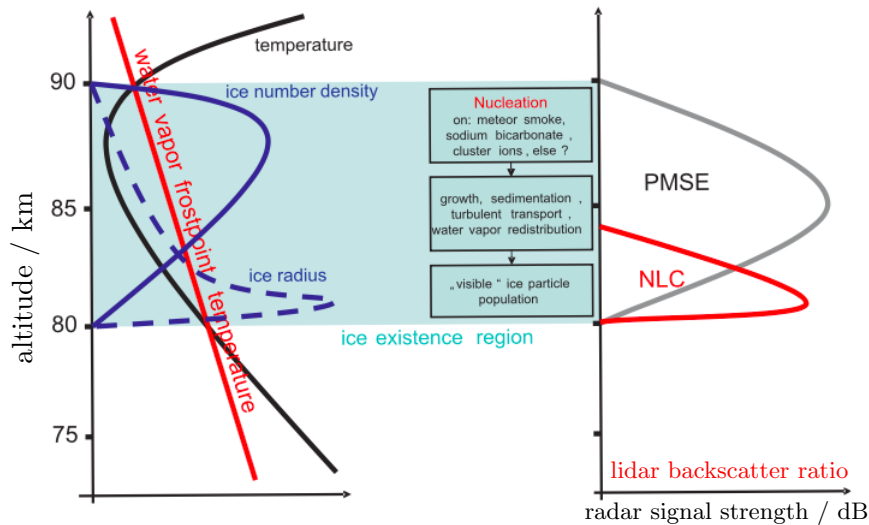


Figure 3.5: Schematic overview of upper atmosphere's temperature profile during summer months associated with the occurrence of mesospheric ice particles. In addition, an overview of properties of mesospheric particles associated with PMSE and visible NLC is provided [Rapp, M. and Thomas, 2006].

In conclusion, the presence of NLC is an indicator of cold temperatures below the water vapor freezing point T_f . Coincidentally, PMSE are detected by means of radar backscattering in the presence of NLC particles, which exhibits the strongest signal strength at highest ice number density (see Figure 3.5). PMSE

are detected at altitudes up to 90 km. As the small ice particles increase in size over time due to coagulation and condensation, they begin to sediment. At diameters larger than 20 nm, they become visible to the human eye as NLC elements at lower altitudes [Lübken, F.- J., 2005]. A schematic presentation of temperature and dew point along with the evolution of ice number density and ice radius is shown in Figure 3.5 [Rapp, M. and Thomas, 2006].

3.3 The envisaged rocket flight

During the peak season of NLC occurrence, the suborbital measuring flight of a two-stage sounding rocket operated with a gel propellant in the second rocket stage will be launched during the peak season of NLC occurrence and thus during the existence of the NLC elements. In order to set up the fluid flow conditions and dimensions, the technical realization of the envisaged rocket flight is described first. A newly developed gel propellant with the aim of regulating the thrust in order to control the flight attitude is applied. This is of great importance in order to keep the rocket hovering at the target altitude, which is beneficial for atmospheric physics research by sounding rockets. The hovering allows for longer sampling and for studying of the spatial distribution or extent of atmospheric constituents [DLR].

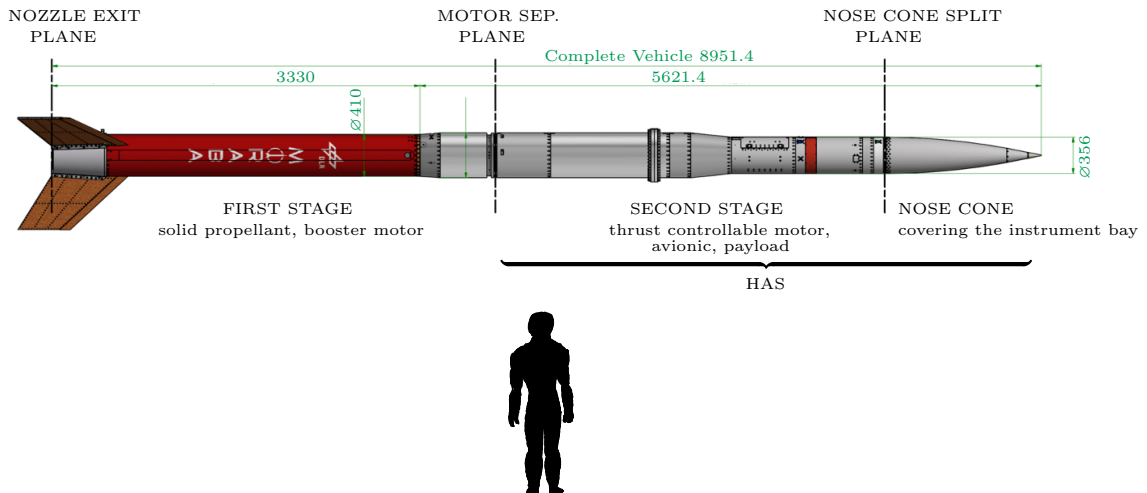


Figure 3.6: Configuration of the sounding rocket, consisting of two stages [Naumann, K. et al., 2020]. Dimensions are given in mm. To give a sense of scale, a human figure of 1800 mm body height is shown.

Figure 3.6 shows a schematic of the sounding rocket [Naumann, K. et al., 2020], which includes all necessary flight systems to launch and control the rocket as well as to perform measurements. The rocket is divided into different segments, which are shown in Figure 3.6: The first stage contains a solid propellant with corresponding booster motor. At the transition to the second stage, called high atmosphere soarer (HAS), is the motor separation plane. The second stage includes the gel propellant with the thrust-controllable engine and the payload. The payload includes, among others, the service module for the avionics, the navigation system, the power supply unit and the payload recovery system. In addition, the payload terminates in a nose cone with a separation plane and the instrument module. Here, some of the scientific instruments are covered by a cowling during ascent for protection [Naumann, K. et al., 2020]. Details about the instrument module are shown in Figure 3.8. Other measuring instruments are not located under the cowling but next to the nose cone split plane.

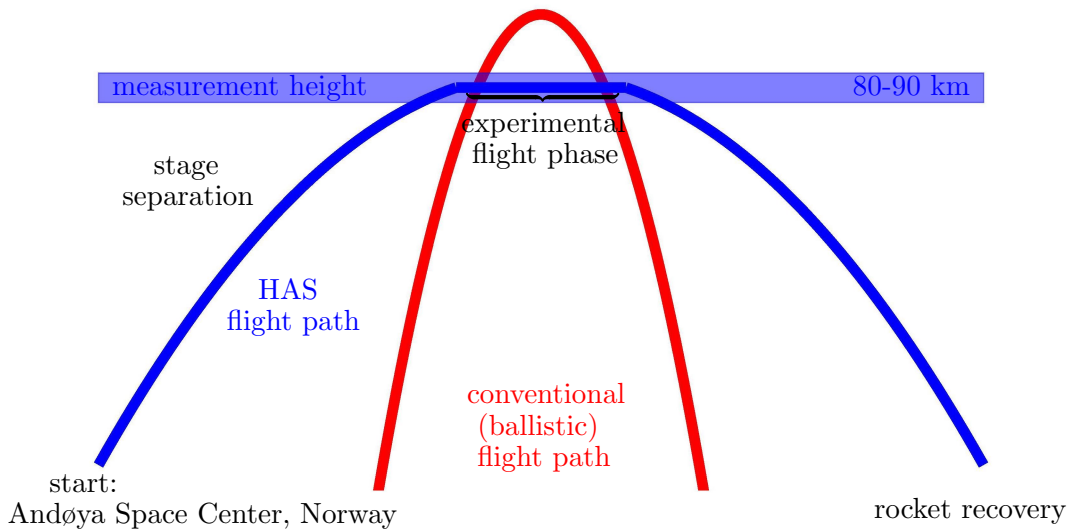


Figure 3.7: Schematic of the flattened ballistic flight path of the sounding rocket, represented by the blue color, which allows an extended measurement at relevant measurement altitudes of 80 to 90 km. Conventional flight paths have a parabolic flight profile, which is illustrated by the red curve.

The design of the sounding rocket is aimed at a suborbital flight with the solid-fuel engine. After the launch phase, just before reaching the target altitude and after the first stage burnout, the stage separation takes place at the appropriate

3 Supersonic flow simulations and impaction processes

separation plane. Then the HAS is powered by an adjustable vector nozzle, which allows regulating not only the thrust vector but also the fuel flow rate (i.e., the magnitude of thrust, to be gradually controlled). At the same time, the nose cone is separated from the rocket's main stage and the scientific instruments underneath are exposed, initiating the measurement phase and the rocket's hover

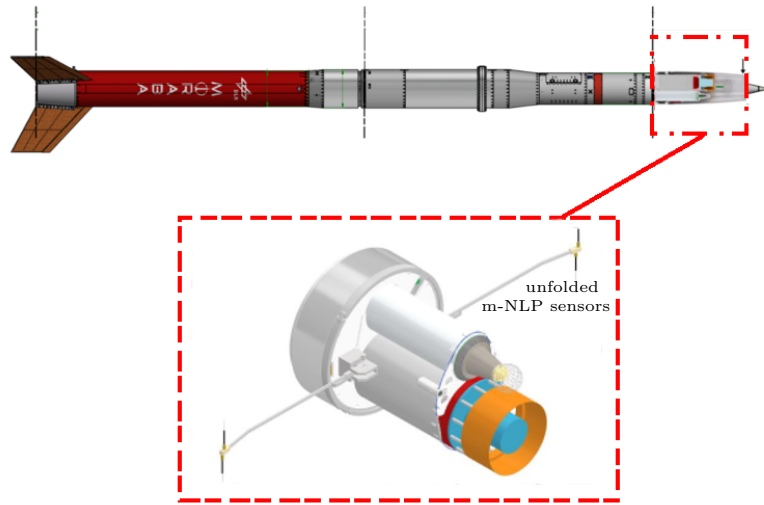


Figure 3.8: Geometry of the HAS instrument module with measuring instruments placed within the nose cone of the rocket [based on Naumann, K. et al., 2020].

The flight phase of the instrument module starts at 80 km altitude and lasts for about 60 s while a horizontal distance of 10 to 25 km is covered, with an apogee at 85 ± 5 km. The flattened parabolic flight pattern during this period is described by flight attitudes (i.e., angles of attack) of $\pm 30^\circ$ (which are the angles between the incident flow direction and the longitudinal axis of the HAS). Consequently, a velocity variation between 300 m s^{-1} and 400 m s^{-1} develops. Higher velocities are obtained at the entry to the target altitude as well as at the fall back of the HAS, slower ones at altitudes around the apogee. During the measuring flight, the orientation of the instrument module is kept constant since instrumental rotation is not desired, which also results in a steady flight phase. After the measurement phase, the HAS will undergo a water landing in the sea and subsequently be recovered. Figure 3.7 illustrates the profile of the

HAS flight (blue curve) with the extended measurement phase in the altitude range of 80 to 90 km. The major advantage of the improved flight path in comparison to the conventional ballistic flight pattern (red curve in Figure 3.7) is that the experimental measurement time remains uninterrupted and is extended, additionally increasing the prospects of mission success.

Figure 3.8 shows the close-up of the instrument module placed beneath the rocket nose cone. Hereby, different scientific instruments are shown inter alia the multi Needle Langmuir Probe (m-NLP), where the two m-NLP sensors are folded out after the nose cone ejection. The measuring instrument (called SPICE) to whose design development the numerical simulations contribute is positioned on the sides of the largest cylinder behind the m-NLP (cf. Figure 3.8 but which is not shown). The SPICE booms with the substrate mounts and impaction substrates are housed in the SPICE compartment (cf. Figure 3.9) from the beginning and are extended radially into the free air flow after the nose cone ejection when the target height is reached.

3.4 Supersonic flow simulations

The objective of the fluid dynamics simulations is to simulate the experimental flight phase of the sounding rocket, applying fluid flow and particle tracking modeling (described in Section 3.5). The mathematical model is conducted with appropriate specified atmospheric conditions. During this flight section, the flattened ballistic flight path (see blue curve in Figure 3.7) is described by angles of attack of $\pm 30^\circ$ and 0° (with the HAS flight attitude of $+30^\circ$ at the beginning of the experimental flight phase before transitioning to 0° and finally to $+30^\circ$ at the end of the experimental flight phase). Since the rocket velocity is within the range of 300 m s^{-1} to 400 m s^{-1} and the speed of sound decreases as a consequence of decreasing temperature and pressure with increasing altitude, a supersonic flight characteristic determines the flow behavior. The numerical results are used to adjust and improve the SPICE booms with substrate mounts. Flow simulation is therefore used to

- a) determine the width of the evolving boundary layer around the instrument module,

3 *Supersonic flow simulations and impaction processes*

- b) determine the effect of the evolving shock wave,
- c) determine the pressure on the SPICE booms,
- d) estimate the temperature field around the instrument module tip that is to be passed by a particle,
- e) determine the streamlines and consequently the particle trajectories that lead to an impaction on the impaction substrates.

Due to the particle properties and the assumed concentrations at the target height, a one-way coupling interaction between the fluid and the particles is considered (i.e., flow properties remain unaffected by the present particles, see Section 3.5.2). As a consequence, the flow simulations can initially be performed separately first. Then, in a second step, particles are introduced into the flow field affected by the instrument module, where particle trajectories can be tracked, which is dealt with in Section 3.5.

3.4.1 Parameters for supersonic flow simulations

Due to the supersonic flight speed and dynamic pressure acting on the geometry of the rocket, the flow simulations must be capable of resolving the partly considerable changes in velocity, temperature, pressure, and fluid density on smallest spatial scales (in the submillimeter range) in the ambient air. The following section addresses the various parameters of the mathematical model (see Section 2.1.4) on the basis of which the results are obtained.

The first step is to define atmospheric parameters prevailing in the polar summer mesopause region at an altitude of about 85 km. The corresponding air temperature is set to 130 K [Lübken, F.-J., 1999; Rapp, M. and Thomas, 2006], the gravitational constant to $g = 9.5 \text{ m s}^{-2}$, and the static pressure to $p = 10^{-2} \text{ hPa}$ [Rapp, M. and Thomas, 2006]. The flow velocity is presumed to be about 300 m s^{-1} to 400 m s^{-1} , corresponding to the intended flight speed of the HAS through the target region at an altitude of $85 \pm 5 \text{ km}$. The following simulation is treated as an extreme value problem for the given velocity range (300 m s^{-1} to 400 m s^{-1}), i.e., the actual solution for selective conditions lies within the range of resulting extrema.

3 Supersonic flow simulations and impaction processes

Based in these parameters, the mean free path λ for the calculation of the Knudsen number Kn can be determined by equation 2.1 [Willeke, K., 1976]. Applying $T = 130$ K and $p = 1 \cdot 10^{-3}$ kPa, the mean free path becomes $\lambda = 2.22 \cdot 10^{-3}$ m and together with the characteristic length of $L = 0.02$ m for the diameter of the impactor obstacle, $Kn = \frac{\lambda}{L} \approx 0.1$ is received. Thus, the required condition for the continuum assumption of the fluid flow, i.e. $Kn \ll 1$, is fulfilled. The simulations are performed by the COMSOL[®] computational fluid dynamics (CFD) module utilizing the supersonic laminar flow interface, which can handle flow conditions at arbitrary Mach numbers. Five simulation equations are required to solve for the five unknowns associated with the flow field: velocity, pressure, fluid density, temperature, and energy (see Section 2.1.3).

To approximate the thermal conductivity k and dynamic viscosity μ , both of which depend on the temperature T , Sutherland's law (cf. Section 2.1.3 with equations 2.49 and 2.50 [White, F. M. and Majdalani, 2006]) is applied. To solve equations 2.49 and 2.50, reference values of $k_{ref} = 0.0241$ W (m K)⁻¹, $T_{ref} = 273$ K, and Sutherland's constant $S_k = 194$ K are substituted into equation 2.49. Furthermore, equation 2.50 includes the parameters $\mu_{ref} = 1.716 \cdot 10^{-5}$ N s m⁻², $T_{ref} = 273$ K, and $S_\mu = 111$ K, resulting in values of $\mu = 8.985 \cdot 10^{-6}$ Pa s and $k = 0.011$ W (m K)⁻¹.

For the simulations of the flow field around the instrument module, the rocket fuselage is considered stationary and the instrument module is exposed to the air flow with velocities corresponding to the HAS speed through the mesospheric target region. This represents a change of reference system without affecting the physics. The relevant airspeed for the simulations with corresponding Mach number Ma is determined according to equation 2.2. Considering the speed of sound c according to the underlying conditions, $c = 228.73$ m s⁻¹ is obtained, which is calculated with the specific heat ratio of $\gamma = 1.4$, the specific gas constant of $R_s = 287.05$ J (kg K)⁻¹, and T , the ambient air temperature in the target region ($T = 130$ K at 85 ± 5 km). Approaching this as extreme value problem for the range of incident flow velocities ($u_{min} = 300$ m s⁻¹ and $u_{max} = 400$ m s⁻¹), the corresponding Mach numbers $Ma_{u_{min}} = 1.31$ and $Ma_{u_{max}} = 1.75$ are obtained.

3 Supersonic flow simulations and impaction processes

Subsequently, the Reynolds number is determined in order to apply the appropriate COMSOL[®] model (for laminar or turbulent flow). For this purpose, the necessary parameters of the fluid density $\rho = 2.68 \cdot 10^{-5} \text{ g cm}^{-3}$, the characteristic length L_i ($i = 1, 2$), with $L_1 = 0.02 \text{ m}$ the height or diameter of the substrate mounts (cf. Figure 3.22) or $L_2 = 0.356 \text{ m}$ for the diameter of the SPICE compartment, the maximum velocity $u = 400 \text{ m s}^{-1}$ and dynamic viscosity $\mu = 8.99 \cdot 10^{-6} \text{ Pa s}$ are inserted into the equation of the Reynolds number

$$Re_i = \frac{\rho L_i u}{\mu}, \quad (3.1)$$

resulting in Reynolds numbers of $Re_1 \approx 24$ and $Re_2 \approx 425$. The calculation yields Re_i values that indicate a purely laminar flow characteristic. Therefore, turbulence models are excluded. The laminar flow behavior for lower flow velocities (e.g., $u = 300 \text{ m s}^{-1}$) can thus be considered for laminar flow simulations as well.

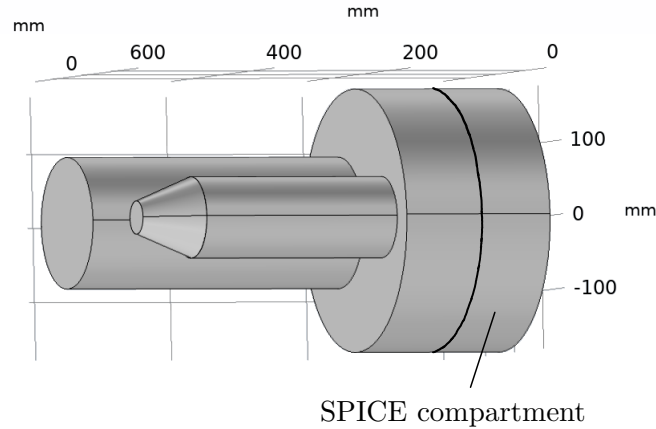


Figure 3.9: Simplified geometry of the instrument module with the SPICE compartment in which the SPICE instrument is integrated.

3.4.2 Model setup for supersonic flow simulations

The previous section describes the parameters arising from the atmospheric conditions that are used to solve the mathematical model for supersonic flows. The following section presents the model settings used with associated boundary conditions.

3 Supersonic flow simulations and impaction processes

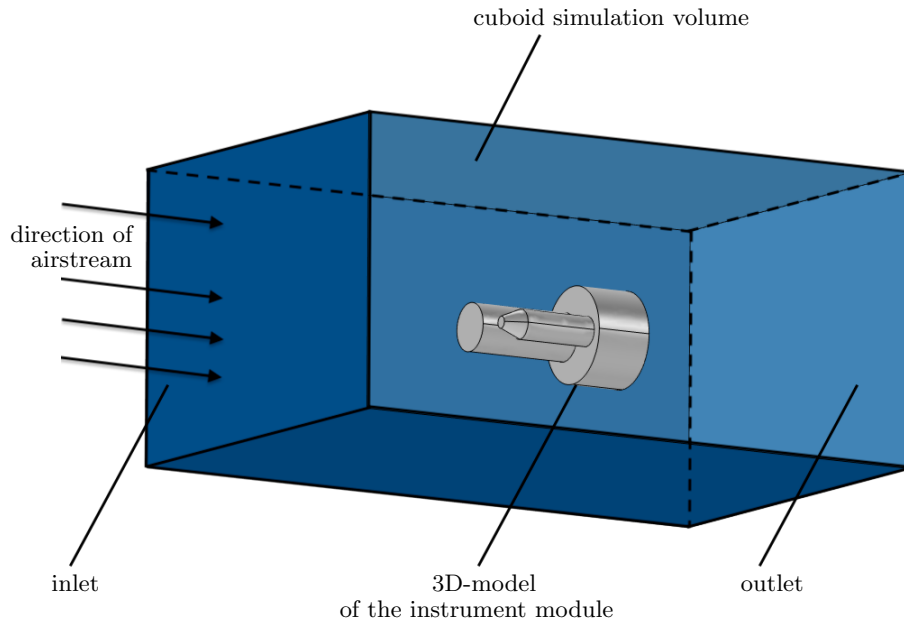


Figure 3.10: Scheme of the simulation geometry setup. The flow inlet into the simulation volume is defined upstream of the instrument module. The flow exits through the outlet boundaries, mainly at the rear of the simulation volume. The 3D model of the instrument module is centered in the simulation volume and aligned with the flow direction [Klug, B. S. et al., 2023].

At first, the COMSOL[®] model is to be set up with the appropriate geometry of the flow obstacle. Therefore, a simplified three-dimensional geometry (with regard to small scale structures whose direct influence on the air flow to the downstream SPICE collectors can be ruled out) of the rocket section with the scientific instrumentation (called instrument module) is imported in the COMSOL Multiphysics[®] model. This is depicted in Figure 3.9 with appropriate scale, where the import geometry is a computer-aided design file in the format of STEP (Standard for the Exchange of Product Data). In essence, the simplified 3D model for the simulation is limited to those structures that are essential for optimizing the position of the SPICE collectors. This geometry allows an analysis of the flow field to estimate the evolution of the boundary layer thickness as the first step in the development of the measuring instrument. It is important to note that other rocket structures downstream of the SPICE collector are also not included in the simplified 3D model, i.e., the 3D model

3 Supersonic flow simulations and impaction processes

is shortened compared to the actual geometry of the instrument module. The investigations carried out here focus exclusively on the direct vicinity of the SPICE compartment and the upstream assemblies.

For the simulation setup (Figure 3.10), the instrument module has been oriented in a horizontal position and is embedded in a cuboid simulation volume. The volume's extent is minimized in the simulations. Since only the physical flow conditions in the immediate vicinity of the instrument module are relevant, this has the advantage of keeping the computational costs as low as possible, which increase with increasing geometry size (and thus with increasing the number of mesh elements). However, it is ensured that the boundary conditions at the limits of the simulation volume have an entirely negligible impact on the simulation results. Subsequently, the physical model is adjusted. The fluid streaming around the instrument module is defined as air, and the corresponding physical constants are applied. Therefore, the surface of the cuboid fluid volume that is parallel to the front of the instrument module upstream is chosen as the inlet (see Figure 3.10). The corresponding inlet velocity is obtained based on the specified Mach number and speed of sound in COMSOL®.

In the numerical study, a stationary flow pattern around the instrument module is aimed for. In this case, however, it is difficult to define a consistent initial solution for the numerical stationary solver. Therefore, a zero initial state is considered, where the incident velocity is increased with time, which is a simple approach to overcome the convergence difficulties of the stationary solver when inconsistent boundary or initial states are defined. The time-dependent study (TDS) is adopted in COMSOL®, which is a calculation method in which parameters vary as a function of time until a steady state is reached. The velocity of the flow heading the inlet is prescribed as follows:

$$\vec{u}_i = -Ma_i x(t) c \vec{n}, \quad (3.2)$$

with Ma_i the specific Mach number, where $i = u_{min}, u_{max}$ denotes the two cases of incident flow velocities (i.e. $Ma_{u_{min}} = 1.31$ or $Ma_{u_{max}} = 1.75$). The expression $x(t)$ describes the piecewise incremental linear ramp function, defined as

3 Supersonic flow simulations and impaction processes

$$x(t) = \begin{cases} 0 & t < 0 \\ 1.56 t & 0 \geq t \leq 0.643 \\ 1 & t > 0.643. \end{cases} \quad (3.3)$$

The incident velocity 3.2 increases incrementally within a duration of 0.643 s until the final velocity $Ma_i c$ is reached (i.e., 300 m s⁻¹ or 400 m s⁻¹). In this way, the zero initial state continues to develop temporarily until the fluid dynamics are reached at flow velocities of 300 m s⁻¹ and 400 m s⁻¹. In addition to the flow velocity, the static pressure of $p_0 = 10^{-2}$ hPa and the temperature $T_0 = 130$ K characterize the initial state.

The remaining boundaries are defined as outlet, where the flow leaves the simulation volume almost exclusively on the opposite side of the inlet. For the simulation it is of importance that the respective outlet surfaces are chosen at an appropriate distance from the flow obstacle, as otherwise the influence of the boundary conditions on the flow pattern may be quite considerable. For the following investigations, the flow obstacle is approximated as a cylindrical body with the dimensions of the instrument module. The ratio of the cylinder length l to the geometry length d , which corresponds to $d = 16l$ with $l = 0.8$ m is chosen. The obstacle is vertically centered, whereby the downstream length is significantly greater than the upstream length (approximately $14l$ see Figure 3.11). Thus, the influence of the outlet condition is minimal. In this study, the subsonic and hybrid outlet conditions for high Mach numbers are tested, which are implemented in COMSOL[®]. To demonstrate the impact of both boundary conditions on the flow patterns, the subsonic boundary condition for the velocity, which is defined as

$$\left[-p\mathbf{I} + (\mu(\nabla\vec{u} + (\nabla\vec{u})^T) - \frac{2}{3}\mu(\nabla\vec{u})\mathbf{I}) \right] \vec{n} = -f_0\vec{n} \quad (3.4)$$

is first investigated, where the total stress is equal to the stress vector of magnitude $f_0 = 1$ N m⁻². The boundary condition for the energy equation is

$$-\vec{n} \cdot \vec{q} = 0, \quad (3.5)$$

where the heat flux \vec{q} across the domain boundary is set to zero. As a

3 Supersonic flow simulations and impaction processes

consequence, the absence of a temperature gradient across the boundary is assured and thus the temperature on one side of the boundary is equal to the temperature on the other side.

The hybrid case covers both cases (i.e., the subsonic as well as the supersonic case) with boundary conditions of

$$\left[-p\mathbf{I} + (\mu(\nabla\vec{u} + (\nabla\vec{u})^T) - \frac{2}{3}\mu(\nabla \cdot \vec{u})\mathbf{I}) \right] \vec{n} = -0.5(p - p_{stat})\vec{n}, \text{ if } Ma < 1, \quad (3.6)$$

where $p_{stat} = 10^{-2}$ hPa is the outlet pressure, and

$$\left[-p\mathbf{I} + (\mu(\nabla\vec{u} + (\nabla\vec{u})^T) - \frac{2}{3}\mu(\nabla \cdot \vec{u})\mathbf{I}) \right] \vec{n} = -p\mathbf{I}\vec{n}, \text{ if } Ma \geq 1, \quad (3.7)$$

which results in

$$(\mu(\nabla\vec{u} + (\nabla\vec{u})^T) - \frac{2}{3}\mu(\nabla \cdot \vec{u})\mathbf{I})\vec{n} = 0 \quad (3.8)$$

together with following equation

$$-\vec{n} \cdot \vec{q} = 0, \quad (3.9)$$

which in the supersonic case leaves the pressure to be free at the outlet. Figure 3.11 shows the relative difference $(\vec{u}_s - \vec{u}_h) \cdot \vec{u}_h^{-1}$ in simulated flow velocities between the subsonic and hybrid boundary conditions with respect to the hybrid boundary condition, with \vec{u}_s the flow velocity with supersonic boundary conditions and \vec{u}_h the velocity values with hybrid boundary conditions. For the incident flow velocity of $\vec{u} = 300 \text{ m s}^{-1}$ (Figure 3.11 a)), the relative differences in flow velocities are present throughout the simulation volume, most pronounced in the shock wave region with the maximum relative difference of (Ω denotes the simulation domain)

$$\text{diff}_{\max}(\vec{u}_s, \vec{u}_h) = \frac{\max_{\Omega} |\vec{u}_s - \vec{u}_h|}{\vec{u}_h} = \frac{\|\vec{u}_s - \vec{u}_h\|_{\infty}}{\vec{u}_h} \approx 0.0687, \quad (3.10)$$

which corresponds to 6.9%. At flow velocities of $\vec{u} = 400 \text{ m s}^{-1}$, the relative differences in flow velocities between the two simulations are almost uniformly distributed in the simulation volume (cf. Figure 3.11 b)) with a higher deviation

3 Supersonic flow simulations and impaction processes

in the near vicinity of the flow obstacle. Furthermore, the maximum relative difference is about 0.3%, with the largest deviations found at the cylinder surface facing the flow.

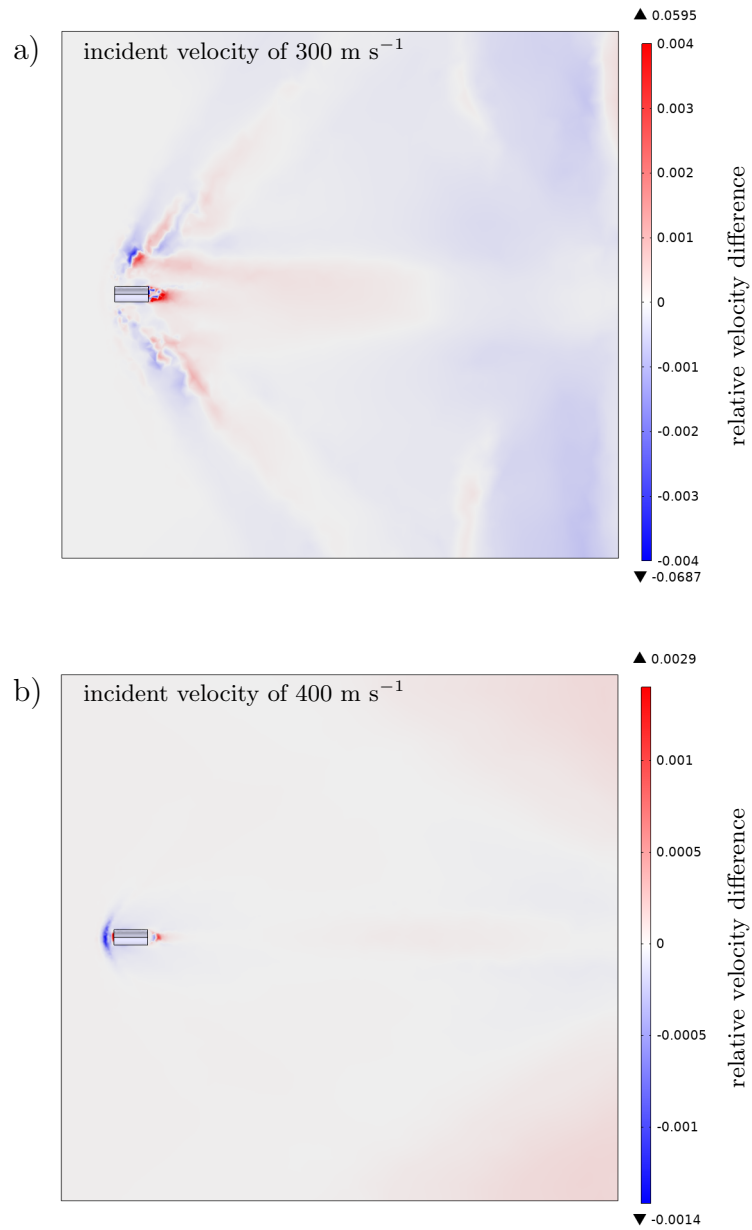


Figure 3.11: Difference in velocities computed for subsonic and hybrid boundary conditions in m s^{-1} . The upper picture shows the difference for the incident flow velocity of 300 m s^{-1} and the lower picture for 400 m s^{-1} .

The difference in the two Figures 3.11 a) and b) can be justified by the two

3 Supersonic flow simulations and impaction processes

incident flow velocities, which lead to different shapes of the Mach cones: at 300 m s^{-1} , the Mach cone is wide open and the shock wave hits the exterior boundary, which can affect the flow field. In contrast, at 400 m s^{-1} , the Mach cone is comparatively narrow, thus it extends over a larger horizontal distance within the simulation volume and abates along the way, resulting in a smoothly shaped velocity gradient when it hits the limit of the simulation volume. The coarse-meshed grid of the simulation chosen for efficiency reasons can also contribute to numerical uncertainties and differences between two simulation results based on deviating boundary conditions.

Since the influence of the different boundary conditions (in our case with high Mach numbers) on the simulated flow field is small and the advantages of the hybrid method outweigh the pure subsonic approach (due to the coverage of both subsonic and supersonic cases), hybrid boundary conditions (equations 3.6 and 3.7) are chosen in upcoming simulations. Moreover, in the supersonic case, no pressure is applied at the limits of the simulation volume.

The boundary conditions for the surfaces of the instrument module are defined by the no-slip condition [Pruppacher, H. R. and Klett, 2010], i.e., the condition

$$\vec{u}|_s = 0 \text{ m s}^{-1} \quad (3.11)$$

is prescribed, where s denotes the physical surface of the instrument module.

Finally, before the simulation starts, the appropriate mesh with variable mesh size is constructed to take into account the balance of the physical resolution and the required computation time. Obviously, the finer the mesh, the lower is the numerical discretization error and thus, the numerical solution. However, the mesh resolution of the three dimensional geometry comes at the cost of computation time. It is important to consider to what extent the mesh needs to be finely resolved over the simulation volume and whether there are areas where finer resolution is more required than in other regions.

For the fluid dynamics simulations, the mesh is automatically generated based on physics controlled settings in the COMSOL[®] mesh node, where the speci-

3 Supersonic flow simulations and impaction processes

fied element size is chosen as *fine*. Due to the three-dimensional problem, the domain is discretized by tetrahedral, pyramidal as well as prismatic mesh elements. Boundary layers at flow obstacles are generated within the geometry and resolved by eight layers of narrow tetrahedral boundary elements. The number of boundary layers has to be defined manually. This ensures that emerging gradients in the immediate vicinity of surfaces, edges and structures of the flow obstacle are adequately resolved. Additionally, the grid is refined at corners, as sharp corners and edges cause disturbances that create particular flow patterns. In contrast, the resolution of free flow regions within the simulation volume is automatically generated by coarser element sizes. To adequately resolve the shock wave, which occurs in form of sharp flow field discontinuities, an additional dynamic mesh refinement in the first simulation step is performed based on the velocity gradient. This leads to a numerical resolution of the region near the shock wave and in the vicinity of surfaces, edges and structures of the flow obstacle and is achieved as follows: Firstly, the time steps of the mesh refinement have to be specified so that they are performed four times every 0.1 s. Secondly, the error indicator for the refinement is given, using the Frobenius-norm of the velocity gradient:

$$\|\nabla\vec{u}\| = \sqrt{\sum_{i,j=1}^3 \left| \frac{\partial u_i}{\partial x_j} \right|^2}. \quad (3.12)$$

The mesh elements are refined by the halving of their longest edge and the process is repeated twice per refinement operation. As a result, the additional mesh refinements are conducted only in critical boundary layer and shock wave regions, while the overall mesh number remains at levels of what is essential and appropriate for efficient calculations. Generated meshes and corresponding details are addressed in Sections 3.4.3 to 3.4.3 below, where the number of mesh elements lies in the range of 10^6 and smallest mesh element sizes in the range of 10^{-3} m.

Solver settings

For the fluid flow simulations, the implemented solver is based on backward differentiation formulas of order $k = 1$ and $k = 2$ described in Section 2.3.3. The adaptive time step sizes are determined by the solver based on a relative error tolerance. Linear continuous finite elements and linear shape functions for

the fluid velocity \vec{u} as well as the fluid pressure p and the temperature T are utilized in the implemented spatial discretization in the FEM (cf. Section 2.3 et seq.). For the stabilization of convective dominated flow regimes, the streamline diffusion stabilization (cf. Section 2.3.2) and the crosswind diffusion stabilization [Hughes, T. J. R. and Mallet, 1986; Johnson, C. et al., 1987; Semper, B., 1994; Hauke, G. and Hughes, 1994] implemented in COMSOL[®] are applied. For the simulations the MUMPS (MULTifrontal Massively Parallel Sparse) direct solver is used, which is well suited for parallelized calculations. High Mach number flow field calculations were performed in parallel on a 6-node cluster with 70 cores and a total memory of 896 Gigabyte, where the calculation time of the subsequent simulations was up to 181 hours.

3.4.3 Flow simulations to design the SPICE instrument

In the following, simulation results are presented on whose the development of the SPICE instrument for the collection of particles in the mesosphere is based on. The questions to be answered are related to the position, design and possible/necessary distance of the impactor surfaces from the vehicle's fuselage. The primary goal is to develop a reliable numerical simulation and consequently to design the aerodynamic shape and arrangement of an impactor geometry to increase the yield of particles. The properties of the collected particles can be analyzed by physico-chemical analyses based on representative particle collection. The design process begins with initial simulation results and analyses of the flow field around a simplified geometry of the instrument module:

- 1) around the geometries and structures located upstream of the SPICE compartment,
- 2) around parts of the vehicle's fuselage in the immediate vicinity of the SPICE compartment,
- 3) more detailed simulation analyses are subsequently carried out on the basis of (1) and (2).

Ultimately, a geometric arrangement for the SPICE instrument is elaborated that is mechanically releasable with a fully autonomous control system and that meets the requirements for the most effective sampling possible under given conditions.

Investigation of the evolving boundary layer

The first analysis of the simulation results targets at determining the evolving boundary layer thickness around the SPICE compartment (cf. Figure 3.9) during the measurement phase of the envisaged rocket flight. In order to also capture the sensitivity of the boundary layer thickness to variable velocity conditions, each of the development steps is performed for the (limiting) flight velocities $u_{min} = 300 \text{ m s}^{-1}$ and $u_{max} = 400 \text{ m s}^{-1}$. With knowledge of the boundary layer thickness and the flow field immediately around the SPICE compartment, the required length and preferred position of SPICE's collecting booms (see Figure 3.16 or 3.22) are identified. This ensures an efficient particle collection within the mostly undisturbed free flow and rules out that the impaction processes are influenced by artifacts (e.g., due to downwash and flow interferences with geometries, surfaces and structures). Particles are deflected by the flow around the given geometry near the surface of the instrument module, resulting in zones of enriched and reduced particle number concentration. Zones of particle enrichment would offer the advantage of sampling with increased probability of particle impactions, while it should be remarked that this sampling does not primarily aim at obtaining absolute particle number concentrations.

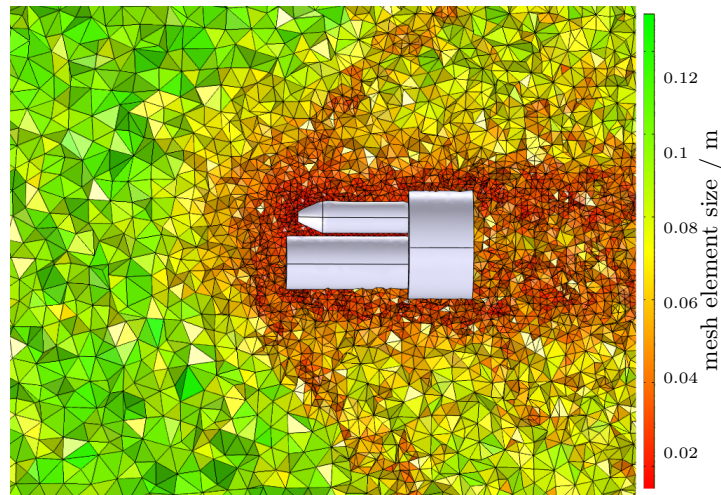


Figure 3.12: Generated mesh with refinement zones. The distribution of mesh sizes is illustrated: the mesh resolution is increased in the immediate vicinity of the flow obstacle as well as along the shock wave, whose position and course were determined by precalculations.

Figure 3.12 represents the computational mesh sizes for the flow field simula-

3 Supersonic flow simulations and impaction processes

tions at an incident velocity of 400 m s^{-1} , the corresponding simulation result is depicted in Figure 3.13 b). Larger mesh elements, for which the flow field is not subject to fluctuations, are dominated in the inlet region of the simulation volume (left-hand part of Figure 3.12). Smaller mesh elements are created based on the velocity gradient error indicator (cf. equation 3.12).

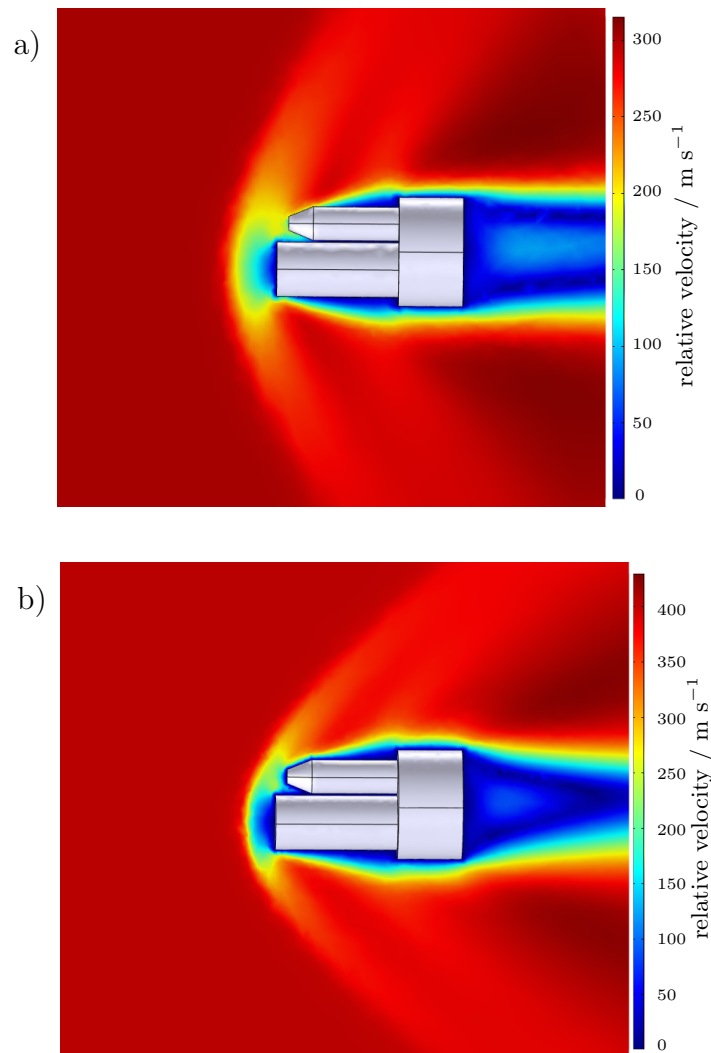


Figure 3.13: Velocity magnitude distribution around the instrument module, shown in a longitudinal vertical plane. The inlet of the air flow into the simulation volume is located on the left side. Figure a) shows the simulation result for the incident flow velocity of 300 m s^{-1} and b) for 400 m s^{-1} .

In the vicinity of surfaces, edges and structures of the flow obstacle and in the area of the shock wave, the mesh is refined. The smallest element size is about

3 Supersonic flow simulations and impaction processes

$8.7 \cdot 10^{-3}$ m and largest elements are about 0.23 m in size with a total number of mesh elements of 612 000, distributed within the entire simulation volume.

The depiction of the velocity magnitude for the incident flow velocities of 300 m s^{-1} and 400 m s^{-1} on a longitudinal sectional plane along the centerline of the simulation volume are shown in Figure 3.13 a) and b). The longitudinal axis of the instrument module is aligned parallel to the flow direction, where the module's tip points towards the defined inlet of the simulation volume on the left side. The color scale assigns the magnitude of the flow velocity to the different positions within the simulation volume. At supersonic speeds, disturbances can no longer propagate upstream, hence they combine to form a standing wave in front of the instrument module as illustrated in Figure 3.13. A stationary velocity gradient is created, which exhibits the characteristics of a shock wave, which is called a bow shock. It should be noted that in the following the flow field downstream of the SPICE instrument position and in particular behind the instrument module is not dealt with in detail. It may be reminded that here a shortened three dimensional model is applied for the simulations, where only the tip of the instrument module and structures upstream of the SPICE instrument position are of relevance - however, the geometry of the instrument module actually continues. Thus, the simulated flow profile behind the three dimensional model of the instrument module is not representative of the reality.

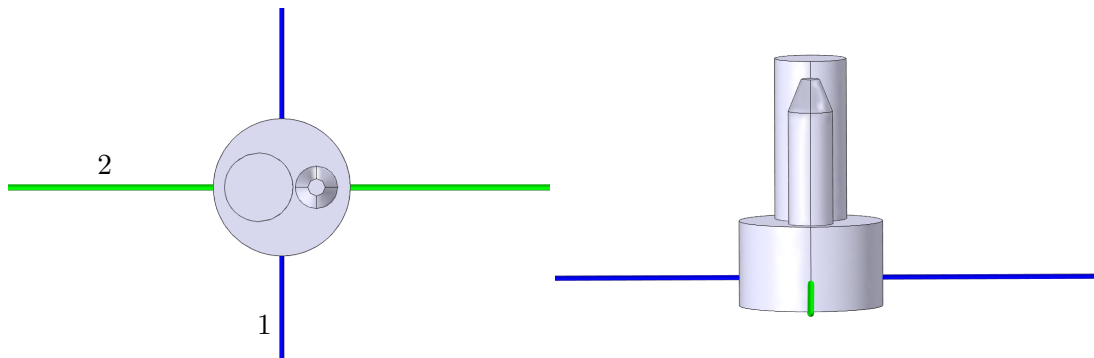


Figure 3.14: Visualization of two cut lines on which flow velocity values are evaluated to determine the boundary layer thickness. The blue color marks cut line 1 and the green color marks cut line 2.

3 Supersonic flow simulations and impaction processes

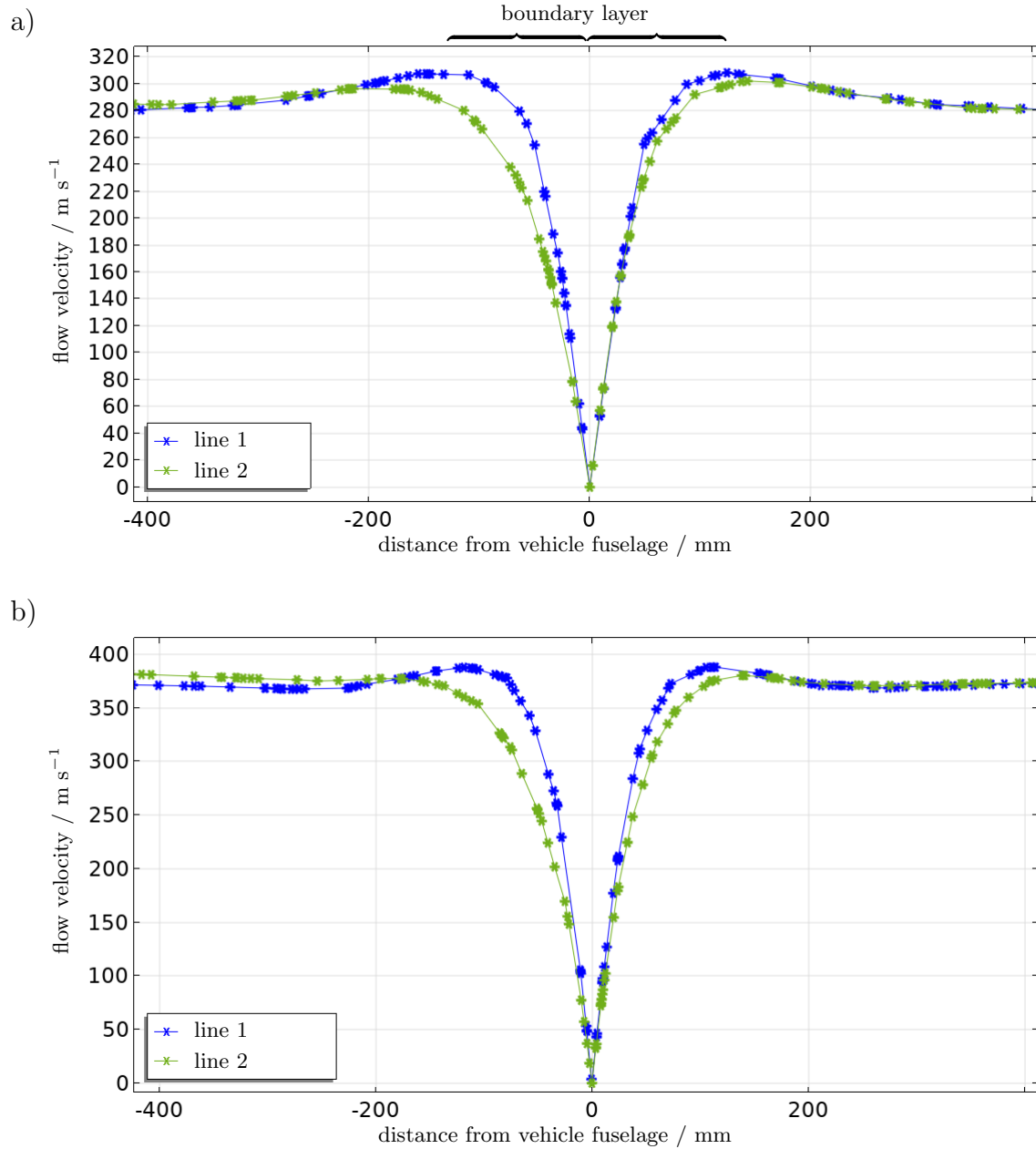


Figure 3.15: Flow velocity profile evaluated along cut lines 1 (blue) and 2 (green) for the incident flow velocities of 300 m s^{-1} in Figure a) and 400 m s^{-1} in Figure b). Crosshair symbols indicate data points at mesh nodes.

The Mach cone illustrated in Figure 3.13 b) is narrower to the one shown in a), which is to be expected given the higher airspeed. In addition, the veloc-

3 Supersonic flow simulations and impaction processes

ity gradient at the tip of the instrument module becomes more distinct as the flow velocity increases. The instrument module with its protuberances hence does not cause a single shock wave at the tip, but affects an extended region downstream with a sustained gradient caused by the protuberances. The drop in velocity at the transition from the free flow to the shock wave is about 15% for the incident velocity of 300 m s^{-1} and about 11% for the incident velocity of 400 m s^{-1} . However, the flow behind the shock wave remains in the supersonic range for both cases. For the following analyses, two cut lines are placed through the instrument module within the simulation volume in two planes perpendicular to the longitudinal axis of the instrument module in the plane of the SPICE instrument (cf. Figure 3.14). Figures 3.15 a) and b) depict flow velocities around the SPICE compartment as a function of the distance from the instrument module surface (x -axis, with the zero point being positioned on the surface) along cut lines 1 and 2 (cf. Figure 3.14) for incident velocities of 300 m s^{-1} and 400 m s^{-1} (data can be found in Appendix G). On decreasing distance from the module surface, the boundary layer around the instrument module is indicated by a steep drop in flow velocities, which rapidly decrease to a value of $u = 0 \text{ m s}^{-1}$ as the module surface is further approached. The free flow field velocity values of 300 m s^{-1} and 400 m s^{-1} outside the boundary layer are not reached in the presented graphs, since the analyses are limited to the near region around the instrument module surface. This region is characterized by the forming bow shock and the slower flow velocities therein. The comparison of the various results may reveal certain differences:

- 1) Since the Mach cone is narrower at higher flow velocities (e.g., 400 m s^{-1}), the slightly different course of the velocity profiles in Figure 3.15 a) compared to 3.15 b) can be explained.
- 2) Since the geometry of the front payload is symmetrical for the course of one cut line (cf. Figure 3.14, line 1 in blue), but asymmetrical to the zero point in the other case (cf. Figure 3.14, line 2 in green), an asymmetrical shape of the corresponding velocity profiles (green lines in Figures 3.15 a) and b)) around the zero point results.
- 3) The maximum flow velocities are found for 400 m s^{-1} at a slightly lower distance from the instrument module surface than in the investigated case of 300 m s^{-1} (compare Figures 3.15 a) and b)). This means that the boundary

layer is thinner at higher than for slower incident flow velocities. Nevertheless, the differences found here between 300 m s^{-1} and 400 m s^{-1} are insignificant and can be neglected in further boundary layer specifications.

The design of the SPICE instrument requires on the one hand the shortest possible booms given the limited space for the payload. On the other hand, sufficiently long booms are needed for representative particle sampling on substrate mounts well outside the disturbed boundary layer. The optimal length of the SPICE booms is determined at best on the basis of a sharply defined boundary layer. Thus, the distance between the instrument module surface and the free (fully developed, undisturbed, i.e., until the velocity gradient within the boundary layer becomes small) flow can be deduced from Figures 3.15 a) and b), where the optimum length of the SPICE booms is determined to be 120 mm, as the best compromise.

Confirmation of the chosen length of the SPICE booms

To determine whether collection on the substrates at the tip of the SPICE booms proceeds effectively, a detailed investigation of the motion of particles is of importance. As particles approach the instrument module, they are deflected by the flow around the given geometry near the surface, which can result in areas of increased and decreased particle number concentration around an obstacle.

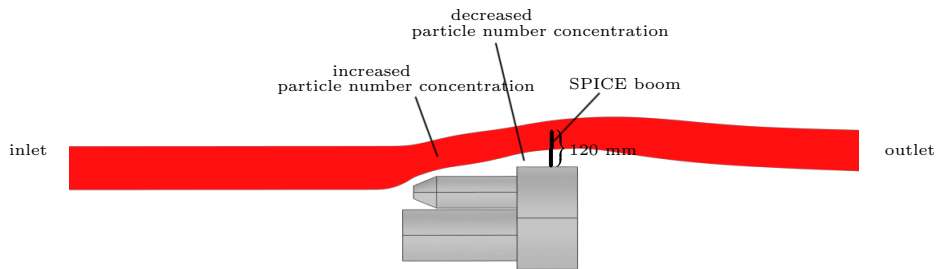


Figure 3.16: Particle trajectories based on the fluid simulation with incident velocity of 400 m s^{-1} are shown in red. The position of a SPICE boom with the length of 120 mm is shown for illustration purposes. Areas with increased and decreased particle number concentration are indicated.

To confirm the deflection of particles and to demonstrate that the chosen length

of the SPICE booms allows effective particle sampling, particle trajectories are numerically simulated. Figure 3.16 shows particle trajectories based on precomputed fluid dynamics at a flow velocity of 400 m s^{-1} . For this simulation, the diameter of the particles is set to 100 nm, since atmospheric lifetimes of particles of this size belong to the longest, as losses due to sedimentation and diffusion are minimal in this size class. An ensemble of 5000 particle trajectories marked in red, starting from a specific particle inlet area, is shown. A detailed description of the particle simulation (with all necessary parameters and the equation) can be found in Section 3.5 ff. Particles are deflected by the deviation in flow direction, which guides around the geometry of the instrument module. An area of increased particle number concentration is shown by a compression of the suite of particle trajectories (shown in Figure 3.16). Decreased particle number concentrations are found near the vehicle's fuselage. Thus, the particle trajectory simulation demonstrates that the planned design of the SPICE instrument, and in particular the length of its booms, provides effective removal of particles from the air flow around the instrument module. In addition, the simulation clearly shows that no particles would be sampled at all for the chosen particle inlet position if the substrate mounts would be placed too close to the surface of the instrument module.

Influence of the m-NLP instrument on the downstream flow field

The entire instrument module of the rocket comprises several measuring instruments for various research projects based on data acquisition. So far, the geometry and extension of a specific measurement instrument has not been considered. However, since the so-called Multi Needle Langmuir Probe (m-NLP) (cf. Section 3.3) with its aerial-type structures significantly affects the downstream flow field (i.e., at the plane of the SPICE booms) the simulation model requires further refinement.

The geometry of the instrument module including m-NLP is presented in Figure 3.17. Moreover, the corresponding refined mesh for flow field calculations of the 3D model is presented. The mesh consists of 1.94 million elements with smallest sizes of $1.89 \cdot 10^{-3} \text{ m}$ and largest elements of 0.19 m. Regions in the simulation volume where strong gradients of the flow velocity emerge are resolved by smaller element sizes (defined a-priori by the default setting of the

3 Supersonic flow simulations and impaction processes

physics controlled mesh for the geometry including the filigran m-NLP). The dynamic mesh refinement during the calculation (as applied in the previous paragraph) is therefore not necessary anymore. The thin tetrahedral mesh elements clustered around the instrument module favor the detailed resolution of the boundary layer around the SPICE compartment. Repeated boundary layer analyses of the flow around the instrument module are carried out to determine at which alignment each SPICE boom stays aloof from any flow disturbance by the m-NLP.

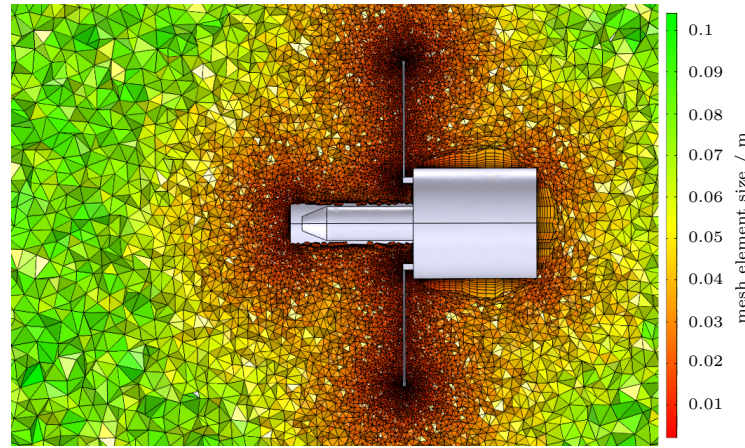


Figure 3.17: Computational mesh for simulations of the instrument module with m-NLP. The mesh resolution is increased around the flow obstacle, boundary layer elements are visible at the instrument module including the SPICE compartment [Klug, B. S. et al., 2023].

Correspondingly to the incident velocities of 300 m s^{-1} and 400 m s^{-1} , the flow field is exhibited in Figures 3.18 a) and b). Both figures clearly display the Mach cone around the tip of the instrument module. The disturbance of the flow field due to the m-NLP is clearly pronounced at both velocities; the tips of the m-NLP cause shock waves that interfere with the shock wave generated at the tip of the instrument module. Downstream of the m-NLP, the deceleration of the incident flow velocities is unambiguous. A well-defined boundary layer forms around the instrument module including the SPICE compartment. Another depiction of the flow field based on the incident flow velocity of 300 m s^{-1} and 400 m s^{-1} is shown in Figures 3.19 a) and b). The cross sectional plane onto which velocity values are plotted is at the level of the

3 Supersonic flow simulations and impaction processes

SPICE instrument (perpendicular to the longitudinal axis of the instrument module). The influence of the m-NLP is limited to their slipstream indicated by locally low velocity values of 256 m s^{-1} (i.e., a deceleration of the incident flow velocity of 17% for 300 m s^{-1}) and 330 m s^{-1} (i.e., a deceleration of 21% for 400 m s^{-1}).

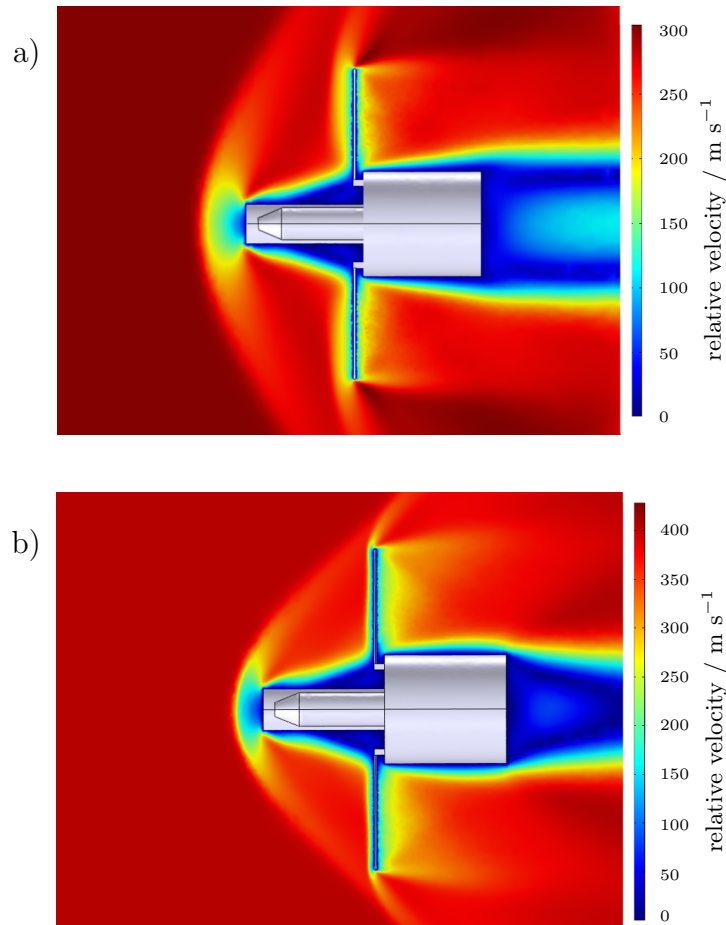


Figure 3.18: Flow field around the instrument module with m-NLP depicted on a longitudinal vertical plane. The inlet for the air flow is on the left-hand side. Figure a) shows the simulation result for the flow velocity of 300 m s^{-1} and b) for 400 m s^{-1} [Klug, B. S. et al., 2023].

Other contours that indicate decelerated velocity values are due to the shock wave. Regarding the SPICE instrument positioned downstream of the m-NLP, it is obvious that an alignment of the SPICE booms in the direct wake of the m-NLP is to be avoided. Positions of the SPICE booms, which are possibly

3 Supersonic flow simulations and impaction processes

unaffected by the flow pattern caused by the m-NLP, are shown as (red, blue, and green) cut lines in Figures 3.19 a) and b). Furthermore, the instrument module with the three intersection lines from two perspectives is shown in Figure 3.20.

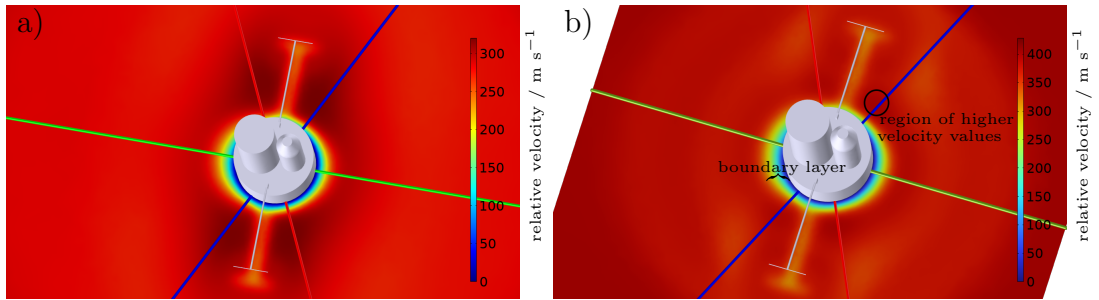


Figure 3.19: Frontal view of the cross-section of the flow velocity field (in the level of the SPICE instrument) for the incident flow velocity of 300 m s^{-1} in a) and 400 m s^{-1} in b). Note: The flowed-around instrument module also comprises the m-NLP booms, whose wake imprint is clearly reflected in the flow velocity field at the level of the SPICE instrument (yellow/orange contours). Colored lines (blue/red/green) indicate potential configurations of the SPICE booms as far as possible away from wake influences of the m-NLP.

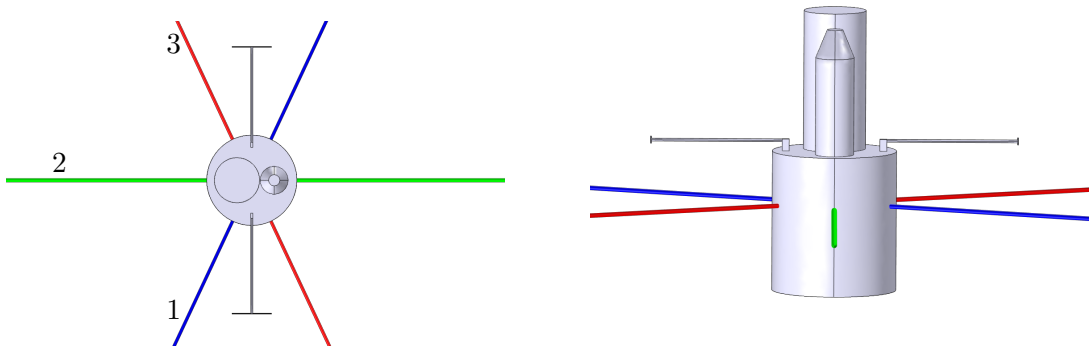


Figure 3.20: Visualization of the cut lines from two different perspectives of the instrument module along which velocity variables are analyzed [based on Klug, B. S. et al., 2023]. The blue color marks cut line 1, the green color cut line 2 and the red color marks cut line 3.

Flow velocities along the cut lines (1, 2, and 3) of the boundary layer region for

3 Supersonic flow simulations and impaction processes

incident flow velocities of 300 m s^{-1} and 400 m s^{-1} , respectively, are depicted in Figures 3.21 a) and b).

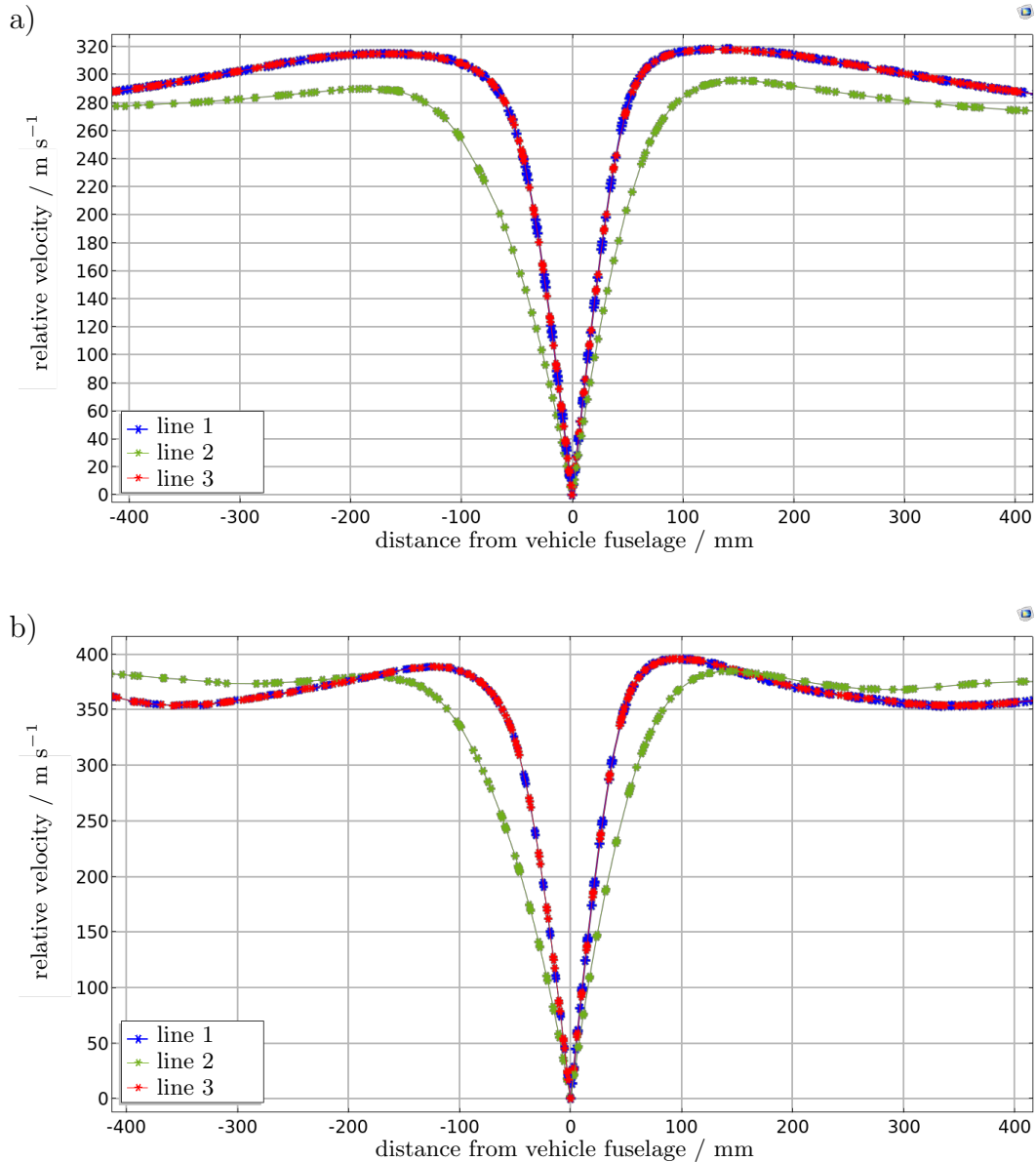


Figure 3.21: Flow velocities evaluated on cut lines 1 (blue), 2 (green) and 3 (red) for the incident flow velocities of 300 m s^{-1} , a) and 400 m s^{-1} , b) [Klug, B. S. et al., 2023]. Crosshair symbols indicate data points at mesh nodes.

Note that cut lines 1 and 3 pass through regions of higher flow velocities compared to cut line 2 (cf. Figure 3.19 b)). Again, the x -axis represents the

3 Supersonic flow simulations and impaction processes

distance from the surface of the instrument module, where the zero point is located on the vehicle's fuselage. Crosshair symbols indicate data points at mesh nodes. The boundary layer, represented by the rapid drop in velocity values near the instrument module surface, is clearly visible. The way to read the course of the evaluated data has already been described in the previous paragraph. The flow velocity difference at the edge of the boundary layer (at a distance of 120 mm from the vehicle fuselage) between cut lines 1 and 2, and cut line 3 is about 25 m s^{-1} (i.e., about 8.6%) lower at the incident velocity of 300 m s^{-1} . In summary, comparing the flow velocities determined at cut lines 2 presented in Figures 3.15 and 3.20 (since the courses are identical), the shape of the profiles of respective velocities are similar. The maximum velocities at the edge of the boundary layer only differ by 2% (i.e., by 6 m s^{-1}). Furthermore, there are no anomalies in the course of the velocity values of cut lines 1 and 3. Thus, almost no influence of the m-NLP instrument can be detected at the selected positions of the corresponding cut lines. For this reason, it seems appropriate to position the SPICE booms analogously to the orientation of the cut lines. However, due to the limited space in the SPICE compartment, it is not possible to construct the booms in all six directions arranged in the cross sectional plane perpendicular to the longitudinal axis of the instrument module.

The best possible compromise between an effective measurement and the limited space for the payload leads to the following design: Three SPICE booms are constructed, each of which is oriented at 120° to each other and corresponding to one of the three half-cut lines. In this way it is ensured that:

- 1) the probe sampling is achieved in different spatial directions and at three independent positions within the free flow field around the rocket body,
- 2) at least one of the substrate mounts is exposed to an almost undisturbed air flow at all times during the flight, regardless of the ballistic flight path (with different flight attitudes) of the HAS,
- 3) the probability of at least one successful sampling is substantially increased by the use of three independent, redundant sampling systems, since in this way partial or total failures of a single sampling are largely compensated.

The evaluation of the flow velocity along the cut lines with regard to the boundary layer thickness around the flowed instrument module also confirms

3 Supersonic flow simulations and impaction processes

that the length of the SPICE booms of 120 mm is appropriate and sufficient to allow for a probe sampling in the free flow field.

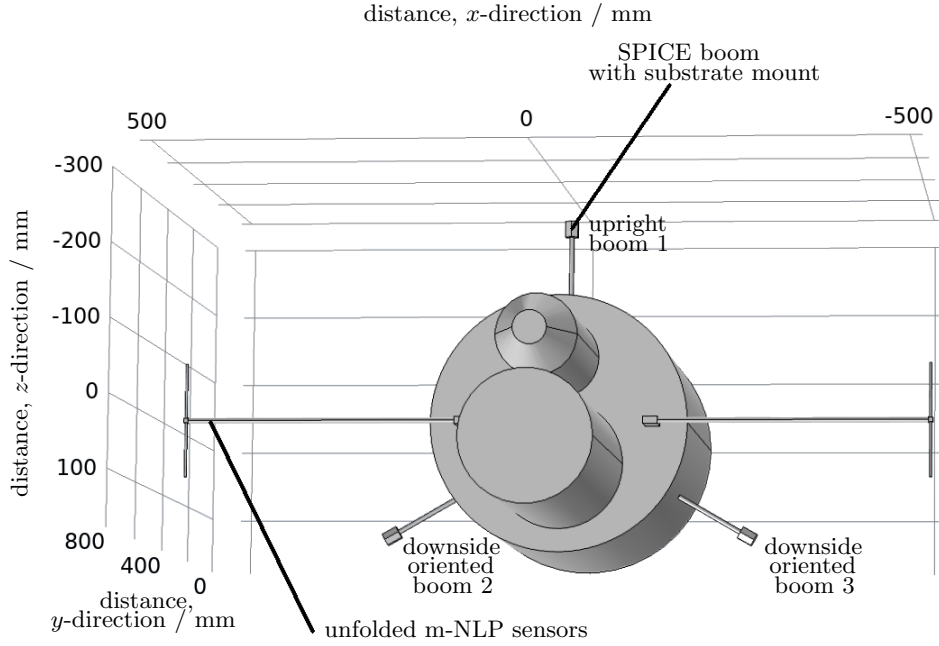


Figure 3.22: Frontal view of the computational geometry of the instrument module showing the ultimate layout of the three SPICE booms bearing the substrate mounts at their tips [based on Klug, B. S. et al., 2023].

Figure 3.22 illustrates the final geometry of the entire instrument module including the selected arrangement of the three SPICE booms. Shown are the m-NLP sensors and SPICE booms with substrate mounts whose positions are offset from each other. The structure of the impact apparatus is shown: hexagonal prisms (0.020 m in diameter and 0.023 m in height) are attached to the tips of the three SPICE booms, with substrates mounted on their side panels, as shown in Figure 3.23. Embedded in their surfaces are transmission electron microscopy (TEM) grids (two TEM grids on each of the six surfaces, resulting in 36 probes to be analyzed), to which the impacting particles adhere. TEM grids are fragile structures on which nanometer-sized particles collide and adhere due to van der Waals forces.

3 Supersonic flow simulations and impaction processes

The advantage of sampling on TEM grids is that collected particles, along with the substrate, can be immediately placed in the transmission electron microscope for analysis without further treatment, thereby minimizing the potential of contamination (although care must be taken during assembly and disassembly to avoid contamination). The TEM grids on the impactor surfaces are underlaid with gold foils. This supports the TEM grid and ensures that even those particles can be collected on a substrate-like surface (i.e., the gold foil) which, for example, strike through the TEM grid due to their kinetic energy.

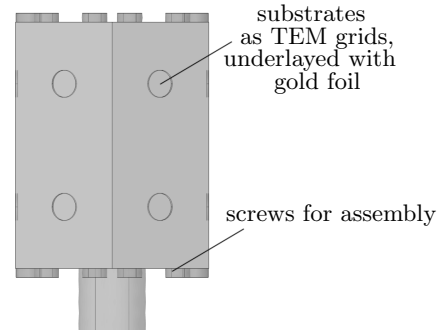


Figure 3.23: Detailed geometry of the substrate mount with recessed impaction substrates.

The decision to use the developed design of the impactor surfaces has several reasons:

- 1) during the hovering flight of the HAS along the flattened ballistic profile (cf. blue flight path in Figure 3.7), the flight attitude changes. Distributed multi-sampling in as many spatial directions as possible ensures that the sampling occurs effectively and is less dependent on the vehicle's flight attitude,
- 2) one side of the hexagonal prism is approximately facing the air flow. This orientation perpendicular to the flow acts as a front surface in a non-aerodynamic shape and contributes to sharp changes in the direction of the streamlines, causing the trajectories of the particles to deviate from them due to the particle inertia and thus leading to impactions,
- 3) there are always some of the surfaces of the hexagonal prism substrate mounts at an angle to the incident flow direction, onto which, however, the deposition of particles from the decelerated air flow may nevertheless occur. Once the flight attitude changes, these surfaces may point exactly against the flow direction, at least for parts of the flight attitude,

3 *Supersonic flow simulations and impaction processes*

- 4) in addition, the symmetrical and fully circumferential configuration of the substrate mounts ensures sampling both within the frontal flow and in the flow shadow,
- 5) finally, the chosen geometry favors the handling of assembly and disassembly the TEM grids on each flank of the hexagonal prism. The proposed design of the substrate mounts and the orientation of its surfaces are analyzed in numerical simulations for particle impaction efficiency, described in Section 3.5.

The geometry of the instrument module with the SPICE booms is symmetric with respect to an axis that is perpendicular to the longitudinal axis of the instrument module. Consequently, the flow around the geometry of the instrument module is also symmetric. This recognition will be exploited later (see Paragraph 3.5.7) to reduce the numerical effort for the particle simulations performed.

Supersonic flow field around the SPICE instrument

So far, fluid dynamics simulations have contributed to optimize the design of the SPICE instrument with the arrangement and orientation of its booms. Now that we have gained knowledge about the shape and position of the impactor surfaces, the third phase of the simulation process can be addressed. Here, the flow field around the substrate mounts is analyzed to ensure that they are unaffected by disturbances origin from the boundary layer around the instrument module or the shock wave forming at the instrument module tip. In particular, the velocity, pressure and temperature fields are analyzed on which the particle tracking simulations (see Section 3.5) are based on. Moreover, the flow field is simulated at different angles of attack of the HAS. Thereby, the extreme values are estimated with $\pm 30^\circ$ as the maximum possible deflection during the measuring flight phase.

The mesh used for the simulations with 3.75 million elements is shown in Figure 3.24. The resolution of the mesh is enhanced around the instrument module, especially at the tip and in the immediate vicinity of the instrument module, where flow variations occur. A total of eight layers of boundary elements (a detailed view of boundary elements is depicted in Figure 3.25) are used to resolve the boundary layer.

3 Supersonic flow simulations and impaction processes

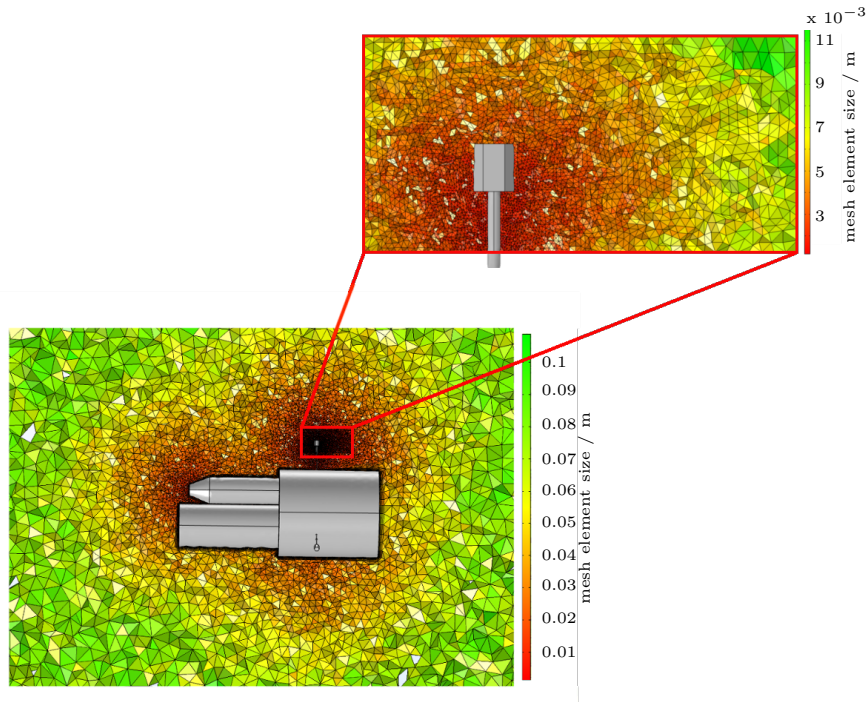


Figure 3.24: Computational mesh for the selected instrument module geometry with substrate mounts on the SPICE booms. In the close-up, the higher resolution of mesh elements around the upright substrate mount is visible [Klug, B. S. et al., 2023].

In addition, a rectangle is placed around each of the substrate mounts, within which the mesh is extremely refined (visible at the upright SPICE boom in Figure 3.24). Due to the additional manual refinement of the mesh in this region, the highly resolved mesh elements spread into the region of the shock wave, and the additional dynamical mesh refinement (as described in Section 3.4.2) is no longer necessary.

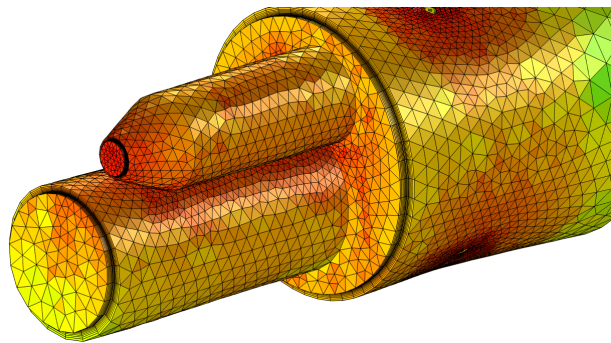


Figure 3.25: Near-surface mesh elements around the instrument module.

3 Supersonic flow simulations and impaction processes

The close-up view (in Figure 3.24) exhibits the refined mesh with minimum mesh element sizes of $1.15 \cdot 10^{-3}$ m. This refinement is primarily aimed at improving the spatial resolution of the flow field around the substrate mounts and the small-scale flow pattern that can evolve in the wake of fore-built structures.

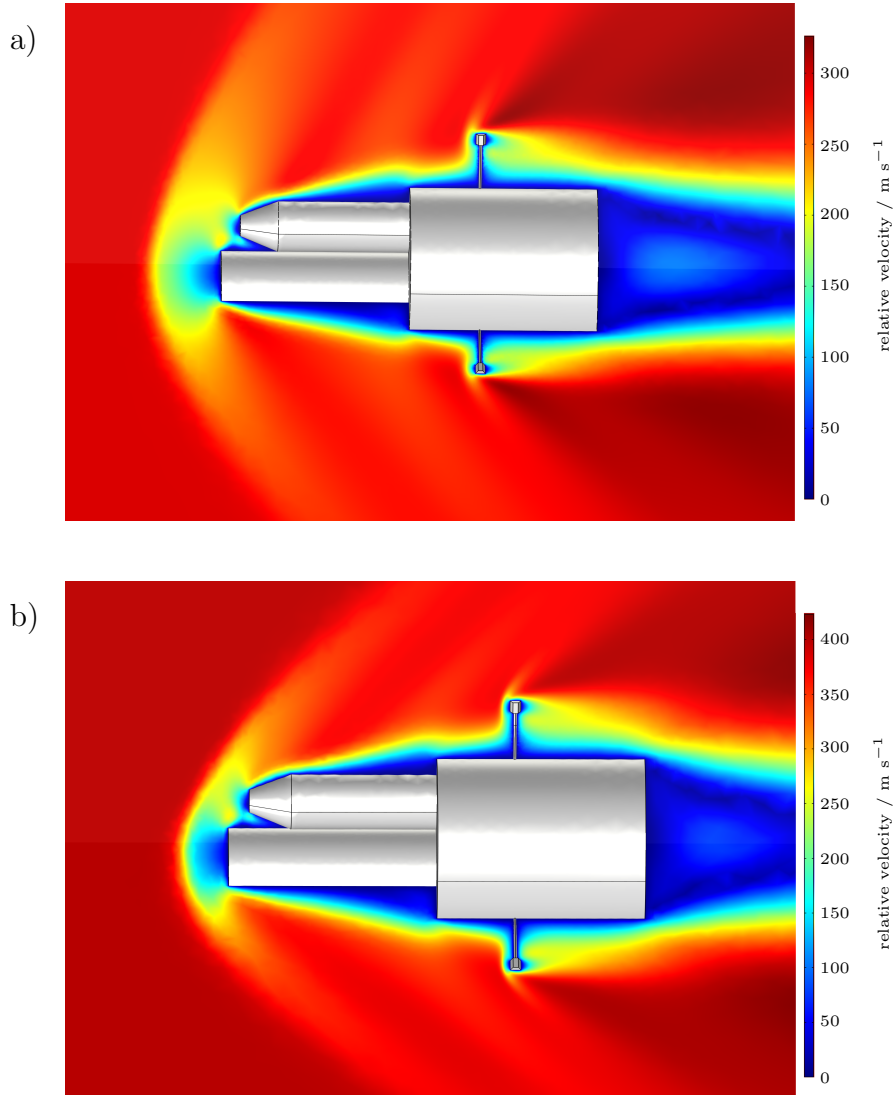


Figure 3.26: Flow field around the instrument module depicted on two cut planes, where the inlet for the air flow is on the left-hand side. Figure a) shows the simulation result for the incident velocity of 300 m s^{-1} and b) for 400 m s^{-1} .

One can recognize from Figure 3.24 that for subsequent fluid dynamics simulations the m-NLP are no longer considered in the geometry. Although

3 Supersonic flow simulations and impaction processes

the aerial-type structure of the m-NLP has an impact on the flow profile (e.g., velocity gradients), the wake effect of the m-NLP does not significantly impact the flow at the dedicated SPICE sample positions. Subsequently, the consideration of the m-NLP geometry appears dispensable for the following simulations. Furthermore, the neglect of this geometry in the refined flow simulations is for the purpose of saving computational costs.

Figures 3.26 a) and b) illustrate velocity fields around the instrument module for incident velocities of 300 m s^{-1} and 400 m s^{-1} , respectively, depicted on two cut planes through the upper SPICE boom 1 and through the downside oriented SPICE boom 3. Note that the flow around the geometry of the instrument module (and thus around the two downside oriented booms 2 and 3) is symmetrical to the vertical axis perpendicular to the longitudinal axis of the instrument module. Again, the flow behavior is analogous to the previous simulation results (cf. Figures 3.13 and 3.18). Additionally, the effect of the substrate mounts at the tips of the SPICE booms protruding from the boundary layer around the instrument module surface is illustrated. However, the SPICE booms themselves cause additional shock waves, and as expected, the shape and range of the shock waves trapping the substrates depend on the flow velocity. While in Figure 3.26 a) the wave front propagates at a larger angle to the longitudinal axis of the instrument module, in Figure 3.26 b) the shock wave caused by the tip of the instrument module and the booms nestles slightly closer to the longitudinal axis of the instrument module due to the higher flow velocity. In addition, a small boundary layer forms around the booms, affecting the downstream flow field over a short distance.

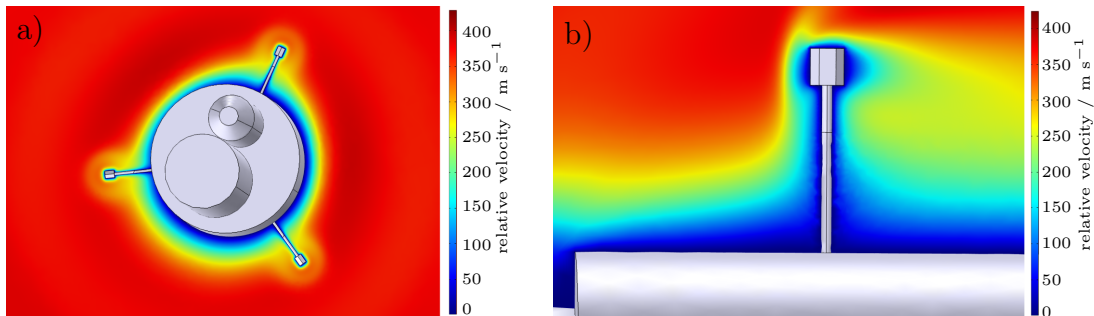


Figure 3.27: Frontal view of the flow field at the level of the SPICE instrument a) and side view of the flow field around one SPICE boom b).

3 Supersonic flow simulations and impaction processes

A closer look at the boundary layer thickness around the instrument module is represented in Figure 3.27 for the incident velocity of 400 m s^{-1} . The velocity profile on a cut plane perpendicular to the instrument module at the level of the SPICE booms is depicted in Figure 3.27 a). Figure 3.27 b) shows a close-up of the flow field around the upright SPICE boom (representative for booms 2 and 3, as the flow field around the individual booms is similar, as can be seen in Figure 3.29 b)).

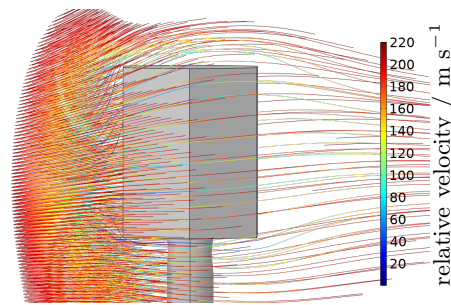


Figure 3.28: Streamlines around one of the substrate mounts for the angle of attack of 0° at the incident velocity of 400 m s^{-1} show velocity values limited to 0 m s^{-1} and 220 m s^{-1} .

Both plots support the choice of the booms' length ensuring the placement of the substrate mounts well outside the boundary layer around the instrument module. Streamlines in the close vicinity around one of the substrate mounts are illustrated in Figure 3.28, where depicted velocity values are limited to 0 m s^{-1} and 220 m s^{-1} . Simulation results of flow field variables are summarized in Figure 3.29, where the temperature field a), velocity field b), fluid density field c), and pressure field d) are illustrated on two cut planes through the upper SPICE boom 1 and through the downside oriented SPICE boom 3 for the incident flow velocity of 400 m s^{-1} . Furthermore, the values of flow field variables measured upstream of SPICE booms 1 and 3 are shown. For the angle of attack of 0° , only marginal differences in the analyzed flow field variables upstream of the substrate mounts can be determined. With regard to the energy conservation, the inverse behavior of temperature and velocity can be observed in figures a) and b), with the velocity values across the shock wave front decreasing sharply while the temperature values increase. This is due to the conversion of the kinetic energy into internal energy, which leads to an increase in temperature.

3 Supersonic flow simulations and impaction processes

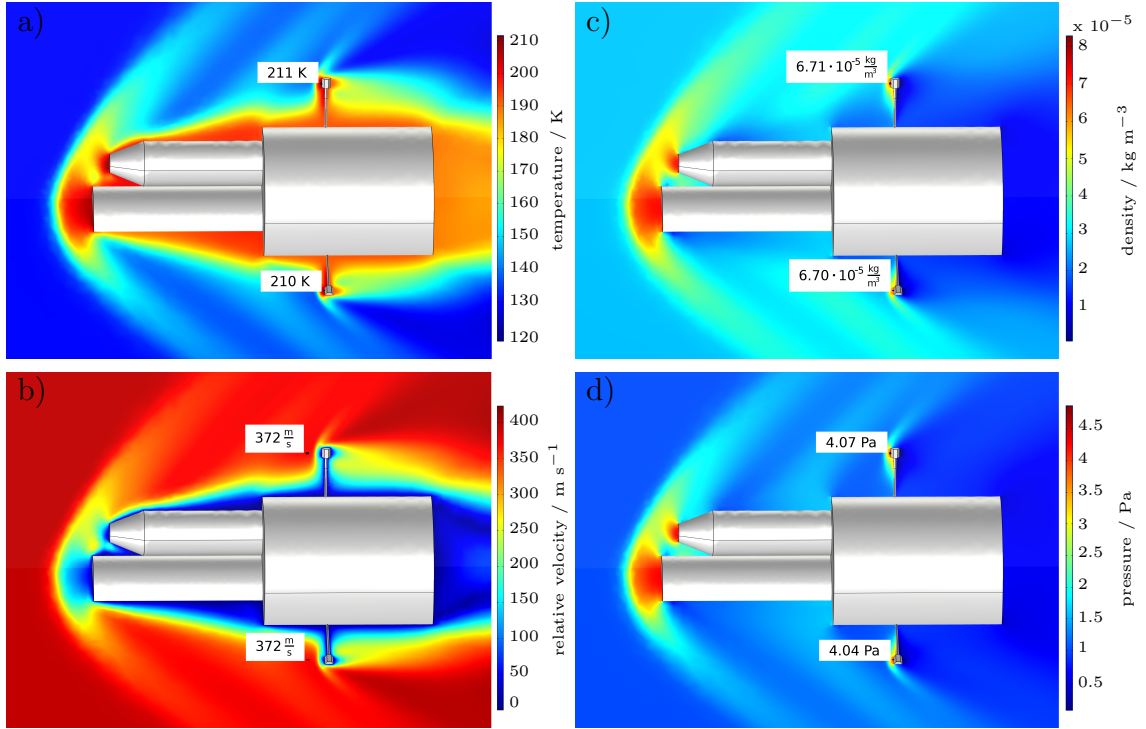


Figure 3.29: Representation of flow field variables, temperature field in a), velocity field in b), fluid density field in c), and pressure field in d) depicted on two cut planes for the incident flow velocity of 400 m s^{-1} .

The temperature increase ΔT in relation to the free flow field is most pronounced at the tip of the instrument module and in front of the SPICE booms, where a ΔT of 81 K upstream of boom 1 is marked in figure a). Since temperature is directly proportional to pressure (according to the ideal gas law, see equation 2.48), and the conservation of mass (cf. expression 2.9) states that density times velocity stays constant, an increase in temperature leads to a pressure increase, and a decreasing velocity to an increasing density. Therefore, a pressure increase Δp in relation to the free flow field is mainly observed at the tip of the instrument module or at the impinged SPICE booms, where in front of boom 1 the pressure increase is about $\Delta p = 3.07 \text{ Pa}$. Just at this point, the fluid density increases by about $\Delta \rho = 4.03 \cdot 10^{-5} \text{ kg m}^{-3}$.

To complete the analyses and to cover several cases of the flow field under variable HAS angles of attack, the simulations around the instrument module are complemented by accounting for the vehicles' maximum deflections of $\pm 30^\circ$.

3 Supersonic flow simulations and impaction processes

The computational mesh for this simulation step consist of 4.44 million elements with smallest element sizes of $3.63 \cdot 10^{-3}$ m, illustrated in Figure 3.30 for the angle of attack of -30° . Again, smaller mesh elements are located around the tip of the instrument module and, in particular, around the SPICE booms.

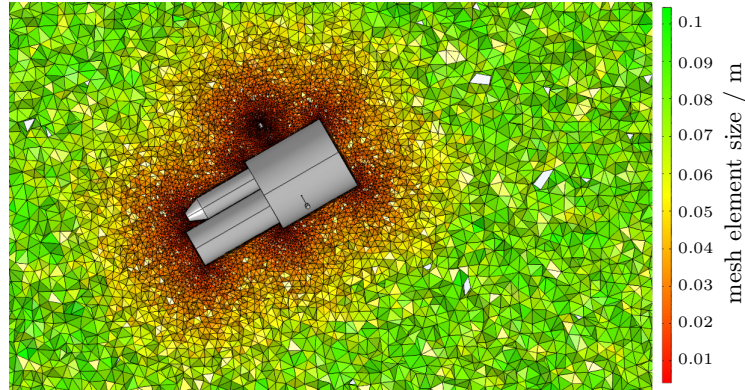


Figure 3.30: Computational mesh for flow simulations for -30° angle of attack.

Figure 3.31 depicts the velocity field around the instrument module for the incident velocity of 400 m s^{-1} , with an asymmetric shock wave forming at the tip of the instrument module. The surface of the instrument module that faces the flow causes a strongly pronounced shock wave, to which the protrusions of the instrument module also contribute.

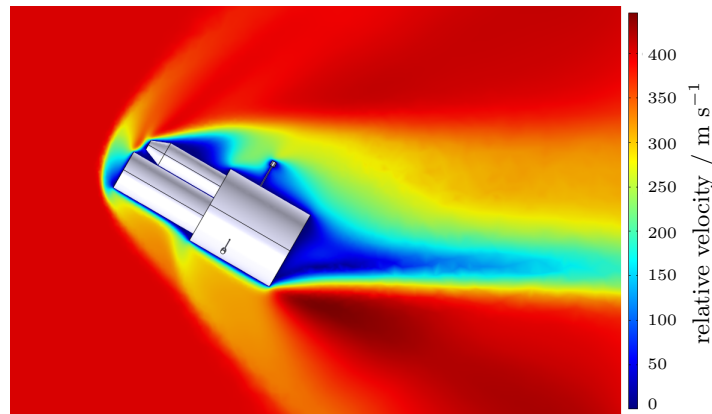


Figure 3.31: Flow field around the instrument module geometry depicted on a cut plane for the incident flow velocity of 400 m s^{-1} for the flight attitude of $+30^\circ$ [Klug, B. S. et al., 2023].

3 Supersonic flow simulations and impaction processes

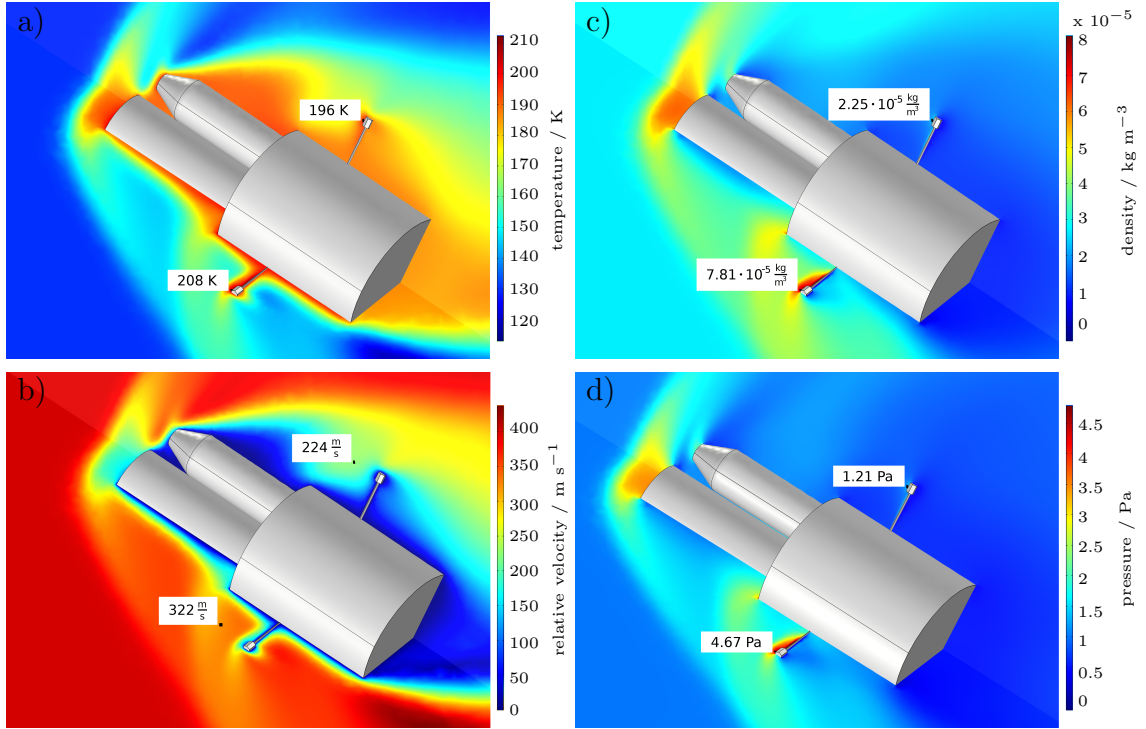


Figure 3.32: Representation of flow field variables, temperature field a), velocity field b), fluid density field c), and pressure field d) for the incident flow velocity of 400 m s^{-1} on two cut planes for the flight attitude of $+30^\circ$.

The simulation results of the four flow field variables temperature a), velocity b), fluid density c) and pressure d) for the flight attitude of $+30^\circ$ are illustrated on two cut planes through the upper SPICE boom 1 and through the downside oriented SPICE boom 3 in Figure 3.32 for the incident flow velocity of 400 m s^{-1} . Moreover, velocity, temperature, density, and pressure values measured upstream of the booms are depicted. The symmetry of the geometry of the instrument module in relation to the vertical axis perpendicular to the longitudinal axis of the instrument module also applies here, whereby only one of the downside oriented booms is considered. Regarding the SPICE booms, the two substrate mounts on the downside fuselage of the instrument module are exposed to the air flow behind the shock wave, while the upright boom is in the flow shadow of the instrument module at $+30^\circ$ flight attitude. The pressure and temperature increases measured upstream of the downside oriented boom 3 (which are higher than for the remaining boom 1) are $\Delta p = 3.67 \text{ Pa}$ and $\Delta T = 78 \text{ K}$ in relation to the free flow field. A closer look of the velocity field and streamlines

3 Supersonic flow simulations and impaction processes

around the SPICE booms is depicted in Figure 3.33 for boom 1 in a) and b) and boom 3 in c) and d) at the incident velocity of 400 m s^{-1} (where velocity values for streamlines are limited to 0 m s^{-1} and 220 m s^{-1}). While boom 1 is embedded in upstream flow velocities of about 224 m s^{-1} and is shielded from the free flow by the upstream instrument module tip, boom 3 is located behind the shock wave in a flow with velocities about 322 m s^{-1} , in which the substrate mount is clearly outside the boundary layer of the instrument module.

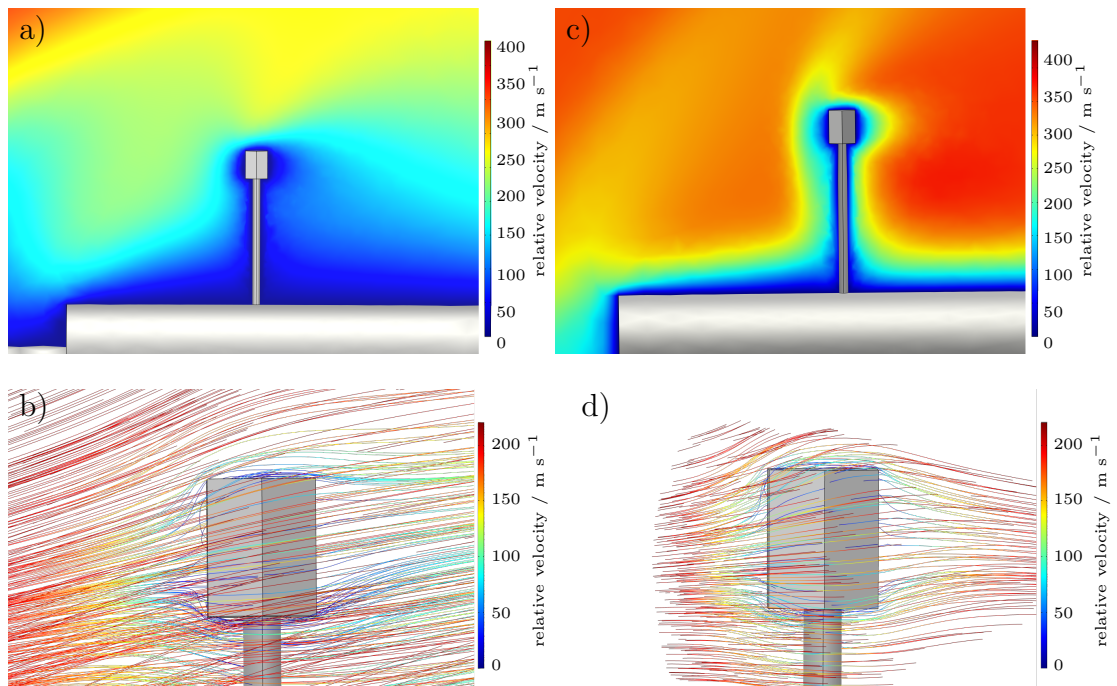


Figure 3.33: Side view of the flow field a) and streamlines b) around the upright SPICE boom and one downside oriented SPICE boom with the flow field c) and streamlines d) for the angle of attack of $+30^\circ$ and the incident velocity of 400 m s^{-1} .

For another flight attitude extreme (i.e., for the -30° angle of attack), the velocity field around the instrument module for the incident velocity of 400 m s^{-1} is illustrated in Figure 3.34. Again, an asymmetric shock wave develops due to the asymmetric geometry of structures at the tip of the instrument module, which faces the flow. In addition, the instrument module appurtenances and the SPICE booms generate other shock wave structures that interfere with each other.

3 Supersonic flow simulations and impaction processes

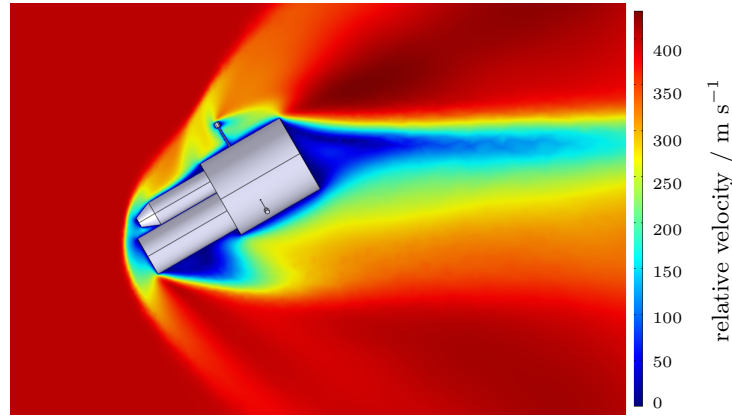


Figure 3.34: Flow field around the instrument module geometry depicted on a cut plane for the incident flow velocity of 400 m s^{-1} for the flight attitude of -30° [Klug, B. S. et al., 2023].

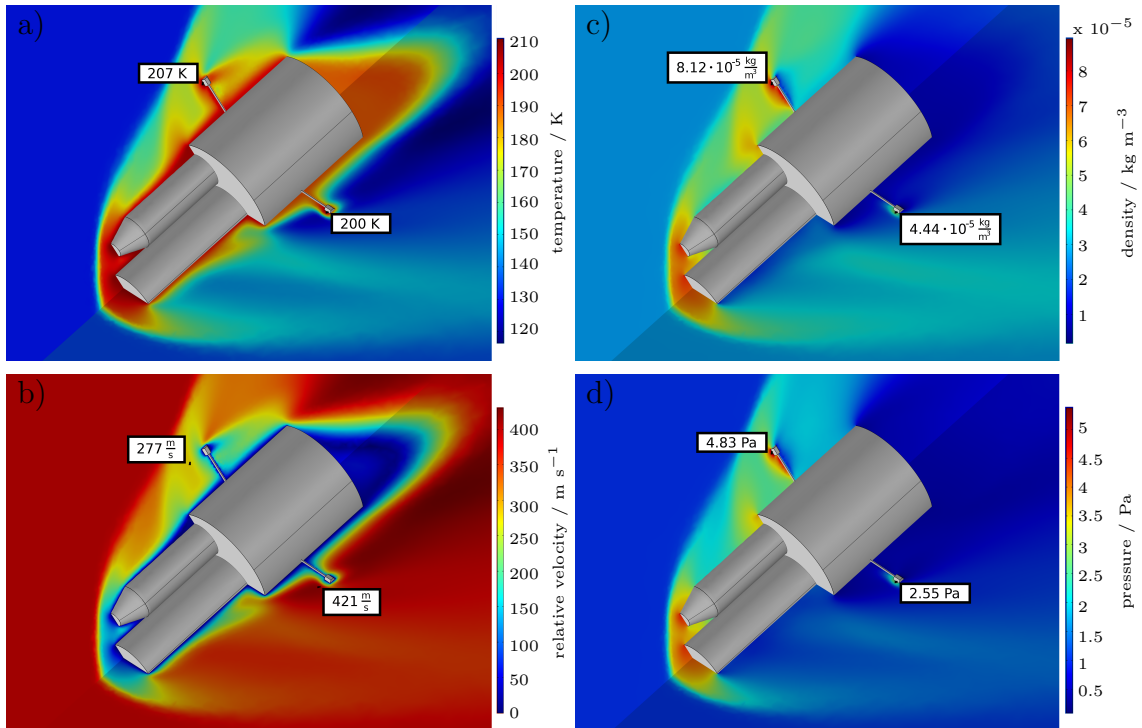


Figure 3.35: Representation of flow field variables, the temperature field a), velocity field b), fluid density field c), and pressure field d) for the incident velocity of 400 m s^{-1} on two cut planes for the flight attitude of -30° .

Corresponding numerical results of the flow variables (temperature a), velocity b), density c), and pressure d)) are summarized in Figure 3.35 for the incident

3 Supersonic flow simulations and impaction processes

velocity of 400 m s^{-1} and are depicted on two cut planes through the upper SPICE boom 1 and through the downside oriented SPICE boom 3. Additionally, velocity, temperature, density, and pressure values measured upstream of the SPICE booms 1 and 3 are shown. While SPICE boom 1 is directly affected by the forming shock wave, SPICE boom 3 is located behind the shock wave. Measured flow variables on a point upstream of SPICE boom 1 depict a temperature increase of $\Delta T = 77 \text{ K}$, a pressure increase of $\Delta p = 3.83 \text{ Pa}$, and a density increase of $\Delta \rho = 5.44 \cdot 10^{-5} \text{ kg m}^{-3}$ in relation to the free flow field.

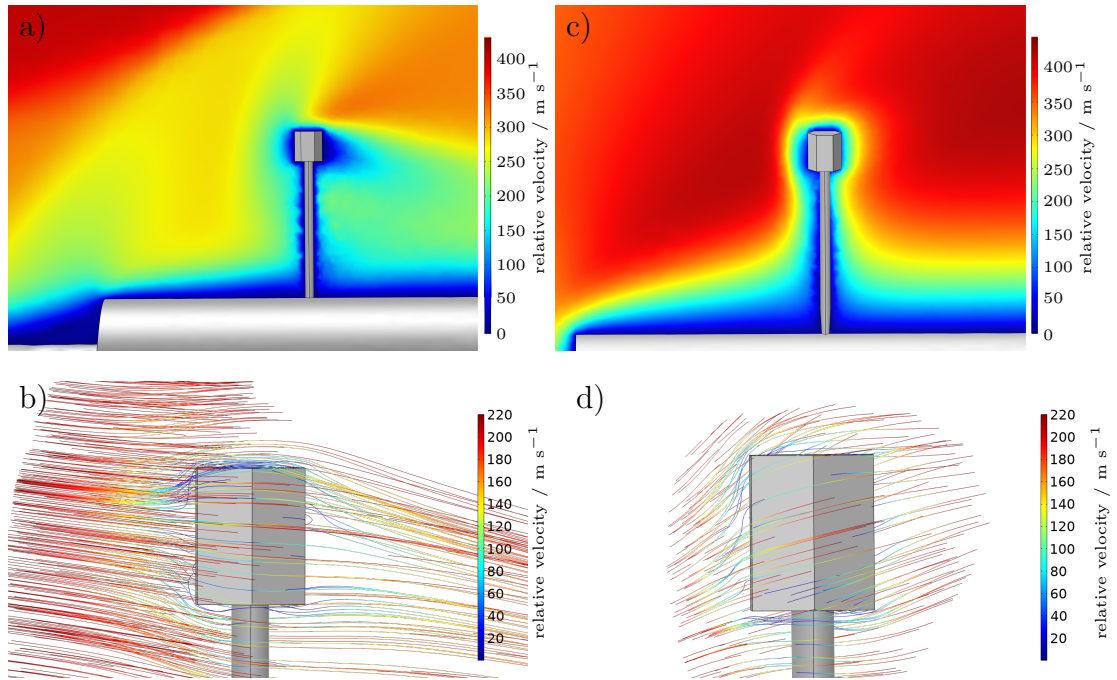


Figure 3.36: Side view of the flow field a) and streamlines b) around the upright SPICE boom and one downside oriented SPICE boom with the flow field c) and streamlines d) for the angle of attack of -30° and the incident velocity of 400 m s^{-1} .

A close-up of the velocity field and streamlines around the SPICE booms for the angle of attack of -30° is depicted in Figure 3.36 for boom 1 in a) and b) and for boom 3 in c) and in d) for the incident velocity of 400 m s^{-1} (where velocity values for the streamlines were limited to 0 m s^{-1} and 220 m s^{-1}). SPICE boom 1 is embedded in the shock wave with upstream flow velocities of about 277 m s^{-1} , which is about 24% higher than for SPICE boom 1 at an angle of attack of $+30^\circ$ (here this boom is in the slipstream of the instrument module).

3 Supersonic flow simulations and impaction processes

SPICE boom 3 is located behind the shock wave, where velocities of up to 421 m s^{-1} are reached, which is about 31% higher than for the corresponding boom at the $+30^\circ$ angle of attack. It is obvious, that in both depictions a) and c) the substrate mounts are clearly located outside the boundary layer of the instrument module. The near-surface flow fields for the angles of attack of $\pm 30^\circ$ are illustrated in Figure 3.37 a) and b), respectively, by streamlines. The color coding refers to velocity values, whereby the displayed velocity magnitude is limited to 0 m s^{-1} and 220 m s^{-1} . In figure a) and b), the upright SPICE boom and its substrate mount is enveloped by flow velocities of about 220 m s^{-1} , while the two substrate mounts on the downside fuselage of the instrument module are exposed to flows with higher velocities (note that these streamlines are not shown in the figure as they exceed the range of scale), confirming the previous evaluations.

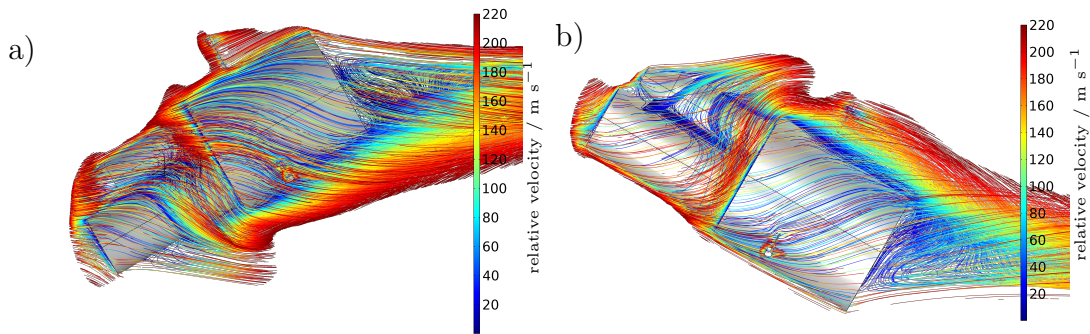


Figure 3.37: Streamlines around the instrument module for the angles of attack of -30° in a) and $+30^\circ$ in b) for the incident velocity 400 m s^{-1} . Streamlines are colored according to velocity values and are filtered out to 0 m s^{-1} and 220 m s^{-1} .

Finally, the velocity, temperature, pressure and density increase upstream of the upright SPICE boom and one downside oriented SPICE boom for the incident velocity of 400 m s^{-1} is summarized in Table 3.1 corresponding to the flight attitudes of $\pm 30^\circ$ and 0° , respectively. The highest flow velocity of 421 m s^{-1} upstream of a substrate mount is achieved for boom 3 at an angle of attack of -30° , which is about 31% higher than for the same boom at an angle of attack of $+30^\circ$ and 13% higher than for the same boom at an angle of attack of 0° . In addition, the velocity values upstream of boom 1 at an angle of

3 Supersonic flow simulations and impaction processes

attack of $+30^\circ$ are about 24% lower than at an angle of attack of -30° and even 66% lower than at an angle of attack of 0° . The highest temperature increase in relation to the free flow field upstream of the substrate mounts is achieved for the angle of attack of 0° with a ΔT of 81 K upstream of boom 1. The highest pressure increase is observed upstream of boom 1 for the angle of attack of -30° with a Δp of 3.83 Pa.

	$+30^\circ$		-30°		0°	
	boom 1	boom 2	boom 1	boom 2	boom 1	boom 2
$u / \text{m s}^{-1}$	224	322	277	421	372	372
$\Delta T / \text{K}$	66	78	77	70	81	80
$\Delta p / \text{Pa}$	0.21	3.67	3.83	1.55	3.07	3.04
$\Delta \rho / 10^{-5} \text{ kg m}^{-3}$	5.13	0.43	5.44	1.76	4.03	4.02

Table 3.1: Velocity, temperature, pressure, and density increase with regard to values of the free flow field measured upstream of SPICE booms 1 and 2 for the different angles of attack of $\pm 30^\circ$ and 0° .

While the pressure increase is so small and therefore irrelevant for the design development, the temperature increase upstream of the substrate mounts is significant. For this reason, in Section 3.5.6 the effect of the temperature increase on the NLC elements consisting of ice a-priori to impactions is investigated.

In essence, the simulation results reveal a significant change in the flow profile, in the evolving shock wave and in the exposure of substrate mounts that serve as a target for particle impactions under varying flight attitudes of the HAS on its flight path. The chosen alignment of the three SPICE booms with their substrate mounts apparently allows effective collection of particles under many flight conditions. It is demonstrated that for different angles of attack at least two of the substrate mounts are exposed to the almost fully developed flow with some reduction in flow velocities, which lies in the range of 8% for the angle of attack of 0° and 24% for the angle of attack of $+30^\circ$ for the downside oriented booms related to the incident flow velocity. Note that for the angle of attack of -30° , the downside oriented booms are exposed to even accelerated velocities, lying 5% above the incident velocity of 400 m s^{-1} . Finally, at an angle of attack of 0° , equal particle sampling efficiencies are expected for all three SPICE booms based on the flow field analyses, where only marginal differences can be detected.

However, at the angles of attack of $\pm 30^\circ$, different sampling efficiencies are to be expected between the upright and downside oriented SPICE booms, assuming that higher flow velocities favor particle impactions.

Detailed investigation of the flow field around substrate mounts

In the following, high-resolution simulations are performed to closely examine the flow field around the substrate mounts. In particular, attention is paid to whether vortex-induced back-flow occurs in the slipstream of the substrate mounts, enabling the particle deposition on downstream surfaces.

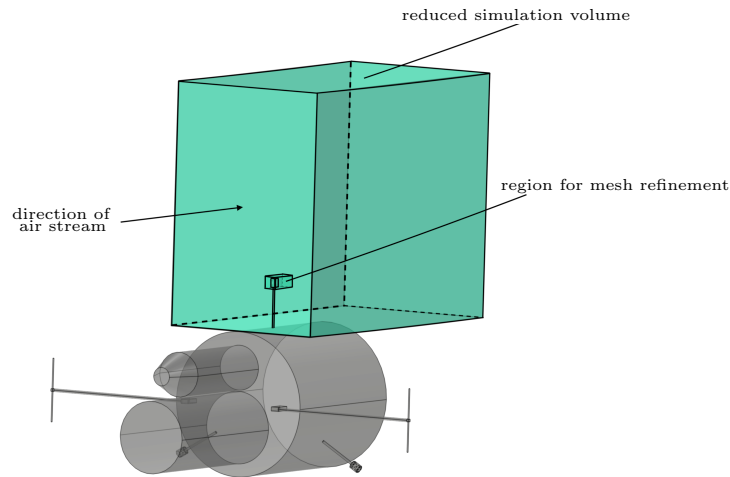


Figure 3.38: Reduced simulation volume including the upright SPICE boom with a mesh refinement region around the substrate mount for high-resolution simulations of the near flow field.

To realize the high-resolution computation, the simulation volume is reduced to one SPICE boom, as can be seen in Figure 3.38. To resolve small-scale flow pattern in the near flow field around the substrate mounts, a cuboid volume is placed around the substrate mount. Within this volume, the mesh elements are reduced in size by a factor of up to 625 compared to largest elements located outside of this cuboid volume. This results in minimum element sizes of $1.76 \cdot 10^{-4}$ m and maximum sizes of $1.06 \cdot 10^{-3}$ m within this region, which is illustrated in Figure 3.39. Eight layers of boundary elements are used to resolve the boundary layer around the substrate mount.

3 Supersonic flow simulations and impaction processes

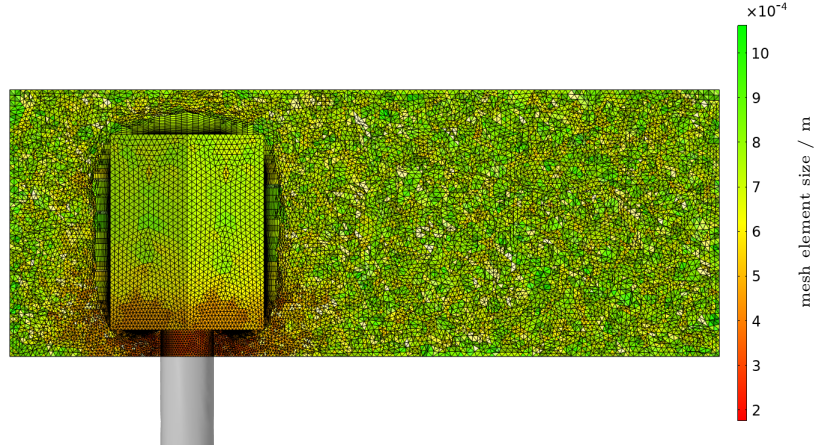


Figure 3.39: Mesh resolution within the cuboid volume around a substrate mount.

Simulations of the flow field around the SPICE boom are performed similar to Paragraph 3.4.1 for inlet velocities of 300 m s^{-1} and 400 m s^{-1} , respectively. To ensure that the flow field in the reduced simulation volume limited to the upright SPICE boom corresponds to the respective flow field in the overall geometry of the instrument module, the boundary condition for the velocity profile at the air flow inlet of the reduced geometry is defined as follows: At first, the inlet surface of the reduced simulation volume within the overall geometry is determined. Then, the velocity profile at this position is extracted from the overall flow simulation results. The inlet velocity as a function of z minus the vertical position (i.e., the vertical distance to the vehicle surface at the central position $y = 0 \text{ m}$) is shown in Figure 3.40 for incident velocities of 300 m s^{-1} and 400 m s^{-1} . Here, the boundary layers around the instrument module are clearly visible in both cases. In the further course of the flow, the streaming pattern is characterized by the velocity fluctuations caused by shock waves achieving finally the incident velocities. Subsequently, the velocity profiles (obtained from the overall flow simulations) are applied as the inlet conditions for the high-resolution reduced volume simulation. The corresponding velocity fields for the incident flow velocities of 300 m s^{-1} and 400 m s^{-1} are shown in Figure 3.41 a) and b) (note that the color scales are limited to the ranges close to the free flow values, i.e., between 260 m s^{-1} and 280 m s^{-1} , and between 350 m s^{-1} and 380 m s^{-1} , respectively). The impact of the shock waves within the covered velocity range is clearly observed at the evaluation positions, which are marked

3 Supersonic flow simulations and impaction processes

by black lines.

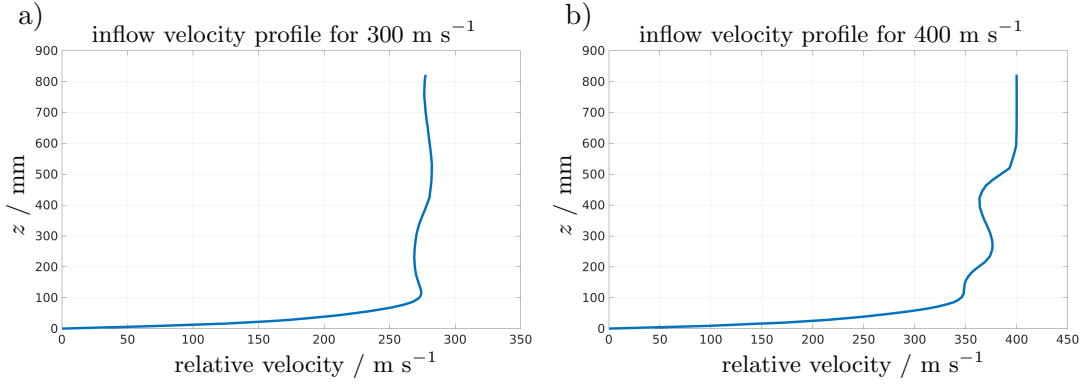


Figure 3.40: Velocity profile used as boundary condition at the inlet surface of the reduced simulation volume for 300 m s^{-1} a) and 400 m s^{-1} b).

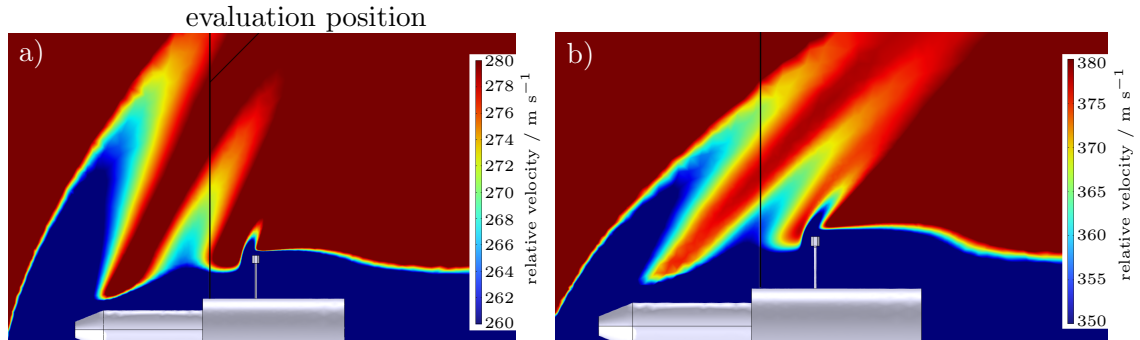


Figure 3.41: Velocity field around the instrument module for determining flow profiles at the evaluation position (marked line) as boundary conditions for high-resolution flow simulations. Figure a) shows the velocity field for the incident flow velocity of 300 m s^{-1} and b) for the incident flow velocity of 400 m s^{-1} , where the color ranges are limited to almost free flow velocities.

Results of high-resolution supersonic flow simulations around the upright substrate mount are presented in Figure 3.42 for both considered incident flow velocities of 300 m s^{-1} in a) and of 400 m s^{-1} in b). Note that the air flow inlet is on the left-hand side. Streamlines are color-coded with velocity magnitude values, the velocity range is limited up to 120 m s^{-1} to filter out high velocity streamlines of the free flow. In the slipstream of the substrate mount, minor vor-

3 Supersonic flow simulations and impaction processes

tices occur at an incident flow velocity of 300 m s^{-1} , whereas at 400 m s^{-1} the convergence and alignment of the streamlines in the downstream flow of the substrate mount is already observed. Thus, some flow disturbances develop in the slipstream at lower incident velocities, but this effect decreases significantly at higher flow velocities.

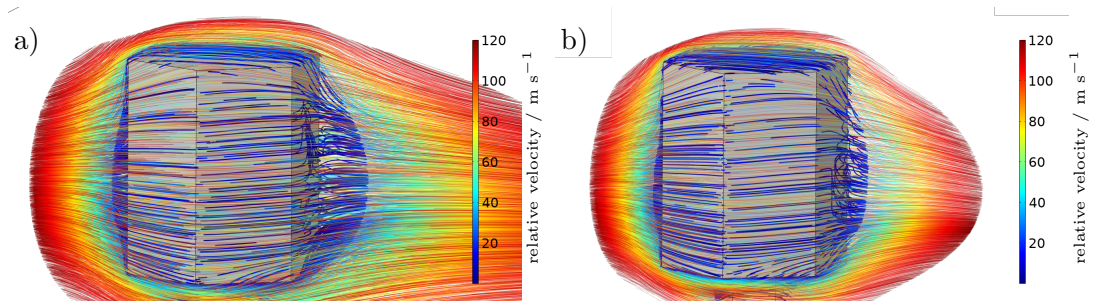


Figure 3.42: Streamlines colored with velocity magnitude values around a substrate mount for the incident flow velocity of 300 m s^{-1} a) and for 400 m s^{-1} b), which are limited to the velocity range covered.

It should be noted that the flight attitude of the HAS varies along its flight path. Therefore, the simulation results of Figure 3.42 describe only a snapshot of the fluid dynamics for the angle of attack of 0° . Even though particle impactions are not expected on the downstream surfaces (as no significant back-flow is detectable), it may be important to mount impaction substrates on each of the six surfaces of the substrate mount, which can enable the collections regardless of particular flight positions.

For even more detailed flow field analyses, the flow field alongside further structural details of the substrate mount is investigated. A detailed geometry of the substrate mount with impaction substrates, which are recessed by $0.2 \cdot 10^{-3} \text{ m}$ relative to the surface plates (cf. Figure 3.23) is considered, where a high-resolution simulation mesh is created to resolve the structural details: Hemispheres are defined around the impaction substrates. Their diameter is chosen larger than the diameter of the impaction substrates so that they are completely enclosed. Within these hemispheres, the element size achieves $1.04 \cdot 10^{-5} \text{ m}$, which is the smallest element size applied in the entire simulation

3 Supersonic flow simulations and impaction processes

process.

The generated mesh within the hemispheres is shown in Figure 3.43, where the close-up view shows small mesh elements in close proximity to the impaction substrates. The high-resolution mesh near the impaction substrates can represent the geometric structure of the recessed substrates of $0.2 \cdot 10^{-3}$ m in detail and ensures resolving the small-scale vortices and flow patterns in close proximity to the recessed impaction substrates.

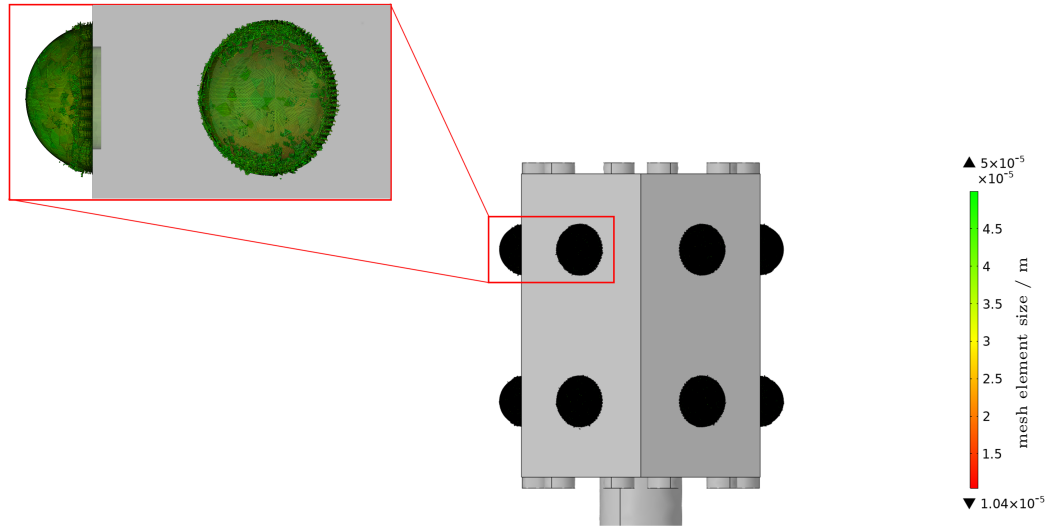


Figure 3.43: Locally refined computational mesh with element sizes ranging from $1.04 \cdot 10^{-5}$ m to $5 \cdot 10^{-5}$ m located at the recessed impaction substrates.

Numerical simulations in the reduced simulation volume (cf. Figure 3.38) with the mesh refinement shown in Figure 3.43 are performed to investigate potential small-scale flow patterns in the vicinity of recessed substrates. Simulation results with use of the above described highly resolved computational mesh for the incident flow velocity of 300 m s^{-1} are shown in Figure 3.44. Streamlines are colored with velocity magnitude values, which are filtered out to the limited range of 0 m s^{-1} and 100 m s^{-1} in a) and 0 m s^{-1} and 10 m s^{-1} in b). The presented streamlines around the substrate mount can be characterized as laminar with small perturbations in the slipstream. However, no effect of the recessed substrates on the flow can be detected from the simulation results. It can be concluded that the recessed substrates of $0.2 \cdot 10^{-3}$ m do not generate significant

3 Supersonic flow simulations and impaction processes

small-scale flow patterns at supersonic velocities.

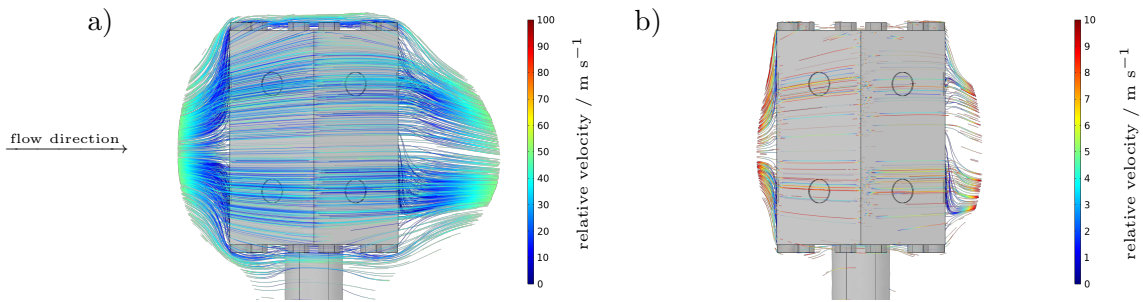


Figure 3.44: Streamlines around the substrate mounts for the incident flow velocity of 300 m s^{-1} . Streamlines are colored with velocity magnitude values, filtered out up to 100 m s^{-1} in a) and up to 10 m s^{-1} in b).

Since higher flow velocities suppress the vortex formations, numerical results of the higher incident flow velocity of 400 m s^{-1} are disregarded.

3.5 Collection of mesospheric particles on substrate mounts

In the following, the effectiveness and efficiency of inertia-based particle collection by impacting the substrates under atmospheric conditions at about 85 km altitude in a supersonic flow regime are investigated. For this purpose, the release of aerosol particles is simulated based on the precomputed flow field. The particles' trajectories are computed by using the corresponding equation of motion, which accounts for all relevant forces acting on the particles. In this way, deposition processes can be predicted and analyzed. With respect to the numerical effort for the calculation of particle trajectories, not the entire 60-s measurement flight is simulated: instead, a small flight segment with a duration of 0.021 s is closely numerically examined. As the flight attitude is variable it is conceivable that the upright and the downside oriented substrate mounts have varying sample yields for each angle of attack. Since both, the flow field and the particle conditions are unique, an overview of particle properties is given in the following Section 3.5.1. Furthermore, in Section 3.5.2 the parameters defining the physical conditions to model particle trajectories are determined before the model settings for calculating them are given in Section 3.5.5, which is followed by the presentation of simulation results in Section 3.5.7.

3.5.1 Properties of MSP and NLC elements

To specify the properties of MSP and NLC elements, literature data from various studies are summarized, which find their application in further simulations. For detailed information about meteoric smoke and noctilucent clouds it is referred to Sections 3.1 and 3.2. Regarding the size of NLC elements (ice particles), estimates are based on analyses of light scattered by mesospheric ice particles. Accordingly, the particles are assumed as spherical elements with a material density of $\rho_p = 1 \text{ g cm}^{-3}$ and diameters of $\leq 0.12 \text{ }\mu\text{m}$ [Tozer, W. F. and Beeson, 1974; Turco, R. P. et al., 1982; Thomas, G. E., 1991; Rapp, M. and Lübken, 2004; Baumgarten, G. and Fiedler, 2008; Hervig, M. E. et al., 2009]. Lübken, F.- J. [2005] and Rapp, M. and Thomas [2006] further constrain this size estimate to particle diameters from 20 to 100 nm. The particle number concentration of the NLC elements is still under debate and is highly variable. It ranges from estimations scaled from $1 - 10 \text{ cm}^{-3}$ [Turco, R. P. et al., 1982],

3 Supersonic flow simulations and impaction processes

from $29 - 133 \text{ cm}^{-3}$ [Baumgarten, G. and Fiedler, 2008], from $46 - 105 \text{ cm}^{-3}$ [Baumgarten, G. et al., 2008], up to $23 - 1078 \text{ cm}^{-3}$ with a mean of 82 cm^{-3} [Von Cossart, G. et al., 1999].

On entry, interplanetary solids, such as asteroids or meteoroids, pass through the Earth's atmosphere at enormous speeds. When cosmic bodies are sufficiently large, collisions and friction with the air molecules of the atmosphere lead to the development of high temperatures, at which the bodies' constituents evaporate. According to Plane, J. M. C. [2003] cosmic bodies of

- diameter $d_p < 100 \text{ nm}$ do not experience frictional heating and no ablation occurs,
- $d_p \approx 1 \text{ }\mu\text{m}$ require entry velocities of over 40 km s^{-1} to get frictionally heated to temperatures of $> 1000 \text{ K}$,
- $d_p > 10 \text{ }\mu\text{m}$ reach boiling temperatures of about $> 2000 \text{ K}$, while further frictional heat input is balanced by vaporization and radiative cooling (i.e., no further temperature rise occurs).

Most of the material from incoming bodies less than $300 \text{ }\mu\text{m}$ in diameter (masses less than $100 \text{ }\mu\text{g}$) remains in the atmosphere and in this way contributes to most of the total imported mass by cosmic entry [Plane, J. M. C., 2003, 2012]. Subsequently, rapid recombination and polymerization of the vaporous components released from the ablating body occurs. This produces the meteoric smoke particles with an assumed material density of $\rho_p = 2 - 3 \text{ g cm}^{-3}$ [Hedin, J. et al., 2007b], sometimes specified with $\rho_p = 2.8 \text{ g cm}^{-3}$ like Plane, J. M. C. [2012] lists. MSP diameters are estimated to be 0.8 to 1.0 nm [Strelnikova, I. et al., 2007], 0.8 to 1.6 nm [Hedin, J. et al., 2014], 0.5 to 3 nm [Rapp, M. et al., 2010, 2012], 1.6 to 4 nm [Horányi, M. et al., 1999; Rapp, M. and Thomas, 2006] or 0.2 to 6 nm [Asmus, H. et al., 2014]. For further investigations MSP sizes of 1.2 nm are applied analogous to the investigations by Hedin, J. et al. [2014].

3.5.2 Parameters for particle modeling

Prior to the mathematical modeling of the trajectories of the airborne particles, the interaction between the continuum phase (i.e., the fluid) and the discrete

3 Supersonic flow simulations and impaction processes

phase (the particles) must first be specified. For this purpose the particle volume fraction as introduced in Paragraph 2.2.1 is calculated using equation 2.51:

$$\Phi_p = \frac{nV_p}{V},$$

where n is the number of particles, V_p is the volume of a single particle, and $V = n V_p + V_f$ is the total volume of the particles and the fluid. Based on the estimation of a NLC element diameter of $d_p = 100$ nm the particle volume is $V_p = 5.23 \cdot 10^{-22}$ m³ and the total simulation volume is $V = 14$ m³. Assuming an exemplary but realistic particle number concentration of $c = 133$ cm⁻³ [Baumgarten, G. and Fiedler, 2008] the overall quantity of particles present in the simulation volume V is $n = 1.86 \cdot 10^9$ particles. Thus, the volume fraction of particles results in $\Phi_p = 6.96 \cdot 10^{-20}$ which is clearly less than the threshold for the application of one-way coupling of $\Phi_p = 10^{-6}$ (cf. Paragraph 2.2.1). This means that the particle-laden stream represents a sparse flow with a comparatively low particle number concentration, in this way supporting the assumption that the flow properties remain unaffected by the particles present.

It is therefore sufficient to numerically calculate the flow field and the advected particle motion in two separate simulation runs [COMSOL®, 2017b]:

- 1) The continuous phase is modeled by the Navier-Stokes equations for compressible fluids. Eulerian formulation is applied as described in detail in Paragraph 2.1.3. As a result, a stationary velocity field around the instrument module is obtained, the detailed presentation of the results can be found in previous Section 3.4.3.
- 2) Particle velocities and positions are determined as a time-dependent process. For this purpose, the study for calculating the particle trajectories is coupled with the flow study: Flow variables are required at the spatial positions of the particles and for each time step in order to calculate the particle trajectories (next positions). This corresponds to the Lagrangian movement description. The methodological approach is referred to as the one-sided Euler-Lagrangian coupling or the Lagrangian point-particle method [Hryb, D. et al., 2009; Gimenez, J. M. et al., 2012]. In the point-particle formulation, particles are considered as point sources of

3 Supersonic flow simulations and impaction processes

momentum and energy, neglecting the particles' spatial dimension.

To investigate the application of Stokes' drag force, the relative Reynolds number (see Section 2.64) of the particles is determined according to equation 2.58: $Re_r = \frac{\rho_f d_p |\vec{u}_r|}{\mu_f} = 3.58 \cdot 10^{-5}$, where $\rho_f = 2.68 \cdot 10^{-5} \text{ kg m}^{-3}$ is the fluid's (air) density, $d_p = 100 \text{ nm}$ is the estimated diameter of a NLC element, $\mu_f = 8.96 \cdot 10^{-6} \text{ Pa s}$ is the dynamic viscosity of the fluid, $\vec{u}_r = 120 \text{ m s}^{-1}$ is the maximum measured particle relative velocity obtained in the near vicinity of substrate mounts (i.e. in regions with strongly decelerated fluid velocities) with respect to the fluid velocity. Considering the application of Stokes' law with the required condition of a relative Reynolds number of $Re_r \ll 1$, the obtained value of $3.58 \cdot 10^{-5}$ fulfills this criterion and supports the application of Stokes' drag law.

The value of the Knudsen number $Kn_p = \frac{2\lambda}{d_p}$ specifies whether Stokes' drag force \vec{F}_D (cf. Section 2.64, equation 2.65) should be considered with the corresponding Cunningham slip corrector C_c . In the considered flow regime, the Knudsen number results in $Kn_p = \frac{2\lambda}{d_p} = 4.4 \cdot 10^4$ where for the mean free path length the value $\lambda = 2.22 \cdot 10^{-3} \text{ m}$ (see Section 3.4.1) is applied. Thus, the Stokes' drag force with the Cunningham slip corrector C_c is applied, according to equation 2.67.

3.5.3 Equation of motion of particles

Particle modeling and the calculation of the particle positions at each time step (i.e. the particle trajectories) is based on the equation of motion of the particles (cf. equation 2.54). The equation incorporates all relevant particle forces that determine the dynamics of the particles. The following Table 3.2 presents all parameters for the flow, as well as for the particle simulations with their corresponding values. A distinction is made between variables that apply to NLC elements (larger particles consisting of ice) and particles that act as condensation nuclei (smaller and denser MSP). Based on the parameters, magnitudes of possible forces (summarized in Table 3.3) acting on particles are estimated.

3 Supersonic flow simulations and impaction processes

parameters	values	descriptions
ambient conditions		
μ_f	$8.99847 \cdot 10^{-6}$ Pa s	Dynamic viscosity of air at 85 km.
ρ_f	$2.6798 \cdot 10^{-5}$ kg m ⁻³	Fluid (air) density at 85 km altitude.
m_f	$2.43 \cdot 10^{-32}$ kg	Mass of fluid, displaced by a particle of $d_p = 1.2 \cdot 10^{-9}$ m.
$\frac{\partial u}{\partial y}$	650 s ⁻¹	Change in velocity, estimated from fluid dynamics simulations.
$\frac{d(\vec{u}_f - \vec{v}_p)}{dt}$	$1 \cdot 10^7$ m s ⁻²	Maximum relative particle acceleration (from fluid dynamics simulations for $ \vec{u}_f = 300$ m s ⁻¹).
∇p	1.05 Pa m ⁻¹	Pressure gradient (from fluid dynamics simulations).
k_B	$1.381 \cdot 10^{-23}$ J K ⁻¹	Boltzmann constant.
\vec{g}	9.5 m s ⁻²	Gravitational acceleration coefficient at 85 km.
particle properties		
\vec{u}_r	120 m s ⁻¹	Maximum relative particle velocity (from fluid dynamics simulations for $ \vec{u}_f = 300$ m s ⁻¹).
d_{pCE}	$100 \cdot 10^{-9}$ m [Rapp, M. and Thomas, 2006]	Diameter of a single NLC element.
ρ_{pCE}	1000 kg m ⁻³	Density of a NLC element.
d_{pMSP}	$1.2 \cdot 10^{-9}$ m [Hedin, J. et al., 2014]	Diameter of a single MSP (condensation nuclei).
ρ_{pMSP}	3000 kg m ⁻³ [Hedin, J. et al., 2007b]	Density of a MSP.
m_p	$2.7 \cdot 10^{-24}$ kg	Mass of a single particle for $d_p = 1.2 \cdot 10^{-9}$ m and $\rho = 3000$ kg m ⁻³ .
C_c	$7.357 \cdot 10^4$	Cunningham slip corrector for particles with $d_p = 1.2 \cdot 10^{-9}$ m.

Table 3.2: Flow field and particle properties.

forces	mathematical expressions	estimated magnitude of forces / N
Brownian force	$\vec{F}_{Brown} = \zeta \sqrt{\frac{6 \pi \mu_f k_B T d_p}{\Delta t C_c}}$	$\sim 10^{-18}$
Stokes' drag force	$\vec{F}_D = 3 \pi \mu_f d_p \vec{u}_r C_c^{-1}$	$\sim 10^{-18}$
Saffman force	$\vec{F}_S = 1.615 d_p^2 \vec{L}_f \sqrt{\rho_f \mu_f \frac{1}{ \nabla \times \vec{u}_r }}$	$\sim 10^{-22}$
gravitational force	$\vec{F}_{G,tot} = m_p \frac{\rho_p - \rho_f}{\rho_p} \vec{g}$	$\sim 10^{-23}$
added mass force	$\vec{F}_{am} = m_f c_{am} \frac{d(\vec{u}_f - \vec{v}_p)}{dt}$	$\sim 10^{-25}$
pressure gradient force	$\vec{F}_p = -\frac{m_p}{\rho_p} \nabla p$	$\sim 10^{-28}$

Table 3.3: Approximated magnitudes of forces acting on particles to estimate their effects on the particle dynamics. Forces highlighted in gray have a negligible magnitude compared to forces inherent with Brownian motion or due to Stokes' drag and therefore remain unconsidered in subsequent particle simulations.

Table 3.3 summarizes forces acting on particles as described in Section 2.2.4. In addition, parameters from Table 3.2 together with an example time step taken by the solver of $\Delta t = 1 \cdot 10^{-5}$ s are used to estimate the magnitude of the forces and thus specify the impact of particular forces on the particle motion. It is obvious that the Stokes' drag force and the force inherent with the Brownian molecular motion (whose influence is generally important for

3 Supersonic flow simulations and impaction processes

particles of nanometer size) are larger than other forces by at least four orders of magnitude. Thus, it is confirmed that both forces play the most important role. The forces highlighted in gray are considered negligible due to their small contribution and are not included in the simulations discussed hereafter.

Finally, inserting the relevant forces in the general particle equation 2.54 and under consideration of a constant particle mass, the particle's equation of motion yields:

$$m_p \frac{d^2 \vec{x}}{dt^2} = \vec{\zeta} \sqrt{\frac{6 \pi \mu_f k_B T d_p}{\Delta t C_c}} + \frac{3 \pi \mu_f d_p \vec{u}_r}{C_c}. \quad (3.13)$$

This model equation is solved to calculate particle trajectories within the fluid based on Stokes' drag force and statistical effects of the Brownian molecular motion, including the normally distributed Gaussian random numbers $\vec{\zeta}$ (cf. equation 2.69). Note that the Stokes' drag force in equation 3.13 includes the particle response time $\tau_p = \frac{\rho_p d_p^2}{18\mu_f}$ (cf. equations 2.55 and 2.61), which is $\tau_p = 1.85 \cdot 10^{-7}$ s (with $d_p = 100$ nm) for the simulations presented herein. Relative to the investigation time of 0.021 s the total simulation time is approximately $11 \cdot 10^4 \tau_p$.

3.5.4 Solver settings for particle simulations

Since different particles in the flow volume around the instrument module are abruptly decelerated and accelerated (depending on their positions), the equation of motion 3.13 for all particles builds a system of stiff ordinary differential equations. For solving equations of such a type, COMSOL[®]'s particle tracking module [COMSOL[®], 2019] is utilized, which uses by default the numerical time-stepping method of generalized alpha (see Section 2.3.4): An implicit second-order scheme (with a parameter α) that is A-stable and has much less damping effects than the BDF (backward differentiation formulas, cf. Paragraph 2.3.3) [Boucher, C., 2020]. The parameter α (with $0 \leq \alpha \leq 1$) determines the damping of high frequencies [COMSOL[®], 2018a]. That is, for $\alpha = 1$ there is no numerical damping and for $\alpha = 0$ the numerical dampening is maximal [COMSOL[®], 2023]. The damping parameter is set to $\alpha = 0.75$ in the current investigations. *Free* time steps are chosen in the time solver, which are adapted to the problem according to the defined relative tolerance for the discretization error. In this study, the relative tolerance is set to 10^{-2} . By this procedure, in general, the

solver tries to choose largest possible time steps, whereby the discretization error estimate stays below the chosen threshold. However, time steps are reduced when necessary (e.g., to resolve abrupt changes in particle velocity) [COMSOL[®], 2023]. In this way, a balance between accuracy and efficiency is sought. By this adjustment, the time step size is up to the order of 10^{-5} s or even smaller. In the flow field near the substrate mounts, the particles are abruptly decelerated, they impact or are accelerated again. Therefore, the selected time steps of the solver are consistently very small (up to 10^{-14} s).

3.5.5 Model setup for particle simulations

To achieve and maintain uniform particle number concentrations within the simulation volume, individual, randomly distributed particles are launched at different times at defined *particle inlets* specified below (i.e., inlet planes, see Figures 3.45 and 3.46). The sequentially launched particles follow the flow such that a uniformly distributed particle number concentration is achieved in space. Due to the airspeed of 300 m s^{-1} and 400 m s^{-1} , and the simulation time of 0.021 s, a large number of particles must be launched in very small time steps (representative particle numbers used in these studies are presented in Table 3.4). In this way, at any time during the simulation, the substrate mounts are surrounded by particles. At the same time, other particles in the free flow field move with their terminal velocity and their resolution usually does not require such small time steps as required to resolve particle impactions. Overall, this simulation takes a considerable number of small time steps ($\sim 10^{11}$) until the final time is reached, which leads to a high computational time for the simulation, especially with a high number of particles.

To reduce the computational cost of the simulations regarding the time steps, randomly distributed particles within the 3D volume are converted into a two-dimensional distribution (i.e., projected onto a plane). Thereby, particles enter the 3D domain randomly distributed at the *particle inlets* where the spatial distribution of particle release positions is driven by a uniform probability distribution. The entering particles' initial velocity is set equal to the particle inlet fluid velocity. By this strategy, the time solver chooses larger time steps for the calculation of particle trajectories in general. The time steps of the solver decrease as soon as the particle cloud reaches the instrument module and the

impaction surfaces (i.e., the substrate mounts).

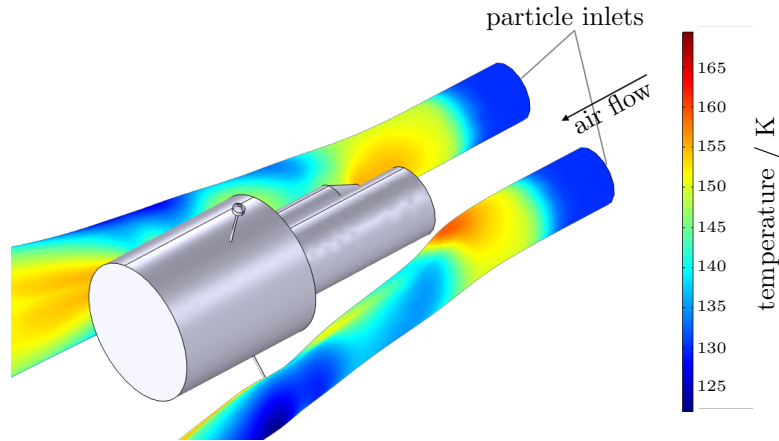


Figure 3.45: Particle trajectories of 10 000 particles originating from specified particle inlet regions and enveloping substrate mounts. The coloring refers to the temperature values at the particle positions.

For further efficiency increase, particles are launched only at specific positions at defined particle inlet planes (i.e., bounded regions embedded in the flow volume called *particle inlets*) from where they are most likely to impact the substrate mounts. This means that for the calculated particle trajectories such entry positions of particles far away from the instrument module are disregarded for this simulation, to save computing capacity. To determine the position of the particle inlets, the following procedure is performed:

- 1) since the nanometer-sized particles are small and agil enough to follow the streamlines very well even at small streamline curvatures, the flow patterns (streamlines) around the impactor surfaces are analyzed in detail,
- 2) utilizing these streamlines, the backward in time trajectories are then used to infer those particle inlet surface positions upstream of the instrument module at which an impact on the substrate mounts is to be expected.

In this way it is ensured that

- 3) the particle inlet regions as well as the distance between the particle inlets and the impactor surfaces are minimized and,

3 Supersonic flow simulations and impaction processes

- 4) the particle inlet positions are located at a sufficient distance upstream of the instrument module (i.e., in the undisturbed free flow field).

Figure 3.45 shows chosen particle inlet positions with according particle trajectories enveloping the substrate mounts.

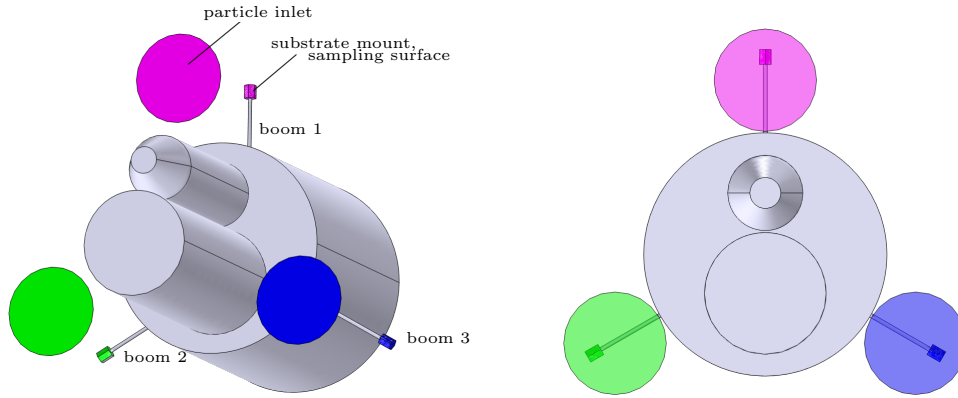


Figure 3.46: Particle inlets upstream of the three different SPICE booms are arranged such that particles flow around substrate mounts.

With knowledge of the particle parameters as well as the particle forces, the initial and boundary conditions for the particle simulations are now to be defined. The aim of these investigations is a proof of concept for obtaining particle impactions. For simplicity, the entire substrate mounts are defined as sampling surfaces (and not only the TEM grids as in reality, cf. Figure 3.23) as illustrated in Figure 3.46 and provided with the corresponding impaction boundary condition: It is assumed that the particles are impacted as soon as their position matches that of the substrate mounts, where they do not move anymore. In COMSOL[®] this is achieved by setting the boundary condition as *freeze*. This means that the position of a particle is retained for all times t after the contact time t_c (i.e., $t > t_c$) with $\vec{x} = \vec{x}_c$. The impaction particle velocity it is set to

$$\vec{v} = \vec{v}_c, \quad (3.14)$$

enabling to analyze the particle velocity \vec{v}_c immediately before impaction. Note that choosing the *stick* boundary condition, the particle position remains the same but the velocity is set to the velocity immediately after the impaction,

3 Supersonic flow simulations and impaction processes

i.e., $\vec{v}_c = 0 \text{ m s}^{-1}$. Remaining surfaces, which are shown in gray in Figure 3.46, are not considered in the impaction counting. These surfaces are equipped with a particle bounce off boundary condition, which is defined by (see also Appendix D, law of reflection):

$$\hat{v} = \hat{v}_c - 2(\hat{v}_c \cdot \hat{n})\hat{n}, \quad (3.15)$$

where \hat{v}_c , \hat{v} , and \hat{n} are the unit vectors of the incidence particle velocity, the reflected particle velocity and the normal vector to the surface. The particles' outlet from the simulation volume is defined on flow outlet planes in such a way that the particles disappear (i.e., they are discarded from further simulations, as soon as they touch the outlet surfaces of the simulation volume). Additionally, particle counters are placed on the sampling surfaces to evaluate the number of impacted particles.

Further, for the simulation process, particle numbers at the particle inlets need to be defined. The three particle inlet regions are shown in Figure 3.46, where particles are launched from a distance of 0.34 m upstream of the substrate mounts. The individual positioning of the inlets ensures that each substrate mount is entirely surrounded by the particle stream (emanating from the corresponding particle inlets as depicted in Figure 3.45). The particle inlet regions upstream of SPICE booms 1, 2 and 3 (see Figure 3.46) are each marked in different colors (each inlet has the color of the respective substrate mount on which released particles impact). Note that the locations of the particle inlets are adapted and extended for different angles of attack of $\pm 30^\circ$.

A further increase of the calculation efficiency is achieved by reducing the total number of released particles, with the aim of minimizing the expansion of the particle inlets: First, particle trajectory calculations are performed originating from the reduced inlets shown in Figure 3.46. Secondly, backward trajectories of impacting particles are calculated as illustrated in Figure 3.47. The result shows: Particles that ultimately deposit on sampling surfaces enter the simulation volume from specific areas of the reduced inlets (marked by blue circles in Figure 3.47). Particles that start outside the blue marked inlet areas do not impact on the sampling surfaces.

3 Supersonic flow simulations and impaction processes

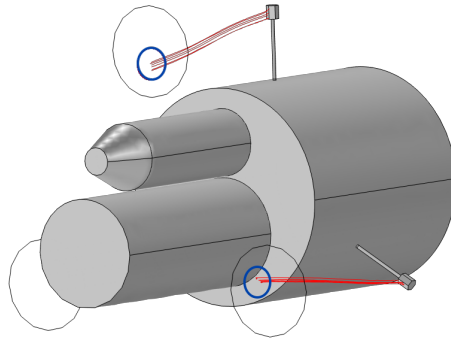


Figure 3.47: Calculated back trajectories of impacted particles (red lines). The impacting particles originate from preferential areas of the particle inlets, which are highlighted by blue contours.

Figure 3.48 confirms the position of one of the selected and adjusted inlets as suitable by illustrating an ensemble of trajectories released from the upper reduced inlet region (presented in Figure 3.47) enclosing the upper substrate mount. With this reduction, 89% of the launched particles could be reduced compared to the number that would have been released on the original inlet regions (cf. Figure 3.46). Subsequently, the refined inlets (blue markers in Figure 3.47) are used for further particle simulations.

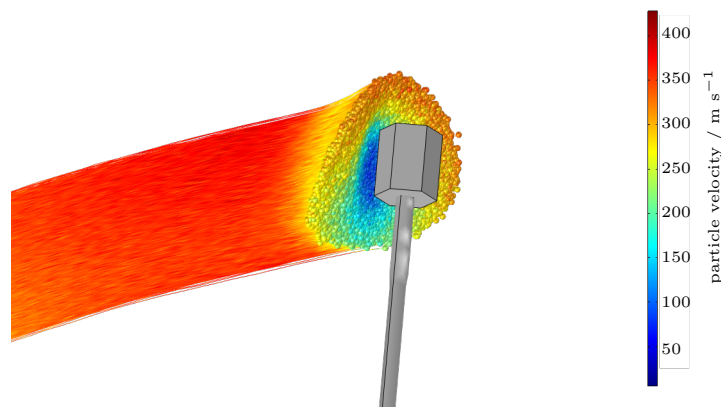


Figure 3.48: Ensemble of 9401 particle trajectories, originating from the reduced inlet heading towards the substrate mount. The color table scales particle velocity values.

3 Supersonic flow simulations and impaction processes

The particle number concentration of NLC elements is highly variable and scales from 1 up to 1078 cm^{-3} (cf. Paragraph 3.5.1 for detailed description) [Turco, R. P. et al., 1982; Von Cossart, G. et al., 1999; Baumgarten, G. et al., 2008; Baumgarten, G. and Fiedler, 2008]. Based on this range of particle number concentrations, analyses with particle numbers from about 19 000 to about 630 000 are performed in arbitrarily chosen steps of about 100 000 released particles. In addition, the corresponding particle number concentrations from 1 to 38 cm^{-3} are summarized in Table 3.4. This conversion has been made by considering a cylindrical volume of air filled with transversing particles (see Appendix F for more details). Lower particle number concentrations (less than 1 cm^{-3}) are unfavorable for the simulation process because statistical effects have a large impact on the deposition numbers (due to the random inlet position). In terms of the numerical computational effort, deliberate attention is paid to a low particle number concentration (cf. Table 3.4), applying a parameter study for the particle number concentrations at the lower limit of the possible values. Higher particle number concentrations are not considered due to high computational costs. Nevertheless, the sampling efficiency is analyzed at various lower particle number concentrations and the results of particle impactions can be extrapolated to higher particle number concentrations. The total calculation time of particle simulations in a parameter study was up to 168 hours.

particle numbers	particle number concentration
18 802	1 cm^{-3}
186 370	11 cm^{-3}
280 060	17 cm^{-3}
411 180	25 cm^{-3}
633 375	38 cm^{-3}

Table 3.4: Numbers of released particles as model input for particle simulations of the impaction processes with corresponding particle number concentrations.

3.5.6 Investigation of the particle size

As described in Section 3.2, the atmospheric conditions of the summer mesopause region are unique at an altitude of 85 km. As the temperature decreases to an atmospheric minimum, as well as the ability of the ambient air to store water vapor, the frost point temperature T_f falls below the ambient

3 Supersonic flow simulations and impaction processes

temperature T (i.e., $T < T_f$). This leads to supersaturation (i.e., the degree of saturation is larger than one). As a result, the existing water vapor is forced to undergo a phase transition and begins to condense on available surfaces such as provided by nuclei, resulting in ice particles. As Thomas, G. E. and McKay [1985], Rusch, D. W. et al. [1991], Rapp, M. and Lübken [2004], Rapp, M. and Thomas [2006], or Baumgarten, G. and Fiedler [2008] describe, the estimated size of NLC elements is 100 nm. According to Von Cossart, G. et al. [1999], the range of particle diameters is 38 - 148 nm with an average value of 100 nm. The estimation of the maximum diameter of 120 nm is given by Baumgarten, G. and Fiedler [2008]. However, the thermodynamic range over which the supersaturation condition occurs is very limited; small changes in temperature have large effects on the supersaturation and thus on the formation and the persistence of ice particles.

Cloud ice particles from NLC thus probably exist under comparatively unstable conditions at mesospheric altitudes. Therefore, when conducting fluid dynamics simulations of a supersonic sounding flight in the mesosphere, the effect of forming shock waves on the endurance of ice particles must be considered. Of particular interest is the temperature rise inherent with air compression as the instrument module moves through the air at supersonic speeds: On their way to the substrate mounts the particles pass through regions of sharp temperature increase which possibly lead to an abrupt subsaturation of the ambient air and thus possibly to the sudden sublimation of ice particles.

Regarding the simulations it should be noted that both, the particle trajectories and impaction processes are calculated based on (a range of) specific particles' masses and thus the particle diameters and material densities. Consequently, an estimate of the particle diameters is essential for further simulations to adequately validate the impaction processes. Therefore, the effect of a temperature increase on the particle diameter (reduction due to sublimation) is of great importance and thus investigated in what follows. Particle simulations are performed based on particles of an initial size estimated with a particle diameter of 100 nm. Figure 3.49 shows the temperature field based on the incident flow velocity of 400 m s^{-1} and trajectories of individual particles impacting on the upright sampling surface. To better analyze the air temperature evolution with

3 Supersonic flow simulations and impaction processes

accurate data along particle trajectories, two deposited particles are randomly selected from the trajectory ensemble. The temperature profile at the particle position along the trajectories as a function of distance from the deposition surface (in m) is shown in Figure 3.50 for the two selected particles.

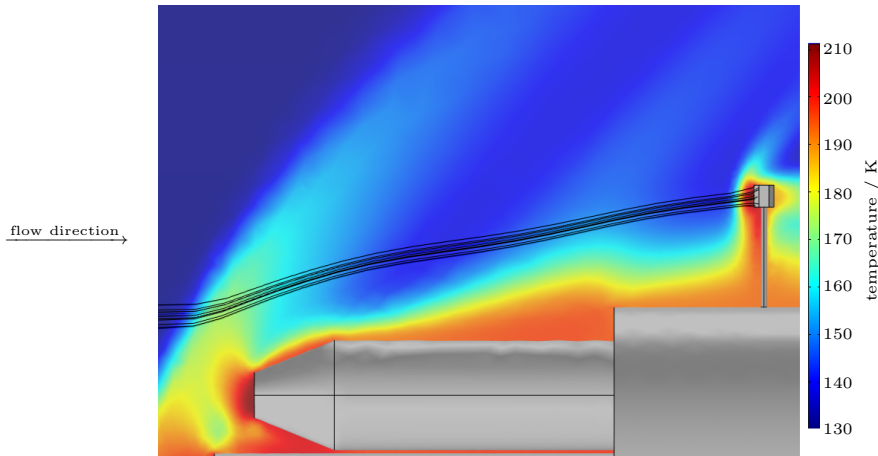


Figure 3.49: Enlargement of the temperature field in K around the instrument module illustrating the temperature increase caused by the shock waves based on the incident flow velocity of 400 m s^{-1} . In addition, the trajectories of individual impacting particles are shown.

Particles within the free flow (farther than 0.6 m upstream of the substrate mount) are in the ambient temperature region of 130 K. Along the particle trajectories, particles experience an initial temperature increase as they pass the shock wave forming at the instrument module tip, with a temperature increase ΔT of about 40 K at ~ 0.5 m upstream of the substrate mount. Thereafter, the air temperature generally remains at a higher value than the ambient temperature of 130 K caused by the general temperature increase around the instrument module. The second prominent temperature increase then occurs immediately before particle impaction, with a temperature increase of $\Delta T = 75$ K compared to the temperature of the free flow field (where the temperature increase shifts the saturation vapor pressure over ice by a factor of $4 \cdot 10^7$ [Murphy, D. M. and Koop, 2005] and the saturation ratio decreases by a factor of 26 [Podolak, M. et al., 1988]). The time a particle is exposed to temperatures of more than $T = 130$ K, i.e., the time that elapses from the first temperature increase at 0.6 m upstream of the substrate mount to the impaction event, is $t = 1.8$ ms.

3 Supersonic flow simulations and impaction processes

The results are based on a particle simulation with an incident flow velocity of 400 m s^{-1} .

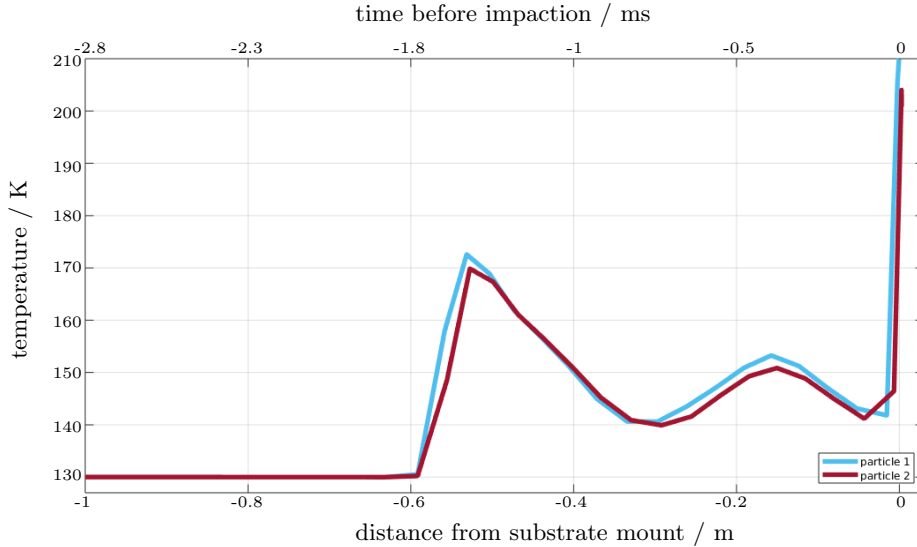


Figure 3.50: Temperature evolution along the trajectories of two impacting particles depicted by the blue and red color, respectively. The coordinate origin (zero) of the x -axis represents the location of the particle impact on the substrate mount.

In order to determine the decrease of the particle diameter with temperature increase of the surrounding air (i.e., in the air compression zone), the time evolution of the ice particle mass (see, e.g., [Stephens, G. L., 1983]) is examined based on simulated air temperature and pressure values evaluated along an exemplary particle trajectory, as presented in Figure 3.50. The initial particles masses assumed for the investigation are based on corresponding particle diameters of 50, 100, 150, 200, 250, and 300 nm. Although it is generally accepted that the relevant particles in the mesosphere are predominantly of diameters around 100 nm, the extended range of particle diameters investigated with this simulation allows for extreme value considerations. The calculations of the change in ice particle mass (m_{ice}) with time t (i.e., $\frac{dm_{ice}}{dt}$) are based on a deposition coefficient α_d of ice crystals, which indicates how efficiently water molecules are introduced into or removed from the crystalline ice structure. The underlying equation reads

3 Supersonic flow simulations and impaction processes

(e.g., [Stephens, G. L., 1983]):

$$\frac{dm_{ice}}{dt} = \frac{2\pi}{R_v} \alpha_d D_v d \left(\frac{p_v}{T_{air}} - \frac{p_s}{T_{ice}} \right), \quad (3.16)$$

with the diffusion coefficient D_v of water vapor in air, which is calculated by [Pruppacher, H. R. and Klett, 2010]:

$$D_v = 2.11 \cdot 10^{-5} \left(\frac{T_{air}}{T_0} \right)^{1.94} \left(\frac{p_0}{p} \right), \quad (3.17)$$

where p is the air pressure, T_{air} is the air temperature, p_v is the partial pressure of environmental water vapor, p_s is the saturation pressure over the curved ice crystal (see Appendix E), and $T_0 = 273.15$ K and $p_0 = 101325$ Pa are reference values. Furthermore, d is the particle diameter, R_v is the gas constant for water vapor, with $R_v = \frac{R}{M_v}$, with the universal gas constant R and the molar mass of water M_v , the ambient temperature T_{air} , and the surface temperature T_{ice} (see Appendix E). The smaller the value of α_d , the less effective is the growth or sublimation of the ice particle (i.e., the slower is the process). The relevant literature gives a wide range of measured α_d coefficients, ranging from 0.005 to 1 [Magee, N. et al., 2006; Pruppacher, H. R. and Klett, 2010]. Due to the uncertainty of α_d , different values are applied, with $\alpha_d = 0.1$, 0.5 [Spichtinger, P. and Gierens, 2009], and 1 leading to different modeling results.

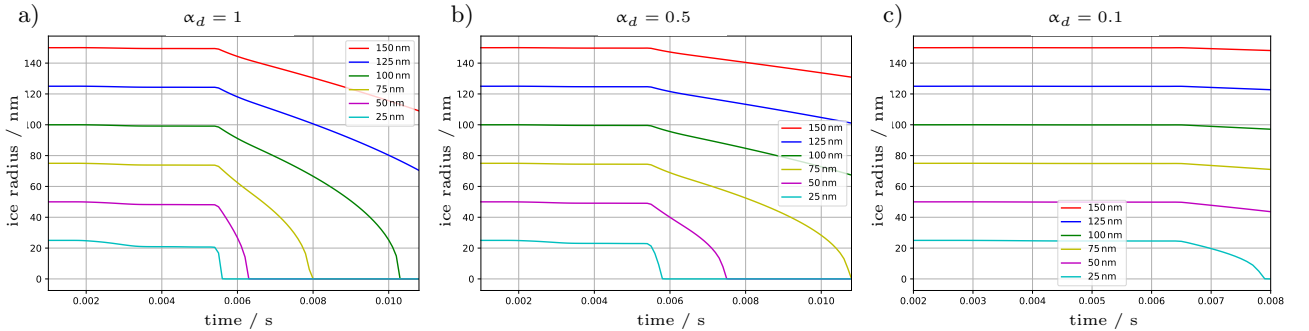


Figure 3.51: Simulated mass behavior of particles of different sizes based on varying values of α_d , from Manuel Baumgartner, Johannes Gutenberg University Mainz, Institute for Atmospheric Physics.

To demonstrate the various mass behavior, equation 3.16 can be numerically integrated to obtain the mass curves with respect to time. The calculation results reveal that for $\alpha_d = 1$, particles with diameters up to 200 nm sublimate

completely on their way to the sampling surfaces, as presented in Figure 3.51 a) (note that only pure ice particles without nuclei are assumed). Analogous results are obtained for $\alpha_d = 0.5$ (where particles with diameters up to 150 nm sublimate completely on their way to the sampling surfaces), while for $\alpha_d = 0.1$ only the smallest particles with diameters of 50 nm would sublimate completely before impaction (see Figure 3.51 c)). Based on the described investigation regarding the uncertainty of the deposition coefficient α_d , a worst-case scenario is considered, assuming a complete sublimation of even the largest ice particles present. After complete sublimation only the remaining condensation nuclei with correspondingly small sizes of 1.2 nm (cf. Paragraph 3.5.1) remain for the deposition. Since these small particles have low inertia, following conclusion could be drawn: If deposition of these nuclei on the substrate mounts occurs, then a fortiori larger particle with greater inertia will be deposited, since smallest particles will essentially be guided around the sampler by the perturbed aerodynamics. Moreover, as can be seen from Figure 3.50 maximum temperatures are about 210 K. As for the ice-embedded refractory cores, these are certainly insensitive over the entire prevailing temperature range. Finally, subsequent particle simulations are thus conducted with a constant MSP diameter of 1.2 nm and a material density of 3 g cm^{-3} (from which the particle mass is calculated indirectly in COMSOL[®] [2017b]). Simulation results focus on the maximum flow velocity of 400 m s^{-1} where the particle response time τ_p becomes even less important.

3.5.7 Efficiency of inertia-based particle collection

The results of numerical simulations of particles confirm that particles impact on surfaces facing the flow field, while no particle impactions are detectable on the downstream substrate mounts as presented in Figure 3.52. This can be explained with a highly resolved flow field around the substrate mounts, which can be found in Section 3.4.3. Here, attention is paid to the flow field and to vortices that may develop in the slipstream of the substrate mounts, which may cause particle impactions on downstream surfaces. The impaction patterns as shown in Figure 3.52 serve as the basis for the analyses of the resulting sampling efficiencies of the SPICE booms. Such particle impactions are evaluated for different particle number concentrations, for each individual substrate mount

3 Supersonic flow simulations and impaction processes

as well as for the three investigated angles of attack of the HAS. The particle counters of COMSOL[®] are defined on the substrate mounts and are utilized to evaluate the number of deposited particles.

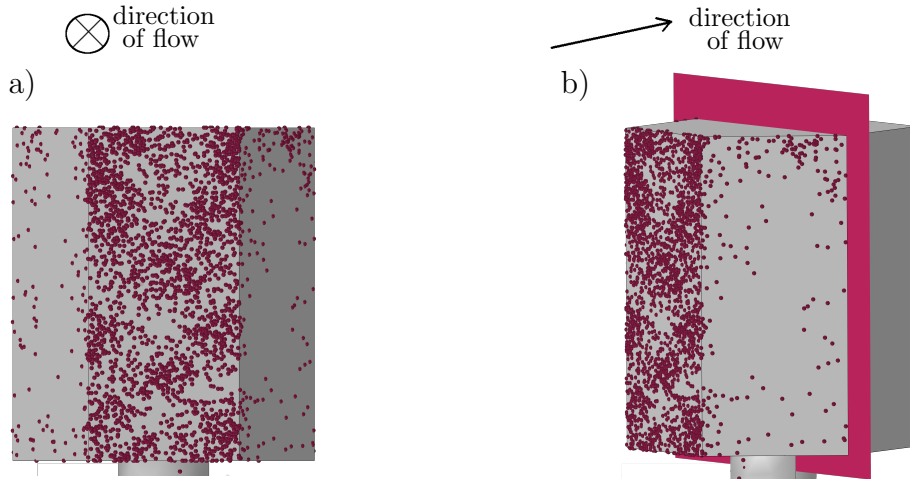


Figure 3.52: Detailed frontal view a) [Klug, B. S. et al., 2023] and side view b) of 2703 impacted particles on substrate mounts for the initial particle number concentration of 11 cm^{-3} . Additionally, the cross-sectional area of the substrate mount perpendicular to the flow direction is illustrated in b) by a cut plane.

In the following, the sampling efficiencies of the individual substrate mounts are presented. To reduce the computational effort, one of the two downside oriented SPICE booms is considered representative for the particle deposition analyses, which can be argued with the symmetry with respect to the y - z -plane (cf. Figure 3.22). The number of impacted particles with respect to ambient particle number concentrations (converted to absolute numbers of particles released at the particle inlets, cf. Table 3.4) is shown in Figure 3.53 (left column) under the HAS angles of attack of 0° a1), -30° b1), and $+30^\circ$ c1). Substrate mounts 1 (upright boom) is marked in magenta and 2 (downside oriented boom) in green. The vertical bars represent the statistical variability of impaction results from four independent simulation runs. As the dashed lines in Figures a1), b1), and c1) depict, an increasing particle number concentration results in a linear increase of particle impactions, which is valid for the different substrate mounts as well as for the different angles of attack, however with different slopes.

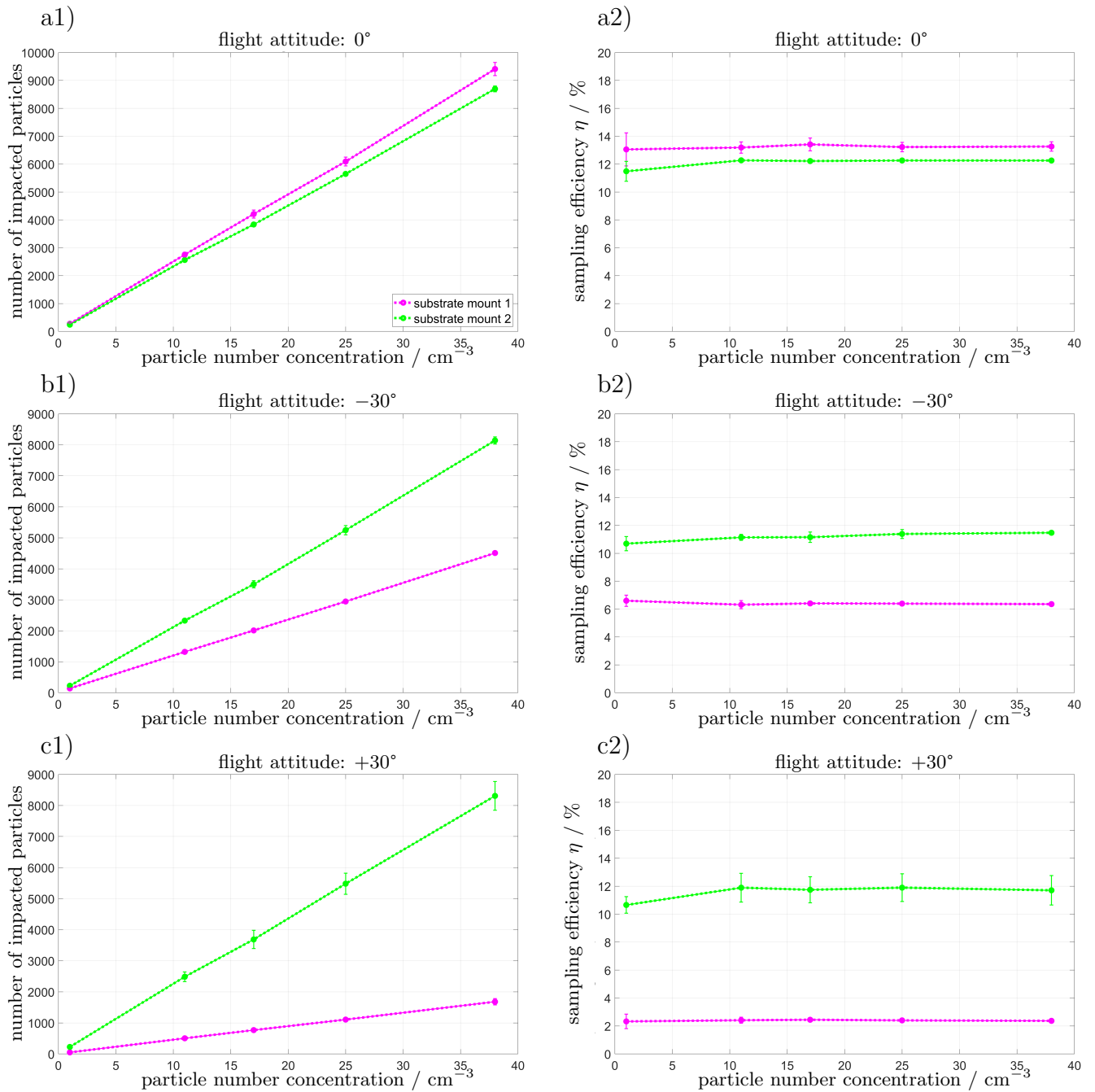


Figure 3.53: **Left column:** Number of impacted particles on substrate mounts with respect to ambient particle number concentrations for the HAS flight attitudes. **Right column:** Sampling efficiency η with respect to ambient particle number concentrations for the HAS flight attitudes. The magenta color represents data from the upright substrate mount 1 and the green color from the downside oriented substrate mount 2. The variability of four independent simulation runs is marked by vertical bars. Figures a1) and a2) are from Klug, B. S. et al. [2023].

3 Supersonic flow simulations and impaction processes

While particle impaction curves for the angle of attack of 0° (cf. Figure 3.53 a1)) are only slightly different for substrate mount 1 and substrate mount 2, they differ for the angle of attack of -30° (cf. Figure 3.53 b1)). Here, the increase of particle impactions is significantly steeper for substrate mount 2 than for substrate mount 1. For the angle of attack of $+30^\circ$ (cf. Figure 3.53 c1)), the number of impacting particles related to the particle number concentration decreases significantly for substrate mount 1 compared to the steep increase of particle impactions of substrate mount 2. Note that the slope of particle impaction curves of downside oriented substrate mounts almost coincide (compare green curves).

To investigate the trends of increasing particle impactions with respect to particle number concentrations the sampling efficiencies η are illustrated in Figure 3.53 right column with

$$\eta = \frac{C_{impacted}/A_{impacted}}{C_{released}/A_{released}}. \quad (3.18)$$

Thereby, η is expressed as a percentage of the number of impacted particles $C_{impacted}$ with respect to the released inlet particle numbers $C_{released}$ related to the particle inlet area $A_{released}$ (cf. blue markers in Figure 3.47) and the cross-section area of the substrate mount $A_{impacted}$ perpendicular to the flow direction (cf. Figure 3.52 b)). The sampling efficiencies are illustrated in Figures 3.53 a2), b2), and c2) for substrate mounts 1 and 2 for different flight attitudes. First of all, an almost constant course of the sampling efficiency η with respect to the ambient particle number concentration can be determined for all flight attitudes and both substrate mounts. Depending on the angle of attack, the impaction efficiency of the upright substrate mount varies and is 13.2% at the flight attitude of 0° and 6.4% at -30° and reaches its lowest value of 2.4% at the angle of attack of $+30^\circ$. These efficiencies are determined as an average over all five investigated particle number concentrations. In contrast, an almost identical impaction efficiency η is achieved for all flight attitudes for the downside oriented substrate mounts, which lies within a narrow range of 11.2% to 12.1%. Concerning the individual flight attitudes, the sampling efficiencies differ for both substrate mounts: At an angle of attack of 0° , this difference is only about 1.1%, while this difference increases to 4.8% at

-30° and the maximum difference of 9.2% is reached at an angle of attack of $+30^\circ$. This represents a significant reduction in efficiency of 82% compared to the maximum efficiency achieved for this substrate mount. The variability of the sampling efficiency of the upright substrate mount at different flight attitudes and its independence from ambient particle number concentrations (cf. Figure 3.53 a2), b2), and c2)) suggests that statistical features resulting from random positions of particle releases are irrelevant (especially for higher concentrations) and confirm a strong influence of the substrate mount positions (i.e., the fluid dynamic patterns).

To emphasize this effect, Figure 3.54 illustrates further details on the flow pattern, with the streamlines flowing around the substrate mounts colored with the velocity magnitude. Additionally, the course of the shock waves is depicted. Depending on the flight attitude (0° in a), -30° in b), and $+30^\circ$ in c)), the substrate mounts are subjected to different flight conditions. In Figure 3.53 a) the streamlines show analogous velocity values in the near-field upstream of the substrate mounts 1 and 2 from 350 m s^{-1} to 400 m s^{-1} , while different velocity values upstream of the substrate mounts are depicted for the angle of attack of -30° in Figure 3.53 b): The upright substrate mount is located behind the shock wave in an area with reduced velocities of 270 m s^{-1} (referring the yellow colored values, see also Figure 3.35 and discussion for more details) resulting in reduced impaction efficiencies, whereas the two downside oriented substrate mounts are exposed to the maximum velocities of 420 m s^{-1} . At the angle of attack of $+30^\circ$ the upright substrate mount lies in the flow shadow of the instrument module tip, so that the corresponding particle inlet upstream of SPICE boom 1 has been enlarged to ensure particle impactions. Figure 3.54 c) depicts streamlines starting from the adjusted particle inlet. Velocity values upstream of substrate mount 1 are reduced to 220 m s^{-1} , while upstream of substrate mount 2 higher velocity values of 320 m s^{-1} are achieved. In general, a higher flow velocity implicates a higher number of particle impacts, since an increased number of particles cannot circumvent the obstacle (substrate mount) due to their higher velocities and inertia at higher flow speeds. In this regard, the sampling efficiency results described above correspond to the flow pattern observed in Figure 3.54.

3 Supersonic flow simulations and impaction processes

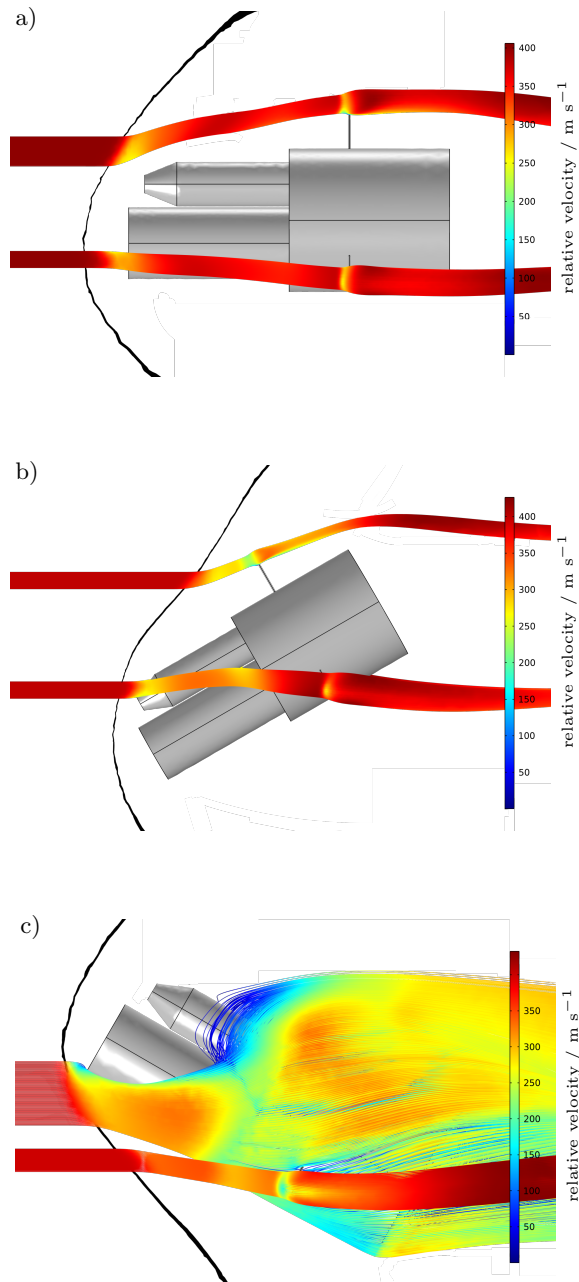


Figure 3.54: Streamlines flowing around substrate mounts for the angles of attack of 0° a), -30° b), and $+30^\circ$ c) for the incident flow velocity of 400 m s^{-1} . Streamlines are colored with reference to the velocity magnitude. For illustration purposes, the course of the shock wave front is indicated by a black line.

The marginal difference in sampling efficiency (substrate mount 1 and 2, cf.

Figure 3.53 a2)) for the angle of attack of 0° is 1% and can solely be explained by the asymmetric tip of the instrument module located upstream of the SPICE booms, which potentially affects the flow pattern. The difference in the sampling efficiency between substrate mount 1 and substrate mount 2 for the flight attitude of -30° (cf. Figure 3.53 b2)) can be explained by the fact that substrate mount 1 is enveloped by the shock wave, whereas the two downside substrate mounts are still exposed to the almost free flow (cf. Figure 3.54 b)). At an angle of attack of $+30^\circ$ (cf. Figure 3.53 c2)), the maximum decrease in sampling efficiency can be explained by the position of substrate mount 1, which is shielded from free flow by the upstream instrument module tip. In this position, hardly any particles reach positions relevant for impaction processes due to the geometry-related deflection of the flow. Furthermore, particles in the near field upstream of substrate mount 1 are in a region of low velocities, which is reflected in an overall low sampling efficiency compared to substrate mount 2.

3.5.8 Summary of particle collection investigations

In summary, the three analyses (for the flight attitudes of 0° , -30° and $+30^\circ$) show an independence on ambient particle number concentrations, but a strong dependence of the sampling efficiency on the flight attitude. In general, the downside oriented SPICE booms show a higher sampling efficiency between 11.2% and 12.1%, which is stable for all three angles of attack and all investigated particle number concentrations. In contrast, the upright SPICE boom shows a reduced efficiency, which is of 2.4% to 6.4% for the flight attitudes of $\pm 30^\circ$. Thus, the two downside oriented SPICE booms are more suitable for the particle collection along the flight path of the measurement section of the HAS. Nevertheless, the upright boom may ensure at least a redundant particle collection in some profitable flight attitudes in the event of an unforeseen malfunction of one of the other booms.

The particle number concentration prevailing in the mesosphere has not yet been conclusively clarified in the available literature. The considerations made in this study were performed for particle number concentrations in the limited range of 1 to 38 cm^{-3} in order to reduce the computational effort at lower total particle numbers (a total of 1 530 000 particles were simulated here). However, the results show that an almost linear relationship develops between the

3 Supersonic flow simulations and impaction processes

impacted particles and the particle number concentrations (i.e., almost constant sampling efficiencies, which provide some guarantee for the extrapolation of the impaction results outside the considered particle number concentration range), such that the actual particle number concentration can be estimated.

4 Outlook for future development of the SPICE instrument

In the present work, approaches of numerical simulations are provided in order to promote the development and improvement of a supersonic particle collector (i.e., the SPICE instrument). It should be mentioned that smallest structures of the simulation geometry (e.g. finest geometry artifacts of the substrate mounts or other measuring devices on a sub-millimeter scale) were not considered, since the computational effort for a more structured geometry (i.e., requiring even higher numbers of mesh elements) does not increase linearly, but exponentially with its resolution. In the following, three approaches are mentioned that contribute to the further improvement of the modeling and simulation and thus to the development of the SPICE instrument.

Macroscopic design optimization to improve the collection efficiency by applying fluid dynamics

The level of detail of the SPICE instrument and the instrument module geometry can be increased in further simulation steps by focussing on single geometry segments minimizing the extension of the simulation volume surrounding finest structures. In this way the computational effort is limited. For the purpose of a detailed investigation of slipstream vortices and small scale flow patterns a more complex fine-structure of one SPICE boom with its substrate mounts and recessed TEM grids (substrates) was detailedly simulated and can be found in Section 3.4.3.

With regard to the design optimization of the substrate mounts, the following comments can be drawn: In the current state of development, the SPICE booms are not designed to be rotatable. This has the disadvantage that although the angle of attack of the HAS changes, the orientation of the

4 Outlook for future development of the SPICE instrument

substrate mounts against the flow direction cannot be adjusted. For the most efficient particle sampling, it would be conceivable to always align one of the substrate mount surfaces against the flow direction during the measurement flight. Such an orientation (i.e., with substrate mounts perpendicular to the flow) yields a non-aerodynamically positioned frontal surface that forces the surrounding streamlines to change direction steeply, which in turn promotes inertia deposition of particles onto the substrates as presented in Figure 3.52. Such a mechanism can be achieved by adding fin-tails to the hexagonal substrate mounts (acting like an oar) and by considering the free rotatability of the whole object in the design concept of the SPICE instrument. In this case the fluid structure simulation can be performed in order to investigate the underlying dynamics, where the fluid dynamic description in Chapter 2 must be generalized to the concept of the moving domain using the so-called *Arbitrary Eulerian-Lagrangian (ALE) Formulation*. However, the fin-tails complicate the design of the SPICE booms; the fin-tails must be retracted and extended during the short duration of the measurement phase or must be considered spatially in the design of the mechanically extendable booms. The fin-tails also make the construction of the SPICE booms more sensitive to vibrations that can occur during the flight. Nevertheless, the continuous alignment of substrate mounts against the flow direction, independent of the flight attitude would be guaranteed in the design concept of the SPICE instrument.

Attempts could also be made to further improve the design of the substrate mounts by using numerical simulations with regard to their technical limitations and fluid dynamic artifacts. In this way, for example, the following considerations could be investigated: How would concave substrate mounts affect the impaction efficiency? Note that a spherical shape is optimal with respect to the flight profile at a variable flight attitude. However, the spherical shape imposes mechanical limitations on the safe mounting of substrates, such as the desired TEM grids because the TEM grids must be clamped tightly to avoid loss due to vibrations and circumstances during exposure. Furthermore, the risk of substrate contamination during TEM grid mounting must be minimized. Preparatory simulations carried out as part of the presented study have shown that spherical and thus streamlined substrate mounts as well as hexagonal substrate mounts with one frontal oriented edge are less suitable for particle im-

4 Outlook for future development of the SPICE instrument

pactions. The abrupt changes in direction of the streamlines inherent with a non-aerodynamic positioning of the impaction surface (i.e., the alignment of a surface against the flow direction) is the advantage of a hexagonal prism as shape for the substrate mounts, which favor particle impactions. The disadvantage of substrate mounts in the form of hexagonal prisms is: some substrates are mounted on surfaces, onto which particles are deposited only to a limited extent (as simulation results in Paragraph 3.5.7 show). The evaluation effort for these potentially weakly loaded samples may seem disproportionate given the potentially low particle yield and low insight gain. Nevertheless, additional collection surfaces may also provide additional valuable information, in particular during the proof-of-concept phase of the SPICE instrument. Sounding rocket flights are very rare, and if an opportunity arises, the sampling periods durate only over a few minutes. Therefore, the design strategy is to enable the exposition of as much collection surfaces as possible at one time as soon as the target region within the mesosphere is reached. Further improvements in the design of the substrate mounts are highly desirable if they increase the substrate mounts' flow resistance and thus the impaction efficiency, in particular for the smallest particles.

Comprehensive analysis of the angles of attack to improve the sampling efficiency estimation

In the simulations performed, the two distinct cases of an HAS angle of attack of $\pm 30^\circ$ each are treated as extreme value considerations and the case with a horizontal orientation (i.e., of 0°) of the HAS are considered. However, the whole range of angles of attack between the limiting cases is not covered. Thus, no continuous prediction of the sampling efficiency as a function of flight attitude is possible. In order to simulate the entire flight profile and draw detailed conclusions about the impaction efficiency, a continuous simulation of the entire angle of attack interval from $+30^\circ$ to -30° , or between larger extremes can be performed in the future applying the moving geometry approach for the fluid obstacle (i.e., the instrument module). Here, the instrument module should be rotated by 60° around the rotation center.

Improved particle trajectory modeling

The particle trajectory calculations are based on MSP sizes as a limiting case with respect to a minimum size assumption similar to Hedin, J. et al. [2014], considering the complete sublimation of the NLC elements and thus the sizes of MSP. Therefore, the particle diameter, which the particle trajectory calculation is based on, is assumed to be constant. However, since the NLC elements are assumed to at least partially sublimate as they pass through the compression zones due to supersonic velocities (increasing temperature and thus sudden subsaturation), another simulation adjustment that targets varying particle sizes may be of importance. As the particle diameter decreases along the particle trajectory, the drag force changes and influences the trajectory of the particles. Although this effect is expected to be minimal, its impact on particle trajectories can be investigated.

Finally, the advantage of numerical simulations for the development of the SPICE instrument must be emphasized. The simulation results replace time-consuming, lengthy and expensive design developments in a supersonic wind tunnel, in an extreme cold chamber and in a low-pressure chamber. In the numerical simulations performed, various physical parameters or geometry changes can be varied in parameter simulation studies with little effort compared to experimental studies. This eliminates the necessity of the production of test objects for the verification of the sampling efficiencies associated with design changes. Once the measurement flight has been carried out and the results are available, the simulation results can be validated and the simulations can be adjusted on the basis of the measurements. In particular, more detailed particle tracking simulations are possible with detailed information on the chemical composition and the shape and size of particles after evaluation of the impaction measurements. Reliable numerical results for particle collection and resulting simulated impaction efficiencies are of great importance for deriving the prevailing MSP concentration in the mesosphere and for confirming the role of MSP as ice nuclei for NLC elements.

5 Summary and conclusion

The objective of the present work was the mathematical and numerical modeling of particle impactions during a supersonic flight. The derived model was used to support the development of an instrument for the inertia-based collection of mesospheric particles (presumably meteoric smoke particles, incorporated into noctilucent cloud elements) to enable their subsequent offline analysis. Equations of conservation laws of fluid variables (temperature, pressure, density, velocity, energy) were considered to obtain the flow dynamical patterns around the sounding rocket's instrument module. The ambient velocities were furthermore included in the particle dynamic description. The particle motion was described on the basis of Newton's second law, considering the Stokes' drag force and the Brownian force. The coupled fluid flow and particle tracking model was implemented in COMSOL Multiphysics[®] using Computational Fluid Dynamics and the particle tracking module. The collection instrument to be developed, named SPICE, is part of the instrument module of a sounding rocket. The collection of mesospheric particles is to be performed during a sounding rocket flight at supersonic speeds using substrates on which the particles impact and adhere. The substrate mounts are part of SPICE booms and are formed as hexagonal prisms, on the sides of which the substrates are recessed. Analysis of the particles will provide information on the number, size, morphology, and chemical composition of MSP that were likely incorporated into mesospheric cloud elements just prior to sampling.

Many of the development steps of the SPICE instrument design were supported or questioned by numerical simulations within this work, resulting in efficient improvements of the design. The following steps were taken to set up the numerical simulation:

- 1) The geometry of the instrument module tip, containing the so-called SPICE compartment (cf. Figure 3.10), was implemented in COMSOL[®].

5 Summary and conclusion

- 2) The fluid flow using the finite element method was calculated by means of the high Mach number continuum flow interface of COMSOL[®], solving the Navier-Stokes equations for compressible fluids. The flow field, temperature, pressure, density, and energy around the implemented geometry were analyzed. The effect of the Multi Needle Langmuir Probe (m-NLP) with its aerial-type structures upstream of the SPICE booms was investigated, and the SPICE booms were arranged to remain unaffected by the flow disturbance of the m-NLP. Moreover, particular attention was paid to the boundary layer at the position of each SPICE boom. Furthermore, care has been taken to ensure that particle collection remained unaffected by the shock waves that build upstream of the SPICE booms.
- 3) The SPICE instrument was gradually configured, on the one hand in line with the respective findings from the numerical simulations and on the other hand on the basis of empiricism with regard to the fully automated detection and collection of aerosol particles at high altitudes, and repeatedly mechanically adapted to the geometrically limited conditions. The almost free-flow collections should be achieved by impacting the particles due to their inertia on substrates, which allow subsequent analysis of the samples. The substrates were located outside the boundary layer (i.e., in the almost undisturbed flow) obtained from numerical simulations for fluid dynamics. The design of the substrate mounts was developed based on aerodynamic effects of the flow around them: they were constructed to avoid flow patterns that are unfavorable for impactions. The resulting shape of the substrate mounts as hexagonal prisms was developed as a compromise between its non-aerodynamic properties in the flow, which favor the impaction collection, and the suitability for mechanical attachment of the substrates on the mounts. Taking into account the ballistic flight profile (i.e., a variable flight attitude and thus changing angles of attack) of the HAS, it was confirmed that SPICE booms arranged radially around the instrument module lead to the exposition of at least two substrate mounts to the almost free airflow at all measuring times.
- 4) Subsequently, the final design of the instrument module tip with SPICE booms was implemented for the fluid dynamics simulations and the flow field was simulated and analyzed based on the final geometry of the instru-

5 Summary and conclusion

ment module with the SPICE instrument specified in point 3) (see also Figure 3.22) for extreme values of flight attitudes of $\pm 30^\circ$, respectively, and for the neutral angle of attack of 0° .

- 5) Finally, the obtained flow field was included into the particle tracking model to simulate particle trajectories and to evaluate the efficiency of particle impactions (for particle sizes of 1.2 nm) on the three substrate mounts during the sounding flight (where different flight attitudes were considered).

In essence, the particle simulations have confirmed the effectiveness of the developed SPICE instrument. It was shown that the substrate mounts as hexagonal prisms are hit by particles with diameters of 1.2 nm and densities of 3 g cm^{-3} . Thus, the particle simulations were able to answer the fundamental question of whether the developed aerodynamic design and the chosen arrangement of the substrate mounts are suitable for intercepting mesospheric particles with as little artifact as possible: The substrate mounts (with a boom length of 120 mm) are located outside the boundary layer and are also localized in such a way that at least two of them remain almost unaffected by the shock wave (low velocities downstream). The particle collection efficiency within the target altitude were estimated as well. The analyses of the collection efficiencies show a clear dependence on the position of the SPICE boom and the angle of attack of the HAS. According to the obtained results, the collection efficiencies of the downside oriented substrate mounts range from 11% to 12% at all investigated angles of attack (0° and $\pm 30^\circ$), and they are thus less sensitive to attitude than the collection efficiency of the upright substrate mount, which ranges from 2% to 13% at the angles of attack of $\pm 30^\circ$ and of 0° . There are at least two of the three SPICE booms permanently exposed during the collection phase independent on the HAS flight attitude, which may cause a reliable interception of particles.

According to the collection success predicted by numerical simulations, the sampling and analyzes of mesospheric particles within noctilucent clouds is highly possible with the designed SPICE instrument and the conduction of the sounding rocket flight to gain further important insight into the processes that occur in the high atmosphere.

Appendices

A List of abbreviations

BDF	backward differentiation formulas
FEM	finite element method
FDM	finite difference method
HAS	high atmosphere soarer
IN	ice nuclei
m-NLP	multi Needle Langmuir Probe
MSP	meteoric smoke particles
NLC	noctilucent clouds
PMC	polar mesospheric clouds
PMSE	polar mesosphere summer echoes
SPICE	Supersonic PartIcle CollEctor
TEM	transmission electron microscopy
TDS	time-dependent study
CFD	computational fluid dynamics

B Nomenclature

A	surface, $[A] = \text{m}^2$
C	particle number concentration, $[C] = \text{cm}^{-3}$
c	speed of sound, $[c] = \text{m s}^{-1}$
c_{am}	added mass coefficient
C_c	Cunningham slip corrector
C_d	drag coefficient
c_{ice}	specific heat capacity of ice, $[c_{ice}] = \text{J (kg K)}^{-1}$
c_v	specific heat capacity, $[c_v] = \text{J (kg K)}^{-1}$
D	deformation tensor, $[D] = \text{s}^{-1}$
D_d	diffusion term, $[D_d] = \text{kg}^2 \text{ m}^2 \text{ s}^{-3}$
d_p	particle diameter, $[d_p] = \text{m}$
e	internal energy, $[e] = \text{J}$
f	frequency, $[f] = \text{s}^{-1}$
\vec{F}	force, $[\vec{F}] = \text{N}$
\vec{F}_p	pressure gradient force, $[\vec{F}_p] = \text{N}$
\vec{F}_{am}	added mass force, $[\vec{F}_{am}] = \text{N}$
\vec{F}_D	drag force, $[\vec{F}_D] = \text{N}$
\vec{F}_B	buoyancy force, $[\vec{F}_B] = \text{N}$
\vec{F}_G	gravitational force, $[\vec{F}_G] = \text{N}$

B Nomenclature

- \vec{F}_S Saffman lift force, $[\vec{F}_S] = \text{N}$
- \vec{F}_t total force, $[\vec{F}_t] = \text{N}$
- \vec{f} body force per unit mass, $[\vec{f}] = \text{N kg}^{-1}$
- g gravitational acceleration, $[g] = \text{m s}^{-2}$
- k_B Boltzmann constant, $[k_B] = \text{J K}^{-1}$
- k thermal conductivity, $[k] = \text{W m}^{-1} \text{K}^{-1}$
- Kn Knudsen number
- Kn_p Knudsen number of particles
- L characteristic length, $[L] = \text{m}$
- L_s latent heat for sublimation, $[L_s] = \text{J kg}^{-1}$
- l_c height of cylinder, $[l_c] = \text{m}$
- m mass, $[m] = \text{kg}$
- m_{ice} ice mass, $[m_{ice}] = \text{kg}$
- Ma Mach number
- N_c number of particles within air volume
- n number of particles
- p static pressure, $[p] = \text{Pa}$
- p_a absolute pressure, $[p_a] = \text{Pa}$
- p_{ice} saturation vapor pressure for ice, $[p_{ice}] = \text{Pa}$
- p_v partial pressure of environmental water vapor, $[p_v] = \text{Pa}$
- p_s saturation pressure over a curved ice crystal, $[p_s] = \text{Pa}$
- Q heat sources, $[Q] = \text{W m}^{-3}$
- \vec{q} heat flow vector, $[\vec{q}] = \text{W m}^{-2}$

B Nomenclature

q_v	water vapor mixing ratio, $[q_v] = \frac{\text{kg}}{\text{kg}}$
R_s	specific gas constant, $[R_s] = \text{J kg}^{-1} \text{K}^{-1}$
R_d	gas constant of water vapor, $[R_d] = \text{J kg}^{-1} \text{K}^{-1}$
Re	Reynolds number
Re_r	particle Reynolds number
R_v	gas constant of dry air, $[R_v] = \text{J kg}^{-1} \text{K}^{-1}$
S	surface, $[S] = \text{m}^2$
St	Stokes number
T	temperature, $[T] = \text{K}$
T_{air}	air temperature, $[T_{air}] = \text{K}$
T_f	frost point temperature, $[T_f] = \text{K}$
T_{ice}	surface temperature of an ice particle, $[T_{ice}] = \text{K}$
t_e	total simulation time, $[t_e] = \text{s}$
t	time, $[t] = \text{s}$
\vec{u}, \vec{u}_f	tree dimensional flow velocity, $[\vec{u}_f] = \text{m s}^{-1}$
u_r	relative velocity, $[u_r] = \text{m s}^{-1}$
V	volume, $[V] = \text{m}^3$
V_c	volume of cylinder, $[V_c] = \text{m}^3$
V_f	fluid volume, $[V_f] = \text{m}^3$
V_p	particle volume, $[V_p] = \text{m}^3$
v_p	particle velocity, $[v_p] = \text{m s}^{-1}$
\vec{x}	tree dimensional position vector, $[\vec{x}] = \text{m}$
Z	white noise

B Nomenclature

α_{CD}	correction factor for drag coefficient
ϵ	ratio R_d/R_v
γ	ratio of specific heats
λ	mean free path length, $[\lambda] = \text{m}$
λ_r	reference mean free path length, $[\lambda_r] = \text{m}$
μ	dynamic viscosity, $[\mu] = \text{kg m}^{-1} \text{s}^{-1}$
μ_f	fluid dynamic viscosity, $[\mu_f] = \text{kg m}^{-1} \text{s}^{-1}$
Φ_p	particle volume fraction
ρ	density, $[\rho] = \text{kg m}^{-3}$
ρ_p	particle density, $[\rho_p] = \text{kg m}^{-3}$
ρ_f	fluid density, $[\rho_f] = \text{kg m}^{-3}$
σ	Cauchy stress tensor, $[\sigma] = \text{N m}^{-2}$
σ_{ice}	surface tension of ice, $[\sigma_{ice}] = \text{N m}^{-2}$
τ	viscous stress tensor, $[\tau] = \text{N m}^{-2}$
τ_f	fluid response time, $[\tau_f] = \text{s}$
τ_p	particle response time, $[\tau_p] = \text{s}$
ζ_i	normally distributed Gaussian random number

C Mathematical notation

Vector

A three-dimensional vector is expressed as $\vec{x} = (x, y, z)^T \in \mathbb{R}^3$, where $x, y, z \in \mathbb{R}$ are the coordinates of the vector \vec{x} .

Matrix

A matrix A over \mathbb{R} is the arrangement of entries $a_{ij} \in \mathbb{R}$, where i denotes the row and j the column, in a rectangular scheme with m rows and n columns, $i, j, m, n \in \mathbb{N}$. For example, let $A = (a_{ij})$ be a 3×3 -matrix over \mathbb{R} with:

$$A = \begin{pmatrix} a_{11} & a_{12} & a_{13} \\ a_{21} & a_{22} & a_{23} \\ a_{31} & a_{32} & a_{33} \end{pmatrix}. \quad (\text{C.1})$$

Dyadic product

For two real vectors $\vec{a}, \vec{b} \in \mathbb{R}^3$, the dyadic product $\vec{a}\vec{b}^T \in \mathbb{R}^{3 \times 3}$ is calculated by:

$$\vec{a}\vec{b}^T = \begin{pmatrix} a_1 \\ a_2 \\ a_3 \end{pmatrix} (b_1, b_2, b_3) = \begin{pmatrix} a_1 b_1 & a_1 b_2 & a_1 b_3 \\ a_2 b_1 & a_2 b_2 & a_2 b_3 \\ a_3 b_1 & a_3 b_2 & a_3 b_3 \end{pmatrix}. \quad (\text{C.2})$$

Cross product

The cross product of two vectors $\vec{x} = (x_1, x_2, x_3)^T$, $\vec{y} = (y_1, y_2, y_3)^T \in \mathbb{R}^3$ is defined as:

$$\vec{x} \times \vec{y} = \det \begin{pmatrix} \vec{e}_1 & \vec{e}_2 & \vec{e}_3 \\ x_1 & x_2 & x_3 \\ y_1 & y_2 & y_3 \end{pmatrix} = \begin{pmatrix} x_2 \cdot y_3 - x_3 \cdot y_2 \\ x_3 \cdot y_1 - x_1 \cdot y_3 \\ x_1 \cdot y_2 - x_2 \cdot y_1 \end{pmatrix} \in \mathbb{R}^3. \quad (\text{C.3})$$

Gradient

Let $f : \mathbb{R}^3 \rightarrow \mathbb{R}$ be a partially differentiable function at a point \vec{x} , with $\vec{x} \in \mathbb{R}^3$. The gradient of f at \vec{x} is the vector of partial derivatives at \vec{x} , which is calculated by:

$$\nabla f(\vec{x}) = \begin{pmatrix} \frac{\partial f(\vec{x})}{\partial x_1} \\ \frac{\partial f(\vec{x})}{\partial x_2} \\ \frac{\partial f(\vec{x})}{\partial x_3} \end{pmatrix}, \quad (\text{C.4})$$

where $\nabla := (\partial x_1, \partial x_2, \partial x_3)^T$ is the Nabla operator. Furthermore, the gradient applied to a vector field \vec{u} , with $\vec{u} = (u_1, u_2, u_3)$, is called the vector gradient and is calculated by:

$$\nabla \vec{u} = \begin{pmatrix} \frac{\partial u_1}{\partial x_1} & \frac{\partial u_1}{\partial x_2} & \frac{\partial u_1}{\partial x_3} \\ \frac{\partial u_2}{\partial x_1} & \frac{\partial u_2}{\partial x_2} & \frac{\partial u_2}{\partial x_3} \\ \frac{\partial u_3}{\partial x_1} & \frac{\partial u_3}{\partial x_2} & \frac{\partial u_3}{\partial x_3} \end{pmatrix}. \quad (\text{C.5})$$

Divergence

Consider a differentiable vector field \vec{v} , with $\vec{v} = (v_1, v_2, v_3)^T$. The divergence operator is the scalar product of the Nabla operator ∇ with the vector field:

$$\nabla \cdot \vec{v} = \sum_{i=1}^3 \frac{\partial v_i}{\partial x_i} = \text{div } \vec{v}. \quad (\text{C.6})$$

The divergence of a matrix function $A : \mathbb{R}^{3 \times 3} \rightarrow \mathbb{R}^{3 \times 3}$ is applied in this thesis to the rows A_j of the matrix A , with entries a_{ij} with $i, j \in \mathbb{N}$ by

$$\nabla \cdot A = \begin{pmatrix} \nabla \cdot A_1 \\ \nabla \cdot A_2 \\ \nabla \cdot A_3 \end{pmatrix} = \begin{pmatrix} \nabla \cdot (a_{11} \ a_{12} \ a_{13})^T \\ \nabla \cdot (a_{21} \ a_{22} \ a_{23})^T \\ \nabla \cdot (a_{31} \ a_{32} \ a_{33})^T \end{pmatrix}. \quad (\text{C.7})$$

Laplace operator

Let $f : \mathbb{R}^3 \rightarrow \mathbb{R}$ be a differentiable function with first partial derivatives and $f \in C^2(\mathbb{R}^3)$. The Laplace operator of f is a second-order differential operator Δf with:

$$\Delta f = \text{div } \nabla f = \sum_{i=1}^3 \frac{\partial^2 f}{\partial x_i^2} = \frac{\partial^2 f}{\partial x_1^2} + \frac{\partial^2 f}{\partial x_2^2} + \frac{\partial^2 f}{\partial x_3^2}, \quad (\text{C.8})$$

where ∇ is the Nabla operator defined above.

D Mathematical formulas

Lemma: Integral average

Let $f \in C(\mathbb{R}^3)$ be a continuous function, $B_\epsilon(x) \subset \mathbb{R}^3$ an open ball with radius ϵ , centered at x . Then

$$\frac{1}{|B_\epsilon(x)|} \int_{B_\epsilon(x)} f(y) dy \rightarrow f(x) \text{ for } \epsilon \rightarrow 0. \quad (\text{D.1})$$

Gauss Theorem

Consider a volume $V \subset \Omega$ with a bounded domain $\Omega \subset \mathbb{R}^3$ with a Lipschitz-boundary S (i.e., the boundary of the domain can be described locally by a Lipschitz-continuous function), and the differentiable vector field \vec{u} . Let further be \vec{n} the outward unit normal vector to the boundary S . The Gauss theorem states that

$$\int_V \nabla \cdot \vec{u} dV = \int_S \vec{u} \cdot \vec{n} dS. \quad (\text{D.2})$$

Reynold's transport theorem

Consider a deformable (bounded) volume $V(t)$, surrounded by a boundary $S(t)$, where the volume contains a quantity $\Phi(\vec{x}, t) : V(t) \times [0, t] \rightarrow \mathbb{R}$. Let \mathcal{L} be the Lagrangian mapping between the reference and the actual material volume, $\mathcal{L} : (\xi, t) \in V_0 \rightarrow \vec{x}(\xi, t) \in V(t)$. Integrating $\Phi(\vec{x}, t)$ over the volume $V(t)$, and considering the temporal change of the integral, the result is:

$$\frac{\partial}{\partial t} \int_{V(t)} \Phi dV = \int_{V(t)} \frac{\partial \Phi}{\partial t} dV + \int_{S(t)} \Phi \vec{u} \cdot \vec{n} dS, \quad (\text{D.3})$$

where this equation D.3 is the Reynold's transport theorem with the outward normal unit vector \vec{n} to the surface $S(t)$, \vec{u} is the three-dimensional moving velocity, where $\vec{u} = \vec{u} \circ \mathcal{L}^{-1}(\vec{x})$, $\mathcal{L}^{-1}(\vec{x}) = \xi$, whereby $\vec{u}(\mathcal{L}^{-1}(\vec{x}), t) = \vec{u}(\xi, t) = \frac{d\vec{x}}{dt}(\xi, t)$, and \vec{x} is the three-dimensional position vector, and t is the time.

Law of reflection

To derive the law of reflection (equation 3.15):

$$\hat{v} = \hat{v}_c - 2(\hat{v}_c \cdot \hat{n})\hat{n}$$

defined as a boundary condition on surfaces of the instrument module for particles, let us assume a particle velocity \vec{v}_c immediately before collision with a surface. Furthermore, let \vec{v} be the reflected particle velocity and \vec{n} the normal vector to the surface. ϕ is the angle between the incident particle velocity and the normal vector (i.e., angle of incidence), while $\phi = \phi'$ is the angle of reflection [Tipler, P. A. and Mosca, 2014]. Moreover, let \hat{v}_c , \hat{v} , and \hat{n} be the normed unit vectors of the incidence particle velocity, the reflected particle velocity and the normal vector to the surface as illustrated in Figure D.1, where the length of the three given vectors are denoted by $v_c = \|\vec{v}_c\|$, $v = \|\vec{v}\|$ and $n = \|\vec{n}\|$.

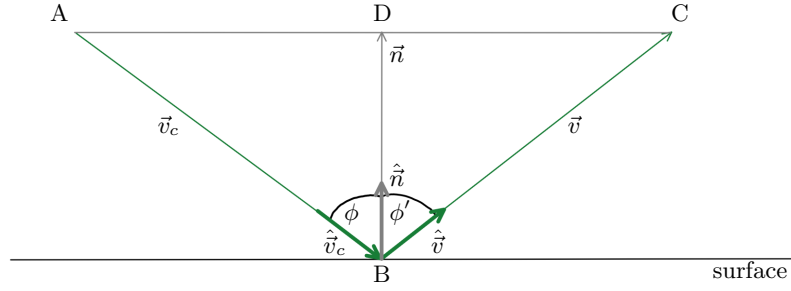


Figure D.1: Particle reflection on a surface.

The following equations result from the vector addition:

$$\overrightarrow{AB} + \overrightarrow{BD} = \overrightarrow{AD}, \text{ and } \overrightarrow{DB} + \overrightarrow{BC} = \overrightarrow{DC}. \quad (\text{D.4})$$

It holds that $\overrightarrow{AD} \approx \overrightarrow{DC}$, where \approx denotes the equivalency on the sense of orientation and size of the vectors, and thus:

$$\overrightarrow{AB} + \overrightarrow{BD} \approx \overrightarrow{DB} + \overrightarrow{BC}. \quad (\text{D.5})$$

Furthermore, $\overrightarrow{AB} = \hat{v}_c v_c$, $\overrightarrow{BC} = \hat{v} v$, $\overrightarrow{BD} = v_c \cos(\phi) \hat{n}$, and $\overrightarrow{DB} = -\overrightarrow{BD} = -v_c \cos(\phi) \hat{n}$. Substituting the expressions in equation D.5, following equivalency yields:

$$\hat{v}_c v_c + v_c \cos(\phi) \hat{n} \approx -v_c \cos(\phi) \hat{n} + \hat{v} v, \quad (\text{D.6})$$

D Mathematical formulas

where $v_c = v$ holds (due to the conservation of the particle kinetic energy of the reflection [COMSOL[®], 2022]). Under consideration of the scalar product of $\vec{v}_c \cdot (-\vec{n})$, the expression of $\cos(\phi)$ can be expressed as $\cos(\phi) = \hat{v}_c \cdot (-\hat{n})$. Finally, from D.6 \hat{v} can be obtained under the consideration of the equivalency of the vectors \overrightarrow{AD} and \overrightarrow{DC} , which results in:

$$\hat{v} = \hat{v}_c + 2 \cos(\phi) \hat{n} = \hat{v}_c - 2(\hat{v}_c \cdot \hat{n}) \hat{n}. \quad (\text{D.7})$$

E Formulas of material properties

Partial pressure of water vapor

Following equation is used to determine the partial pressure of environmental water vapor p_v [Lohmann, U. et al., 2016]:

$$p_v = \frac{p q_v}{\epsilon + q_v}, \quad (\text{E.1})$$

where p is the environmental pressure, q_v is the environmental water vapor mixing ratio, and $\epsilon = \frac{R_d}{R_v}$, where R_d is the gas constant of dry air and R_v is the gas constant of water vapor.

Saturation pressure over a curved ice crystal

To determine the saturation pressure over a curved ice crystal p_s , following equation is applied [Lohmann, U. et al., 2016]:

$$p_s = \frac{2 p_{ice}(T_{ice}) \exp(2 \sigma_{ice}(T_{ice}))}{R_v \rho T_{ice} d}, \quad (\text{E.2})$$

where $p_{ice}(T_{ice})$ is the saturation vapor pressure for ice [Murphy, D. M. and Koop, 2005], T_{ice} is the surface temperature of the ice particle, $\sigma_{ice}(T_{ice})$ is the surface tension of ice [Ketcham, W. M. and Hobbs, 1969], ρ is the density of liquid water, and d is the diameter of the ice particle.

Change in ice crystal temperature

The change in ice crystal surface temperature (T_{ice}) with time t is determined by following equation [Lohmann, U. et al., 2016]:

$$\frac{dT_{ice}}{dt} = \frac{L_s \frac{dm_{ice}}{dt} + 2\pi d k (T_{air} - T_{ice})}{m_{ice} c_{ice}}, \quad (\text{E.3})$$

E Formulas of material properties

where L_s is the latent heat for the sublimation, m_{ice} is the mass of the ice particle, k is the thermal conductivity in air, T_{air} is the ambient temperature, and c_{ice} is the specific heat capacity of ice.

F Determination of particle numbers

To define the boundary condition for the planar particle inlet regions the particle number concentration C per cm^{-3} has to be translated into a total number of particles as implemented in the COMSOL[®] particle tracking module. Following considerations are conducted: First, a circular particle inlet of diameter d perpendicular to the flow and upstream of the impactor surfaces is applied. Subsequently, the volume of air V_c inside a cylinder of the base area with diameter d and an exemplary height $l_c = 1$ cm is calculated as

$$V_c = \pi \left(\frac{d}{2} \right)^2 l_c. \quad (\text{F.1})$$

Then, the number of particles N_c within the volume V_c yields

$$N_c = V_c C. \quad (\text{F.2})$$

The length of the cylinder l_c is divided by the incident flow velocity u to obtain the time t_c required for an air molecule to travel from the particle inlet through the cylinder of length l_c :

$$t_c = \frac{l_c}{u}. \quad (\text{F.3})$$

Thus, during the whole simulation time t_e , the released particles ideally fill a cylindrical volume of a total length $l_e = \frac{l_c t_e}{t_c}$ and correspondingly the total number of particles N released at a circular particle inlet surface during the simulation time t_e is:

$$N = N_c \frac{t_e}{t_c} = V_c C \frac{t_e u}{l_c} = \pi \left(\frac{d}{2} \right)^2 C t_e u. \quad (\text{F.4})$$

Note that the total number of particles can be released in several different time steps.

G Tables of simulation data

Calculated flow velocities evaluated on cut line 1 and cut line 2 (cf. Section 3.4.3) in the vicinity of the vehicle's fuselage are given for the incident flow velocity of 300 m s^{-1} in Table G.1 and for the incident flow velocity of 400 m s^{-1} in Table G.2, respectively. Furthermore, flow velocities evaluated on cut lines 1, 2 and 3 (cf. Section 3.4.3) are given in Tables G.3 and G.4 for the incident flow velocity of 300 m s^{-1} and in Tables G.5 and G.6 for the incident flow velocity of 400 m s^{-1} . Since the flow velocities are evaluated at mesh nodes and the generated mesh is not symmetrical with respect to the spatial directions, various distance values are given starting from the vehicle's fuselage at 0 mm . The distance values are given in mm and velocity values are given in m s^{-1} and are divided into values evaluated in positive x -axis orientation (v^+) and values evaluated in negative x -axis direction (v^-). Here, the distance values in negative x -axis direction are given as absolute values.

Table G.1: Flow velocity values (v_{line1}^- , v_{line1}^+ , v_{line2}^- , v_{line2}^+) evaluated at node points for cut lines 1 and 2 for the incident velocity of 300 m s^{-1} . Velocity values are divided into evaluations along the positive axis direction (v^+), starting from the vehicle's fuselage at 0 mm , and evaluations along the axis direction in the negative direction (v^- , where distance values are given as absolute values).

distance / mm	v_{line2}^- / m s^{-1}	distance / mm	v_{line2}^+ / m s^{-1}	distance / mm	v_{line1}^- / m s^{-1}	distance / mm	v_{line1}^+ / m s^{-1}
0.00	0.00	0.00	0.00	0.00	0.00	0.00	0.00
12.75	63.68	2.58	15.88	6.84	43.27	9.02	52.86
15.68	78.29	2.62	16.12	7.01	44.33	9.09	53.22
15.72	78.48	9.25	56.89	9.81	62.06	12.53	73.41
15.76	78.71	9.30	57.16	9.82	62.13	12.55	73.50
30.82	137.05	12.10	72.88	17.67	110.89	23.26	132.45
34.32	150.64	12.32	74.09	18.17	113.96	23.44	133.46

G Tables of simulation data

Continued Table G.1 from page 149

distance / mm	v_{line2}^- / m s ⁻¹	distance / mm	v_{line2}^+ / m s ⁻¹	distance / mm	v_{line1}^- / m s ⁻¹	distance / mm	v_{line1}^+ / m s ⁻¹
34.43	151.03	20.28	118.77	21.55	135.02	27.52	155.91
34.56	151.54	20.40	119.47	21.59	135.25	27.53	155.95
34.60	151.69	20.45	119.75	21.60	135.29	27.61	156.44
35.76	155.87	23.80	137.63	23.07	144.29	29.27	165.52
35.77	155.92	23.85	137.95	23.08	144.34	29.28	165.56
35.80	156.04	27.86	156.84	23.09	144.39	29.29	165.61
35.85	156.22	28.02	157.59	24.86	155.07	29.40	166.16
37.24	161.41	35.26	185.62	24.87	155.12	31.38	176.22
37.29	161.62	35.48	186.45	24.89	155.25	31.39	176.27
37.36	161.82	35.85	187.78	24.95	155.49	31.43	176.43
37.44	162.04	46.67	223.21	26.05	160.44	31.74	177.84
39.65	168.32	48.22	228.30	29.13	174.27	36.95	201.45
41.22	171.99	48.70	229.26	33.11	188.32	38.41	207.86
42.39	175.19	54.37	242.29	40.25	216.34	49.16	255.06
45.82	184.56	60.96	257.45	41.16	219.94	51.89	259.47
56.42	213.27	69.27	266.48	49.94	254.51	56.32	263.64
61.85	222.59	74.25	271.30	57.09	270.42	64.84	273.48
64.14	226.77	77.63	274.58	57.12	270.50	77.20	287.73
67.08	232.12	94.89	292.03	63.54	279.63	87.73	299.74
71.94	238.09	117.02	297.12	86.64	297.59	99.17	302.38
97.52	266.37	118.34	297.43	93.49	300.73	111.31	305.85
102.99	271.54	121.64	298.43	94.12	301.02	115.25	306.60
104.78	272.96	127.35	299.51	109.66	306.66	124.10	308.29
113.89	280.19	137.14	301.70	132.20	307.10		
138.24	288.75	142.59	302.14	143.82	307.33		
145.02	291.12			146.33	307.35		
152.51	293.73						
162.24	295.28						
165.68	295.89						
166.78	295.99						

G Tables of simulation data

Continued Table G.1 from page 149

distance / mm	v_{line2}^- / m s ⁻¹	distance / mm	v_{line2}^+ / m s ⁻¹	distance / mm	v_{line1}^- / m s ⁻¹	distance / mm	v_{line1}^+ / m s ⁻¹
166.94	296.01						

Table G.2: Flow velocity values evaluated at node points for cut lines 1 and 2 for the incident flow velocity of 400 m s⁻¹. Velocity values are divided into evaluations along the positive axis direction (v^+), starting from the vehicle's fuselage at 0 mm, and evaluations along the axis direction in the negative direction (v^- , where distance values are given as absolute values).

distance / mm	v_{line1}^- / m s ⁻¹	distance / mm	v_{line1}^+ / m s ⁻¹	distance / mm	v_{line2}^- / m s ⁻¹	distance / mm	v_{line2}^+ / m s ⁻¹
0.00	0.00	0.00	0.00	0.00	0.00	0.00	0.00
9.33	81.55	5.38	46.62	7.10	47.63	5.10	41.75
11.35	99.14	10.89	93.63	7.14	47.92	8.40	68.82
16.19	142.95	11.91	102.34	7.25	48.68	11.35	93.63
19.10	169.27	20.89	175.72	7.31	49.07	13.12	108.48
20.61	179.60	28.46	225.95	20.46	138.57	15.68	128.88
20.81	180.97	31.01	243.67	29.16	176.15	17.10	137.36
28.14	229.31	31.87	249.67	29.59	177.95	24.07	178.96
36.60	283.49	33.44	256.60	36.60	205.86	25.59	187.62
37.63	286.84	36.96	272.17	37.03	207.60	30.73	215.07
44.45	309.24	45.61	311.38	41.67	226.80	35.65	241.34
53.62	337.11	47.17	316.31	48.76	246.65	35.71	241.70
54.52	339.66	50.36	326.22	49.01	247.37	35.74	241.81
56.28	343.59	53.26	334.18	51.00	252.48	36.05	242.95
65.05	363.32	57.48	345.73	51.30	253.28	37.97	249.99
66.96	367.07	68.93	361.89	56.45	267.02	40.74	260.16
68.48	370.07	72.39	367.05	65.62	287.44	43.05	268.39
68.75	370.61	73.62	368.91	81.27	317.05	43.40	269.64
72.59	373.92	76.18	372.48	83.69	321.82	45.99	278.90
73.64	374.41	76.20	372.52	89.84	334.14	52.63	302.43
83.56	379.08	80.31	378.99	90.67	335.23	55.35	308.85

G Tables of simulation data

Continued Table G.2 from page 151

distance / mm	v_{line1}^- / m s ⁻¹	distance / mm	v_{line1}^+ / m s ⁻¹	distance / mm	v_{line2}^- / m s ⁻¹	distance / mm	v_{line2}^+ / m s ⁻¹
91.38	382.97	82.65	380.91	95.49	340.00	55.75	309.59
94.29	384.19	82.67	380.93	97.06	341.60	59.42	316.39
100.46	386.79	85.51	382.15	98.85	343.43	70.57	334.25
117.87	385.81	92.70	383.41	100.13	344.68	73.35	338.84
118.55	385.78	96.72	384.11	113.52	358.30	77.88	346.33
118.96	385.77	101.48	384.46	120.00	364.93	79.27	348.61
119.54	385.80	104.94	384.86	121.54	366.49	80.24	350.18
126.46	386.51	119.24	386.56	122.69	367.11	81.92	351.88
129.57	386.83	122.97	386.76	129.38	370.79	86.57	356.59
134.80	385.92	123.70	386.80	132.12	371.72	98.44	367.17
138.76	385.24	131.83	385.90	147.80	374.24	102.64	369.50
143.27	384.41	132.80	385.80	154.71	375.37	108.54	372.78
145.95	383.61	139.71	385.09	161.42	376.38	121.62	377.65
152.58	381.91	145.11	383.95	167.29	376.93	124.70	377.95
166.15	378.45	163.58	379.60	167.59	376.95	132.99	378.81
166.74	378.30	182.21	375.97	177.19	377.21	135.33	379.06
166.79	378.28	183.05	375.79	187.94	376.96	143.75	379.43
166.85	378.27	184.01	375.60	191.07	376.92	144.04	379.47
194.99	373.55	185.52	375.29	215.97	376.68	147.66	379.48
208.25	370.81	191.97	373.95	253.00	375.87	155.39	379.53
208.47	370.77	202.59	371.76	257.50	375.84	162.13	378.38
208.55	370.75	212.39	369.74	265.89	375.78	178.36	377.00
216.32	368.91	213.51	369.62	269.67	375.76	183.04	376.59
221.91	368.65	219.53	368.96	270.35	375.79	183.25	376.57
222.33	368.63	227.89	368.06	270.98	375.84	193.41	375.70
258.03	368.25	239.19	367.23	271.56	375.92	193.71	375.66
268.37	368.04	245.61	366.75	272.68	376.07	198.59	374.94
278.16	368.45	252.76	366.98	278.20	376.54	202.53	374.36
283.77	368.54	254.23	367.05	280.47	376.72	217.66	372.12
289.24	368.42	254.69	367.07	305.21	377.61	222.29	371.45
321.55	369.83	255.95	367.18	320.87	378.18	224.09	371.43

G Tables of simulation data

Continued Table G.2 from page 151

distance / mm	v_{line1}^- / m s ⁻¹	distance / mm	v_{line1}^+ / m s ⁻¹	distance / mm	v_{line2}^- / m s ⁻¹	distance / mm	v_{line2}^+ / m s ⁻¹
328.38	370.18	266.26	367.82	340.14	378.91	245.15	371.01
338.16	370.67	283.93	368.82	344.19	379.14	260.91	370.92
341.56	370.94	303.13	369.38	348.64	379.43	272.00	371.25
342.44	371.02	310.47	369.91	374.46	381.01	277.81	371.35
343.44	371.04	332.99	371.15	384.57	381.53	289.25	371.55
343.91	371.06	335.56	371.30	389.68	381.79	300.30	371.82
346.56	371.16	338.14	371.39	415.44	382.41	310.05	371.90
358.59	371.83	349.49	371.80	419.78	382.52	311.84	371.85
386.12	373.38	363.54	372.45			315.52	371.93
394.65	373.49	366.69	372.60			329.93	372.43
396.68	373.52	381.02	373.05			365.20	373.93
398.27	373.55	384.91	373.22			365.44	373.94
408.67	373.57	387.85	373.32			367.06	374.01
416.60	373.58	399.81	373.56			377.25	374.10
417.15	373.59	405.73	373.67			396.32	374.26
417.83	373.59	406.70	373.68			396.84	374.27
419.17	373.60	410.49	373.77			397.82	374.26
						410.82	374.27

Table G.3: Flow velocity values evaluated at node points for cut lines 1, 2, and 3 for the incident flow velocity of 300 m s⁻¹. Evaluation of velocity values is in positive axis direction (v^+), starting from the vehicle's fuselage at 0 mm.

distance / mm	v_{line1}^+ / m s ⁻¹	distance / mm	v_{line2}^+ / m s ⁻¹	distance / mm	v_{line3}^+ / m s ⁻¹
0.00	0.00	0.00	0.00	0.00	0.00
1.10	7.40	1.51	7.68	0.92	5.72
2.41	16.45	2.13	10.86	2.89	19.51
2.62	17.87	3.79	19.32	2.93	19.79
2.77	18.93	3.79	19.32	3.01	20.38
4.06	27.85	5.59	28.31	3.98	27.09

G Tables of simulation data

Continued Table G.3 from page 153

distance / mm	v_{line1}^+ / m s ⁻¹	distance / mm	v_{line2}^+ / m s ⁻¹	distance / mm	v_{line3}^+ / m s ⁻¹
5.64	38.75	5.59	28.31	6.36	43.70
5.88	40.46	8.33	41.94	6.40	44.02
6.06	41.72	8.33	41.94	6.50	44.72
7.61	52.40	10.50	52.34	7.63	52.52
9.50	65.39	10.50	52.34	10.51	72.40
9.80	67.43	13.79	68.13	10.57	72.77
10.02	68.93	13.79	68.13	10.69	73.60
11.88	81.59	16.39	80.01	12.01	82.54
14.14	96.99	16.39	80.01	15.50	106.21
14.50	99.39	20.33	98.05	15.57	106.63
14.76	101.16	20.33	98.05	15.71	107.61
17.00	115.91	23.45	111.30	17.24	117.58
19.71	133.79	23.45	111.30	21.49	145.20
20.14	136.58	28.19	131.43	21.56	145.67
20.44	138.61	28.19	131.43	21.74	146.79
23.14	155.18	31.93	145.61	23.50	157.36
26.40	175.22	31.93	145.61	28.68	188.32
26.90	178.33	37.61	167.16	28.76	188.81
27.27	180.59	37.61	167.16	28.97	190.05
30.51	198.03	42.10	181.39	30.98	200.26
34.42	219.09	42.10	181.39	37.30	232.27
35.03	222.34	48.92	203.02	37.39	232.74
35.46	224.69	48.92	203.03	37.64	234.01
39.36	240.86	54.30	216.16	39.91	242.30
44.05	260.35	54.30	216.16	47.65	270.62
44.77	263.34	62.49	236.15	47.75	271.00
45.29	265.49	62.49	236.15	48.05	272.09
46.41	268.63	62.49	236.15	48.17	272.39
46.49	268.85	64.47	240.26	48.34	272.82
49.16	275.82	66.33	244.12	48.45	273.09
49.91	277.77	69.88	251.21	48.69	273.67

G Tables of simulation data

Continued Table G.3 from page 153

distance / mm	v_{line1}^+ / m s ⁻¹	distance / mm	v_{line2}^+ / m s ⁻¹	distance / mm	v_{line3}^+ / m s ⁻¹
51.81	282.88	70.59	252.50	54.39	287.47
52.82	284.72	74.58	258.21	56.68	291.50
53.40	285.88	76.38	260.79	57.07	292.18
56.51	292.12	77.13	261.92	57.09	292.22
57.24	293.15	79.36	265.23	58.40	294.07
59.78	296.83	82.23	268.41	61.69	298.74
62.10	299.39	82.77	269.00	64.12	301.76
63.84	301.30	89.75	276.82	67.46	304.73
66.19	303.98	91.49	278.22	68.43	305.38
67.35	304.79	95.47	281.00	74.66	309.29
68.43	305.54	104.63	286.34	82.09	312.35
72.00	308.16	104.69	286.38	83.57	312.96
73.49	309.20	104.90	286.47	84.60	313.34
76.41	310.40	110.78	288.95	85.90	313.66
81.05	312.35	117.93	291.97	88.81	314.41
82.58	312.97	118.95	292.27	89.87	314.57
84.27	313.65	119.53	292.44	102.91	316.53
86.38	314.11	121.50	292.81	106.54	316.99
88.48	314.56	125.23	293.50	106.75	317.00
94.14	315.69	126.77	293.80	107.04	317.02
97.93	316.35	131.59	294.45	107.20	317.03
99.22	316.38	140.71	295.68	117.75	317.64
104.37	316.76	143.30	295.68	122.05	317.88
112.65	317.45	146.66	295.67	122.58	317.91
116.88	317.84	154.81	295.68	122.94	317.93
117.60	317.90	161.68	295.48	126.11	317.86
120.50	318.02	163.05	295.44	137.13	317.60
120.78	318.03	164.59	295.30	139.34	317.62
123.59	317.92	175.92	294.23	146.29	317.69
137.43	318.25	181.46	293.69	150.65	317.67
140.47	318.30	182.78	293.55	157.15	317.03

G Tables of simulation data

Continued Table G.3 from page 153

distance / mm	v_{line1}^+ / m s ⁻¹	distance / mm	v_{line2}^+ / m s ⁻¹	distance / mm	v_{line3}^+ / m s ⁻¹
140.62	318.30	187.84	293.01	163.52	316.72
141.08	318.30	195.41	292.14	167.09	316.41
141.44	318.29	196.37	292.03	173.51	316.03
141.76	318.29	198.94	291.75	180.69	315.57
164.95	317.01	222.24	289.42	190.82	314.50
166.34	316.96	227.96	288.76	191.30	314.45
166.73	316.92	231.13	288.39	191.48	314.43
170.78	316.49	237.78	287.60	193.05	314.31
178.81	315.95	252.73	286.01	195.74	314.09
179.87	315.86	255.96	285.67	204.32	313.41
185.66	315.39	261.66	285.07	204.69	313.38
188.72	315.06	277.60	283.46	207.94	313.14
190.47	314.87	284.70	282.77	208.01	313.13
194.32	314.66	285.35	282.71	208.17	313.12
196.95	314.37	302.22	281.13	211.79	312.63
200.37	313.83	330.61	279.11	214.94	312.16
205.89	312.94	349.71	277.54	216.77	311.89
211.65	312.12	350.18	277.51	228.44	310.20
212.33	312.02	354.11	277.22	235.21	309.34
215.73	311.70	354.89	277.18	237.16	309.14
218.58	311.49	362.28	276.82	246.91	307.87
219.30	311.43	364.14	276.73	248.17	307.71
224.48	310.72	368.82	276.43	249.45	307.53
228.77	310.24	394.70	274.79	254.01	306.98
229.67	310.14	399.03	274.52	256.85	306.64
232.08	309.85	402.13	274.48	261.15	305.82
234.66	309.55	408.80	274.30	264.35	305.35
243.76	308.19	408.88	274.30	264.41	305.34
249.46	307.67	408.90	274.30	277.02	303.79
255.25	307.26			277.07	303.78
260.29	306.40			280.10	303.43

G Tables of simulation data

Continued Table G.3 from page 153

distance / mm	v_{line1}^+ / m s ⁻¹	distance / mm	v_{line2}^+ / m s ⁻¹	distance / mm	v_{line3}^+ / m s ⁻¹
263.17	306.08			285.46	302.72
263.55	306.07			288.25	302.33
265.18	305.85			288.42	302.31
280.63	303.54			296.30	301.18
281.16	303.46			302.29	300.41
286.28	302.84			304.78	300.08
288.16	302.58			314.96	298.59
290.47	302.23			318.32	298.10
291.53	302.06			318.56	298.07
292.10	301.98			323.43	297.41
296.97	301.28			327.35	296.88
308.23	299.66			328.02	296.80
311.67	299.18			333.37	296.17
313.81	298.87			343.77	294.96
315.25	298.72			348.56	294.24
317.71	298.40			351.99	293.87
318.36	298.31			357.86	293.04
319.06	298.21			361.44	292.53
332.50	296.26			364.05	292.16
333.54	296.11			368.41	291.64
335.48	295.82			371.16	291.31
335.99	295.75			378.14	290.52
336.68	295.67			379.08	290.38
339.28	295.36			379.72	290.28
350.26	294.00			385.04	289.71
351.51	293.84			390.15	289.15
355.05	293.40			395.00	288.59
356.88	293.19			398.51	288.20
358.05	293.05			399.12	288.13
365.90	291.94			399.58	288.07
370.74	291.37			399.91	288.04

G Tables of simulation data

Continued Table G.3 from page 153

distance / mm	v_{line1}^+ / m s ⁻¹	distance / mm	v_{line2}^+ / m s ⁻¹	distance / mm	v_{line3}^+ / m s ⁻¹
377.19	290.53			400.16	288.01
381.75	289.90			403.42	287.68
383.75	289.70				
389.09	289.15				
391.67	288.91				
393.26	288.75				
403.66	287.70				
406.43	287.37				
407.24	287.27				

Table G.4: Flow velocity values evaluated at node points for cut lines 1, 2, and 3 for the incident flow velocity of 300 m s⁻¹. Evaluation of velocity values is in negative axis direction (v^- , where distance values are given as absolute values), starting from the vehicle's fuselage at 0 mm.

distance / mm	v_{line1}^- / m s ⁻¹	distance / mm	v_{line2}^- / m s ⁻¹	distance / mm	v_{line3}^- / m s ⁻¹
0.00	0.00	0.00	0.00	0.00	0.00
1.89	12.55	1.34	5.68	1.09	6.89
2.15	14.30	3.24	13.77	2.43	15.79
2.21	14.69	3.24	13.78	2.64	17.13
2.52	16.70	3.24	13.78	2.74	17.83
4.82	31.74	4.85	20.37	3.99	26.07
5.14	33.83	7.14	29.79	5.61	36.70
5.21	34.29	7.14	29.79	5.85	38.31
5.58	36.72	7.14	29.79	5.98	39.15
8.34	54.53	9.06	37.38	7.48	48.84
8.72	56.99	11.81	48.22	9.41	61.36
8.80	57.54	11.81	48.23	9.71	63.26
9.25	60.42	11.81	48.23	9.86	64.27
12.56	81.38	14.12	56.87	11.66	75.58

G Tables of simulation data

Table G.1 Continued

distance / mm	v_{line1}^- / m s ⁻¹	distance / mm	v_{line2}^- / m s ⁻¹	distance / mm	v_{line3}^- / m s ⁻¹
13.02	84.27	17.41	69.21	13.98	90.21
13.12	84.91	17.41	69.22	14.34	92.44
13.66	88.31	17.41	69.23	14.52	93.62
17.63	112.64	20.18	78.93	16.68	106.6
18.17	115.96	24.13	92.77	19.46	123.44
18.30	116.70	24.14	92.79	19.89	126.00
18.94	120.66	24.14	92.80	20.12	127.38
23.72	148.14	27.46	103.45	22.69	141.86
24.36	151.85	32.20	118.64	26.04	160.67
24.51	152.68	32.21	118.68	26.55	163.55
25.29	157.18	32.21	118.69	26.83	165.11
31.02	186.66	36.20	130.04	29.91	180.33
31.79	190.59	41.88	146.23	33.93	200.19
31.96	191.48	41.89	146.28	34.54	203.23
32.90	196.33	41.90	146.29	34.88	204.89
39.79	224.82	46.68	158.03	38.57	219.33
40.70	228.56	53.49	174.76	43.40	238.22
40.90	229.40	53.51	174.83	44.13	241.11
42.04	234.12	53.52	174.84	44.55	242.73
43.70	239.52	53.53	174.85	45.19	244.86
44.29	241.28	60.70	190.99	45.72	246.35
50.20	257.83	65.15	200.72	47.92	252.42
53.70	267.91	79.23	224.09	48.12	252.98
55.64	271.22	79.25	224.12	52.09	264.10
57.21	274.07	80.80	226.90	54.02	267.91
65.76	286.30	83.39	230.92	54.31	268.47
67.00	288.07	84.17	232.14	60.13	279.65
67.57	288.89	84.21	232.19	61.06	281.12
68.12	289.56	84.87	233.13	63.01	283.38
68.62	290.09	100.98	255.29	69.28	290.81
70.86	291.85	101.23	255.62	71.48	293.29

G Tables of simulation data

Table G.1 Continued

distance / mm	v_{line1}^- / m s ⁻¹	distance / mm	v_{line2}^- / m s ⁻¹	distance / mm	v_{line3}^- / m s ⁻¹
78.86	298.38	102.10	256.79	72.84	294.59
79.41	298.83	102.68	257.30	73.50	295.02
80.47	299.36	104.61	259.01	82.33	300.83
85.68	301.99	114.73	268.82	84.33	301.98
86.20	302.26	117.18	271.15	87.97	303.66
91.84	305.04	119.78	272.62	95.13	306.35
97.16	307.05	122.03	273.94	95.46	306.47
97.61	307.23	133.10	280.23	100.36	308.12
99.04	307.63	137.16	282.61	101.43	308.41
107.26	309.99	141.91	284.03	101.53	308.44
110.34	310.61	154.92	287.79	102.63	308.65
111.10	310.77	155.53	287.95	102.73	308.67
112.14	310.94	156.35	288.18	113.80	310.82
113.75	311.19	157.05	288.33	117.73	311.57
114.75	311.34	158.19	288.59	119.09	311.75
122.89	312.58	158.54	288.67	125.93	312.77
130.10	313.23	158.66	288.68	128.82	313.17
133.79	313.60	159.60	288.71	131.03	313.35
146.65	314.48	162.27	288.82	137.69	313.74
146.97	314.50	166.35	288.99	140.06	313.91
148.11	314.52	167.99	289.06	144.37	314.23
152.75	314.73	172.65	289.28	146.71	314.35
156.17	314.78	183.38	289.89	153.83	314.70
162.56	314.87	188.01	289.88	159.18	314.71
167.39	314.95	192.99	289.76	159.37	314.71
170.54	314.93	199.16	289.61	159.77	314.71
171.41	314.93	208.76	289.15	163.76	314.72
177.73	314.84	217.40	288.53	163.92	314.72
183.70	314.76	231.45	287.40	164.09	314.73
187.56	314.67	236.26	287.04	166.33	314.76
190.60	314.55	242.96	286.55	174.87	314.79

G Tables of simulation data

Table G.1 Continued

distance / mm	v_{line1}^- / m s ⁻¹	distance / mm	v_{line2}^- / m s ⁻¹	distance / mm	v_{line3}^- / m s ⁻¹
195.94	314.34	255.06	285.68	180.18	314.79
202.90	314.06	259.88	285.33	180.37	314.79
206.73	313.74	264.17	285.01	181.27	314.75
210.24	313.37	265.98	284.89	187.00	314.50
214.00	312.97	285.74	283.44	187.61	314.48
218.46	312.60	286.36	283.40	191.68	314.33
223.52	312.18	299.63	282.47	200.27	314.07
227.14	311.81	302.67	282.26	203.25	313.98
231.26	311.30	311.24	281.78	205.76	313.93
236.56	311.05	326.59	280.91	209.99	313.72
243.54	310.29	329.81	280.71	215.82	313.30
246.55	309.86	336.06	280.32	224.54	312.66
252.94	308.95	339.53	280.11	227.62	312.39
256.88	308.64	342.05	280.02	228.12	312.36
260.63	308.35	359.59	279.33	229.52	312.29
261.62	308.22	380.40	278.51	229.96	312.25
264.80	307.64	382.00	278.45	230.2	312.24
267.04	307.17	392.59	278.08	230.27	312.24
272.25	306.09	403.36	277.46	235.02	311.62
275.50	305.70	411.46	277.44	235.16	311.6
291.06	303.91			252.43	309.37
291.25	303.88			262.20	308.19
296.26	302.89			264.79	307.76
300.09	302.42			268.99	307.17
307.08	301.57			271.54	306.92
309.83	301.28			274.81	306.41
312.94	300.85			282.14	305.16
320.51	299.77			286.20	304.46
329.62	298.46			300.65	302.46
331.49	298.18			300.76	302.44
333.80	297.84			300.86	302.43

G Tables of simulation data

Table G.1 Continued

distance / mm	v_{line1}^- / m s ⁻¹	distance / mm	v_{line2}^- / m s ⁻¹	distance / mm	v_{line3}^- / m s ⁻¹
335.24	297.62			302.48	302.19
339.25	296.98			304.00	301.98
343.09	296.38			305.66	301.76
346.35	295.89			306.29	301.67
346.75	295.85			318.39	299.70
350.59	295.49			322.04	299.28
360.72	294.22			325.67	298.76
368.59	293.15			329.49	298.24
374.54	292.41			338.49	297.00
374.63	292.39			341.97	296.45
375.33	292.31			353.73	294.98
376.88	292.12			354.84	294.84
381.60	291.51			363.72	293.72
382.60	291.38			363.93	293.70
389.10	290.66			364.16	293.67
392.14	290.31			372.25	292.6
393.31	290.18			374.06	292.36
399.68	289.46			377.58	291.92
403.30	289.04			379.45	291.69
407.20	288.58			381.68	291.43
				388.86	290.61
				392.50	290.17
				394.06	289.98
				409.64	288.3
				409.82	288.28
				411.31	288.13

G Tables of simulation data

Table G.5: Flow velocity values in m s^{-1} evaluated at node points for cut lines 1, 2, and 3 for the incident flow velocity of 400 m s^{-1} . Evaluation of velocity values is in positive axis direction (v^+), starting from the vehicle's fuselage at 0 mm.

distance / mm	v_{line1}^+ / m s^{-1}	distance / mm	v_{line2}^+ / m s^{-1}	distance / mm	v_{line3}^+ / m s^{-1}
0.00	0.00	0.00	0.00	0.00	0.00
1.48	13.79	3.08	20.83	0.16	0.62
2.73	25.97	3.08	20.84	2.60	24.56
2.89	27.49	3.22	21.80	2.80	26.43
2.97	28.28	3.22	21.80	2.81	26.56
4.70	44.81	6.91	46.01	2.89	27.31
6.17	58.75	6.91	46.06	5.83	55.51
6.35	60.50	7.08	47.18	6.05	57.67
6.44	61.36	7.08	47.18	6.07	57.83
8.60	81.46	11.50	75.07	6.17	58.73
10.29	97.13	11.51	75.16	9.70	91.72
10.51	99.12	11.72	76.46	9.96	94.19
10.60	100.03	11.72	76.46	9.98	94.38
13.33	124.39	17.01	108.25	10.10	95.47
15.25	141.57	17.03	108.41	14.34	133.69
15.50	143.80	17.28	109.89	14.65	136.46
15.60	144.73	17.28	109.89	14.68	136.70
19.07	173.96	23.61	145.56	14.83	137.98
21.21	191.97	23.66	145.81	19.92	181.42
21.50	194.40	23.96	147.48	20.27	184.45
21.60	195.28	23.96	147.49	20.31	184.74
26.08	229.43	31.54	186.54	20.50	186.21
28.37	246.85	31.61	186.89	26.62	233.86
28.70	249.37	31.96	188.74	27.03	237.03
28.80	250.12	31.97	188.75	27.07	237.39
34.71	287.30	41.04	229.98	27.31	238.95
36.98	301.58	41.14	230.45	34.66	287.51
37.36	303.95	41.57	232.43	35.13	290.58

G Tables of simulation data

Continued Table G.5 from page 163

distance / mm	v_{line1}^+ / m s ⁻¹	distance / mm	v_{line2}^+ / m s ⁻¹	distance / mm	v_{line3}^+ / m s ⁻¹
37.44	304.47	41.58	232.44	35.19	290.97
45.46	338.66	52.42	274.09	35.48	292.43
47.34	346.64	52.58	274.70	44.32	335.73
47.76	348.44	53.11	276.72	44.85	338.30
47.81	348.66	53.11	276.73	44.93	338.69
47.93	348.99	53.11	276.75	45.47	341.00
48.70	351.10	53.76	278.93	45.82	342.51
49.91	354.43	54.49	281.38	46.20	343.71
53.22	363.92	59.51	298.29	47.50	348.28
54.62	367.18	64.04	310.51	48.72	352.57
56.51	370.84	64.98	313.07	51.41	359.38
56.89	371.57	66.20	316.37	52.01	360.89
62.07	380.37	67.01	318.51	53.09	363.99
62.22	380.54	69.82	324.52	53.98	366.57
62.79	381.20	71.27	327.62	54.63	367.86
67.35	385.45	72.48	330.19	57.02	372.66
68.76	386.78	77.31	339.95	60.65	378.15
69.84	387.80	79.53	343.67	62.04	379.81
72.43	390.30	79.79	344.12	66.52	385.16
75.12	391.47	82.70	349.13	67.80	386.32
76.23	391.98	89.88	359.84	73.95	390.04
82.61	393.82	95.76	366.41	74.72	390.51
83.77	394.16	96.91	367.66	76.37	391.16
83.91	394.19	97.83	368.33	80.24	392.93
84.18	394.24	109.29	376.54	82.39	393.92
84.72	394.32	110.93	377.71	87.76	395.09
90.75	395.27	111.42	378.09	90.98	395.53
99.88	395.54	111.54	378.19	93.13	395.82
104.52	395.31	117.46	380.68	93.59	395.87
106.09	395.23	117.93	380.88	93.89	395.85
108.12	395.15	117.98	380.90	98.90	395.52

G Tables of simulation data

Continued Table G.5 from page 163

distance / mm	v_{line1}^+ / m s ⁻¹	distance / mm	v_{line2}^+ / m s ⁻¹	distance / mm	v_{line3}^+ / m s ⁻¹
117.20	393.36	124.55	382.83	99.30	395.49
125.51	391.77	125.81	382.99	99.68	395.47
127.72	391.34	126.21	383.06	106.30	395.10
128.75	391.12	135.85	384.67	110.93	394.82
130.82	390.57	142.21	384.58	112.43	394.74
134.16	389.55	144.07	384.56	113.12	394.72
135.91	389.01	148.46	384.51	113.63	394.70
138.08	388.17	157.72	383.64	115.09	394.52
149.88	384.72	162.02	383.11	115.28	394.49
153.17	383.61	167.87	382.40	118.84	393.64
154.12	383.29	175.47	381.51	130.68	390.71
155.70	382.70	178.80	380.91	136.90	388.84
158.61	381.79	181.99	380.36	144.97	386.61
160.07	381.33	185.24	379.78	147.69	385.97
171.13	378.43	188.93	379.12	147.92	385.92
175.17	377.07	190.93	378.77	153.74	384.13
179.60	375.98	209.94	375.40	153.88	384.09
180.97	375.65	212.14	375.01	157.38	382.99
189.63	373.27	229.59	372.44	160.21	382.29
189.82	373.21	231.37	372.20	163.11	381.61
195.83	371.94	233.31	371.94	170.15	379.82
203.38	369.87	238.11	371.42	171.78	379.29
203.41	369.87	242.72	370.80	185.04	375.02
203.64	369.83	246.19	370.45	185.09	375.00
211.13	368.58	248.26	370.24	185.11	375.00
211.66	368.47	262.98	368.67	185.17	374.98
215.95	367.57	269.52	368.66	191.46	373.20
220.15	366.76	272.66	368.54	196.31	372.12
224.07	366.00	276.15	368.42	206.69	369.80
225.60	365.79	290.51	368.25	209.81	369.05
225.75	365.77	301.66	368.12	213.61	368.13

G Tables of simulation data

Continued Table G.5 from page 163

distance / mm	v_{line1}^+ / m s ⁻¹	distance / mm	v_{line2}^+ / m s ⁻¹	distance / mm	v_{line3}^+ / m s ⁻¹
233.38	364.62	302.43	368.16	222.00	366.65
234.59	364.36	302.72	368.19	222.21	366.61
235.23	364.31	307.02	368.63	222.44	366.57
251.14	362.12	309.63	368.87	231.37	364.71
251.85	362.02	331.45	370.64	234.17	364.15
255.16	361.51	351.79	372.31	242.46	363.20
258.00	361.08	356.76	372.82	248.14	362.56
259.10	360.95	360.24	373.19	248.55	362.50
259.43	360.91	362.99	373.33	249.40	362.38
259.74	360.87	363.42	373.35	249.83	362.29
261.50	360.64	363.84	373.38	251.21	362.09
270.70	359.46	375.62	373.99	251.67	362.04
272.55	359.28	405.11	375.28	257.89	361.27
276.49	358.88	409.43	375.33	266.38	360.23
283.33	358.04			270.28	359.99
288.82	357.15			285.63	358.09
292.54	356.55			285.67	358.09
292.80	356.52			285.67	358.09
298.25	355.96			285.69	358.09
303.12	355.46			291.11	357.43
306.26	355.22			291.40	357.38
309.15	355.29			303.42	355.63
309.37	355.27			304.61	355.45
315.63	354.68			304.73	355.44
318.52	354.46			305.47	355.37
323.98	354.04			309.24	355.17
328.15	353.72			313.65	354.91
330.77	353.50			317.81	354.71
331.74	353.41			326.89	354.22
335.58	353.18			328.77	354.17
342.24	353.81			331.55	354.09

G Tables of simulation data

Continued Table G.5 from page 163

distance / mm	v_{line1}^+ / m s ⁻¹	distance / mm	v_{line2}^+ / m s ⁻¹	distance / mm	v_{line3}^+ / m s ⁻¹
344.47	353.74			333.12	354.02
352.39	353.50			333.80	354.02
357.49	353.82			335.68	353.98
362.83	354.10			337.58	353.94
363.97	354.08			348.12	353.61
372.36	353.92			350.26	353.78
375.57	354.42			352.82	353.98
380.50	354.82			356.51	354.12
388.29	355.49			360.73	353.77
395.48	356.01			364.45	353.46
397.14	356.13			365.14	353.76
399.11	356.29			368.33	354.25
402.11	356.57			371.75	354.35
409.66	357.27			383.12	355.11
				388.22	355.45
				390.84	355.67
				395.02	356.31
				400.85	357.17
				418.86	358.22

Table G.6: Flow velocity values evaluated at node points for cut lines 1, 2, and 3 for the incident flow velocity of 400 m s⁻¹. Evaluation of velocity values is in negative axis direction (v^- , where distance values are given as absolute values), starting from the vehicle's fuselage at 0 mm.

distance / mm	v_{line1}^- / m s ⁻¹	distance / mm	v_{line2}^- / m s ⁻¹	distance / mm	v_{line3}^- / m s ⁻¹
0.00	0.00	0.00	0.00	0.00	0.00
0.13	0.33	0.35	2.00	2.07	17.21
2.37	19.58	2.79	15.77	2.75	23.06
2.38	19.73	2.79	15.80	2.94	24.69

G Tables of simulation data

Continued Table G.6 from page 167

distance / mm	v_{line1}^- / m s ⁻¹	distance / mm	v_{line2}^- / m s ⁻¹	distance / mm	v_{line3}^- / m s ⁻¹
2.57	21.33	2.79	15.80	2.97	24.95
2.61	21.69	3.22	18.13	5.39	45.47
5.29	44.54	6.13	34.08	6.17	52.01
5.32	44.73	6.14	34.15	6.39	53.92
5.53	46.59	6.14	34.16	6.42	54.19
5.59	47.04	6.65	36.83	9.40	78.73
8.81	73.83	10.14	55.14	10.26	85.82
8.84	74.06	10.16	55.28	10.53	88.03
9.09	76.19	10.17	55.29	10.57	88.31
9.16	76.73	10.78	58.34	14.24	117.48
13.03	107.88	14.94	79.17	15.18	124.94
13.06	108.16	14.99	79.41	15.50	127.47
13.36	110.59	14.99	79.42	15.54	127.75
13.45	111.23	15.72	82.85	20.09	161.91
18.09	146.89	20.70	106.27	21.09	169.36
18.13	147.23	20.78	106.64	21.47	172.20
18.48	149.92	20.78	106.66	21.50	172.46
18.59	150.68	21.66	110.46	27.18	211.18
24.17	190.47	27.60	136.37	28.18	218.02
24.22	190.87	27.73	136.91	28.63	221.08
24.63	193.77	27.73	136.94	28.66	221.28
24.76	194.63	28.78	141.08	35.77	262.16
31.46	237.05	35.87	169.15	36.70	267.49
31.53	237.49	36.06	169.93	37.23	270.54
32.00	240.47	36.07	169.96	37.25	270.67
32.17	241.36	37.32	174.36	46.21	309.20
40.22	283.20	45.76	204.08	46.93	312.30
40.31	283.66	46.06	205.12	47.55	314.98
40.85	286.46	46.07	205.16	47.56	315.02
41.19	288.03	46.14	205.40	47.56	315.04
41.44	289.19	46.72	207.39	48.53	318.02

G Tables of simulation data

Continued Table G.6 from page 167

distance / mm	v_{line1}^- / m s ⁻¹	distance / mm	v_{line2}^- / m s ⁻¹	distance / mm	v_{line3}^- / m s ⁻¹
42.06	291.78	46.95	208.20	49.74	321.79
42.13	292.07	47.28	209.30	52.91	331.83
47.82	315.77	49.88	218.51	53.84	334.14
50.88	325.76	57.91	242.08	54.70	336.34
51.00	326.07	58.45	243.63	56.12	339.97
55.13	337.23	58.93	245.08	58.50	344.89
55.86	339.10	61.47	252.67	61.20	350.04
61.17	349.65	62.10	254.35	61.45	350.52
65.22	355.53	62.82	256.25	64.56	356.39
67.30	359.31	71.65	278.93	65.61	358.25
68.71	361.90	74.25	285.00	65.72	358.40
72.40	366.28	74.44	285.42	66.31	359.23
72.85	366.75	78.82	294.92	69.83	363.91
76.52	370.58	83.88	306.32	69.92	364.04
81.17	374.98	87.59	313.64	70.24	364.35
82.29	375.90	98.87	334.28	73.35	367.44
86.59	378.39	99.56	335.57	77.75	371.90
88.53	379.53	100.12	336.31	80.26	374.45
93.75	382.61	102.61	339.52	81.02	375.09
98.29	384.03	111.56	351.06	82.31	375.80
102.41	385.41	118.82	359.48	88.54	379.79
106.84	386.89	121.94	361.79	91.52	381.84
110.55	387.92	126.59	365.22	92.52	382.28
112.97	388.14	128.41	366.54	99.08	384.82
116.73	388.26	133.94	370.50	99.47	384.94
123.33	388.49	134.33	370.78	108.81	387.77
128.22	388.60	135.90	371.47	109.51	387.92
129.90	388.36	141.98	374.17	110.01	387.95
131.65	388.11	143.46	374.89	110.48	387.99
138.84	387.36	146.54	375.48	116.83	388.38
145.53	386.75	152.26	376.53	120.39	388.64

G Tables of simulation data

Continued Table G.6 from page 167

distance / mm	v_{line1}^- / m s ⁻¹	distance / mm	v_{line2}^- / m s ⁻¹	distance / mm	v_{line3}^- / m s ⁻¹
147.12	386.61	154.55	376.95	124.42	388.95
148.93	386.37	155.17	377.11	134.77	387.74
158.01	384.90	161.66	378.79	135.14	387.72
163.05	383.64	162.39	378.94	141.13	387.51
164.46	383.24	165.98	379.46	141.66	387.49
169.43	381.81	183.57	379.34	142.32	387.41
170.83	381.49	188.20	379.30	160.57	384.02
177.46	380.17	189.19	379.29	162.19	383.83
183.89	378.88	196.02	379.22	166.78	382.89
184.90	378.71	197.50	379.10	174.75	381.37
186.10	378.57	204.19	378.63	175.25	381.27
189.49	377.93	210.26	378.10	175.69	381.16
200.59	375.85	212.06	377.94	179.48	380.23
200.67	375.83	223.45	376.84	183.06	379.57
201.05	375.75	235.66	375.87	186.10	378.87
216.41	372.64	239.14	375.56	196.53	376.51
217.71	372.38	241.43	375.36	203.78	374.80
220.46	371.81	244.08	375.21	207.43	374.09
221.63	371.53	245.17	375.14	213.60	373.17
222.47	371.37	262.16	374.32	221.08	371.74
229.67	370.10	265.54	374.17	221.28	371.70
243.36	367.78	267.52	374.08	233.28	369.21
243.99	367.68	274.73	373.62	237.97	368.94
245.75	367.35	274.84	373.61	240.24	368.57
250.95	366.38	282.78	373.49	248.87	366.41
251.22	366.32	283.04	373.49	251.68	365.73
251.98	366.20	283.19	373.49	253.62	365.27
261.16	364.74	309.84	373.72	262.34	363.99
268.93	363.65	318.08	374.59	263.19	363.85
270.20	363.48	326.52	375.45	265.28	363.50
271.52	363.30	348.91	377.19	274.28	361.98

G Tables of simulation data

Continued Table G.6 from page 167

distance / mm	v_{line1}^- / m s ⁻¹	distance / mm	v_{line2}^- / m s ⁻¹	distance / mm	v_{line3}^- / m s ⁻¹
278.44	362.11	365.96	378.39	279.67	361.26
279.74	361.86	366.41	378.43	281.25	361.05
280.04	361.79	366.49	378.44	284.15	360.65
286.97	360.25	366.84	378.49	288.62	359.86
287.90	360.16	366.90	378.50	291.11	359.42
290.99	359.83	366.96	378.50	295.57	358.73
301.37	358.80	367.27	378.52	305.26	357.50
308.40	357.70	388.84	380.35	306.96	357.29
308.55	357.67	393.76	380.76	310.08	356.90
308.67	357.66	403.98	381.60	310.54	356.83
314.24	356.66	414.41	382.31	311.76	356.70
316.83	356.20			313.72	356.48
326.80	354.55			324.77	355.24
328.66	354.32			328.17	354.92
332.12	353.88			328.90	354.86
339.24	354.69			337.74	354.99
344.94	354.75			338.90	354.94
351.43	354.19			339.85	354.90
356.34	353.83			344.29	354.66
370.58	354.89			346.81	354.53
374.08	355.10			353.41	354.31
374.54	355.12			357.69	353.74
379.68	355.41			357.83	353.73
383.99	356.12			357.95	353.72
389.02	356.95			358.17	353.74
392.00	357.23			368.41	354.50
394.68	357.82			381.14	355.46
410.07	361.20			386.39	357.09
				391.69	356.99
				392.30	357.19
				393.74	357.48

G Tables of simulation data

Continued Table G.6 from page 167

distance / mm	v_{line1}^- / m s ⁻¹	distance / mm	v_{line2}^- / m s ⁻¹	distance / mm	v_{line3}^- / m s ⁻¹
				407.94	360.85
				412.94	362.06

List of Figures

2.1	Particle velocity evolution and particle distance with time of a particle with a diameter of $1.2 \cdot 10^{-9}$ m initially at rest. The vertical marker depicts the particle's response time of $\tau_p = 2.67 \cdot 10^{-11}$ s.	32
2.2	Particle velocity evolution with time under consideration of the Stokes' drag and the Brownian force of a particle with a diameter of $1.2 \cdot 10^{-9}$ m initially at rest.	33
2.3	Boundaries of stability regions of different orders k of the BDF method, absolute stability (A-stability) is guaranteed for the order up to $k = 2$, where Re states the real axis and Im the imaginary axis. Higher orders up to $k \leq 6$ are $A(\alpha)$ -stable (based on [Bärwolff, G., 2015]).	43
3.1	Detailed geometry of the instrument module.	46
3.2	Noctilucent clouds [Süßen, M., 2019].	50
3.3	Temperature distribution (in K) as a function of latitude for July [Plane, J. M. C., 2003] from MSIS-E-90 model.	52
3.4	Vertical temperature profile for the upper atmosphere in polar regions. The red line shows the vertical profile as found in summer months, the green line is the vertical profile for winter months. The frost point temperature T_f is represented by the blue line [Lübken, F.- J., 2005].	53
3.5	Schematic overview of upper atmosphere's temperature profile during summer months associated with the occurrence of mesospheric ice particles. In addition, an overview of properties of mesospheric particles associated with PMSE and visible NLC is provided [Rapp, M. and Thomas, 2006].	54

List of Figures

3.6	Configuration of the sounding rocket, consisting of two stages [Naumann, K. et al., 2020]. Dimensions are given in mm. To give a sense of scale, a human figure of 1800 mm body height is shown.	55
3.7	Schematic of the flattened ballistic flight path of the sounding rocket, represented by the blue color, which allows an extended measurement at relevant measurement altitudes of 80 to 90 km. Conventional flight paths have a parabolic flight profile, which is illustrated by the red curve.	56
3.8	Geometry of the HAS instrument module with measuring instruments placed within the nose cone of the rocket [based on Naumann, K. et al., 2020].	57
3.9	Simplified geometry of the instrument module with the SPICE compartment in which the SPICE instrument is integrated. . . .	61
3.10	Scheme of the simulation geometry setup. The flow inlet into the simulation volume is defined upstream of the instrument module. The flow exits through the outlet boundaries, mainly at the rear of the simulation volume. The 3D model of the instrument module is centered in the simulation volume and aligned with the flow direction [Klug, B. S. et al., 2023].	62
3.11	Difference in velocities computed for subsonic and hybrid boundary conditions in m s^{-1} . The upper picture shows the difference for the incident flow velocity of 300 m s^{-1} and the lower picture for 400 m s^{-1}	66
3.12	Generated mesh with refinement zones. The distribution of mesh sizes is illustrated: the mesh resolution is increased in the immediate vicinity of the flow obstacle as well as along the shock wave, whose position and course were determined by precalculations. . .	71
3.13	Velocity magnitude distribution around the instrument module, shown in a longitudinal vertical plane. The inlet of the air flow into the simulation volume is located on the left side. Figure a) shows the simulation result for the incident flow velocity of 300 m s^{-1} and b) for 400 m s^{-1}	72
3.14	Visualization of two cut lines on which flow velocity values are evaluated to determine the boundary layer thickness. The blue color marks cut line 1 and the green color marks cut line 2. . . .	73

List of Figures

3.15	Flow velocity profile evaluated along cut lines 1 (blue) and 2 (green) for the incident flow velocities of 300 m s^{-1} in Figure a) and 400 m s^{-1} in Figure b). Crosshair symbols indicate data points at mesh nodes.	74
3.16	Particle trajectories based on the fluid simulation with incident velocity of 400 m s^{-1} are shown in red. The position of a SPICE boom with the length of 120 mm is shown for illustration purposes. Areas with increased and decreased particle number concentration are indicated.	76
3.17	Computational mesh for simulations of the instrument module with m-NLP. The mesh resolution is increased around the flow obstacle, boundary layer elements are visible at the instrument module including the SPICE compartment [Klug, B. S. et al., 2023].	78
3.18	Flow field around the instrument module with m-NLP depicted on a longitudinal vertical plane. The inlet for the air flow is on the left-hand side. Figure a) shows the simulation result for the flow velocity of 300 m s^{-1} and b) for 400 m s^{-1} [Klug, B. S. et al., 2023].	79
3.19	Frontal view of the cross-section of the flow velocity field (in the level of the SPICE instrument) for the incident flow velocity of 300 m s^{-1} in a) and 400 m s^{-1} in b). Note: The flowed-around instrument module also comprises the m-NLP booms, whose wake imprint is clearly reflected in the flow velocity field at the level of the SPICE instrument (yellow/orange contours). Colored lines (blue/red/green) indicate potential configurations of the SPICE booms as far as possible away from wake influences of the m-NLP.	80
3.20	Visualization of the cut lines from two different perspectives of the instrument module along which velocity variables are analyzed [based on Klug, B. S. et al., 2023]. The blue color marks cut line 1, the green color cut line 2 and the red color marks cut line 3.	80
3.21	Flow velocities evaluated on cut lines 1 (blue), 2 (green) and 3 (red) for the incident flow velocities of 300 m s^{-1} , a) and 400 m s^{-1} , b) [Klug, B. S. et al., 2023]. Crosshair symbols indicate data points at mesh nodes.	81

List of Figures

3.22	Frontal view of the computational geometry of the instrument module showing the ultimate layout of the three SPICE booms bearing the substrate mounts at their tips [based on Klug, B. S. et al., 2023].	83
3.23	Detailed geometry of the substrate mount with recessed impaction substrates.	83
3.24	Computational mesh for the selected instrument module geometry with substrate mounts on the SPICE booms. In the close-up, the higher resolution of mesh elements around the upright substrate mount is visible [Klug, B. S. et al., 2023].	86
3.25	Near-surface mesh elements around the instrument module.	86
3.26	Flow field around the instrument module depicted on two cut planes, where the inlet for the air flow is on the left-hand side. Figure a) shows the simulation result for the incident velocity of 300 m s^{-1} and b) for 400 m s^{-1}	87
3.27	Frontal view of the flow field at the level of the SPICE instrument a) and side view of the flow field around one SPICE boom b).	88
3.28	Streamlines around one of the substrate mounts for the angle of attack of 0° at the incident velocity of 400 m s^{-1} show velocity values limited to 0 m s^{-1} and 220 m s^{-1}	89
3.29	Representation of flow field variables, temperature field in a), velocity field in b), fluid density field in c), and pressure field in d) depicted on two cut planes for the incident flow velocity of 400 m s^{-1}	90
3.30	Computational mesh for flow simulations for -30° angle of attack.	91
3.31	Flow field around the instrument module geometry depicted on a cut plane for the incident flow velocity of 400 m s^{-1} for the flight attitude of $+30^\circ$ [Klug, B. S. et al., 2023].	91
3.32	Representation of flow field variables, temperature field a), velocity field b), fluid density field c), and pressure field d) for the incident flow velocity of 400 m s^{-1} on two cut planes for the flight attitude of $+30^\circ$	92

List of Figures

3.33	Side view of the flow field a) and streamlines b) around the upright SPICE boom and one downside oriented SPICE boom with the flow field c) and streamlines d) for the angle of attack of $+30^\circ$ and the incident velocity of 400 m s^{-1}	93
3.34	Flow field around the instrument module geometry depicted on a cut plane for the incident flow velocity of 400 m s^{-1} for the flight attitude of -30° [Klug, B. S. et al., 2023].	94
3.35	Representation of flow field variables, the temperature field a), velocity field b), fluid density field c), and pressure field d) for the incident velocity of 400 m s^{-1} on two cut planes for the flight attitude of -30°	94
3.36	Side view of the flow field a) and streamlines b) around the upright SPICE boom and one downside oriented SPICE boom with the flow field c) and streamlines d) for the angle of attack of -30° and the incident velocity of 400 m s^{-1}	95
3.37	Streamlines around the instrument module for the angles of attack of -30° in a) and $+30^\circ$ in b) for the incident velocity 400 m s^{-1} . Streamlines are colored according to velocity values and are filtered out to 0 m s^{-1} and 220 m s^{-1}	96
3.38	Reduced simulation volume including the upright SPICE boom with a mesh refinement region around the substrate mount for high-resolution simulations of the near flow field.	98
3.39	Mesh resolution within the cuboid volume around a substrate mount.	99
3.40	Velocity profile used as boundary condition at the inlet surface of the reduced simulation volume for 300 m s^{-1} a) and 400 m s^{-1} b).	100
3.41	Velocity field around the instrument module for determining flow profiles at the evaluation position (marked line) as boundary conditions for high-resolution flow simulations. Figure a) shows the velocity field for the incident flow velocity of 300 m s^{-1} and b) for the incident flow velocity of 400 m s^{-1} , where the color ranges are limited to almost free flow velocities.	100
3.42	Streamlines colored with velocity magnitude values around a substrate mount for the incident flow velocity of 300 m s^{-1} a) and for 400 m s^{-1} b), which are limited to the velocity range covered.	101

List of Figures

3.43	Locally refined computational mesh with element sizes ranging from $1.04 \cdot 10^{-5}$ m to $5 \cdot 10^{-5}$ m located at the recessed impaction substrates.	102
3.44	Streamlines around the substrate mounts for the incident flow velocity of 300 m s^{-1} . Streamlines are colored with velocity magnitude values, filtered out up to 100 m s^{-1} in a) and up to 10 m s^{-1} in b).	103
3.45	Particle trajectories of 10 000 particles originating from specified particle inlet regions and enveloping substrate mounts. The coloring refers to the temperature values at the particle positions.	111
3.46	Particle inlets upstream of the three different SPICE booms are arranged such that particles flow around substrate mounts.	112
3.47	Calculated back trajectories of impacted particles (red lines). The impacting particles originate from preferential areas of the particle inlets, which are highlighted by blue contours.	114
3.48	Ensemble of 9401 particle trajectories, originating from the reduced inlet heading towards the substrate mount. The color table scales particle velocity values.	114
3.49	Enlargement of the temperature field in K around the instrument module illustrating the temperature increase caused by the shock waves based on the incident flow velocity of 400 m s^{-1} . In addition, the trajectories of individual impacting particles are shown.	117
3.50	Temperature evolution along the trajectories of two impacting particles depicted by the blue and red color, respectively. The coordinate origin (zero) of the x -axis represents the location of the particle impact on the substrate mount.	118
3.51	Simulated mass behavior of particles of different sizes based on varying values of α_d , from Manuel Baumgartner, Johannes Gutenberg University Mainz, Institute for Atmospheric Physics.	119
3.52	Detailed frontal view a) [Klug, B. S. et al., 2023] and side view b) of 2703 impacted particles on substrate mounts for the initial particle number concentration of 11 cm^{-3} . Additionally, the cross-sectional area of the substrate mount perpendicular to the flow direction is illustrated in b) by a cut plane.	121

List of Figures

3.53	Left column: Number of impacted particles on substrate mounts with respect to ambient particle number concentrations for the HAS flight attitudes. Right column: Sampling efficiency η with respect to ambient particle number concentrations for the HAS flight attitudes. The magenta color represents data from the up-right substrate mount 1 and the green color from the downside oriented substrate mount 2. The variability of four independent simulation runs is marked by vertical bars. Figures a1) and a2) are from Klug, B. S. et al. [2023].	122
3.54	Streamlines flowing around substrate mounts for the angles of attack of 0° a), -30° b), and $+30^\circ$ c) for the incident flow velocity of 400 m s^{-1} . Streamlines are colored with reference to the velocity magnitude. For illustration purposes, the course of the shock wave front is indicated by a black line.	125
D.1	Particle reflection on a surface.	144

List of Tables

2.1	Relation of different forces to Stokes' drag force.	30
3.1	Velocity, temperature, pressure, and density increase with regard to values of the free flow field measured upstream of SPICE booms 1 and 2 for the different angles of attack of $\pm 30^\circ$ and 0°	97
3.2	Flow field and particle properties.	108
3.3	Approximated magnitudes of forces acting on particles to estimate their effects on the particle dynamics. Forces highlighted in gray have a negligible magnitude compared to forces inherent with Brownian motion or due to Stokes' drag and therefore remain unconsidered in subsequent particle simulations.	108
3.4	Numbers of released particles as model input for particle simulations of the impaction processes with corresponding particle number concentrations.	115
G.1	Flow velocity values (v_{line1}^- , v_{line1}^+ , v_{line2}^- , v_{line2}^+) evaluated at node points for cut lines 1 and 2 for the incident velocity of 300 m s^{-1} . Velocity values are divided into evaluations along the positive axis direction (v^+), starting from the vehicle's fuselage at 0 mm, and evaluations along the axis direction in the negative direction (v^- , where distance values are given as absolute values).	149
G.2	Flow velocity values evaluated at node points for cut lines 1 and 2 for the incident flow velocity of 400 m s^{-1} . Velocity values are divided into evaluations along the positive axis direction (v^+), starting from the vehicle's fuselage at 0 mm, and evaluations along the axis direction in the negative direction (v^- , where distance values are given as absolute values).	151

List of Tables

G.3	Flow velocity values evaluated at node points for cut lines 1, 2, and 3 for the incident flow velocity of 300 m s^{-1} . Evaluation of velocity values is in positive axis direction (v^+), starting from the vehicle's fuselage at 0 mm.	153
G.4	Flow velocity values evaluated at node points for cut lines 1, 2, and 3 for the incident flow velocity of 300 m s^{-1} . Evaluation of velocity values is in negative axis direction (v^- , where distance values are given as absolute values), starting from the vehicle's fuselage at 0 mm.	158
G.5	Flow velocity values in m s^{-1} evaluated at node points for cut lines 1, 2, and 3 for the incident flow velocity of 400 m s^{-1} . Evaluation of velocity values is in positive axis direction (v^+), starting from the vehicle's fuselage at 0 mm.	163
G.6	Flow velocity values evaluated at node points for cut lines 1, 2, and 3 for the incident flow velocity of 400 m s^{-1} . Evaluation of velocity values is in negative axis direction (v^- , where distance values are given as absolute values), starting from the vehicle's fuselage at 0 mm.	167

Bibliography

Allen, M. D. and O. G. Raabe. Re-evaluation of Millikan's oil drop data for the motion of small particles in air. *Journal of Aerosol Science*, 13(6):537–547, 1982.

Allen, M. D. and O. G. Raabe. Slip correction measurements of spherical solid aerosol particles in an improved Millikan apparatus. *Aerosol Science and Technology*, 4(3):269–286, 1985.

Altenbach, H. *Kontinuumsmechanik*. Springer, 2012.

Anderson, J. D. *Fundamentals of aerodynamics*. Tata McGraw-Hill Education, 2010.

Appel, O., F. Köllner, A. Dragoneas, A. Hünig, S. Molleker, H. Schlager, C. Mahnke, M. Weigel, R. and Port, C. Schulz, F. Drewnik, B. Vogel, S. F., and S. Borrmann. Chemical analysis of the Asian Tropopause Aerosol Layer (ATAL) with emphasis on secondary aerosol particles using aircraft based in situ aerosol mass spectrometry. *Atmospheric Chemistry and Physics Discussions*, pages 1–37, 2022.

Arnold, M. and O. Brüls. Convergence of the generalized- α scheme for constrained mechanical systems. *Multibody System Dynamics*, 18(2):185–202, 2007.

Asmus, H., H. Wilms, B. Strelnikov, and M. Rapp. On the heterogeneous nucleation of mesospheric ice on meteoric smoke particles: Microphysical modeling. *Journal of Atmospheric and Solar-Terrestrial Physics*, 118:180–189, 2014.

Bärwolff, G. *Numerik I, aktueller Vorlesungsstand by Günter Bärwolff*. 2015.

Baumgarten, G. and J. Fiedler. Vertical structure of particle properties and water content in noctilucent clouds. *Geophysical research letters*, 35(10), 2008.

BIBLIOGRAPHY

- Baumgarten, G., J. Fiedler, F.-J. Lübken, and G. Von Cossart. Particle properties and water content of noctilucent clouds and their interannual variation. *Journal of Geophysical Research: Atmospheres*, 113(D6), 2008.
- Bayramov, N. R. and J. K. Kraus. On the stable solution of transient convection–diffusion equations. *Journal of Computational and Applied Mathematics*, 280: 275–293, 2015.
- Bird, G. A. *Molecular gas dynamics and the direct simulation of gas flows*. Oxford University Press; 002 Edition, 1994.
- Blackhouse, T. W. The luminous cirrus cloud of June and July. *Meteorol. Mag.*, 20:133, 1885.
- Bonelli, A., O. S. Bursi, S. Erlicher, and L. Vulcan. Analyses of the generalized- α method for linear and non-linear forced excited systems. In *Structural Dynamics-EURODYN*, volume 2, pages 1523–1528. Citeseer, 2002.
- Boucher, C. COMSOL® Blog; What Formulation Should I Use for Particle Tracing in Fluids. <https://www.comsol.com/blogs/what-formulation-should-i-use-for-particle-tracing-in-fluids/>, 2020. Accessed: 14.06.2023.
- Brennen, C. E. A Review of Added Mass and Fluid Inertial Forces. *Naval Civil Eng. Lab., Port Hueneme, Calif., Report CR82.010*, 1982.
- Breuer, M., H. T. Baytekin, and E. A. Matida. Prediction of aerosol deposition in 90° bends using LES and an efficient Lagrangian tracking method. *Journal of Aerosol Science*, 37(11):1407–1428, 2006.
- Brooks, A. N. and T. J. R. Hughes. Streamline upwind/Petrov-Galerkin formulations for convection dominated flows with particular emphasis on the incompressible Navier-Stokes equations. *Computer methods in applied mechanics and engineering*, 32(1-3):199–259, 1982.
- Burgmann, S., N. Van der Schoot, C. Asbach, J. Wartmann, and R. Lindken. Analysis of tracer particle characteristics for micro PIV in wall-bounded gas flows. *La houille blanche*, (4):55–61, 2011.
- Ceplecha, Z., J. Borovička, W. G. Elford, D. O. ReVelle, R. L. Hawkes, V. Porubčan, and M. Šimek. Meteor phenomena and bodies. *Space Science Reviews*, 84(3):327–471, 1998.

BIBLIOGRAPHY

- Chung, J. and G. M. Hulbert. A time integration algorithm for structural dynamics with improved numerical dissipation: the generalized- α method. *Journal of Applied Mechanics*, 60(2):371–375, 1993.
- Chung, J. and J. M. Lee. A new family of explicit time integration methods for linear and non-linear structural dynamics. *International Journal for Numerical Methods in Engineering*, 37(23):3961–3976, 1994.
- COMSOL Multiphysics®. *COMSOL AB, Stockholm, Sweden. Version 6.1*, 2023. URL www.comsol.com.
- COMSOL®. Particle Tracing Module User’s Guide 4.3, 2012.
- COMSOL®. Particle Tracing Module Module Application Library Manual 5.3, 2017a.
- COMSOL®. Introduction to the Particle Tracing Module, 2017b.
- COMSOL®. COMSOL Multiphysics Reference Manual 5.5, 2018a.
- COMSOL®. The Finite Element Method (FEM), 2018b. URL <https://www.comsol.com/multiphysics/finite-element-method>. Cited 27.04.2022.
- COMSOL®. Particle Tracing Module User’s Guide 5.4, 2019.
- COMSOL®. Particle Tracing Module User’s Guide 5.6, 2020.
- COMSOL®. Introduction to the Particle Tracing Module, 2022.
- COMSOL®. BDF, Generalized Alpha, and Runge-Kutta Methods. <https://www.comsol.de/support/knowledgebase/1062>, 2023. Accessed: 16.05.2023.
- Courant, R., K. Friedrichs, and H. Lewy. Über die partiellen Differenzgleichungen der mathematischen Physik. *Mathematische annalen*, 100(1):32–74, 1928.
- Crowe, C. T., J. D. Schwarzkopf, M. Sommerfeld, and Y. Tsuji. *Multiphase Flows with Droplets and Particles*. CRC Press, 2012.
- Date, A. W. *Introduction to computational fluid dynamics*. Cambridge university press, 2005.

BIBLIOGRAPHY

- Davies, C. N. Definitive equations for the fluid resistance of spheres. *Proceedings of the Physical Society*, 57(4):259, 1945.
- de Vahl Davis, G. and G. D. Mallinson. An evaluation of upwind and central difference approximations by a study of recirculating flow. *Computers & Fluids*, 4(1):29–43, 1976.
- DLR. Suborbital Spaceflight. Space Operations and Astronaut Training. https://moraba.de/wp-content/uploads/2020/11/2020_05_15.Suborbital-Space-Flight.pdf. Accessed: 09.08.2021.
- Dong, S., L. Zheng, X. Zhang, S. Wu, and B. Shen. A new model for Brownian force and the application to simulating nanofluid flow. *Microfluidics and nanofluidics*, 16(1):131–139, 2014.
- Elghobashi, S. On predicting particle-laden turbulent flows. *Applied scientific research*, 52(4):309–329, 1994.
- Erlicher, S., L. Bonaventura, and O. S. Bursi. The analysis of the generalized- α method for non-linear dynamic problems. *Computational mechanics*, 28(2): 83–104, 2002.
- Fentzke, J. T., D. Janches, I. Strelnikova, and M. Rapp. Meteoric smoke particle properties derived using dual-beam Arecibo UHF observations of D-region spectra during different seasons. *Journal of atmospheric and solar-terrestrial physics*, 71(17-18):1982–1991, 2009.
- Frankland, V. L., A. D. James, J. D. Carrillo-Sánchez, D. Nesvorný, P. Pokorný, and J. M. C. Plane. CO oxidation and O₂ removal on meteoric material in Venus’ atmosphere. *Icarus*, 296:150–162, 2017.
- Frei, W. Keeping Track of Element Order in Multiphysics Models. <https://www.comsol.com/blogs/keeping-track-of-element-order-in-multiphysics-models>, 2016. Accessed: 27.04.2022.
- Fung, T. C. Numerical dissipation in time-step integration algorithms for structural dynamic analysis. *Progress in Structural Engineering and Materials*, 5(3): 167–180, 2003.

BIBLIOGRAPHY

- García Pérez, M., E. Vakkilainen, and T. Hyppänen. A brief overview of the drag laws used in the Lagrangian tracking of ash trajectories for boiler fouling CFD models. *Impacts of Fuel Quality on Power Production*, 26th international conference, 2016.
- Gelinas, L. J., K. A. Lynch, M. C. Kelley, R. L. Collins, M. Widholm, E. MacDonald, J. Ulwick, and P. Mace. Mesospheric charged dust layer: Implications for neutral chemistry. *Journal of Geophysical Research: Space Physics*, 110(A1), 2005.
- Gimenez, J. M., D. Ramajo, and N. M. Nigro. Particle transport in laminar/turbulent flows. *Mecánica Computacional*, 31(2):151–164, 2012.
- Gresho, P. M. and R. L. Lee. Don't suppress the wiggles – they're telling you something! *Computers & Fluids*, 9(2):223–253, 1981.
- Hairer, E., S. P. Norsett, and G. Wanner. *Solving Ordinary, Differential Equations I, Nonstiff problems, Vol.: 1*. 2Ed. Springer-Verlag, 2000.
- Hauke, G. and T. J. R. Hughes. A unified approach to compressible and incompressible flows. *Computer Methods in Applied Mechanics and Engineering*, 113(3-4):389–395, 1994.
- Hedin, J., J. Gumbel, and M. Rapp. On the efficiency of rocket-borne particle detection in the mesosphere. *Atmospheric Chemistry and Physics*, 7(14):3701–3711, 2007a.
- Hedin, J., J. Gumbel, T. Waldemarsson, and F. Giovane. The aerodynamics of the MAGIC meteoric smoke sampler. *Advances in Space Research*, 40(6):818–824, 2007b.
- Hedin, J., F. Giovane, T. Waldemarsson, J. Gumbel, J. Blum, R. M. Stroud, L. Marlin, J. Moser, D. E. Siskind, K. Jansson, R. W. Saunders, M. E. Summers, P. Reissaus, J. Stegman, J. M. C. Plane, and M. Horónyi. The MAGIC meteoric smoke particle sampler. *Journal of Atmospheric and Solar-Terrestrial Physics*, 118:127–144, 2014.
- Hervig, M., R. E. Thompson, M. McHugh, L. L. Gordley, J. M. Russell III, and M. E. Summers. First confirmation that water ice is the primary component of polar mesospheric clouds. *Geophysical Research Letters*, 28(6):971–974, 2001.

BIBLIOGRAPHY

- Hervig, M. E., L. L. Gordley, L. E. Deaver, D. E. Siskind, M. H. Stevens, J. M. Russell III, S. M. Bailey, L. Megner, and C. G. Bardeen. First satellite observations of meteoric smoke in the middle atmosphere. *Geophysical Research Letters*, 36(18), 2009.
- Hervig, M. E., M. Rapp, R. Latteck, and L. L. Gordley. Observations of mesospheric ice particles from the ALWIN radar and SOFIE. *Journal of Atmospheric and Solar-Terrestrial Physics*, 73(14-15):2176–2183, 2011.
- Hervig, M. E., L. E. Deaver, C. G. Bardeen, J. M. Russell III, S. M. Bailey, and L. L. Gordley. The content and composition of meteoric smoke in mesospheric ice particles from SOFIE observations. *Journal of Atmospheric and Solar-Terrestrial Physics*, 84:1–6, 2012.
- Hinds, W. C. and Y. Zhu. *Aerosol technology: properties, behavior, and measurement of airborne particles*. John Wiley & Sons, 2022.
- Horányi, M., J. Gumbel, G. Witt, and S. Robertson. Simulation of rocket-borne particle measurements in the mesosphere. *Geophysical research letters*, 26(11):1537–1540, 1999.
- Hryb, D., M. Cardozo, S. Ferro, and M. Goldschmit. Particle transport in turbulent flow using both Lagrangian and Eulerian formulations. *International Communications in Heat and Mass Transfer*, 36(5):451–457, 2009.
- Hughes, T. J. R. and M. Mallet. A new finite element formulation for computational fluid dynamics: Iii. the generalized streamline operator for multidimensional advective-diffusive systems. *Computer methods in applied mechanics and engineering*, 58(3):305–328, 1986.
- Hunten, D. M., R. P. Turco, and O. B. Toon. Smoke and dust particles of meteoric origin in the mesosphere and stratosphere. *Journal of Atmospheric Sciences*, 37(6):1342–1357, 1980.
- James, A. D., J. S. A. Brooke, T. P. Mangan, T. F. Whale, J. M. C. Plane, and B. J. Murray. Nucleation of nitric acid hydrates in polar stratospheric clouds by meteoric material. *Atmospheric Chemistry and Physics*, 18(7):4519–4531, 2018.
- James, A. D., V. L. F. Frankland, J. M. Trigo-Rodríguez, J. Alonso-Azcárate, J. C. G. Martín, and J. M. C. Plane. Synthesis and characterisation of analogues

BIBLIOGRAPHY

for interplanetary dust and meteoric smoke particles. *Journal of Atmospheric and Solar-Terrestrial Physics*, 162:178–191, 2017.

Janches, D., L. P. Dyrud, S. L. Broadley, and J. M. C. Plane. First observation of micrometeoroid differential ablation in the atmosphere. *Geophysical Research Letters*, 36(6), 2009.

Jay, O. L. and D. Negrut. A second order extension of the generalized- α method for constrained systems in mechanics. In *Multibody Dynamics*, pages 143–158. Springer, 2009.

Jesse, O. Luminous Clouds. *Nature*, 43:59–61, 1890.

John, V. and E. Schmeyer. On finite element methods for 3d time-dependent convection-diffusion-reaction equations with small diffusion. In *BAIL 2008-Boundary and Interior Layers: Proceedings of the International Conference on Boundary and Interior Layers-Computational and Asymptotic Methods, Limerick, July 2008*, pages 173–181. Springer, 2009.

Johnson, C., A. H. Schatz, and L. B. Wahlbin. Crosswind smear and pointwise errors in streamline diffusion finite element methods. *Mathematics of computation*, 49(179):25–38, 1987.

Katopodes, N. D. *Free-surface flow: environmental fluid mechanics*. Butterworth-Heinemann, 2018.

Ketcham, W. M. and P. V. Hobbs. An experimental determination of the surface energies of ice. *Philosophical Magazine*, 19(162):1161–1173, 1969.

Klekociuk, A. R., P. G. Brown, D. W. Pack, D. O. ReVelle, W. N. Edwards, R. E. Spalding, E. Tagliaferri, B. B. Yoo, and J. Zagari. Meteoritic dust from the atmospheric disintegration of a large meteoroid. *Nature*, 436(7054):1132–1135, 2005.

Klug, B. S. Numerical simulations of turbulence at a vertical wind tunnel. Master’s thesis, Particle Chemistry, Max Planck Institute for Chemistry, Max Planck Society. Johannes Gutenberg University Mainz, Institute for Atmospheric Physics, 2018.

BIBLIOGRAPHY

- Klug, B. S., A. Hundertmark, and R. Weigel. Comsol[®] simulations of supersonic flow fields to study trajectories of aerosols and their impact efficiency on a rocket-borne particle collector. *Comsol Conference 2023 Munich*, 2023.
- Knothe, K. and H. Wessels. *Finite elemente*. Springer, 7 edition, 2017.
- Knudsen, M. and S. Weber. Luftwiderstand gegen die langsame Bewegung kleiner Kugeln. *Annalen der Physik*, 341(15):981–994, 1911.
- Kopp, E. On the abundance of metal ions in the lower ionosphere. *Journal of Geophysical Research: Space Physics*, 102(A5):9667–9674, 1997.
- Kuerten, J. G. M. Point-Particle DNS and LES of Particle-Laden Turbulent flow—a state-of-the-art review. *Flow, turbulence and combustion*, 97(3):689–713, 2016.
- Kulkarni, P., P. A. Baron, and K. Willeke. *Aerosol measurement: principles, techniques, and applications*. John Wiley & Sons, 2011.
- Lewis, R. W., P. Nithiarasu, and K. N. Seetharamu. *Fundamentals of the finite element method for heat and fluid flow*. John Wiley & Sons, 2004.
- Lohmann, U., F. Lüönd, and F. Mahrt. *An introduction to clouds: From the microscale to climate*. Cambridge University Press, 2016.
- Lübken, F.-J. Eisteilchen in 80–90 km Höhe: Indikatoren für die niedrigsten Temperaturen in der Erdatmosphäre. *Promet*, 31(1):19–24, 2005.
- Lübken, F.-J. Thermal structure of the Arctic summer mesosphere. *Journal of Geophysical Research: Atmospheres*, 104(D8):9135–9149, 1999.
- Lynch, K. A., L. J. Gelinis, M. C. Kelley, R. L. Collins, M. Widholm, D. Rau, E. MacDonald, Y. Liu, J. Ulwick, and P. Mace. Multiple sounding rocket observations of charged dust in the polar winter mesosphere. *Journal of Geophysical Research: Space Physics*, 110(A3), 2005.
- Magee, N., A. M. Moyle, and D. Lamb. Experimental determination of the deposition coefficient of small cirrus-like ice crystals near $-50\text{ }^{\circ}\text{C}$. *Geophysical research letters*, 33(17), 2006.

BIBLIOGRAPHY

- Megner, L., M. Rapp, and J. Gumbel. Distribution of meteoric smoke—sensitivity to microphysical properties and atmospheric conditions. *Atmospheric Chemistry and Physics*, 6(12):4415–4426, 2006.
- Mei, R. and J. F. Klausner. Shear lift force on spherical bubbles. *International journal of heat and fluid flow*, 15(1):62–65, 1994.
- Millikan, R. A. The general law of fall of a small spherical body through a gas, and its bearing upon the nature of molecular reflection from surfaces. *Physical Review*, 22(1):1, 1923.
- Murad, E. and I. P. Williams. *Meteors in the Earth’s Atmosphere: Meteoroids and Cosmic Dust and Their Interactions with the Earth’s Upper Atmosphere*. Cambridge University Press, 2002.
- Murphy, D. M. and T. Koop. Review of the vapour pressures of ice and supercooled water for atmospheric applications. *Quarterly Journal of the Royal Meteorological Society: A journal of the atmospheric sciences, applied meteorology and physical oceanography*, 131(608):1539–1565, 2005.
- Naumann, K., C. Kirchberger, O. Drescher, D. Hargarten, M. Zurkaulen, A. Haubl, S. Rest, H. Niedermaier, and J. Ramsel. Design of a hovering sounding rocket stage for measurements in the high atmosphere. 2020.
- Naumann, Z. and L. Schiller. A drag coefficient correlation. *Z. Ver. Deutsch. Ing*, 77(318):e323, 1935.
- Novotný, J. and L. Manoch. The criterion of choosing the proper seeding particles. *Engineering Mechanics*, 2012.
- Plane, J. M. C. Atmospheric chemistry of meteoric metals. *Chemical reviews*, 103(12):4963–4984, 2003.
- Plane, J. M. C. Cosmic dust in the earth’s atmosphere. *Chemical Society Reviews*, 41(19):6507–6518, 2012.
- Plane, J. M. C., W. Feng, and E. M. Dawkins. The mesosphere and metals: Chemistry and changes. *Chemical reviews*, 115(10):4497–4541, 2015.
- Podolak, M., J. B. Pollack, and R. T. Reynolds. Interactions of planetesimals with protoplanetary atmospheres. *Icarus*, 73(1):163–179, 1988.

BIBLIOGRAPHY

- Prof. Dr. J. Lorenz. Die Navier-Stokes-Gleichungen für kompressible Flüssigkeiten. <https://www.igpm.rwth-aachen.de/Download/reports/reichelt/Navier.pdf>, 1994. Accessed: 09.02.2023.
- Prof. J. M. Melenk. Numerik von Differentialgleichungen. https://www.asc.tuwien.ac.at/~melenk/teach/num_DGL_SS10/ODE_teil6.pdf, 2010. Accessed: 19.05.2022.
- Pruppacher, H. R. and J. D. Klett. *Microphysics of Clouds and Precipitation*. Springer Science & Business Media, 2010.
- Quarteroni, A., R. Sacco, and F. Saleri. *Numerical mathematics*, volume 37. Springer Science & Business Media, 2010.
- Rapp, M. and F.-J. Lübken. Polar mesosphere summer echoes (PMSE): Review of observations and current understanding. *Atmospheric chemistry and physics*, 4(11/12):2601–2633, 2004.
- Rapp, M. and G. E. Thomas. Modeling the microphysics of mesospheric ice particles: Assessment of current capabilities and basic sensitivities. *Journal of Atmospheric and Solar-Terrestrial Physics*, 68(7):715–744, 2006.
- Rapp, M., I. Strelnikova, and J. Gumbel. Meteoric smoke particles: Evidence from rocket and radar techniques. *Advances in Space Research*, 40(6):809–817, 2007.
- Rapp, M., I. Strelnikova, B. Strelnikov, P. Hoffmann, M. Friedrich, J. Gumbel, L. Megner, U.-P. Hoppe, S. Robertson, S. Knappmiller, M. Wolff, and D. R. Marsch. Rocket-borne in situ measurements of meteor smoke: Charging properties and implications for seasonal variation. *Journal of Geophysical Research: Atmospheres*, 115(D1), 2010.
- Rapp, M., J. M. C. Plane, B. Strelnikov, G. Stober, S. Ernst, J. Hedin, M. Friedrich, and U.-P. Hoppe. In situ observations of meteor smoke particles (MSP) during the Geminids 2010: constraints on MSP size, work function and composition. In *Annales geophysicae*, volume 30, pages 1661–1673. Copernicus Publications Göttingen, Germany, 2012.
- Reddy, J. N. and D. K. Gartling. *The finite element method in heat transfer and fluid dynamics*. CRC press, 2010.

BIBLIOGRAPHY

- Rezzolla, L. Numerical methods for the solution of partial differential equations. https://itp.uni-frankfurt.de/~rezzolla/lecture_notes/2007/ECT_hyperbolic_PDEs_0807.pdf, July 2013. Accessed: 25.08.2023.
- Roos, H.-G. and Zarin, H. The streamline-diffusion method for a convection-diffusion problem with a point source. *Journal of computational and applied mathematics*, 150(1):109–128, 2003.
- Rosinski, J. and R. H. Snow. Secondary particulate matter from meteor vapors. *Journal of Atmospheric Sciences*, 18(6):736–745, 1961.
- Roy, G. *Combustion processes in propulsion: control, noise, and pulse detonation*. Butterworth-Heinemann, 2006.
- Rusch, D. W., G. E. Thomas, and E. J. Jensen. Particle size distributions in polar mesospheric clouds derived from Solar Mesosphere Explorer measurements. *Journal of Geophysical Research: Atmospheres*, 96(D7):12933–12939, 1991.
- Saffman, P. G. T. The lift on a small sphere in a slow shear flow. *Journal of fluid mechanics*, 22(2):385–400, 1965.
- Saunders, R. W., S. Dhomse, W. S. Tian, M. P. Chipperfield, and J. M. C. Plane. Interactions of meteoric smoke particles with sulphuric acid in the Earth’s stratosphere. *Atmospheric chemistry and physics*, 12:4387–4398, 2012.
- Schlegel, F. COMSOL® Blog; Understanding Stabilization Methods. <https://www.comsol.de/blogs/understanding-stabilization-methods/>, 2014. Accessed: 14.06.2023.
- Schmidt, H. and S. Suter. Die Navier Stokes Gleichung. Mathematisches Institut der Universität Basel. <http://snovit.math.umu.se/~david/Teach/FEM09/navir2.pdf>, 2009. Accessed: 10.02.2022.
- Schneider, J., R. Weigel, T. Klimach, A. Dragoneas, O. Appel, A. Hünig, S. Molleker, F. Köllner, H.-C. Clemen, O. Eppers, P. Hoppe, P. Hoor, C. Mahnke, K. M., C. Rolf, J.-U. Groß, A. Zahn, F. Obersteiner, F. Ravegnani, A. Ulanovski, H. Schlager, M. Scheibe, G. S. Diskin, J. P. DiGangi, J. B. Nowak, M. Zöger, and S. Borrmann. Aircraft-based observation of meteoric material in lower-stratospheric aerosol particles between 15 and 68° N. *Atmospheric chemistry and physics*, 21(2):989–1013, 2021.

BIBLIOGRAPHY

- Schwarz, H.-R. and N. Köckler. *Numerische Mathematik*. Springer-Verlag, 2013.
- Semper, B. Numerical crosswind smear in the streamline diffusion method. *Computer methods in applied mechanics and engineering*, 113(1-2):99–108, 1994.
- Shimazaki, Y., M. Okubo, T. Yamamoto, and A. Yoshida. Three-Dimensional Numerical Simulation of Nanoparticle Inhalation and Indoor Pollution Around Breathing Human. *Journal of Environment and Engineering*, 4(1):145–161, 2009.
- Sommerfeld, M. *Best practice guidelines for computational fluid dynamics of dispersed multiphase flows*. Ercoftac, 2008.
- Spichtinger, P. and K. M. Gierens. Modelling of cirrus clouds—Part 1a: Model description and validation. *Atmospheric Chemistry and Physics*, 9(2):685–706, 2009.
- Stephens, G. L. The influence of radiative transfer on the mass and heat budgets of ice crystals falling in the atmosphere. *Journal of Atmospheric Sciences*, 40(7):1729–1739, 1983.
- Strelnikova, I., M. Rapp, S. Raizada, and M. Sulzer. Meteor smoke particle properties derived from Arecibo incoherent scatter radar observations. *Geophysical Research Letters*, 34(15), 2007.
- Süßen, M. Licence: license CC BY-SA, SIKIMEDIA COMMONS. <https://commons.wikimedia.org/w/index.php?search=noctilucent&title=Special:MediaSearch&go=Go&type=image>, 2019. Accessed: 02.06.2021.
- Sutherland, W. LII. The viscosity of gases and molecular force. *The London, Edinburgh, and Dublin Philosophical Magazine and Journal of Science*, 36(223): 507–531, 1893.
- Theon, J. S., W. Nordberg, and W. S. Smith. Temperature measurements in noctilucent clouds. *Science*, 157(3787):419–421, 1967.
- Thomas, G. E. Mesospheric clouds and the physics of the mesopause region. *Reviews of Geophysics*, 29(4):553–575, 1991.

BIBLIOGRAPHY

- Thomas, G. E. and C. P. McKay. On the mean particle size and water content of polar mesospheric clouds. *Planetary and Space Science*, 33(10):1209–1224, 1985.
- Tipler, P. A. and G. Mosca. *Physik: Für wissenschaftler und ingenieure*. Springer-Verlag, 2014.
- Tozer, W. F. and D. E. Beeson. Optical model of noctilucent clouds based on polarimetric measurements from two sounding rocket campaigns. *Journal of Geophysical Research*, 79(36):5607–5612, 1974.
- Turco, R. P., O. B. Toon, R. C. Whitten, R. G. Keesee, and D. Hollenbach. Noctilucent clouds: Simulation studies of their genesis, properties and global influences. *Planetary and Space Science*, 30(11):1147–1181, 1982.
- Verlet, L. Computer „experiments“ on classical fluids. I. Thermodynamical properties of Lennard-Jones molecules. *Physical review*, 159(1):98, 1967.
- Vincent, R. A. The dynamics of the mesosphere and lower thermosphere: A brief review. *Progress in Earth and Planetary Science*, 2(1):1–13, 2015.
- Vladimirov, V. A., M. R. E. Proctor, and D. W. Hughes. Vortex dynamics of oscillating flows. *Arnold Mathematical Journal*, 1(2):113–126, 2015.
- Volpe, G. and G. Volpe. Simulation of a Brownian particle in an optical trap. *American Journal of Physics*, 81(3):224–230, 2013.
- Volpe, G. and Volpe, G. Numerical simulation of Brownian particles in optical force fields. *Conference Paper. The international society for optical engineering*, 8810:358–363, 2013.
- Von Cossart, G., J. Fiedler, and U. Von Zahn. Size distributions of NLC particles as determined from 3-color observations of NLC by ground-based lidar. *Geophysical Research Letters*, 26(11):1513–1516, 1999.
- Voß, H. *Numerische Simulation*. Technical University of Hamburg-Harburg. Institut for numerical simulations, 2010.
- White, F. M. and J. Majdalani. *Viscous fluid flow*, volume 3. McGraw-Hill New York, 2006.

- Willeke, K. Temperature dependence of particle slip in a gaseous medium. *Journal of Aerosol Science*, 7(5):381–387, 1976.
- Wilms, H., M. Rapp, and A. Kirsch. Nucleation of mesospheric cloud particles: Sensitivities and limits. *Journal of Geophysical Research: Space Physics*, 121(3):2621–2644, 2016.
- Yin, C., L. Rosendahl, S. K. Kær, and H. Sørensen. Modelling the motion of cylindrical particles in a nonuniform flow. *Chemical Engineering Science*, 58(15):3489–3498, 2003.
- Zhao, Y., S. Hu, and Q. Wang. Simulation and analysis of particle trajectory caused by the optical-induced dielectrophoresis force. *Microfluidics and nanofluidics*, 16(3):533–540, 2014.

Danke

Ich möchte meinen besonderen Dank an Prof. Dr. Anna Hundertmark richten, für die Möglichkeit und Realisierung meiner Promotion. Danke, Anna, für Deine Unterstützung, die Diskussionen, die vielen Erklärungen, der Austausch und die gute Arbeitsatmosphäre. Dies alles hat zum Gelingen dieser Arbeit beigetragen. Danke für die Freiheit, die Du mir gegeben hast, in Bezug auf meine Forschung.

Mein weiterer besonderer Dank gilt Dr. Ralf Weigel, der mit diesem Forschungsprojekt auf unsere AG Numerische Simulation in Landau zugekommen ist. Ich möchte mich für eine Zusammenarbeit voller Hilfsbereitschaft, Unterstützung und Verlässlichkeit bedanken. Danke, Ralf, für die voranbringenden und fruchtbaren Diskussionen zu dieser Dissertation, für den fachlichen Input, aber auch die Lebensansichten, die Du mir mit auf den Weg gegeben hast.

Aus dem Mainzer *SPICE-Team* möchte ich zudem Thomas Böttger, Harald Rott, Christian von Glahn, Klaus Wilhelm und Prof. Dr. Konrad Kandler danken, ebenfalls für die unzähligen Diskussionen und regelmäßigen Besprechungen, welche den Entwicklungsprozess fundamental vorangebracht haben. Danke, Thomas, für die Zuverlässigkeit in der Erstellung von immer weiteren Geometriemodellen.

Ein weiterer Dank gilt der Arbeitsgruppe MORABA des Deutschen Zentrums für Luft- und Raumfahrt, hier vor allem Herr Oliver Drescher, die mit der Entwicklung des *High Atmosphere Soarers* die Grundlage für jegliche Messrealisierung geschaffen und die Geometriemodelle des Instrumentenmoduls als Basis dieser Arbeit geliefert hat.

Danke, Herr Rellum, für Ihre Unterstützung und für Ihre Begleitung, und dass Sie immer an mich geglaubt haben.

Danke, Marvin, dass Du mir die Kraft gabst, immer weiterzumachen und durchzuhalten. Danke für Deine Motivation und Deine immer positive Art.

Lebenslauf

Name Birte Salome Klug
Staatsangehörigkeit Deutsch



Schulausbildung

1999 – 2003 Grundschule Laumersheim
2003 – 2012 Karolinen Gymnasium Frankenthal
03/2012 Allgemeine Hochschulreife

Studium

2012 – 2016 B.Sc., Studium der Atmosphärenphysik am Institut für Physik der Atmosphäre, Johannes Gutenberg-Universität Mainz
2017 Erasmus Stipendium, Auslandssemester, UNIS; The University Centre in Svalbard, Spitzbergen, Norwegen
2015 – 2018 M.Sc., Studium der der Atmosphärenphysik am Institut für Physik der Atmosphäre, Johannes Gutenberg-Universität Mainz
Masterarbeit: *Numerical simulations of turbulence at a vertical wind tunnel*

Promotionsstudium

07/2019 Annahme als Doktorandin an der RPTU, Institut für Mathematik in Landau unter Betreuung von Prof. Dr. Anna Hundertmark

Berufstätigkeit

04/2018 – heute
Wissenschaftliche Mitarbeiterin, Promotionsstudentin und Dozentin am Institut für Mathematik der Rheinland-Pfälzischen Technischen Universität Kaiserslautern-Landau am Campus Landau

Forschung

Numerische Simulationen:
Entwurf und Entwicklung eines raketentragenen Aerosolsammlers mit COMSOL Multiphysics®

Publikationen

2019 The effect of turbulence on the accretional growth of graupel, with Jost A., Szakáll M., Diehl K., Mitra S. K., Hundertmark A., Borrmann S., *Journal of the Atmospheric Sciences*.
doi.org/10.1175/JAS-D-18-0200.1

2023 COMSOL® simulations of supersonic flow fields to study trajectories of aerosols and their impact efficiency on a rocket-borne particle collector, with Hundertmark A., Weigel R., *Comsol Conference 2023 Munich*. ISBN 978-1-7364524-1-7

Lehre

Eigene Vorlesungen, Klausuren und Übungen.
Lehrzertifikat des Fachbereichs Natur- und Umweltwissenschaften der RPTU als Preis für die beste von einer/einem befristeten Nachwuchswissenschaftler*in gehaltenen Lehrveranstaltung des evaluierten Studienjahres 2022 für die Veranstaltung *Übung Arithmetik*

08/2015 – 03/2018
Hilfswissenschaftlerin im Windkanallabor, Johannes Gutenberg-Universität Mainz

10/2015 – 02/2016
Übungsleiterin: Physik für Biologen und Geologen, Johannes Gutenberg-Universität Mainz